Strain Engineering of Ge/GeSn Photonic Structures

Ross W Millar

School of Engineering

University of Glasgow

A thesis submitted for the

Degree of Doctor of Philosophy

Oct 2016

Abstract

Silicon compatible light sources have been referred to as the "holy grail" for Si photonics. Such devices would give the potential for a range of applications; from optical interconnects on integrated circuits, to cheap optical gas sensing and spectroscopic devices on a Si platform. Whilst numerous heterogeneous integration schemes for integrating III-V lasers with Si wafers are being pursued, it would be far easier and cheaper to use the epitaxial tools already in complementary-metal-oxide-semiconductor (CMOS) lines, where Ge and SiGe chemical vapour deposition is used in a number of advanced technology nodes.

Germanium is an efficient absorber, but a poor emitter due to a band-structure which is narrowly indirect, but by only 140 meV. Through the application of strain, or by alloying with Sn, the Ge bandstructure can be engineered to become direct bandgap, making it an efficient light emitter. In this work, silicon nitride stressor technologies, and CMOS compatible processes are used to produce levels of tensile strain in Ge optical micro-cavities where a transition to direct bandgap is predicted. The strain distribution, and the optical emission of a range of Ge optical cavities are analyzed, with an emphasis on the effect of strain distribution on the material band-structure. Peak levels of strain are reported which are higher than that reported in the literature using comparable techniques.

Furthermore, these techniques are applied to GeSn epi-layers and demonstrate that highly compressive GeSn alloys grown pseudomorphically on Ge virtual substrates, can be transformed to direct bandgap materials, with emission $> 3\,\mu$m wavelength – the longest wavelength emission demonstrated from GeSn alloys. Such emission is modeled to have a good overlap with methane absorption lines, indicating that there is huge potential for the such technologies to be used for low cost, Si compatible gas sensing in the mid-infrared.

Publications

Journal Publications

1. F. Pezzoli, A. Giorgioni, K. Gallacher, F. Isa, P. Biagioni, **R.W. Millar**, E. Gatti, E. Grilli, E. Bonera, G. Isella, D.J. Paul, and L. Miglio "Disentangling nonradiative recombination processes in Ge micro-crystals on Si substrates" Applied Physics Letters 108 262103 (2016)
2. **R.W. Millar**, K. Gallacher, J. Frigerio, A. Ballabio, A. Bashir, I. MacLaren, G. Isella and D. J. Paul, "Analysis of Ge micro-cavities with in-plane tensile strains above 2 %" Optics Express 24(5), pp. 4365 - 4374 (2016)
3. K. Gallacher, A. Ballabio, **R. W. Millar**, J. Frigerio, A. Bashir, I. Maclaren, G. Isella, M. Ortolani, and D.J. Paul, "Mid-infrared intersubband absorption from p-Ge quantum wells grown on Si substrates" Applied Physics Letters 108, 091114 (2016)
4. **R.W. Millar**, K. Gallacher, A. Samarelli, J. Frigerio, D. Chrastina, G. Isella, T. Dieing and D.J. Paul "Extending the emission wavelength of Ge nanopillars to 2.25 μm using silicon nitride stressors" Optics Express 23(14), pp. 18193 - 18202 (2015)
5. P. Biagioni, J. Frigerio, A. Samarelli, K. Gallacher, L. Baldassarre, E. Sakat, E. Calandrini, **R.W. Millar**, V. Giliberti, G. Isella, D.J. Paul and M. Ortolani "Group-IV midinfrared plasmonics" Journal of Nanophotonics(1), 093789 (2015)
6. D.C.S. Dumas, K. Gallacher, **R.Millar**, I. MacLaren, M. Myronov, D.R. Leadley and D.J. Paul, "Silver antimony Ohmic contacts to moderately-doped n-type germanium" Applied Physics Letters 104, 162101 (2014)

Conference Papers

1. **R.W. Millar**, K. Gallacher ,J. Frigerio, A. Ballabio, A. Bashir, I. MacLaren, G. Isella , and D. J. Paul "Engineering Large Biaxial Tensile Strains in Ge Microdisks, Microrings and Racetrack Optical Cavities", ECS Transactions, Prime (2016).
2. K. Gallacher, A. Ballabio , **R.W. Millar**, J. Frigerio, A. Bashir, I. MacLaren, G. Isella, M. Ortolani, and D. J. Paul, "Mid-Infrared Intersubband Absorption from p-Ge Quantum Wells Grown on Si Substrates", ECS Transactions, Prime (2016).
3. **R.W. Millar**, K. Gallacher, A. Samarelli, J. Frigerio, D. Chrastina, T. Dieing, G. Isella and D.J. Paul, "Expanding the Ge emission wavelength to 2.25 μm with Si_xN_y strain engineering" Thin Solid Films 602, pp. 60 - 63 (2016)
4. **R.W. Millar**, K. Gallacher, J. Frigerio, D. Chrastina, G. Isella and D.J. Paul, "Highly strained Ge on Si microdisks with silicon nitride stressors" Proceedings IEEE Group IV Photonics 2015, pp. 65 - 66 (2015)
5. K. Gallacher, A. Ballabio, **R.W. Millar**, A. Samarelli, J. Frigerio, D. Chrastina, G. Isella, L. Baldassarre, M. Ortolani, E. Sakat, P. Biagioni and D.J. Paul, "Mid-infrared intersubband absorption in p- Ge/SiGe quantum wells grown on Si" Proceedings IEEE Group IV Photonics 2015, pp. 15 - 16 (2015)
6. **R.W. Millar**, K. Gallacher, A. Samarelli, D.C.S. Dumas, M. Myronov, D.R. Leadley and D.J. Paul, "Process induced tensile strain of Ge on Si nanopillars by ICP-PECVD SiN stressor layers" Proceedings of the IEEE Group IV Photonics, Paris, August (2014)
7. P. Velha, D.C. Dumas, K. Gallacher, **R.W. Millar**, M. Myronov, D.R. Leadley and D.J. Paul, "Strained germanium nanostructures on silicon mmitting at > 2.2 μm wavelength" Proceedings of 2013 IEEE 10th International Conference on Group IV Photonics (GFP) 2013

Acknowledgements

Firstly I would like to thank my supervisor Prof. Doug Paul for taking me on as a student, and for the support and guidance he has given me over the course of my PhD. I've greatly appreciated that he has always had an open door whenever I've needed assistance. Thanks to the The Engineering and Physical Sciences Research Council for funding my scholarship.

I would like to thank Dr. Kevin Gallacher for all the help and advice he has given me over the years, which has been invaluable. I am extremely grateful too, for the frequent assistance I've had from the Group's post-docs; Lourdes, Derek, Muhammad, Gary and previously Antonio, who have always been willing to discuss problems and provide guidance. I also thank my fellow PhD students, Francesco, Jarek, Emanuele, Nivedha, Richard and Ugne. I have also been fortunate enough, to benefit from the experience of countless helpful lab users. The staff in the James Watt Nanofabrication Centre, and in the Rankine building have been fantastic, and I thank them for ensuring the labs run smoothly, and for all their assistance.

I also could not have achieved these results without a number of collaborators. This includes the material growth experts at the L-Ness facility at the Politecnico Di Milano, and at the University of Warwick as well as Dr Aneeqa Bashir, Dr Ian MacLaren, and Dr Thomas Dieing. I thank them sincerely for all their effort, and input.

When I've escaped the lab, I've required the support and friendship of David, Scott, Chris, the Samsons, Neil, Ross, Alan, Adam, Fraser, Archie, and the Williams brothers. I thank my parents for their support and encouragement, which they have always given me, and is very much appreciated. Finally, I would like to thank my girlfriend Katie, whose patience and understanding has been immeasurable - I could not have done this without you!

Contents

List of Figures

1

Introduction

1.1 Introduction

For generations growing up this millennium, it will be difficult to imagine a time without the complete ubiquity of integrated circuits (ICs), which underpin almost every aspect of modern life. Such technologies have revolutionised industry, science, banking, the stock market, navigation, and the automotive industry, as well as personal devices such as smart-phones, tablets, laptops and games consoles. The growth of the internet has pushed world wide connectivity, with yearly traffic set to pass the zettabyte mark by the end of 2016 [16].

The building blocks for modern ICs were first developed in the 1960s using Ge and Si materials [17], and over the coming years ICs became denser, with smaller transistors and increased performance. Gordon Moore, the co-founder of Intel, predicted that this trend would continue for the foreseeable future. Specifically, he predicted that transistor dimensions, and the cost per transistor, would half approximately every 18 months, which has become known as "Moore's law" [1]. With reduced dimensions, denser, faster processors are delivered, providing an exponential increase in computing power. The so called 'law' is effectively self-fulfilling, with the superior performance driving demand and therefore spawning increased investment from manufacturers, who aim to keep pace with the prediction. While, to date, the transistor scaling has been on track, clock speeds have begun to saturate [18], Fig. 1.1, as huge power densities lead to significant heat generation [19]. In essence, performance is no longer scaling with dimensionality, the discrepancy being known as Moore's Gap. This led to a shift of focus, to the implementation of parallel

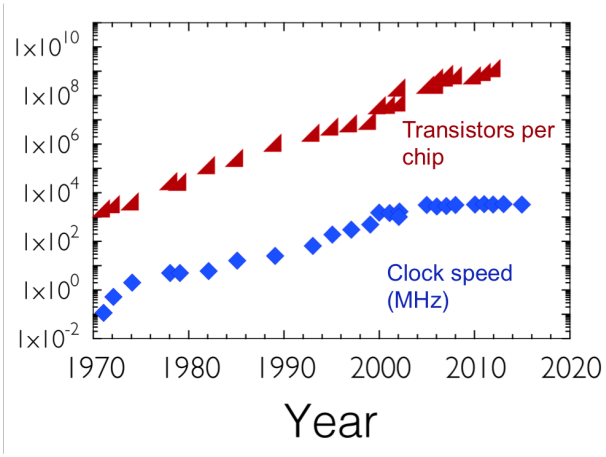

Figure 1.1: Clock speeds of ICs in MHz and the number of transistors per chip for a given year. Data from [1].

architectures, in the form of multi-core processors [20]. The theory being, that 4 cores operating at a given clock frequency, is approximately equivalent to a single core at 4 times the speed. This however, isn't without its own problems, as complex algorithms are required to effectively parallelise computation; a problem that will only worsen with the increased complexity that is brought with additional cores.

A major contributor to the bottle neck of processor speeds is the power dissipation from metal interconnects, which constituted 50 % of the power loss at the 50 nm node [21], and causes higher losses with smaller dimensions and higher frequencies, due to the skin effect and the resultant increase in resistance [22].

A potential solution is to use photons instead of electrons, in the form of optical interconnects, which have the potential to reduce heating, with other benefits such as reduced cross talk at high frequencies [23, 24]. In order to realise such photonics links, a full suite of photonics components would be required, with the requirement that they can be integrated in a manner which conforms with complementary metal oxide semiconductor (CMOS) processes. This would require active components including an electrically driven laser diode, modulators and photodiodes, as well as passive components such as waveguides to route the light on chip. Modulators [25], waveguides [26], and photodiodes [27] can already be achieved using Si and Ge; the missing link however, is the source. Unfortunately, the easily integrable Group IV materials are not efficient light-emitters due to band-structures that are unfavourable for radiative recombination. The conduction

band minima for Si and Ge are at a different momentum to the valence band maxima, i.e. they are indirect bandgap materials. This means that optical transitions across this bandgap require a phonon to conserve crystalline momentum, making these second order transitions less probable, and resulting in low radiative recombination efficiencies.

This is not the case with III-V materials, as almost all have conduction and valence band minima at the Γ point, and such devices have been used for efficient lasers at telecoms wavelengths for a number of years. While impressive performance has been achieved by III-Vs on Si [28,29], flip chip bonding techniques are generally used, which can often pose difficulties for alignment of sources to passive on chip optics. Recently, advances have been made with the heterogenous growth of III-Vs on Si substrate [30,31], however the typical materials such as Ga, As, Sb and P are dopants for Group IV materials, therefore causing a risk of contamination in CMOS fabrication. Furthermore, many of the III-V materials for lasers require rare materials such as indium, so finding a practical replacement which could be used on large wafers for future Si photonics is required.

Approaches have been taken to obtain Group IV lasers previously, with success in the form of all Si Raman lasers [32,33], and Erbium (Er) doped Si [34,35]. Neither approach, however, is appropriate for large scale integration, as the stimulated Raman scattering process has an inherent requirement for optical pumping. Erbium doped Si has shown lasing, however the solubility of Er in Si is low, and extremely high Q cavities are required for net optical gain.

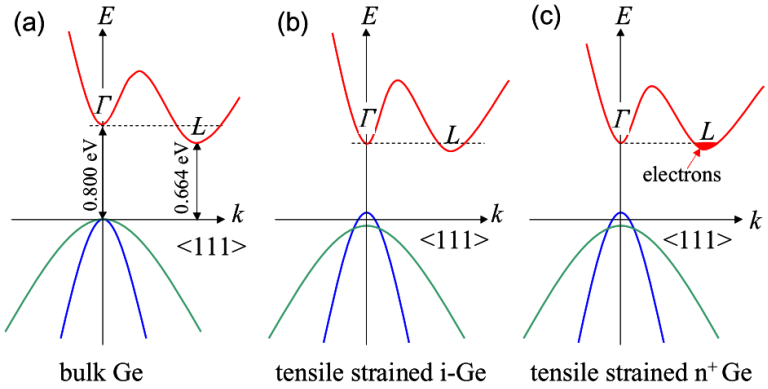

Figure 1.2: Diagrams of the band structure of Ge. The Γ to L energy difference reduces with strain and the light-hole becomes the ground state in the valence band. With n-type doping electrons fill the L valley. Image from [2].

Silicon is not just indirect, but significantly indirect, in that the direct Γ band is 2.3 eV above the 6 fold degenerate Δ-valleys [36]. With Ge however, the L valley is the conduction band minima, and is only ∼ 140 meV below the Γ. This modest energy difference means that electrically accessing this band is feasible. Degenerate n-type doping was employed by MIT in order to push the Fermi-level close to that of the Γ, as shown in Fig. 1.2, improving the occupation probability of injected carriers at the direct band. From degenerate doping, optically [37] and electrically [38] pumped Ge lasers were demonstrated operating ∼ 1550 nm, sparking a renewed interest in the prospect of a Ge source. These devices, however, had extremely high lasing thresholds, and comparable results have only been replicated by one research group [39].

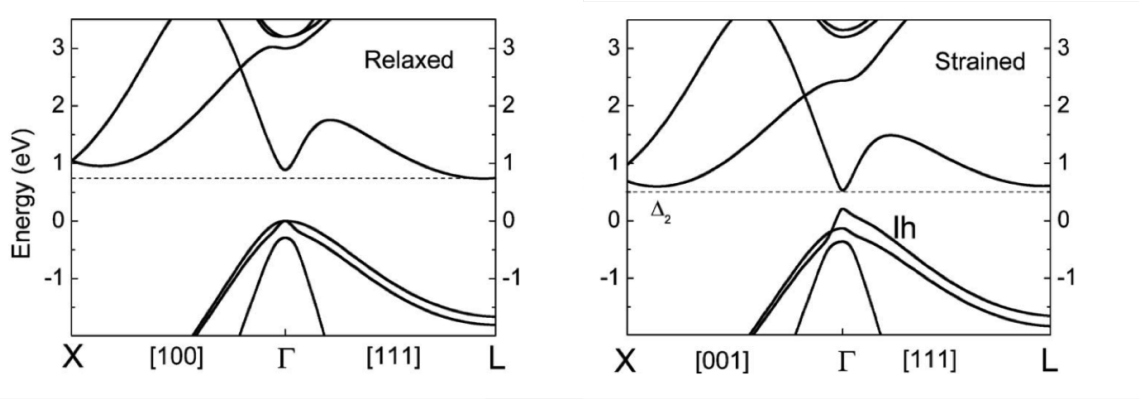

Figure 1.3: Bandstructure of unstrained and strained Ge calculated by a 30 x 30 band k.p model, showing the transition to a direct bandgap. Figures from [3].

As will be discussed in more detail in Chapters 2 and 3, aside from degenerate n-type doping, there are other means of making the Ge direct band accessible, and thereby lowering the lasing threshold by reducing free carrier losses. The application of biaxial or uniaxial tensile strain was predicted to move the Γ band to lower energies at a greater rate than the L-valley, thus transforming Ge to a direct bandgap material, at predicted biaxial tensile strains between 1.5 and 1.9 % [40–42]. The bandstructure under strain is shown in Fig. 1.3, highlighting this transformation. Given that silicon nitride stressor layers have been used for strain engineering in CMOS processes [43], the integration of strained Ge light sources using these technologies is an extremely interesting prospect.

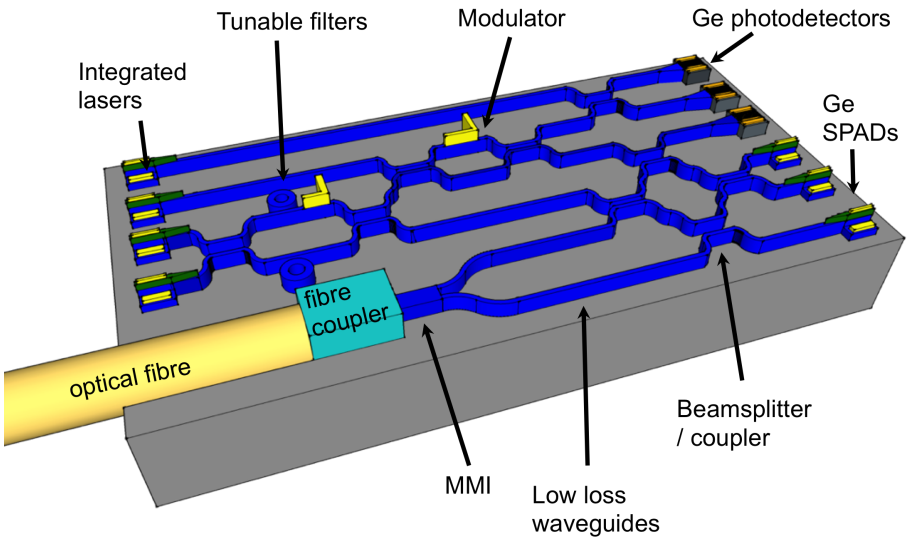

Figure 1.4: Illustration of an integrated optical circuit with active and passive optical components integrated monolithically.

An alternative, and more recent approach, is to alloy Ge with Sn. As will be introduced in Chapters 2 and 3, Sn is a semi-metal, which upon alloying with Ge moves the bands in a similar manner to hydrostatic tensile strain. With a sufficiently high enough Sn content, the alloy has been shown to become direct bandgap [11], and lasing has been demonstrated at low temperatures [11, 12]. The application of external strain could can further enhance the direct-bandgap, and potentially provide the ultimate goal of room temperature lasing, by increasing the carrier concentration at the Γ-valley.

Already, Ge is used in CMOS processes in strained SiGe channels, and with the highest hole mobility of all semiconductors, it has been touted as a replacement channel material for future nodes [44]. Therefore, the ability to band-engineer Ge through strain or Sn alloying, has the potential to make efficient light emitters that lead to a fully compatible and monolithic electronics and photonics platform. Aside from on chip or chip to chip optical communication, such a feat could open doors to fully integrated optical circuits, allowing for passive and active photonics components to be integrated in a low cost Si platform, illustrated in Fig. 1.4.

The amount of strain or Sn alloying required to lower lasing thresholds to acceptable levels, will determine the associated technology required for such optical circuits. This

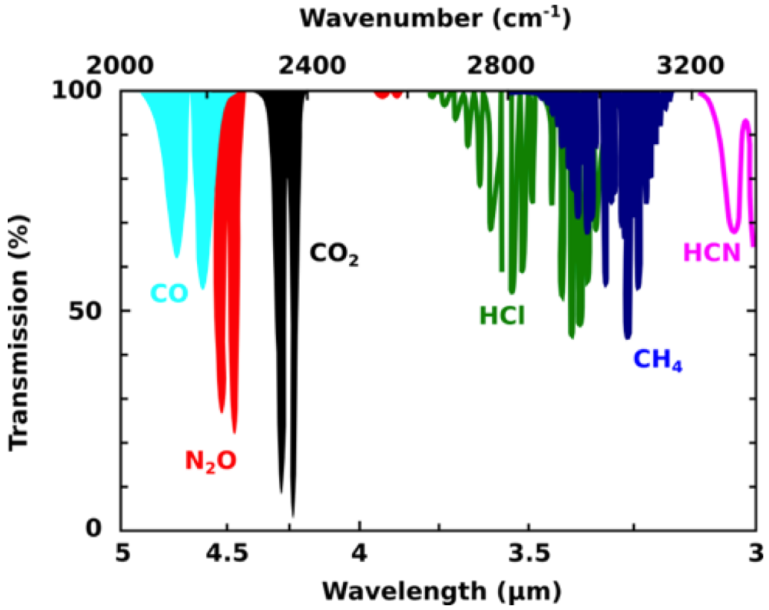

Figure 1.5: Transmission of a number of molecules in the mid-infrared, showing absorption in the 3 - 5 μm window.

is due to the associated red-shift of emission brought with both techniques. Silicon on Insulator (SOI) technologies have been shown to be low loss up to 3.39 μm [45], however at longer wavelengths there is potential to use unstrained Ge for passive optics, which remains transparent past 10 μm wavelength [46]. Such optical circuits could still be suitable for on chip or chip-to-chip communication, but could not be directly integrated with long haul fiber communication networks operating at 1550 nm wavelength.

The red-shift of the direct band emission with strain and increasing Sn content can also potentially allow for optical sources with a tuneable emission wavelength. Using a combination of these techniques can potentially lead to emission in the mid-infrared (MIR). The MIR sensing market alone is expected to reach $7 billion by 2019 [47], and has a a huge range of applications including medical diagnostics, pollution monitoring and explosives and chemical warfare detection. Currently, such sensing systems require expensive sources such as quantum cascade lasers [48]. Particularly for highly strained GeSn alloys, there is a real possibility of obtaining emission in the 3 - 5 μm sensing window, Fig. 1.5. With CMOS compatibility, such devices can potentially leverage the benefits that come from very large scale integration (VLSI) to provide cheap MIR light sources.

1.1.1 Thesis Outline

The Chapters in this thesis are organised as outlined below.

- **Chapter 2** - The relevant theory for this work is introduced. An overview is given for the origin of band-structures in crystals, with a particular emphasis on the physics of optical transitions, such as spontaneous emission, absorption and gain. The bandstructure of Ge is discussed, and it is shown why inherently Ge is a poor emitter. The ways to improve the light emitting properties of Ge are shown with regard to strain and Sn alloying, and how both techniques have the possibility to make Ge a direct bandgap material.

- **Chapter 3** - The literature is reviewed, discussing the various techniques that have been employed to improve the light emitting properties of Ge(Sn). With regard to strain engineering, the focus is primarily on the light emitting properties of Ge. Subsequently the challenges of GeSn growth are discussed, and presented along with recent progress with GeSn light emitters.

- **Chapter 4** - The fabrication, characterisation and growth techniques employed in this work are presented in this chapter.

- **Chapter 5** - This chapter presents the characterisation of high stress silicon nitride layer, and shows their application to square topped Ge nanopillar structures. Photoluminescence is measured from the strained pillars, with emission past 2 μm demonstrated; a hallmark of progression towards direct bandgap. The strain is characterised by Raman spectroscopy, and finite element models are used to provide an insight into strain distributions in the structure. Finally, band structure modelling is carried out showing the benefits of a hydrostatic strain component induced by sidewall stressors.

- **Chapter 6** - Micro-disk, ring and racetrack cavities are demonstrated using novel wet etching techniques. The cavities are stressed by high stress silicon nitride layers. It is shown that strain at the top plane can reach a level where a transition to direct bandgap is expected, >2 %. The cavities are characterised by Raman spectroscopy, and the differences between the in-plane uniformity and strain transfer for the different cavity types is discussed, with an emphasis on the effect on the bandstructure.

The effects of off diagonal shear strain components on the carrier concentration at the direct band gain is calculated and discussed.

- **Chapter 7** - Pseudomorphic GeSn alloys grown on Ge virtual substrates are characterised by temperature dependent photoluminescence, Raman and X-ray diffraction. GeSn on Ge microdisk structures are fabricated using the wet-etching techniques developed in Chapter 6. The cavities are strained, and it is shown that the alloys can be taken from highly compressive to tensile. The strained emission is upwards of 3 μm and is shown to have a good overlap with a methane absorption line, highlighting the potential of strained GeSn for gas detection in the mid-infrared. Raman spectroscopy, and the temperature dependence of the photoluminescence suggests that the strained materials are direct bandgap.

- **Chapter 8** - The conclusions of this work are given, and the future work required is discussed.

2

Theory and literature review

2.1 Bandstructure

In order to understand the optical properties of a material, the band structure has to be understood, which requires a quantum treatment of crystals. In this chapter, a brief summary will be given of the band structure in crystals by means of the nearly free electron model and k.p theory. Subsequently, an overview will be given of the physics of optical transitions in semiconductors. These will then be discussed with regard to the Ge band structure, and the challenges of making an efficient Ge light emitter will be discussed. Basic concepts of stress and strain will be then introduced and discussed as a means for improving the light emission properties of Ge and GeSn structures.

2.1.1 Crystals

A crystal is defined as the combination of a lattice, and a basis. The theoretical lattice is an infinite, perioidic structure, which can be described with lattice vectors, Eq 2.1. These types of lattice form a Bravais lattice, which when repeated, fill all space. This can be generated by a lattice vector r', where n_i are integers, and a_i are primitive vectors:

$$r' = n_1 a_1 + n_2 a_2 + n_3 a_3 \tag{2.1}$$

Equation 2.1 indicates that the lattice can be translated by a lattice vector without changing it, i.e. the view of the lattice from a point remains the same after a translation.

The lattice can be viewed as a host for a secondary structure, known as the basis, which sits at every lattice point. The combination of the lattice and the basis forms the crystal.

Frequently it is convenient to describe a lattice in reciprocal space, which can simplify the mathematics describing interactions of waves with the structure. This is achieved with the use of reciprocal lattice vectors, each of which define a set of planes in real space. The reciprocal lattice vector direction is defined such that it is perpendicular to the set of planes it describes, and the length of the vector is inverse to the plane spacing. It is therefore similar to a wavevector in that it describes a spatial frequency.

The set of reciprocal lattice vectors are defined in terms of the real space directions, such that:

$$b_1 = \frac{2\pi a_2 \times a_3}{a_1.a_2 \times a_3} \ , \ \ b_2 = \frac{2\pi a_3 \times a_1}{a_2.a_3 \times a_1} \ , \ \ b_3 = \frac{2\pi a_1 \times a_2}{a_3.a_1 \times a_2} \tag{2.2}$$

These vectors have the property that:

$$b_i.a_j = 2\pi\delta_{ij} \tag{2.3}$$

The set of reciprocal vectors can be used to generate a reciprocal lattice, using Eq. 2.4, similarly to how the set of real vectors defined the real space lattice. Here, G is a reciprocal lattice vector, and h,k and l are integers. This construct is convenient for determining the properties of the material, for example when describing Bragg scattering in crystals, and more generally for representing crystal planes by means of a Fourier series expansion, which mathematically simplifies dealing with electron-crystal interactions. The periodicity of the lattice ends up having a number of ramifications for the band structure.

$$G = hb_1 + kb_2 + lb_3 \tag{2.4}$$

2.1.2 Schrodingers Equation

Following the discovery of the photoelectric effect, which showed light has particle like behaviour, De Broglie hypothesised that electrons should also exhibit wavelike behaviour. Using Einstein's relationship, $E = cp = mv^2$ and $E = \hbar\omega$, (where c is the speed of light, p the momentum, $\hbar$ is planks reduced constant and ω is the frequency) he proposed that the wavelength of the electron is inversely proportional to its momentum, resulting in the de Broglie relation, expressed in Eqs. 2.5 and 2.6:

$$\lambda = \frac{h}{p} \tag{2.5}$$

$$k = \frac{2\pi}{\lambda} = \frac{2\pi p}{h} = \frac{p}{\hbar} \tag{2.6}$$

The wavelike behaviour of the electron was confirmed experimentally in 1927 by Clinton Davisson and Lester Germer [49], who showed a diffraction pattern of electrons fired at a crystalline nickel target; a property that only waves should exhibit. This means that the electron can be described by a wave equation, such as the Helmholtz wave equation, which gives solutions such as ψ= sin(kx), cos(kx) and exp(ikx), with wave vectors k describing their spatial frequency and therefore wavelength. The wave vector is therefore related linearly to the particle's momentum through de Broglie's relationship, Eq 2.5. The wave equation for electron waves can therefore be shown as Eq 2.7.

$$\frac{\partial^2 \psi}{\partial x^2} = -k^2 \psi \tag{2.7}$$

By substituting de Broglies relationship, Eq 2.6 into 2.7, the wave-function can then be expressed as in terms of the particle's momentum.

$$\hbar^2 \frac{\partial^2 \psi}{\partial x^2} = p^2 \psi \tag{2.8}$$

Subsequently dividing both sides by $2m$ (where m is the electron mass) yields the classical expression for kinetic energy, suggesting that the operation on the wave function on the left hand side of Eq. 2.9 , is equivalent and also is an expression of kinetic energy.

$$\frac{\hbar}{2m} \frac{\partial^2 \psi}{\partial x^2} = \frac{p^2}{2m} \psi = Kinetic\,Energy \ \times \ \psi \tag{2.9}$$

Given that the Total Energy = Kinetic Energy + Potential energy, this gives some intuition for the postulation of the time independent Schrodinger equation, in Eq 2.10, where $V(r)$ is the potential, and E is the total energy.

$$\Big(\frac{-\hbar}{2m} \frac{\partial^2}{\partial x^2} + V(r)\Big)\psi(r) = E\psi(r) \tag{2.10}$$

The time independent Schrodinger equation therefore describes how the wave function of an electron is related to its total energy. The wave function of a particle cannot be directly measured, however the square of the wave function give the probability of finding

an electron at a position, x. Therefore, the squared wavefunction is a probability density function, Eq. 2.11.

$$|\psi(x,t)|^2 = \psi(x,t) \times \psi(x,t)^* = \rho(x,t) \tag{2.11}$$

2.1.3 Nearly free electron model

The Schrodinger equation shows that the potential $V(r)$ influences the total energy of the electron. Therefore, in order to examine the energy states of electrons in crystals, the periodic coloumbic potential from the ion cores has to be described. Given that the potential is periodic, and V(x) = V(x+R), where R is a lattice vector, it can be expanded as a Fourier series in the reciprocal lattice vectors, which therefore have the periodicity of the lattice, Eq 2.12.

$$V_g(x) = \sum_G V_G e^{iGx} \tag{2.12}$$

A 1-dimensional crystal, containing N unit cells of length d is used as an example. Mathematically it is suitable to use periodic boundary conditions, i.e. $\psi(x) = \psi(x+Nd)$. This sets conditions on the allowed wave vectors for the wave function, k, which have to be an integer number of $2\pi/Nd$. The wave function can therefore be expanded as a discrete Fourier series in k, as shown in Eq. 2.13, where C_k are Fourier coefficients.

$$\psi(x) = \sum_k C_k e^{ikx} \tag{2.13}$$

Substituting both the Fourier expansions, Eqs. 2.12, 2.13 for the wave function and the potential into the time independent Schrodinger equation therefore gives:

$$\sum_k \frac{(\hbar.k)^2}{2m} C_k e^{(ikx)} + \sum_k \sum_G C_k V_G e^{(i(k+G)x)} = E \sum_k C_k e^{(ikx)} \tag{2.14}$$

The summation variables can be substituted to k = k' - G, which will still sum over every element of the double sum, merely in a different order. Given the fact this is still a sum to infinity, the variable k' can in fact be relabelled as k, yielding the following:

$$\sum_k e^{(ikx)} \left(\left(\frac{(\hbar.k)^2}{2m} - E \right) . C_k + \sum_G C_{k-G} V_G \right) = 0 \tag{2.15}$$

For non-trivial solutions, the bracketed term must equal zero:

$$\frac{(\hbar.k)^2}{2m}C_k + \sum_G C_{k-G}V_G = EC_k \tag{2.16}$$

This results in the Central Equation, Eq. 2.16, which shows that electrons with wave vector k are coupled to all other electrons whose wavevectors only differ by an integer number of G, the reciprocal lattice vector. Furthermore it shows that the degree of this coupling depends on the Fourier coefficients of the periodic potential.

The Fourier expansion of the wave function can therefore be limited to values of k separated by reciprocal lattice vectors.

$$\psi(x) = \sum_G C_{k-G}e^{i(k-G)x} = e^{(ikx)}\sum_G C_{k-G}e^{(iGx)} = e^{(ikr)}u_k(r) \tag{2.17}$$

This directly leads to Bloch's theorem, which states that the wave function can be expressed as a plane wave and a function which has the periodicity of the lattice. This has important ramifications for the optical transitions of electrons in semiconductors and is discussed in a later section of this chapter. Bloch's theorem also highlights that an electron does not have just one k-vector that can be associated with its momentum, as shown in the Fourier expansion.

2.1.4 1D Bandstructure

In order to calculate a 1D band structure, a simple periodic potential could be chosen, such as a cosine function:

$$V(x) = 2Vcos(x) = V(e^ix + e^{-i}x) \tag{2.18}$$

The central equation is therefore replaced by:

$$\frac{\hbar^2(k+nG)^2}{2m}C_{k+nG} + VC_{k+(n-1)G} + VC_{k+(n+1)G} = EC_{k+nG} \tag{2.19}$$

The set of simultaneous equations generated by Eq. 2.19 can be solved as an eigenvalue problem. For a given value of k, the eigenvalues give a number of solutions each with different energy. Computing a range of k values then leads to smooth bands. For k $> \frac{\pi}{a}$ the band structure is periodic and therefore for lower k all the information of the bands

is contained. This region is known as the first Brillioun zone. The wavevector in Bloch's theorem for the plane wave term is always within the 1st Brillioun zone, and this value of k defines the crystaline momentum $\hbar k$. Comparing band structures with and without a potential, Fig. 2.1, it is clear that the potential causes energies where there are no available solutions, i.e bandgaps. The magnitude of the gap is related to the size of the potential, in this case 2V.

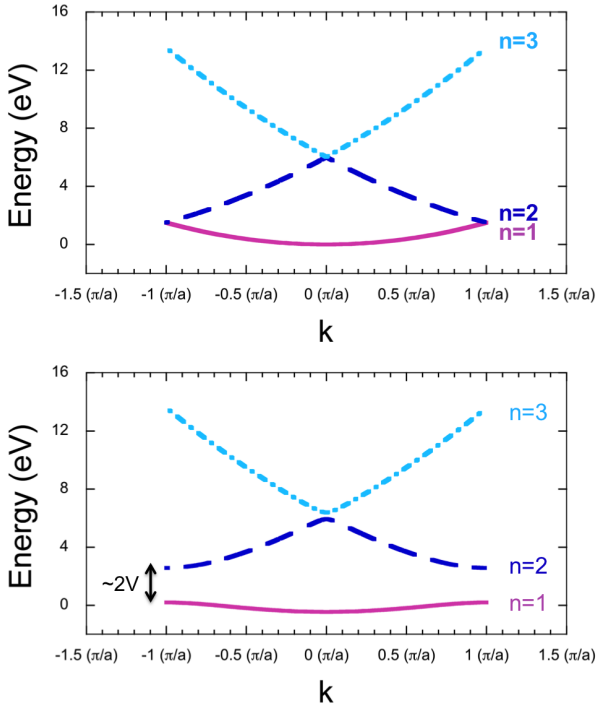

Figure 2.1: Band structures of a 1D lattice with a cosine potential calculated using the nearly free electron model. Top - the potential is set to zero and no bandgaps are present. Bottom - The potential is set to V and bandgaps are opened at the brillioun zone edge.

The formation of bands can equivalently be described by the creation of standing waves in the crystal, which occur when the wave functions are Bragg scattered. This leads to two counter propagating waves which form a standing wave with two possible solutions, sin(kx) and cos(kx). As shown in Eq. 2.11, the squared wave function gives the probability density of the electron's position and therefore the two standing waves lead to a build up of charge in two locations, one of which is close to an ion core, where it will feel a strong potential, and an other in between ions, where the potential energy is

minimum. Therefore, a splitting in energy occurs. In general, where a Bragg condition is met there will be a splitting in energy and the formation of a bandgap. In 1 dimension, the Bragg condition can be shown in the reciprocal lattice, by marking the points that $k = \frac{\pi}{a}$. As explained previously, this defines the Brillouin zone, and describes the full crystal structure completely. This can be extended to 3 dimensions, and is shown in Fig 2.2. In a 3D representation of the Brillouin zone, each plane represents a set of k vectors for which the wave function will be Bragg scattered, and bandgaps will be formed.

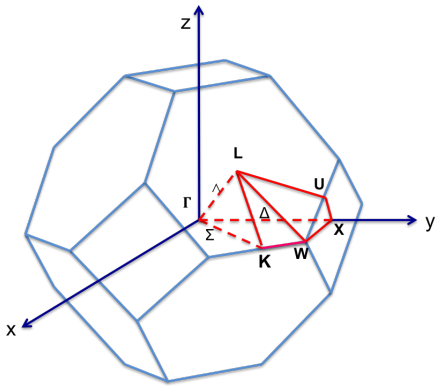

Figure 2.2: The first Brillouin zone of Ge showing the points of high symmetry. Each plane indicates where an electron will be Bragg scattered and therefore where a bandgap will be opened.

In the simple band structure example given the minimum of the conduction band and the maximum of the valence band occur at the same point in k-space. This defines a direct bandgap material. In an indirect material the respective maximum and minimum are at different points in k space. As will be shown in the remainder of the chapter, this defines a number of the optical properties of semiconductor devices.

2.1.5 k.p perturbation theory basics

In practise, the nearly free electron model is not used to compute real band structures, and other methods are used such as k.p perturbation theory. As shown in the nearly free electron model, a full description of the potentials is required in order to obtain the Fourier coefficients of the Bloch waves. In practise it is sufficient to have a knowledge of the dispersion near the band edges, as this is where the majority of the carriers will lie -

this is what is calculated with k.p theory. The principle is based on the fact that for a given value of k, the cell periodic part of the wavefunctions, u_{mk}, for each band form a complete orthonormal set, where k is a wave vector and m is a band index. This allows an arbitrary wave function, at a different k to be expressed as a Fourier series in u_{mk}, where m is a band index and k is a wave vector in the 1st Brillioun zone. For example, using the set formed by the cell periodic functions at k = 0, u_{m0}. The Bloch waves are:

$$\psi = u_{mk}(r)exp(ik.r) = \left[\sum_m c_m u_{mo}(r)\right] exp(ik.r) \tag{2.20}$$

Expanding the Schrodinger equation in terms of the Bloch waves gives rise to the k.p term:

$$\left[-\frac{\hbar^2}{2m_o}\nabla^2 + \frac{\hbar^2 k^2}{2m_o} + \frac{\hbar}{m_o}k.p + V(r)\right] u_{mk}(r) = E_n(k)u_{nk}(r) \tag{2.21}$$

When k = 0 this can be expressed as:

$$\left[-\frac{\hbar^2}{2m_o}\nabla^2 + V(r)\right] u_{mk}(r) = E_n(0)u_{nk}(r) \tag{2.22}$$

The solutions of Eq. 2.22 form a complete orthonormal set. As indicated by Eq. 2.20, this allows the solutions at k $\neq$ 0 to be expressed in terms of the k=0 solutions for a number of other bands, using perturbation theory. For instance, for a band structure with a minimum at E_{m0}, the Bloch functions at u_{mk} can be expressed in terms of the solutions at u_{m0}.

$$u_{mk} = u_{mo} + \frac{\hbar}{m}\sum_{n\neq m}\frac{k.p_{mn}}{E_{m0} - E_{n0}}u_{no} \tag{2.23}$$

Similarly for the energy:

$$E_{mk} = E_{mo} + \frac{\hbar^2 k^2}{2m} + \frac{\hbar^2}{m^2}\sum_{n\neq m}\frac{k.p_{mn}^2}{E_{m0} - E_{n0}} \tag{2.24}$$

Where p_{nm} is the optical matrix element, which introduces coupling between the bands:

$$p_{nm} = \int_{V_c} u_{m0}\ p\ u_{n0}\ d^3r \tag{2.25}$$

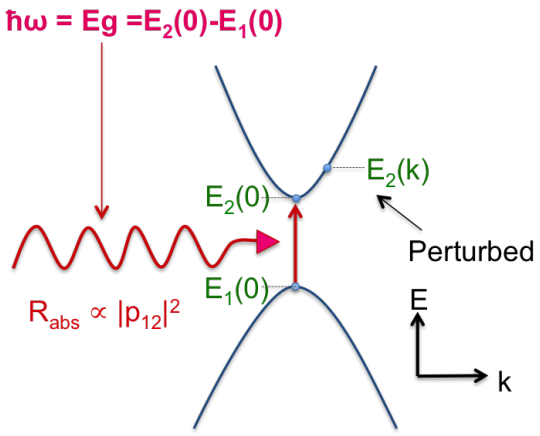

Figure 2.3: Diagram indicating how in a 2 band k.p model, the energy of the states at k=0 can be used along with the momentum matrix element to find a state at a different value of k.

The dispersion can therefore be given by expressing the perturbation as an effective mass term, shown in Eq. 2.26 and 2.27. This highlights that the effective mass has a dependence on the coupling between the bands, as well as the bandgap.

$$E_{mk} = E_{mo} + \frac{\hbar^2 k^2}{2m^*} \tag{2.26}$$

$$\frac{1}{m^*} = \frac{1}{m} + \frac{2}{m^2 k^2} \sum_{n \neq m} \frac{k.p_{mn}^2}{E_{m0} - E_{n0}} \tag{2.27}$$

This indicates why k.p theory can be useful. In order to calculate a state E_{nk}, knowledge of the energies at k=0 are required, plus the momentum overlaps shown in Eq. 2.25. Both the energies at k=0, and the matrix elements can be measured experimentally fitting to optical absorption measurements, as illustrated in Fig. 2.3. Following the development of k.p theory, Luttinger and Kane extended the model to include the effects of spin orbit interaction, and later Pikus and Bir included strain effects in the model, which are discussed later.

2.2 Optical transitions in semiconductors

2.2.1 k-selection rules

The optical processes of interest for this work are absorption, spontaneous emission, and optical gain. All of these processes are described by the interaction of electromagnetic radiation with the crystal, and each involves changing the energy state of an electron to either absorb or emit electromagnetic radiation, Fig. 2.4.

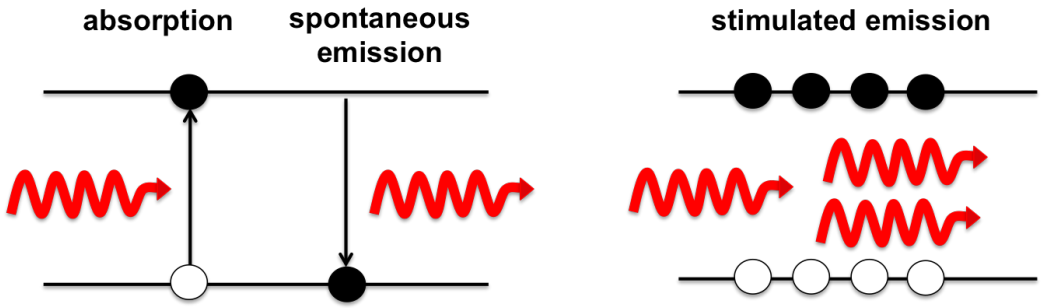

Figure 2.4: Sketch showing absorption, spontaneous and emission processes in semiconductors. The upper line represents a conduction band, and the lower the valence band. When light is absorbed an electron is promoted from the valence to the conduction band, leaving behind a hole. For spontaneous emission an electron recombines with a hole to emit a photon. For stimulated emission, population inversion is required and light is amplified.

Changes of state can be described by Fermi's golden rule, based on a 2^{nd} order perturbation theory, which treats the electromagnetic field as a perturbation to the energy of an electron. The scattering rate of an electron from an initial state to a final state due to the absorption of a photon can be shown as:

$$w_{fi} = \frac{2\pi}{\hbar}\langle\psi_f|\hat{H}_{po}|\psi_i\rangle^2\delta(E_{fi} - \hbar\omega) \tag{2.28}$$

Where $\hat{H}_{po}$ is the perturbing hamiltonian, ψ_f and ψ_i are the final and initial states respectively, and E_{fi} is the energy difference between the final and initial states. Other symbols have their usual meanings.

The initial and final wave functions can be expressed as Bloch states, and the perturbing hamiltonian due to an electromagnetic field is shown to be related to the vector potential with amplitude A_o, as shown in Eq 2.30.

$$\psi_i = u_v(r)e^{ik_i.r}, \qquad \psi_f = u_c(r)e^{ik_f.r} \tag{2.29}$$

$$\hat{H_{po}} = \frac{-eA_o e^{(ik_{op}.r)}}{2m_o} e.\hat{p} \tag{2.30}$$

The overlap integral of the initial and final states is then:

$$\langle \psi_f | \hat{H_{po}} | \psi_i \rangle = -\frac{eA_o}{2m_o} \int [u_v(r)e^{ik_i.r}]e^{ik_{op}.r} e.\hat{p}[u_c(r)e^{ik_f.r}]d^3r \tag{2.31}$$

where, k_{po} is the photon wave vector, and k_i and k_f are the wave vectors of corresponding to the initial and final Bloch states, m_o is the electron mass, When evaluating this integral, it can be shown that due to orthogonality of the Bloch functions that there will only be absorption when:

$$k_i - k_f + k_{op} = 0 \tag{2.32}$$

The photon wavevector is negligibly small compared to the crystalline momentum, therefore the requirement for absorption becomes:

$$k_i \approx k_f \tag{2.33}$$

This shows that the conservation of crystalline momentum is a fundamental selection rule in the optical transitions in semiconductor materials. Within the first Brillouin zone, this transition would be shown as a vertical line on an E-k dispersion plot. Here the conservation of spin and angular momentum is not explicitly detailed. For interband transitions in this work it is assumed that electron spin is conserved. Angular momentum can be considered by treating the symmetry of the Bloch functions in spherical coordinates, which also has ramifications for the momentum overlap integrals, and leads to further selection rules. In the following sections, where Fermi's golden rule is used to calculate absorption and emission processes, the angular momentum and spin conservation can be accounted for fully by the matrix element, p_{cv} ,which can be calculated using 8x8 k.p methods.

2.2.2 Absorption

As shown above, the momentum overlap of the Bloch states in the conduction and valence bands mean that crystalline momentum has to be conserved in an optical transition. With regard to absorption, in semiconductors, this condition is met easily in direct bandgap materials, however, as shown in Fig.2.5, a phonon is required to absorb at energies corresponding to the indirect band. The requirement for phonon emission or absorption means that transition probabilities are reduced compared to direct bandgap materials.

The selection rule for indirect transitions is modified to:

$$k_i - k_f + k_{phonon} = 0 \tag{2.34}$$

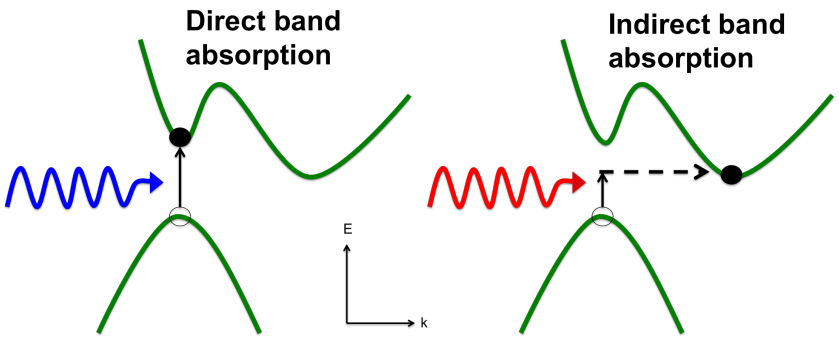

Figure 2.5: Band diagram sketch showing absorption at the direct band (left) and at the indirect band (right). Direct processes represent a vertical transition in k-space. Indirect processes require a phonon to conserve crystalline momentum.

The absorption coefficient is proportional to the transition rates calculated by Fermi's golden rule, however, it also depends on the density of states in the conduction and valence bands. Under the assumption of parabolic bands, this can be expressed using a reduced mass term, Eq. 2.35, which effectively allows the separate densities to be expressed as a joint density.

$$m_r^{-1} = m_c^{-1} + m_v^{-1} \tag{2.35}$$

The joint density of states can therefore be expressed as:

$$g(\omega) = \frac{1}{2\pi}\left(\frac{2m_r}{\hbar^2}\right)^{3/2}(\hbar\omega - E_g)^{1/2} \tag{2.36}$$

The total absorption coefficient is given in Eq. 8.1 . This model assumes that there is zero occupation in the conduction band and full occupation in the valence band. In practise the absorption has to be integrated over the valence band states, including the polarisation dependence of the matrix elements where appropriate.

$$\alpha(\hbar\omega) = \frac{\hbar e^2}{2\pi m_o c\varepsilon_o}\frac{1}{n_r}\frac{|p_{cv}|^2}{m_o}\left(\frac{2m_r}{\hbar^2}\right)^{3/2}(\hbar\omega - E_g)^{1/2} \tag{2.37}$$

The absorption coefficient can be used by Beer's law to describe the exponential decay of light based in an absorbing material:

$$I(z) = Io \times exp(-\alpha(\hbar\omega)z) \tag{2.38}$$

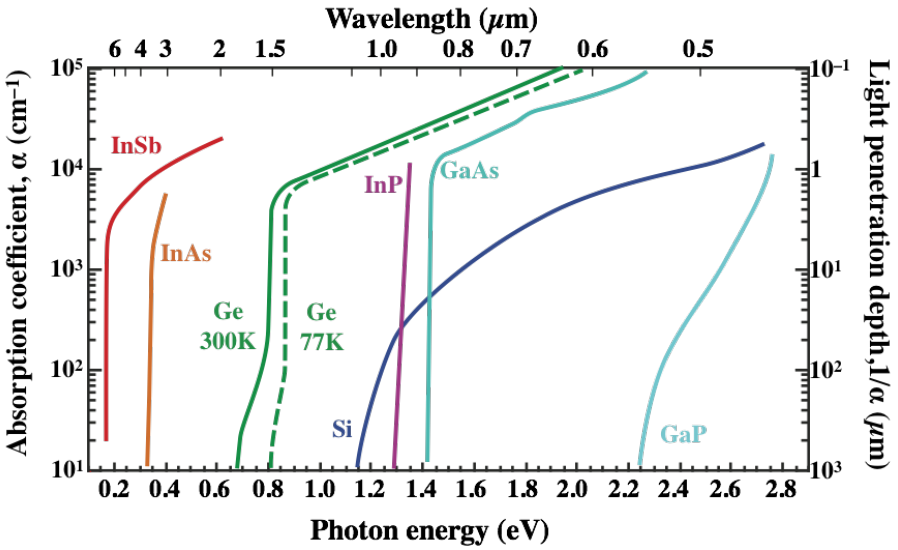

Figure 2.6: Fitted absorption coefficients for a range of semiconductors, as a function of energy (wavelength). The penetration depth is also given. Data from [50].

When the light has propagated a distance z = $\alpha(\hbar\omega)$, the intensity has been reduced by 1/e ($\approx$ 37 %) the initial intensity. This is frequently used as a figure of merit for the absorption of semiconductor materials. Figure 2.6 shows the absorption coefficients for a range of semiconductor materials.

2.2.3 Spontaneous Emission

Spontaneous emission is the reverse process of absorption whereby a material emits light by the recombination of excited electron hole pairs, Fig. 2.7. These electron hole pairs can be injected optically (i.e. by the absorption of light) or electrically, the emission from which is described as photoluminescence, and electroluminescence respectively. Electroluminescence is the working principal of LEDs, for example.

As described above, the transition rate can be derived from Fermi's Golden rule, and leads to a relationship showing that the spontaneous transition rate is proportional to the joint probability of occupation of an electron in the conduction band and a hole in the valence band, with their energy difference equal to the emitted photon energy. This can be expressed as:

$$R(\hbar\omega) = \frac{n_r \omega e^2}{3\pi c^3 \hbar \varepsilon_o m_o^2} \frac{1}{(2\pi)^3} \int |p_{cv}(k)|^2 f_c(1 - f_v)\delta(E_c(k) - E_v(k) - \hbar\omega) d^3k \qquad (2.39)$$

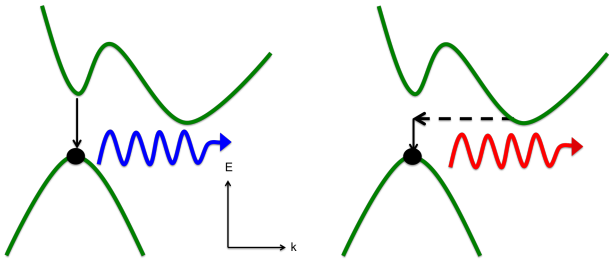

Figure 2.7: Band diagram sketch showing spontaneous emission in semiconductors. Direct transitions are vertical in k-space while indirect transitions require a phonon to conserve crystalline momentum. Photons are emitted as electrons recombine with holes.

Under continuous optical or electrical injection for example, the electron concentration (hole) concentration in the conduction (valence) band can be increased substantially. While initially the carriers may have kinetic energies significantly higher than the average thermal energy of the material, they quickly thermalise towards the band-edge via phonon scattering process, and reach an equilbrium within that band. This distribution of carriers can no longer be described by a single Fermi-function, however quasi Fermi levels can be used to described the carrier distribution within the band. There are therefore electron and hole quasi Fermi levels that describe the carrier distribution under injection. By

knowing the carrier distribution and the density of states, the spontaneous emission at a single wavelength can be calculated by integrating over all the energy states corresponding to a given photon energy. The wavelength of photo or electroluminscense therefore gives an indication of the bandgap.

Much like with absorption, for indirect processes k-selection rules dictate that a phonon has to take part in the process in order to change the momentum of the recombining electron. The phonon does not only change the momentum of the particle, but can increase or decrease the energy of the particle before radiative recombination. As a result, emission peaks tend to be broader, and there is also the possibility to absorb or emit photons with energy below the bandgap, as the missing energy is accounted for by the phonon.

2.2.4 Optical gain

The third optical process of relevance is optical gain by stimulated emission. Under optical or electrical injection, electrons begin to populate the conduction band edge, and holes populate the valence band edge. If the injection is sufficiently high, the electron and hole quasi Fermi levels move into the conduction and valence bands respectively. At the point where there are more carriers in an excited state than in unexcited states, this can be described as population inversion.

With increased injection, no further absorption is possible as there are no available electrons to be promoted from the valence band, and no available state for an electron to be promoted to in the conduction band, leaving the material transparent. Above transparency, gain by stimulated emission can occur. An electron can be stimulated to recombine with a hole by an incoming photon, and the photon emitted by this transition can trigger a subsequent recombination, thus providing optical gain in the condition that population inversion can be maintained. This process can be viewed as a negative absorption coefficient, Eq. 2.40.

$$g(\hbar\omega) = -\alpha(\hbar\omega) \tag{2.40}$$

The requirement for population inversion can be seen by the Bernard-Duraffourg condition. Stimulated emission and absorption are competing processes which depend on the Einstein coefficients B_{21} and B_{12}, which are equal at all photon energies. These rate equations are shown in Eqs. 2.41 and 2.42.

$$R_{abs} = B_{12}(1 - F_c)Fv\rho_c\rho_v \tag{2.41}$$

$$R_{stim} = B_{21}F_c(1 - F_v)\rho_c\rho_v \tag{2.42}$$

In order for stimulated emission to be greater than absorption there is the requirement that $F_c - F_v > 0$. In terms of the quasi-Fermi levels introduced previously, this can equivalently be stated as:

$$E_{f,e} - E_{f,v} > \hbar\omega > Eg \tag{2.43}$$

Lasing can be achieved by placing a material exhibiting optical gain in an optical cavity. This is only possible if the round trip gain for propagating light is higher than the losses in the cavity, including the light emitted from the cavity. The point at which these are balanced is known as threshold.

$$R_1R_2 \times exp(2g_{threshold}l) \times exp(-2\alpha l) = 1 \tag{2.44}$$

The threshold gain therefore depends on the reflectivities, R_1 and R_2, the cavity length l, and the cavity losses α, and can be expressed as:

$$g_{threshold} = \alpha - \frac{1}{2l}ln(R_1R_2) \tag{2.45}$$

This also highlights the importance of the mirror reflectivity in achieving a low threshold.

2.2.5 Non-radiative loss mechanisms

There are a number of a mechanisms by which an electron-hole pair can recombine without emitting a photon, known as non-radiative recombination. Minimising these processes is crucial to the performance of lasers because electron hole pairs that recombine non-radiatively cannot participate in the stimulated emission process, and thereby reduce the inversion factor term in the optical gain equation.

Figure 2.8 illustrates a number of such processes. In crystals a number of trap states can exist including threading dislocations, point defects and deep level impurities. An electron can transition to a trap state, before recombining with a hole in the valence

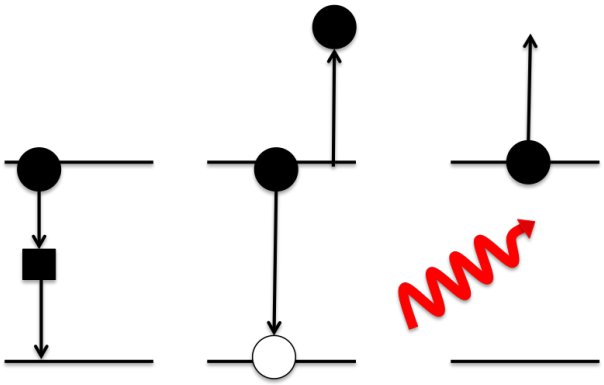

Figure 2.8: Sketch showing non-radiative loss mechanisms in semiconductors. Shockley Read Hall recombination is shown on the left, where an electron recombines with a hole via a trap within the band. Auger recombination is represented in the middle, whereby a recombining electron hole pair transfers energy to a free carrier. Free carrier absorption is shown in the right, where a free carrier absorbs a photon, and the carrier is moved higher in energy within the band.

band. This alternative path is non-radiative, and is described by Shockley Read Hall recombination models:

$$R_{SRH} = \frac{v_{th}\sigma_n\sigma_p N_t(pn - n_i^2)}{\sigma_p[p + n_i exp((E_i - E_t)/K_bT)] + \sigma_n[n + n_i exp((E_t - E_i)/K_bT)]} \tag{2.46}$$

where p and n hole and electron concentrations (assuming low injection), v_{th} is the thermal velocity of the carriers, Nt is the concentraiton of traps σ_n and σ_p are the capture cross section for electrons and holes respectively, n_i is the intrinsic carrier concentration, and E_t is the energy of the traps.

Assuming the electron and hole cross capture sections are equal, and $\sigma_n = \sigma_p = \sigma_o$, the expression can be simplified to:

$$R_{SRH} = v_{th}\sigma_o N_t \frac{p_n n_n - n_i^2}{p_n + n_n + 2n_i cosh\left(\frac{E_t - E_i}{k_bT}\right)} \tag{2.47}$$

The dependence of the recombination rate on the position of the trap in energy can be seen from the dependence of the cosh term on the denominator. When E_t - $E_i = 0$, and the trap is in the middle of the bandgap the recombination rate is at its highest. This

is particularly relevant in this work due to the presence of a high number of threading dislocations which stem from the lattice mismatch of Ge on Si. Such dislocations locally break the crystal symmetries, which leads to solutions of the wave function inside the bandgap, and the creation of mid-gap states. From a theoretical standpoint this can be somewhat intuitive, as the periodicity assumptions used (for example in Eq. 2.19) led to the formation of the band structure, and therefore breaking the periodicity can lead to additional states within the bandgap. In the work of [51], the dark currents in reverse bias Ge pin diode structures were correlated to the density of threading dislocations, and fitted to experimental works using a Shockley Read Hall recombination model.

Surface recombination is similar in nature to the SRH model. At surfaces, where the periodicity of the lattice is broken, electronic states in the mid-gap can be formed. Particularly with etched structures, this leads to surface recombination which causes a depletion region around the perimeter. The decreased carrier density in this region leads to a diffusion current from the bulk region which can be described generally by a surface recombination velocity. Such a description can be used for recombination towards defective interfaces as well as surfaces, for instance at the interface between Ge epilayers and Si substrates. For defective Ge on Si epilayers with high threading dislocations of 10^9, the excess carrier lifetime has been measured to be $\sim$ 1 ns [52].

At high injection, other loss mechanisms can dominate lifetimes. Auger recombination is a three particle process where a recombining electron hole pair transfer energy to a free carrier within a band. This was shown in the sketch in Fig 2.8. The Auger recombination rates are expressed below, where B_n and B_p are the electron and hole Auger coefficients, and n and p are the electron and hole carrier concentrations.

$$R_{Aug} = B_n n^2 p \quad - for\ n\ type \tag{2.48}$$

$$R_{Aug} = B_p n p^2 \quad - for\ p\ type \tag{2.49}$$

Unlike SRH, surface recombination, and Auger, free carrier absorption is a loss mechanism for emitted light, therefore not effecting the internal quantum efficiency but increasing the losses that need to be overcome to achieve lasing.

The absorption process can be derived by a Drude model, which treats the carriers as a plasma which is accelerated by an electromagnetic wave. The damping term stems

from electron scattering processes. This leads to the following relationship, where q is the electron charge, m_n and m_p are the electron and hole masses, and μ_n and μ_p are the electron and hole mobilities:

$$\alpha_{fc} = \frac{\lambda^2 q^3}{4\pi c^3 n^* \varepsilon_o}\left[\frac{n}{m_n^2 \mu_n} + \frac{p}{m_p^2 \mu_p}\right] \tag{2.50}$$

The dependency on the effective mass shows how this absorption is higher for lighter bands. The free carrier absorption in semiconductors, however, is often found by empirical fitting to the power law, Eq. 2.51. Here k_e, k_h, a_e, and a_h are constants, and n_c and n_h are the electron and hole concentrations respectively.

$$\alpha_{fc} = k_e n_c \lambda^{a_e} + k_h p_v \lambda^{a_h} \tag{2.51}$$

Michel et al [2] fitted the absorption from doped Ge epilayers to show that the FCA can be described by Eq. 5.17, where n_c and n_v are the electron and hole concentrations in cm^{-3} and λ is the wavelength in nm.

$$\alpha_{fc} = -3.4 \times 10^{-25} n_c \lambda^{2.25} - 3.2 \times 10^{-25} n_v \lambda^{2.43} \tag{2.52}$$

Understanding the combination of all these loss elements is crucial for engineering a semiconductor laser. High internal non-radiative loss processes inhibit the ability to achieve population inversion, while losses such as FCA cause additional losses in the cavity which further increases the threshold injection.

2.3 Ge bandstructure

Germanium is an indirect bandgap material, with a conduction band minimum at the L valley, in the {111} directions, Fig. 2.9. However the direct band at the Γ is only $\sim$ 140 meV above the L valley in energy. This means that it exhibits pseudo direct bandgap behaviour with regard to its optical properties.

Absorption is therefore strong across the direct band, with an absorption coefficient of $\sim 8{\times}10^3$ cm^{-1} at 1550 nm, allowing for compact photodiodes operating in the telecoms C band. Efficient photon emission however is severely limited due to the carrier occupation at the direct band. The indirect L valleys are four fold degenerate, and have relatively

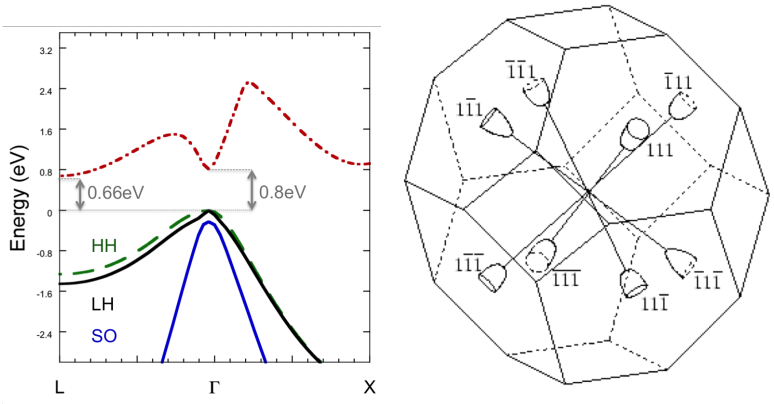

Figure 2.9: First brillioun zone of the Ge bandstructure calculated using the nanohub bandstructre tool [4]. The L valley is 140 meV lower in energy than the direct Γ valley. Heavy hole (HH), light hole (LH) and spin orbit (SO) bands are shown.

large effective masses compared to the Γ. This is most evident comparing the effective density of states masses, which are 0.032 m_o for the Γ and 0.553 m_o for the L-valley.

The carrier concentration can be calculated based on the product of the density of states, and the Fermi probability that the state is occupied, as shown in Eq. 2.53. The dependence on the effective mass can be seen in Eq. 2.54 and 2.55. Populating the Γ band is therefore challenging, because even when degenerately doped, a smaller tail of the Fermi-function extends into the Γ than to the L, and the difference in carrier concentration is exacerbated by the difference in the density of states.

$$n = \int_{E_c}^{\infty} g(E)f(E)dE = \int_{E_c}^{\infty} \frac{g(E)dE}{1 + e^{(E-E_F)/k_BT}} \tag{2.53}$$

$$g_{3d}(E) = \frac{(2m^*)^{3/2}}{2\pi^2\hbar^3}\sqrt{E - E_c} \tag{2.54}$$

$$n = \frac{(2m^*)^{3/2}}{2\pi^2\hbar^3}\int_{E_c}^{\infty} \frac{\sqrt{E - E_c}}{1 + e^{(E-E_F)/k_BT}}dE \tag{2.55}$$

This makes it particularly problematic with regard to achieving optical gain. Under injection, it would require carrier densities greater than $10^{20}\ cm^{-3}$ to push the quasi Fermi level into the Γ band, and therefore a greater injection to achieve population inversion.

The high injection required for population inversion is of itself undesirable for low power devices, however more critically, the associated free carrier and intra-valence band

losses with this injection severely degrade the device performance, and make achieving net gain extremely challenging. As shown in Eq. 5.17, the injected holes contribute more significantly to the free carrier losses due to the smaller effective mass of the valence band.

This led to the approach taken by Michel et al, who used degenerate n-type doping to fill the L valley close to the level of the Γ [2]. As a result, most of the required electron injection has been achieved without the injection of holes, and the total free carrier losses are reduced. This can be seen in Fig 2.10, which shows the band structure of Ge, including the Γ and L valleys in the conduction band, and the HH band in the valence band. The left image shows intrinsic Ge, where the Fermi level lies near the centre of the bandgap. The quasi Fermi levels under injection are shown in the conduction and valence bands. Under high enough injection to populate the Γ band, the quasi Fermi level is deep into the valence band. In Fig. 2.10 the right image shows degenerately doped Ge, and therefore the injection required to move the electron quasi-fermi level into the Γ is reduced. As a result, there is significant hole population for population inversion however the number excess holes is dramatically reduced.

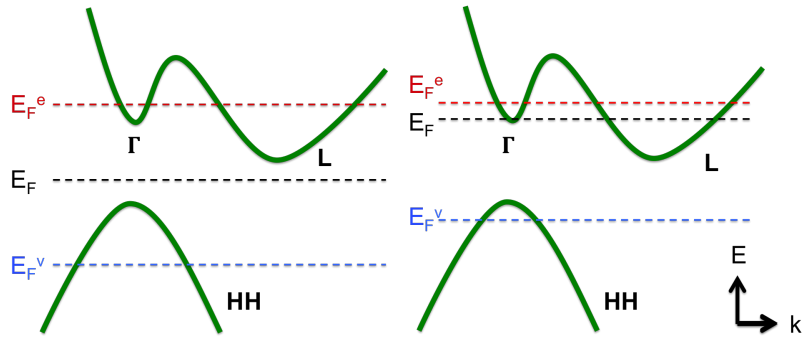

Figure 2.10: Sketch of a Ge band structure under optical injection, showing the fermi level, as well as the electron and hole quasi Fermi levels. On the left, intrinsic Ge is shown with high enough injection to move the quasi Fermi levels into their respective bands, achieving population inversion. On the right, the Ge is degenerately n-type doped and the fermi level is into the L band. Reduced optical injection is required to achieve population inversion.

Through these techniques, lasing was demonstrated in Ge for the first time, with both PL and EL devices. Ge layers were grown selectively in oxide trenches, which minimises threading dislocations, as when annealed, threads can glide to the edge of the trench where they terminate. This helps minimise SRH recombination through reducing the

mid-gap trap density from reducing threads, while the free surfaces are passivated by the SiO_2 trench. These results sparked a significant drive into the research of Ge for active optical devices.

2.4 Stress, Strain and Elasticity

A further advantage of the Michels device compared to bulk Ge, aside from the degenerate n-type doping, is the small amount of residual tensile strain in the Ge layer, as a result of the thermal expansion mismatch between Si and Ge. As will be discussed in the remainder of this chapter, tensile strain modifies the band structure of Ge in a manner that is favourable for light emission, as the Γ band moves to lower energies at a greater rate than the L valley, eventually leading to a transition where the Γ is the direct band minimum, and the material is therefore direct bandgap. Even with modest strain, carrier concentration at the Γ (and therefore population inversion) can be significantly improved as the Γ reduces in energy relative to the L.

2.4.1 Stress and strain tensors

In simple terms, strain relates purely to the relative deformation of a material, while the stress describes the forces per unit area associated with the deformation. The mathematics of such properties are described in this section.

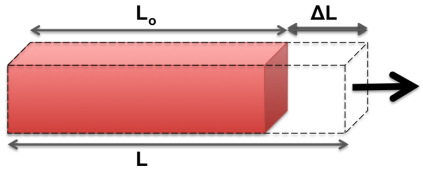

Figure 2.11: Drawing of a material block that has been strained in 1 dimension, showing an expansion Δ L, of its original length L_o, to its new length L.

In simple 1d cases, Fig. 2.11, strain is described as a fractional change in the initial length of a material:

$$\varepsilon = \frac{L - L_0}{L_0} \tag{2.56}$$

For general varying strains, a tensor component can be written as,

$$\varepsilon_{\alpha,\beta} = \frac{\partial u_\alpha}{\partial x_\beta} \tag{2.57}$$

Where u_α is the displacement of a point in the direction x_β. In order to fully describe the strain state of a 3 dimensional anisotropic system, a 2nd order tensor is required:

$$\varepsilon = \begin{pmatrix} \varepsilon_{11} & \varepsilon_{12} & \varepsilon_{13} \\ \varepsilon_{21} & \varepsilon_{22} & \varepsilon_{23} \\ \varepsilon_{31} & \varepsilon_{32} & \varepsilon_{33} \end{pmatrix}$$

In equilibrium, the strain tensor is required to be symmetric about the tensor trace, as otherwise this would describe a rotation. A tensor component can therefore be described as

$$\varepsilon_{\alpha,\beta} = \frac{1}{2}\left[\frac{\partial u_\alpha}{\partial x_\beta} + \frac{\partial u_\beta}{\partial x_\alpha}\right] \tag{2.58}$$

This means that the 9 tensor components can be uniquely described by 6 independent terms: ε_{xx},ε_{yy},ε_{zz},ε_{zx}, ε_{yz} and ε_{xy}.

In the linear elastic regime, stress and strain are linearly related. The stress tensor can be understood by considering that components $\sigma_{\alpha,\beta}$ describes a force α acting on an area with normal in the β direction. This can be viewed graphically on an infinitesimal cube as shown in Fig. 2.12. Similarly to the strain tensor, the stress tensor is symmetric; the non-trace components of the tensor describe torque, which must disappear inside a solid. This means that the stress tensor can also be uniquely described by 6 tensor components: σ_{xx},σ_{yy},σ_{zz},σ_{zx}, σ_{yz} and σ_{xy}.

Unlike in isotropic cases, the relationship between stress and strain is described by a 4^{th} order tensor with 81 elements, described by Eqs. 2.59 and 5.10, where S_{ijkl} and C_{ijkl} are the elastic compliance and elastic stiffness tensors.

$$\varepsilon_{ij} = S_{ijkl}\sigma_{kl} \tag{2.59}$$

$$\sigma_{ij} = C_{ijkl}\varepsilon_{kl} \tag{2.60}$$

However, due to the simplifications previously made to the stress and strain tensors, described above, this can be reduced to 36 components. In systems with cubic symmetry, such as Si and Ge, further simplifications can be made. Any transformation made

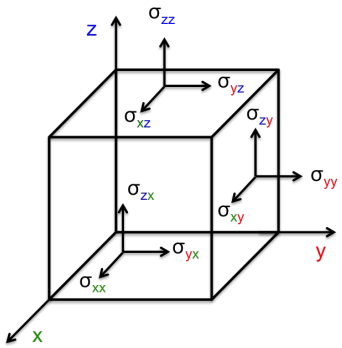

Figure 2.12: Illustration showing the stress tensor on an infinitesimal cube, with faces orientated in the x y and z directions.

to the coordinate system should leave the tensor unchanged; by making transformation that should posses cubic symmetry, it can be deduced that in order for the tensor to remain unchanged, certain tensor components are required to be zero. As a result, only 3 independent components are required to describe the compliance tensor.

$$\begin{pmatrix} \sigma_{11} \\ \sigma_{22} \\ \sigma_{33} \\ \sigma_{23} \\ \sigma_{13} \\ \sigma_{12} \end{pmatrix} = \begin{pmatrix} C_{11} & C_{12} & C_{12} & 0 & 0 & 0 \\ C_{12} & C_{11} & C_{12} & 0 & 0 & 0 \\ C_{12} & C_{12} & C_{11} & 0 & 0 & 0 \\ 0 & 0 & 0 & C_{44} & 0 & 0 \\ 0 & 0 & 0 & 0 & C_{44} & 0 \\ 0 & 0 & 0 & 0 & 0 & C_{44} \end{pmatrix} \begin{pmatrix} \varepsilon_{11} \\ \varepsilon_{22} \\ \varepsilon_{33} \\ 2\varepsilon_{23} \\ 2\varepsilon_{13} \\ 2\varepsilon_{12} \end{pmatrix}$$

This tensor describes the coupling between stress in a given direction, and strain in another. The tensor has been given using the truncated notation, below. For example, C_{12} couples ε_{22} with σ_{11}.

Tensor notation	11	22	33	23,32	31,13,	12,21
Matrix notation	1	2	3	4	5	6

2.4.2 Hydrostatic strain

Hydrostratic strain is volumetric dilation or expansion, as shown in Fig 2.13. The stress and strain tensors only have trace components, and therefore all crystal symmetries are

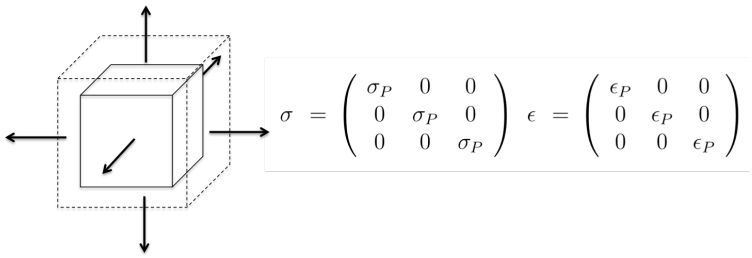

Figure 2.13: Volumetric expansion is shown pictorially, as a result of tensile hydrostatic strain. This is characterised by equal strains along the three principal axes.

left unchanged. For band structures this means that all band degeneracies are maintained. In practise, however, it is extremely difficult to apply this type of strain.

The hydrostatic component of strain of a strain tensor relates to the relative change in volume, which can be expressed as the sum of the strain trace:

$$\delta = \frac{\delta V}{V} = \varepsilon_{xx} + \varepsilon_{yy} + \varepsilon_{zz} \tag{2.61}$$

2.4.3 Biaxial

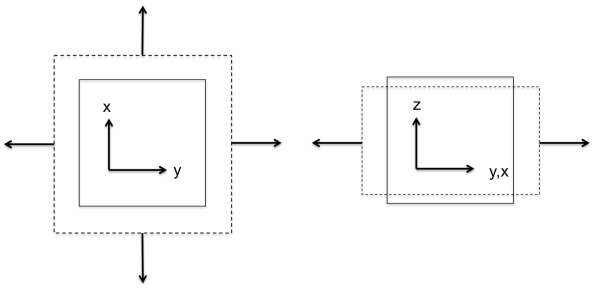

Figure 2.14: Illustration showing tensile biaxial strain. Left - the x y plane (top down), showing that there is an equal percentage expansion in the x and y directions, which are perpendicular to each other. Right - the associated compression in the z direction is shown, which is perpendicular to both x and y directions. This shows that the bulk cubic structure has been transformed into a tetragonal crystal.

Biaxial stress describes stresses applied equally in the two perpendicular directions in a plane. This is shown schematically in Fig 2.14. This can be expressed as $\sigma_{xx} = \sigma_{yy} =$

σ_{bi} and leads to biaxial strain in the plane. In the case of thin films, whether externally stressed or possessing inherent strain from lattice match, there is the requirement that the out of plane stress is zero in equilibrium, leading to

$$\varepsilon_{zz} = \frac{-(\varepsilon_{xx} + \varepsilon_{yy})C_{12}}{C_{11}} = -\varepsilon_{bi}\frac{2C_{12}}{C_{11}} \tag{2.62}$$

The resulting stress and strain tensors are therefore:

$$\sigma = \begin{pmatrix} \sigma_{bi} & 0 & 0 \\ 0 & \sigma_{bi} & 0 \\ 0 & 0 & 0 \end{pmatrix} \quad \varepsilon = \begin{pmatrix} \varepsilon_{bi} & 0 & 0 \\ 0 & \varepsilon_{bi} & 0 \\ 0 & 0 & -2\frac{C_{12}}{C_{11}}\varepsilon_{bi} \end{pmatrix}$$

This type of strain is common during growth of strained epilayers, and leads to a tetragonal lattice. This has ramifications for valence band splitting in Ge, which will be discussed later. This relationship in Eq. 2.62 is generally used to simplify calculations for biaxial approximations of the bandgap using deformation potentials, and for Raman spectroscopy.

2.4.4 Uniaxial strain

True uniaxial strain is defined as where only a single axis is displaced. This is rarely the case, and often, authors refer to the strain resulting form uniaxial stress, as uniaxial strain. This is shown in tensor form below, where ν is Poisson's ratio and is equivalent to -$\frac{S_{12}}{S_{11}}$ in cubic systems:

$$\sigma = \begin{pmatrix} \sigma_{uni} & 0 & 0 \\ 0 & 0 & 0 \\ 0 & 0 & 0 \end{pmatrix} \quad \varepsilon = \begin{pmatrix} \varepsilon_{uni} & 0 & 0 \\ 0 & -\nu\varepsilon_{uni} & 0 \\ 0 & 0 & -\nu\varepsilon_{uni} \end{pmatrix}$$

This shows the coupling through the elasticity tensor that causes strain in the other principal directions. For instance, with a suspended nanowire pulled at each end, there is a tensile uniaxial stress which couples to tensile strain down the length of the wire, but compressive strain in the two orthogonal directions. The symmetry considerations here are comparable to that of biaxial strain. Similarly to the biaxial assumptions, the assumption of uniaxial strain can be used to simplify deformation potential models and strain shift coefficients using Raman spectroscopy.

2.4.5 Shear Strain

In some notations, biaxial and uniaxial strains are seen as a type of shear strain as it is not purely hydrostatic, and modifies that crystal symmetries. This can be achieved by only looking at trace elements of the strain transfer. The other type of shear strain that can occur is due to off-diagonal elements, which changes the angles between the sides of an infinitesimal square.

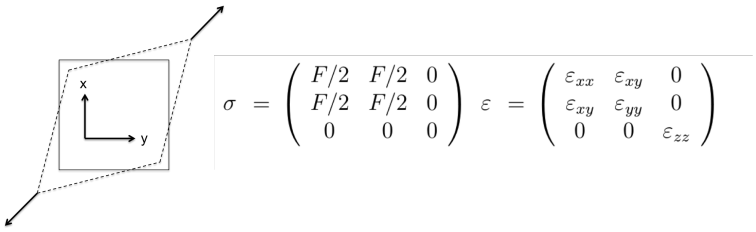

Figure 2.15: Illustration showing off diagonal shear strain. The stress tensor shows the result of a force F in the diagonal direction i.e. [110], which results in off diagonal shear strain components.

Shear strains can emerge from a uniaxial stress which is not orientated in a principal direction of a crystal. For instance, for a force applied in the [110] direction, the stress tensor and resulting strain tensors are shown in Fig. 2.15. This has at effect of splitting bands with star degeneracy, such as the L valley in Ge. The previously equivalent $\langle 111 \rangle$ directions are now modified by the presence of the shear strain, and this leads to two of the L valleys moving higher in energy, and two moving lower. This has been depicted in Fig 2.16.

2.4.6 Strain effects on band structure

The effect of the various strain distributions explained above are shown pictorially in Fig. 2.16. When unstrained, the L-valley is the conduction band minimum, and the LH and HH states are degenerate. As discussed, hydrostatic strain maintains crystal symmetries of the bulk material, and therefore the degenerate LH and HH valence bands remain degenerate. Hydrostatic strains above ~ 0.8 % will transform Ge into a direct bandgap material, with the Γ valley at the conduction band minimum. In practise, this type of strain transfer is not practical to apply.

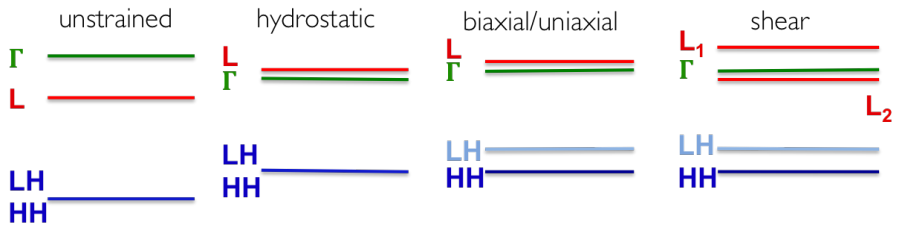

Figure 2.16: Illustration showing the effects of strain configuration on the band structure energies and degeneracies of Ge.

Uniaxial and biaxial strains results in a tetragonal unit cell, which effects the Ge valence band. This causes the normally degenerate LH and HH bands to split. For biaxial tensile strains, the LH band becomes the ground state, which has ramifications for optical gain and is explained later in the Chapter. Biaxial tensile strains between 1.6 % and 1.9 % are predicted to transform Ge to direct bandgap, where uniaxial strains $>$ 4 % are required.

Unstrained Ge possesses 8 degenerate $\langle 111 \rangle$ directions, each containing half an L-valley within the first Brillouin zone, resulting in 4 degenerate bands (see Fig. 2.9). The $\langle 111 \rangle$ directions can be characterised by glide reflection symmetry, which is broken by the shear strains described by the non-trace elements of the strain tensor, such as ε_{xy}. This causes a splitting of the L-valleys, with 2 degenerate bands moving to higher energy, and 2 moving to lower energy.

2.4.7 Deformation Potentials

In order to calculating the strained band structure, Pikus and Bir [53] used a modified k.p theory which treats the strain as a perturbation. This gives rise to deformation potential constants, which describe the energy shift per unit strain of a band. The deformation potentials are commonly shown for the trace strain trace components.

a_c and $\Xi_d + \frac{1}{3}\Xi_u$ are the hydrostatic deformation potential constants for the Γ and L bands respectively. They describe the movement of the conduction band minima, and demonstrate that the bands move at the maximum rate with hydrostatic strain.

$$E_\Gamma = E_\Gamma^0 + a_c(\varepsilon_{xx} + \varepsilon_{yy} + \varepsilon_{zz}) \tag{2.63}$$

$$E_L = E_L^0 + (\Xi_d + \frac{1}{3}\Xi_u)(\varepsilon_{xx} + \varepsilon_{yy} + \varepsilon_{zz}) \tag{2.64}$$

The valence band movements are described by a model constructed from the Luttinger-Kohn Hamiltonian, by adding terms proportional to the strain tensor components. Again, this assumes that the off-diagonal tensor components are zero. The energies of the LH and HH bands are described below. The valence band deformation potentials are a_v and b,which are the hydrostatic and shear deformation potentials respectively. The deformation potential constants used in this work are summarised in table 2.1 (at the end of the chapter).

$$E_{HH} = E_{HH}^0 - P_e - Q_e \tag{2.65}$$

$$E_{LH} = E_{LH}^0 - P_e + \frac{1}{2}(Q_e - \Delta + \sqrt{\Delta^2 + 2Q_e\Delta + 9Q_e^2}) \tag{2.66}$$

$$P_e = -a_v(\varepsilon_{xx} + \varepsilon_{yy} + \varepsilon_{zz}) \tag{2.67}$$

$$Q_e = -\frac{b}{2}(\varepsilon_{xx} + \varepsilon_{yy} - 2\varepsilon_{zz}) \tag{2.68}$$

The valence band splitting can be seen to be a function of Q_e, which is only non-zero for strains which cause tetragonal symmetries. In terms of biaxial tensile strain, the LH band becomes the ground state. This can be seen in Fig. 2.17, which shows the interband transitions as a function of biaxial tensile strain. This highlights the red-shift of emission accompanying the transition to direct bandgap, which extends towards the mid-infrared at 2 % biaxial tensile strain. The accompanying valence band splitting is also significant in terms of population inversion across the direct band due to the reduced density of states of the LH compared to the HH. For lighter bands, a given carrier injection will move the quasi Fermi level at a greater rate than heavier bands. However, with increased biaxial strains, there is significant warping of the valence bands and the LH band only remains light in the direction transverse to the plane of strain, while the density of states masses for the LH and HH become comparable.

Figure 2.18 shows the required injection for the electron quasi Fermi level to reach the Γ minimum as a function of biaxial tensile strain, for a range of doping levels. This is

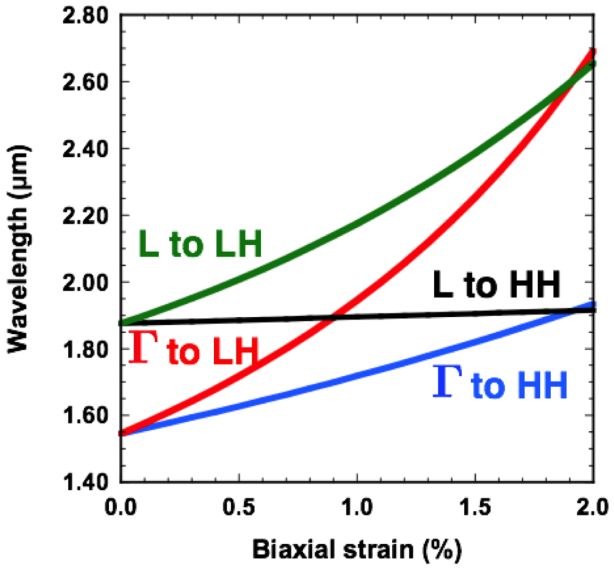

Figure 2.17: Calculated emission wavelengths corresponding to various interband transitions as a function of biaxial tensile strain. The Γ, L, light hole (LH), and heavy hole (HH) bands are considered. At $\sim$ 1.9 % there is a transition to direct bandgap.

calculated by Fermi-Dirac statistics, and includes the changes to the effective mass of the Γ band with strain, calculated by 8 x 8 k.p modelling using the Nextnano3 package [54].

The associated free carrier absorption associated with these doping and injection levels is also shown in Fig. 2.18. The free carrier losses are evaluated at a wavelength corresponding to the strained bandgap, using Eq. 5.17. This highlights that for a given strain level, there is an optimal n-type doping density. When the Fermi level at zero injection is already in the Γ band, increased strain causes higher losses due to the wavelength dependence of the free carrier absorption. This shows the potential reduction in free carrier losses that can be achieved with strain engineering.

A further consideration with the splitting of the valence band is the polarisation dependence of the emission. While the conduction band has s-like orbital symmetry, the valence band are a linear combination of p-type orbitals. This means that each valence band has Bloch functions with different symmetries, which results in the optical matrix elements relating the conduction and valence bands having a polarisation dependance [55].

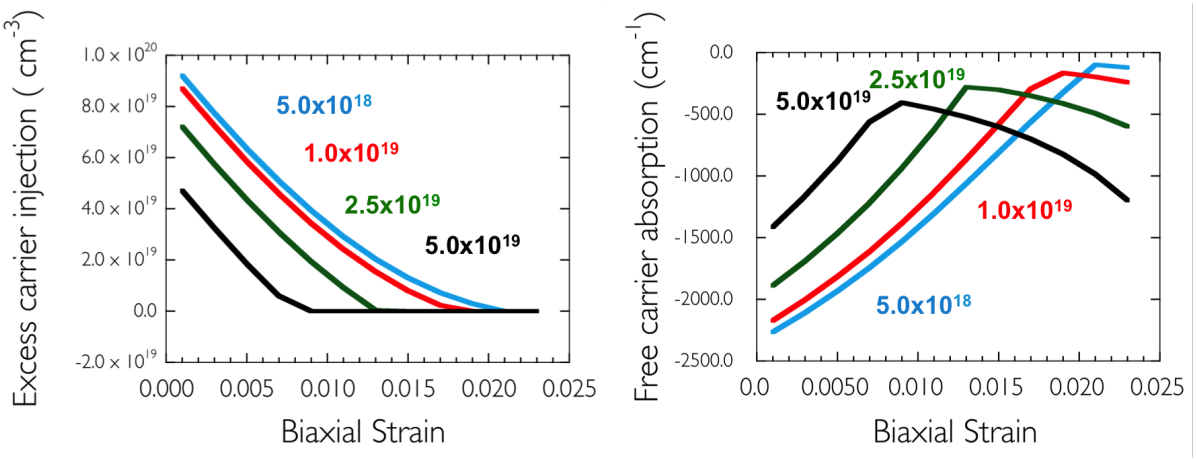

Figure 2.18: Left - Required injection for the electron quasi-Fermi level to reach the Γ minimum, as a function of biaxial strain, for a range of n-type doping. Right - the associated free carrier losses from the required injection, and from the n-type doping, as a function of biaxial tensile strain.

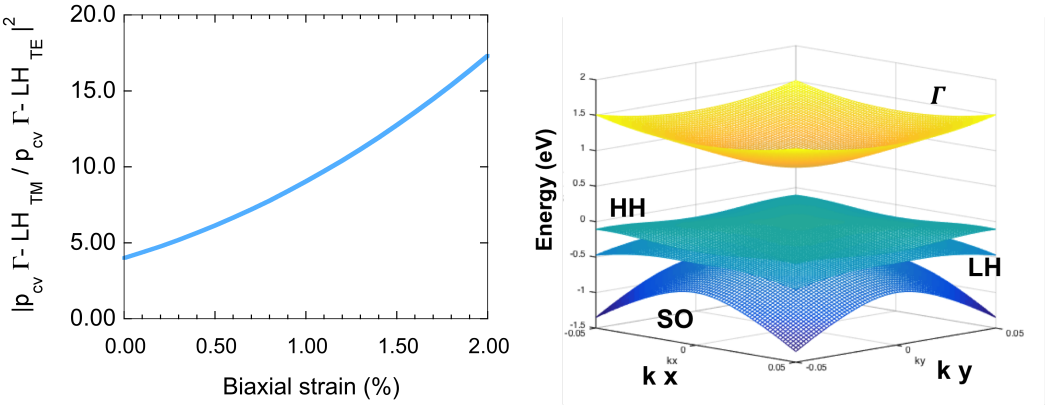

Figure 2.19: Ratio of the matrix elements for the Γ to light hole transitions for transverse electric and transverse magnetic polarisations. Right - calculated band structure by nextnano3 for a constant k_z, for a range of k_x and k_y.

As shown in Eq 2.39, the momentum matrix elements are proportional to the emission intensity. This has ramifications for PL emission as well as the potential optical gain in Ge lasers, as, particularly at high strain, only TM modes couple strongly to the Γ to LH transition. Plotting the ratio of the TM to TE matrix elements for the Γ to LH transition, as in Fig. 2.19, it can be seen that at 2 % strain the TM matrix element is ∼ 17 times

that of the TE. However, deviation from parabolic bands - which has been shown to be the case at high levels of strain - leads to a relaxation of these selection rules.

2.5 Sn alloying

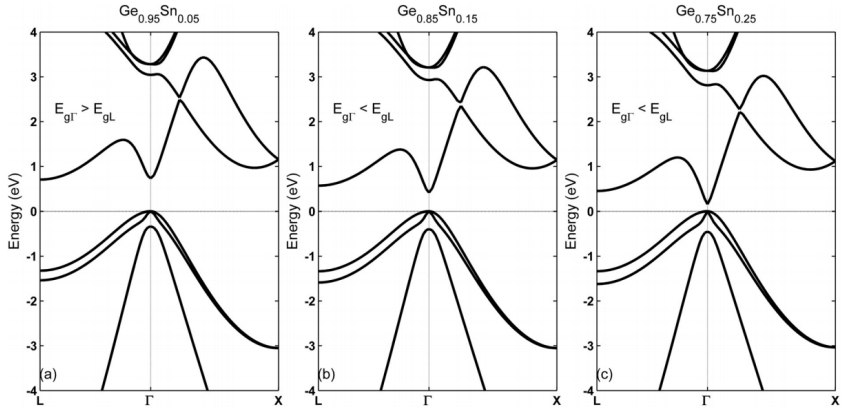

Figure 2.20: Bandstructure of GeSn alloys with varying Sn concentration calculated by density functional theory, from [5].

The alternative approach to acheiving direct bandgap Ge is through alloying with α - Sn. Similarly to strain, with increasing Sn the Γ band moves to lower energies as a greater rate than the L-valley. While the Sn concentration required for the transition varied substantially though theoretical modelling of the band structure, recent demonstrations of a GeSn laser have found the crossing to be less than 12.6 % Sn.

$$E_{GeSn}^{\Gamma,L} = E_{Ge}^{\Gamma,L}(1-x) + E_{Sn}^{\Gamma,L} - x(1-x)b^{\Gamma,L} \tag{2.69}$$

In general, the bandgap of two alloys can be described to the first approximation by a Vergard's law, which is simply a linear interpolation of the bandgaps. GeSn has been found to deviate significantly from linearity, and requires a bandgap bowing parameter to describe the direct and indirect bandgaps as a function of Sn, Eq. 2.69, where $E_{GeSn}^{\Gamma,L}$ indicates either the Γ or L bandgap energies for the alloy, and with the other energy terms representing each material. $b^{\Gamma,L}$ represents the Γ or L bandgap bowing parameters. There is still a degree of uncertainty in the bandgap bowing. The bandstructure of GeSn alloys for varying Sn concentrations are shown in Fig. 2.20, as calculated by density functional

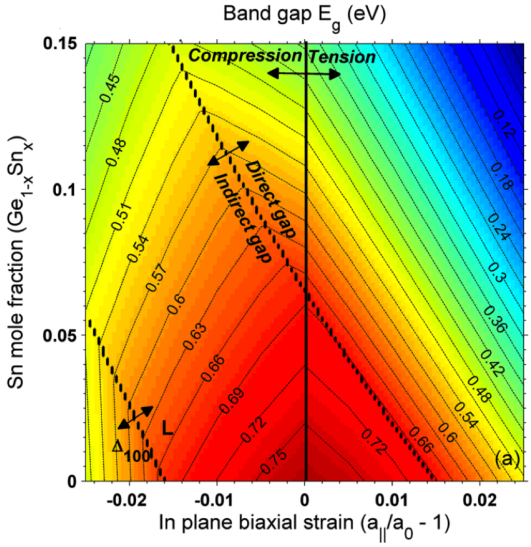

Figure 2.21: Calculated band structure of GeSn alloy as a function of Sn concetration and in plane biaxial strain, image from [5].

theory [5]. This shows that there is a Ge like band structure for low Sn concentrations, with the L-valley at the conduction band minima. With increasing Sn concentration the material becomes direct, as shown in Fig. 2.20 for the 15 % and 25 % Sn concentrations.

As will be discussed in the literature review, the application of strain moves the bands in a similar manner to that of Ge, with a modification to the deformation potentials, which are taken using a Vergards approximation. The effect of strain and Sn on the bandgap was shown in Fig. 2.21, from the work of Gupta et al [5]. From this work, both the Sn content and the strain to reach direct bandgap appears to be slightly underestimated, based on recent experimental works, but the general trends are well demonstrated. For instance, according to Fig. 2.21, the crossover to direct bandgap is expected for a Sn concentration of ~ 7 %, with zero strain, which is low compared to the work of [11] which gives a crossing for > 8 %. Fig. 2.21 highlights the importance of tensile strain for growth of GeSn on a Group IV platform. Growing GeSn on either Si substrates, or Ge virtual substrates, leads to compressive strain, which for levels of Sn currently achievable still leads to an indirect material. Strain engineering is therefore critical to produce direct materials on a Group IV platform.

The material parameters for Ge and Sn used in this work are summarised in Table 2.1. For Δ, the value given in the Sn column is that of the GeSn alloy, which includes a

bowing term.

Material constant	Ge value	Sn value
a_c	-8.24 eV [40] [56]	-6.0
a_v	1.24 eV [40] [56]	1.58
b	-2.16 eV [42]	-2.7
$\Xi_d + \frac{1}{3}\Xi_u$	-2.34 eV [56]	-2.14
Δ	0.29 [55]	0.284+0.744x-0.200x^2 *($Ge_{1-x}Sn_x$)
E_Γ^0	0.802 eV [55]	-0.408
E_L^0	0.661 eV [55]	0.1202
C_{11}	129.2 GPa [57]	69
C_{12}	47.9 GPa [57]	29

Table 2.1: Deformation potential constants and material parameters used in this work. The Sn parameters are reported in [11].

2.6 Chapter Summary

A brief introduction was given into crystals and the reciprocal lattice. The Schrodinger equation was introduced and was applied to a 1-dimensional crystal to show the formation of electron bands through the free electron model. More practical band-solving techniques were then introduced with k.p perturbation theory. Following this, optical transitions in semiconductors were discussed based on Fermi's Golden rule, including absorption, spontaneous emission and optical gain. The threshold condition of lasing was then shown based on the balancing of cavity losses and optical gain. A number of non-radiative loss mechanisms were then discussed including Shockley-Read-Hall recombination, Auger recombination, surface recombination and free carrier absorption. The Germanium band structure was then shown and related to the various optical processes, highlighting why Germanium can act as an efficient absorber but a poor light emitter. The means of improving quantum efficiency is discussed by degenerate n-type doping, before the application of tensile biaxial strain is discussed as an alternative approach to achieve gain. The various types of strain configurations were shown and discussed with regard to the effect

on the Ge band structure, with an emphasis on the band degeneracies lifted due to the strain symmetry. The effect of strain on the polarisation of Ge emission, and potential gain was shown, and finally the effect of Sn alloying on the Ge band structure was shown.

3

Literature Review

The first transistor was demonstrated in 1947 in Bell labs using bulk Ge crystals, which at the time was the most common semiconductor material. It wasn't for a further 7 years before a Si transistor was demonstrated [58], and it quickly become the dominant technology due to a number of factors. Unlike Ge, Si has a high quality and stable native oxide, low leakage currents, and is extremely abundant; all of which have allowed for mass production, and very large scale integration (VLSI). However since then, Ge has been used in CMOS technologies in form of SiGe alloys [43], and with the highest hole mobilities of any semiconductor, it has been touted as a potential channel material for future technology nodes [44]. This ability to integrate the material systems has lead to considerable interest in Ge as an active optical material.

Over the course of the last two decades, the improved epitaxial growth of Ge on Si through the two step growth technique [59], has given the capability to grow Ge epilayers with threading dislocation densities (TDDs) of $\sim 10^7$ cm^{-3}. As a result, a number of Ge based optical devices have been demonstrated, and many are commercially available. This includes, photodiodes [27, 60, 61], avalanche photodiodes (APDs) [62, 63], single photon avalanche photodiodes (SPADs) [64] , quantum confined stark effect (QCSE) modulators [65–67] , and intersubband detectors [68–71]. Recently Ge has also been used for passive optical structures such as waveguides in the mid-infrared (MIR) [72, 73] and plasmonic antennas [74].

The missing link however, is a Ge source, or for that matter, an alternative Si compatible source. As demonstrated in Chapter 2, this stems from the band structure which is inherently indirect, but only by $\sim$ 140 meV. Unfortunately, this modest energy gap is

exacerbated by a difference in the density of states (DOS) mass, with the L valley mass $\sim$ 13 times that of the Γ [3]. This makes populating the direct band extremely challenging, with injection of $\sim 10^{20}\ cm^{-3}$ carriers required before the quasi-Fermi level reaches the Γ minimum. As previously discussed, this has resulted in a number of techniques to improve carrier concentration at the direct gap, including degenerate n-type doping, tensile strain, and alloying with Sn, all of which were introduced in Chapter 2. In this chapter, the literature shall be reviewed with regard to the means by which these techniques have been employed, and how effective they have been in making an efficient Ge(Sn) source a possibility.

3.1 Strain engineering of Ge

A number of groups have investigated the PL and EL properties of n-type Ge epilayers. Light emitting diodes (LEDs) have been demonstrated, including surface normal [2,75] and waveguide geometry [76] multiple quantum well (MQW) devices. Such devices showed emission from the direct band, which was blue-shifted from quantisation, and showed near linear increase in the EL intensity with current. The required injection to obtain bright direct-gap emission in such devices, however, is significant enough that Blackbody radiation begins to dominate the spectra.

As detailed in the theory chapter, Michel et al [77] proposed the use of degenerate phosphorous n-type doping to move the quasi Fermi level into the L valley and thereby reducing the concentration of excess holes injected while inverting the Γ band and achieving population inversion. The technique was used for the first demonstration of an optically pumped Ge laser [37], with doping of 1×10^{19} cm^{-3}. Ge ridges were grown selectively in oxide trenches to minimise threading dislocation densities (TDDs) by giving a shorter glide length for threads to travel before terminating on the oxide sidewall. A small beneficial biaxial tensile strain of $\sim 0.25\%$ was reported from the growth. The waveguide was optically pumped by a Q switched 1064 nm YAG, and showed gain at $\sim$ 1594 nm. Despite the employed techniques, high thresholds of 30 kW/cm^2 were found, which are unpractical for device lifetimes in a commercial device. Subsequently, an electrically pumped laser was demonstrated by the same group [78]. For the Ge layer, a delta-doping technique was employed to give doping densities of $\sim 4 \times 10^{19}$ cm^{-3}. A doped poly-Si layer was used to provide a top contact, which allows for optical confinement in the Ge layer. This

was the first demonstration of an electrically pumped Ge device. Similarly to the PL device, thresholds were high, at around 280 kA/cm^2, and it was reported that device failure prevented subsequent measurements, likely due to the aluminium contacts spiking under high injection.

For optically pumped devices, the main optical losses were attributed to the free carrier losses and the mirror losses, with additional losses in the EL device due to optical losses in the contacts. The free carrier losses were measured in Ge in prior work by Michel et al, following the power law given in Chapter 2 [2]. For example, with 10^{20} cm^{-3} electrons there is an optical loss of $\sim$ 500 cm^{-1} at 1550 nm.

Some doubt has been cast on the initial reports of lasing, by Carrol et al [79]. Pump probe measurements were carried out on degenerately doped n-Ge, using a 1064 nm YAG as the excitation source, which is comparable to the source used in the report of the optically pumped Ge laser. Measurements of the free carrier plasma frequency were used to calculate the carrier concentration as a function of injection, and it was confirmed that an injection of $\sim 10^{20}$ is required for the quasi-Fermi level to reach the Γ band. Significant gain from the direct bandgap was measured, up to 850 cm^{-1}, however this was dwarfed by high free carrier and intra-valence band absorption, leading to net losses. In effect, this net loss is due to the excess holes injected while filling the L valley. These reports could explain the lack of further demonstrations of lasing in Ge. There has only since been one report of lasing from Ge Fabry-Perot resonators, for which the observed threshold behaviour occurred close to the point of device breakdown [39].

Michel et al went on to highlight the significance of Γ to L scattering, by showing that there is a large inherent gain possible across the Ge direct band (higher than the modal gains reported). Femto-second pulse probe measurements were used, during which optical bleaching was observed and gains of > 1300 cm^{-1} were found in n-Ge and nominally intrinsic Ge on insulator (GeOI) materials (comparable to gains in III-V structures) [80]. Critically, the probe pulse was in within the Γ to L scattering time of 235 $\pm$ 25 fs, highlighting that a large inherent gain is achievable when neglecting the scattering to the L valley.

These considerations opened the door to the possibility of using strained Ge as a gain medium [2] as reducing the Γ to L valley difference should allow this inherent gain to be accessed. Theoretical calculations in the framework of deformation potential theory showed that strain is predicted to give a direct bandgap between 1.6 and 1.9 % biaxial

tensile strain [40–42] (depending on the deformation potential constants). Even with moderate tensile strain, the doping required to fill the L-valley could be substantially reduced, in the process reducing free carrier absorption compared to the prior devices.

A number of groups considered theoretically the combination of strain and n-type doping which would provide the lowest thresholds [3, 6, 79, 81]. The results from Dutt et al. are shown in Fig. 3.1, and show that theoretically thresholds of $< 1\text{kA/cm}^2$ for strains of ~ 2 % and n-doping of $\sim 2 \times 10^{19}$ cm^{-3}. For reference, III-V quantum well lasers typically have threshold current densities on the order of 0.1 kA/cm^2, with quantum dot technologies capable of reducing this by a further by approximately an order of magnitude [82]. It can be seen that even at high levels of strain, n-type doping is still advantageous as the large density of states available in the L-valley makes significant population inversion difficult, even if Ge is moderately direct bandgap. This is at odds, however, with the more recent work of Prost et al [83], who found that the non-radiative carrier lifetime reduction caused by the introduction of dopants impedes carrier injection, i.e. the carrier concentration for a given injection is reduced. It was concluded in that work that above biaxial tensile strains of 1.5%, intrinsic material gives lower thresholds.

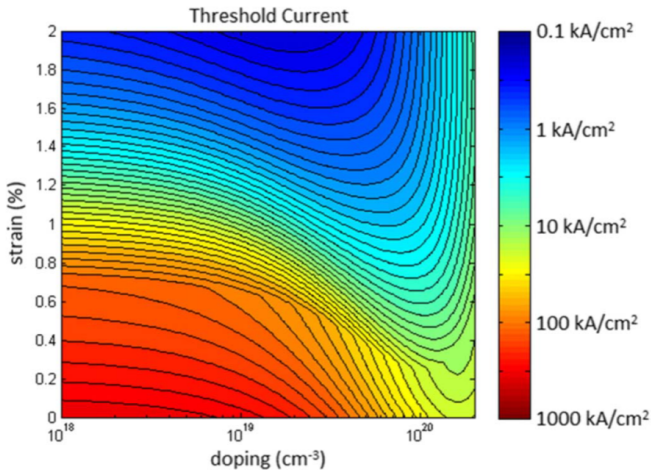

Figure 3.1: Calculated threshold current for a Ge laser as a function of biaxial strain and n-type doping. Figure from [6].

Early demonstrations of strained Ge were made by epitaxial growth of Ge on Si on substrates with larger lattice constants such as InGaAs [77, 84], and used electroreflectance

measurements to measure a number of the deformation potential constants [85]. Subsequently, stress was investigated mechanically by using thin Ge membranes bonded to polyimide films, by Sanchez-Perez et al [86]. This gave the ability to mechanically stress the films by bonding them to an otherwise rigid cavity, which could be filled by a high pressure gas, in order to stress the membranes. In this work, the mechanical properties of the Ge films gave a limitation on the film thickness, but strains up to 2% were achieved in 24 nm thin membranes. In general, a trend of increasing photolumiscence intensity with increasing strain was observed. Two Gaussians could be fitted to PL spectra in 40 nm thick membranes showing the separate contributions from heavy hole (HH) and light hole (LH) transitions, however the 20 nm Ge film had emission intensities which were significantly reduced (despite higher strains) and therefore interband transitions could not easily identified. In their optical setup, Γ to HH emission dominated the highly strained spectra, which was attributed to the TM polarization of the Γ to LH transitions, which is discussed in Chapter 5.

Further work from the group demonstrated this effect [87]. The surface of the membrane was patterned by a periodic grating by using amorphous Ge structures, with a Bragg wavelength of 2.3 μm for TM modes propagating in the plane of the strained layer. For high levels of strain this revealed an additional long-wavelength peak, attributed to the Γ to LH transition, for a 1.9% strained sample a peak at $\sim$ 2.5 μm was observable, with emission continuing up to the detector cut-off of 2.6 μm. The inclusion of the Γ to LH transition provided an intensity increase, which was more in keeping with theory for the levels of strain considered. For instance, at 1.3 % strain, an 11 times increase in the number of emitted photons was calculated, compared a maximum of a 4 times increase for structures without a grating. This work highlighted the applicability of strained Ge structures for MIR applications including sensing in the 2 to 2.5 μm atmospheric window.

Such demonstrations showed that emission intensities can be improved in strained Ge, however, methods of strain that allow for integration with on chip optics became the focus of the field. Top down approaches were later investigated by Suess et al [7], which have the advantage that the strain levels can be tuned by changing the geometry of the structure. Ge on Si, and Ge on SOI materials were dry etched to form bridge structures. These are subsequently undercut using potassium hydroxide or HF wet etches (for the relevant material system), which release the wire, but negligibly etch the Ge [88]. The Ge epliyer relaxes near the pads, in the process constricting the wire and transferring uniaxial tensile

strain down the wire length. Figure 3.2 shows an SEM of the micro bridge structures. The strain in the wire can be tuned as a function of the geometry of the pads, and is limited only by the mechanical limits of the wire. This opened the door to pattern-able structures with lithographically tuneable strain. The strain in such structures is uniaxial down the [100] directions, meaning that there is compression in the [010] and [001] directions, a maximum value of 3.1% strain was measured using Raman spectroscopy, which probes the shift to the Ge longitudinal optial (LO) phonon caused by strained [89]. PL was found to red shift to by 210 meV, and increased in intensity by 25 times. Calculations showed that gain levels of 460 cm^{-1} should be achievable for injections above 3×10^{19} cm^{-3} in 1×10^{19} cm^{-3} n-doped Ge, however this model neglected surface recombination effects and considered free carrier and intra-valence band absorption to be the dominant loss mechanism, which may not necessarily be the case in free standing structures.

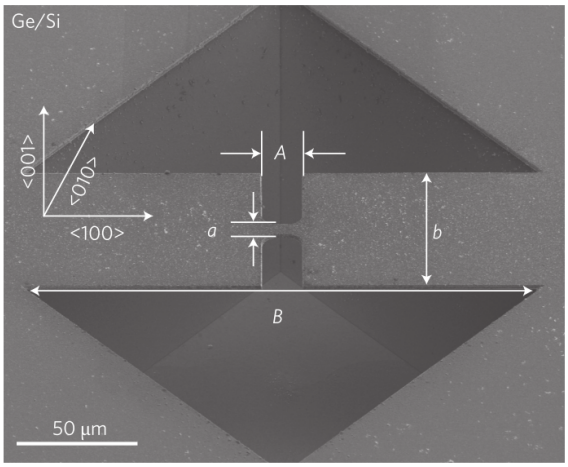

Figure 3.2: Scanning electron microscope of a strained Ge microbridge, from ref [7].

A number of variants of this device style have been since been investigated. In initial demonstrations clear peaks could not be resolved to distinguish the contributions from the LH and HH bands. This was carried out by Nam et al, who used uniaxially strained wires up to 1.6%, and measured the photoluminescence with a polarizer aligned parallel and perpendicular to the strain axis [90]. In the case of uniaxial strain, this can be achieved by surface normal measurement, given that the strain axis is only in 1 direction. Results showed that with increasing strain, the transverse polarization dominates the spectra at longer wavelengths, i.e. due to transitions with the upper most valence band (LH). This

is due to the symmetry of the LH Bloch functions [91], and is in keeping with the results in [87].

Significantly higher levels of strains were subsequently achieved using the same technique [92]. 5.7 %uniaxial strain was measured by Raman spectroscopy, which should theoretically be direct bandgap based on deformation potential theory, however gain was not demonstrated. Photoluminescence measurements were limited to lower levels of strain due to a detector cut-off of 600 meV (~ 2 μm wavelength). This work highlighted that even when direct bandgap, the fraction of electrons in the Γ band is only $\sim 2\%$. It is noted that up to 8.0% uniaxial strain is required before 50% of electrons reside in the Γ.

A remaining challenge for such a device was to form a device structure that allows for lasing, and for which the optical emission can be routed on chip. The fabrication of an optical cavity from such geometry was tackled by using an etched Bragg mirror structure at the ends of each wire [93]. Measured Qs reached that of 2000, in uniaxially strained devices with 2.6% strain. In this device, stiction caused the Ge ridge to bond to the oxide layer, which the authors cited gave improved heat syncing compared to free standing structures. An increase in Q was found for increased strain in otherwise identical structures, indicating the onset of line width narrowing. This showed an increased yet still negative, net-gain i.e. decreased losses.

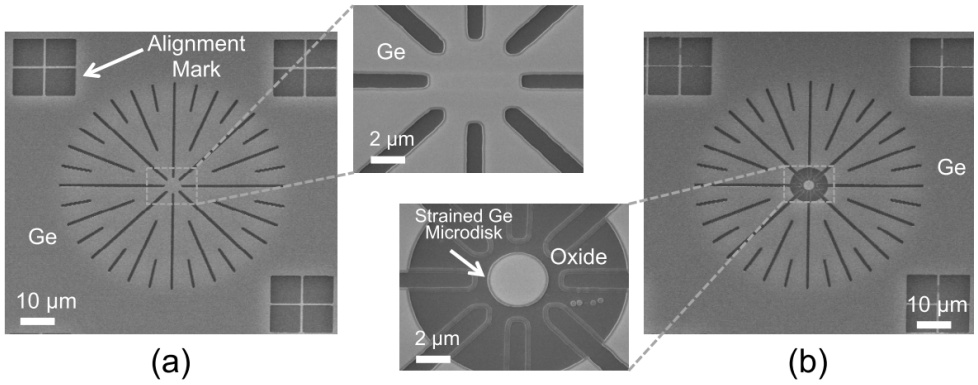

Figure 3.3: Scanning electron microscope of a strained Ge microbridge, from ref [8]. a) the biaxially strained disk before patterning b) the patterned disk with a silicon nitride top stressor.

Stiction has also been used as a means of maintaining induced biaxial strains into Ge microdisks structures. Similarly to the microbridge stuctures, Sukhdeo et al used a

suspended microdisk structure, which is dry etched, leaving supporting arms around the disk circumference [8]. This is then released by wet-etching, at which point the arms constrict and pull at the central disk, inducing a biaxial tensile strain, Fig. 3.3. The disk can subsequently bonded to a lower oxide layer via stiction and the arms can be released, leaving a tensile strained disk. Silicon nitride stressors can then be deposited on the top surface. Tensile strains of approximately 0.7 % were realized by this method.

An alternative approach which received interest is the use of silicon nitride stressor layers to induce a tensile strain in Ge layers, which is the focus of this work. Such processes were used in CMOS foundries to induce strain in Si channels, in order to provide mobility enhancement [43]. The fact these techniques have been used extensively in CMOS made this an attractive technology, as incorporating silicon nitride strained Ge sources into Si foundry process flows could be simplified compared to other techniques.

Initially strained straight waveguides were the subject of interest. Structures with widths ranging from 1- 8 μm were investigated with compressive silicon nitride stressors [94]. 500 nm thick n-type Ge epilayers were grown on GaAs substrates, allowing them to be lattice matched and therefore minimising threading and misfit dislocations. Uniaxial strain of up to 1 % was measured using Raman spectroscopy, and emission was found to red-shift to $\sim$ 1.65 μm. This work highlighted the importance of waveguide orientation, as waveguides lying in the [110] directions induce an L-valley splitting, which reduces carrier concentration in the Γ. This effect is discussed in chapter 6 with regard to strained Ge microdisks. Similar structures even showed optical gain in undercut photonic wires with only 0.4% tensile strain [95], showing a superlinear increase of emission intensity at 1.7 μm with increase wire length. Gain of 80 cm^{-1} was measured, however no lasing action was reported.

Further work was reported from strained Ge on SOI waveguides, using a CMOS compatible process [9]. So called I and H structures were used, which either had constrictions at the end of the ridge, giving the H type structure, or were standalone ridges, giving the I type structures, Fig. 3.4. It was found that increased tensile strain was observed along the waveguide length in I structures where the ends were free to expand. Peak biaxial equivalent strains of 0.7 % were measured, and an intensity increase was observed of approximately 12 times. The advantage of top stressors were discussed, and it was highlighted that the reduced bandgap at the top plane is convenient, as in effect it forms a potential well which reduces the diffusion of carriers towards the defective interface.

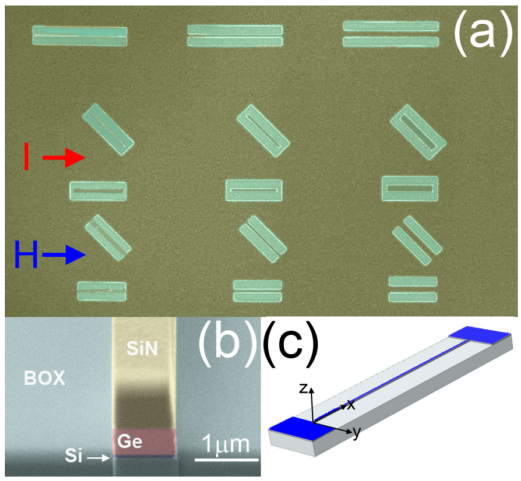

Figure 3.4: a) Top down scanning electron microscope (SEM) image of the I and H type waveguide structures. b) False coloured SEM of a Ge waveguide with silicon nitride stressor. c) Illustration showing the orientation of COMSOL model. Image from [9].

Silicon nitride stressor work was furthered by the first demonstration of a strained Ge microdisk cavity [96]. Ge microdisk cavities have been a subject of interest even without stressors, due to the potential to realise high Q structures with good optical confinement [97]. Ghrib et al used undercut Ge on GaAs cavities, and applied high stress silicon nitride layers [96]. A range of diameter disks were investigated and photoluminescence results were used to infer a strain of 1 % in 4 μm disks, with emission towards 2 μm wavelength. In this work, the high strain gradient in the vertical direction was discussed, which is potentially problematic for a good overlap of the mode with a gain region. This is discussed with regard to the work in this thesis, in Chapter 6. This was supplemented by the demonstration of an electroluminescence device for which 0.7 % strain was achieved, using no undercut to the disk structure [98], and it was shown that a ring contact geometry was preferable for optimum strain transfer opposed to central circular contacts. Fabry-perot resonances were observed, and Q factors were found to be comparable to optically pumped structures, suggesting that the metal contacts do not cause significant optical loss in this geometry. This was the first electrically driven Ge device strained by a silicon nitride stressor.

In order to reduce the strain gradients predicted by finite element modelling of the first strained Ge microdisks [96], a double bonding technique [10] was employed to improve

strain profiles in the vertical direction. First, Ge epilayers are grown on GaAs substates, and patterned into microdisk structures. They are subsequently coated with a high stress silicon nitride layer, and flip chip bonded using a gold layer, to a new substrate, Fig. 3.5. A second high stress silicon nitride layer can then be deposited, fully encasing the disk in silicon nitride. Biaxial strains up to 1.5 % were realised at the top plane using these techniques. The double bonding has the advantage that strain uniformity is improved in the vertical direction, and strain is extremely homogeneous at the top plane compared top only stressors. Modal gain modelling in this work suggested that a > 50 times improvement in modal gain could be obtained by using all around stressors. However, as will be discussed in this work, the maximum strain found to be achievable for single stressor layers was 1.3 %, which is significantly less than strains reported in this thesis.

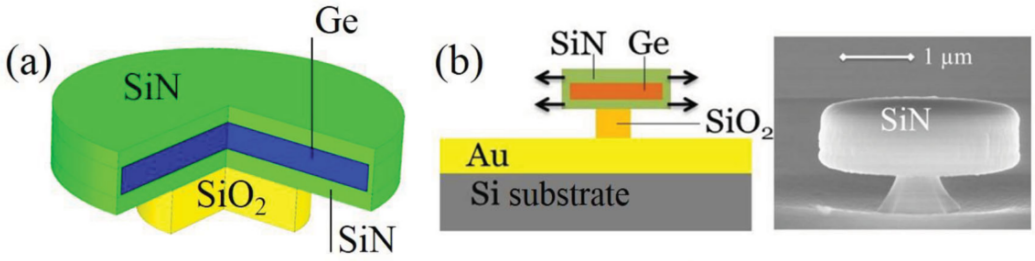

Figure 3.5: a) and b) show an illustration of a Ge microdisk with an all-around silicon nitride stressor. c) scanning electron microscope image of an Ge microdisk with a silicon nitride stressor. Image from [10].

In subsequent work, using temperature dependent PL, Kurdi et al inferred that such double bonded structures are in fact direct bandgap [99]. Measurements on a 1.67 % biaxially strained 9 μm diameter disk, showed that the Γ and L valleys are approximately degenerate, and therefore the higher strained structures, which could not be measured experimentally at low temperatuers due to increased laser heating, should be direct.

The state of the art strained Ge devices have therefore reached the levels of a direct bandgap material, however, for the case of silicon nitride stressed devices in [10], this has required CMOS incompatible processes using Au as a bonding layer for the flip chip bonding process. The alternative approach of using uniaxially strained micro bridge structures, have also shown direct strains where a direct bandgap is expected. With either approach, however, lasing has not been demonstrated.

It should also be noted the means of inducing strain detailed in this chapter are by no means exhaustive, and that other methods of applying external stress have been demonstrated. For example, lead zirconate titanate (PZT) stressors were used to induce strain the arms of a Ge Mach Zehnder (push-pull configuration), in order to modify the refractive index and thereby modulate the output [100]. The maximum strain induced by these means, however, was significantly lower than the other techniques described in this chapter, reaching peak values of 0.4 % transverse to the waveguide direction. There is potential however, that such techniques could be used in conjunction with other processes in emitters to allow for dynamic tuning of the emission wavelength.

3.2 GeSn alloys

The alternative approach to strain, and another means of reducing the Γ to L energy difference is by alloying with Sn, as was introduced in the previous chapter. Sn exists in two solid phases; α-Sn and β-Sn. The former is a semimetal with a negative bandgap and a diamond crystal structure, and is the phase of interest for alloying with Ge. The latter, β-Sn is metallic, with a body centred tetragonal lattice, and is the stable Sn phase above 13.29 °C.

In general, the bandgap of binary alloys can be described by a Vergard's approximation, which is a linear extrapolation between the two bandgaps. Between α-Sn and Ge, the difference in the Γ valleys is far larger than the difference in the L-valleys, meaning that above a particular Sn concentration, GeSn alloys will become a direct-bandgap material. However vergaards approximations often deviate significantly from the actual alloy bandgaps, and therefore the addition of a bowing parameter is required, which introduces a quadratic dependency of the bandgap on the alloy concentration. While it was expected that Sn alloying would lead to a direct bandgap alloy, the bandgap bowing was relatively unknown.

While GeSn growth techniques were still in their infancy, a number of theoretical works were carried out to calculate the point at which GeSn alloys would become direct. The authors in [101] used a tight-binding model using the virtual crystal approximation (VCA) to predict the transition should occur at > 20 % Sn, close to that of Vergard's approximation which suggest a direct bandgap transition at 21 %.

A transition at 14 % was suggested by [102] using a band anti-crossing model. The lower bound for this crossing came from first principals calculations using density-functional theory, requiring Sn concentrations of only 6.3 % [103]. Therefore, a large discrepancy was clearly present, however experimental investigations were inhibited by a number of growth challenges, even at the lower bound of the theoretical transition.

Such challenges stem from a large lattice mismatch with Ge ($\sim$ 14 %), and the fact that in Germanium, α-Sn has a low solid solubility limit, of just 1.1 % [104], with excess Sn forming β-Sn precipitates [105]. Non-equilibrium growth conditions are therefore required to give super-saturated α-Sn concentrations [106], which is challenging due to the tendency of Sn to segregate on the surface [107]. This is thought to be the dominant effect during growth, opposed to bulk precipitation, due to the fact that it is energetically favourable for a Sn atom to swap to a surface state in a Ge matrix [108]. This can be mitigated by employing low temperature growth techniques, which reduces the mobility of the Sn atom at the surface, and therefore minimises precipitation. Fast growth techniques are also advantageous, and further help reduce the time window in which a Sn atom can exchange with a Ge surface atom.

Initially, successful growth techniques were achieved by molecular beam epitaxy (MBE), requiring low growth temperatures of less than 200 °C, which produced a number of good quality GeSn layers. As a result of the large lattice mismatch between GeSn and Si, Ge virtual substrates and a range of III-V substrates were used for MBE growth to decrease the lattice mismatch. This work allowed for the initial investigation of the optical properties of GeSn layers with absorption measurements [107, 109, 110]. By fitting to the absorption curves, and taking into account direct and indirect transitions, He et al [110] inferred that there was a transition to direct bandgap in $Ge_{0.85}Sn_{0.15}$ films, and derived a bandgap bowing parameter of 2.8 eV, therefore suggesting that the lower bound estimates of the direct bandgap transition were more accurate than that of vergaards approximations. Despite the fact that high Sn contents were demonstrated, however, the inability of MBE growths to grow device quality layers lead to a decline in scientific interest ($\sim$ the year 2000) [111].

Initially, the use of CVD growth was prohibited by the absence of available gaseous precursors, due to the weak bonding of the Sn-H bond, which leads to unstable precursors. The first CVD growth was demonstrated by Taraci et al [112], and shortly after SnD_4 precursors were proposed and demonstrated [113], giving high quality GeSn alloys.

This precursors, however, had short lifetimes [114], thereby limiting investigations. Commercially available $SnCl_4$ precursors have since been used by Vincent et al [106] and are now more common than SnD_4 due to the improved stabilities. While germane (GeH) precursors can be used, they require growth temperatures above 350 °C for acceptable growth rates [115], which can be problematic in minimising Sn precipitation. It was found that digermane [116] and tri-germane [117] can provide higher growth rates at low temperatures due to the reduced activation energies for dissociations and are therefore more appropriate precursors than GeH. The previously developed technologies for Ge growth have also been critical for realising high quality GeSn alloys on Si substrates, as Ge VSs are often used, and are generally grown using the two temperature growth technique in order to minimise TDDs and provide low surface roughness. The advent of these techniques led to device grade GeSn layers, and brought back interest in the material system. In recent years, both MBE and CVD have demonstrated high quality, device grade GeSn alloys with Sn contents at levels where a direct bandgap transition is expected (particularly based on lower bound estimates), allowing for the optical properties to be examined, in the form of photoluminescence and absorption measurements.

As expected with the decreasing energy of the Γ band, PL intensities were found to increase with Sn content [30], showing that high quality layers were being produced without significant degradation of carrier lifetimes from high levels of Sn incorporation. CVD grown layers showed emission up to 2.4 μm [118], which at the time of publication was the longest wavelength emission observed from the material system. In [119], bowing bandgap bowing parameters were measured to be approximately 2.1 eV for the direct band, suggesting further experimental evidence that a direct transition would occur close to the level predicted by DFT, at 7.1 % for unstrained material. This was hugely significant, as the technological problems associated with reaching device grade structures with Sn concents of > 20 % is non-trivial. Based on their calculated bandgap bowing values, it was inferred that their 8.6 % alloys should be direct band materials, however no further evidence was provided to prove this fundamentally. By this time a number of optical and electrical devices had also been demonstrated, including photodetectors [120, 121], transitors [122] , avalanche diodes [123], and LEDs [116, 124].

Subsequently, and most significantly, lasing was achieved in partially relaxed $Ge_{(1-x)}Sn_x$ layers with 12.6 % Sn, and a detailed experimental analysis of low temperature photoluminescence was used to show that the material has a fundamental direct bandgap. This

was demonstrated by employing a model which uses an effective mass approximation to use calculate the joint density of states. This gives an approximation of the spontaneous emission, when considering the joint probability of occupation for electrons in the conduction band, and holes in the valence band, at an energy separation corresponding to the photon frequency. These functions have temperature dependence, primarily due to the change of the carrier distrubition, as the Fermi-function moves closer to a step-like function, which in essence means, that with two conduction band valleys in close proximity (in energy), carriers condensate into the lower band at low temperatures. Given that there is significantly higher recombination efficiencies at the direct band, the extent to which the PL intensity increases at low temperatures can be used to calculate how close in energy the Γ and L valleys are. This model was subsequently employed for strained Ge layers [99].

Given that all the layers considered in their work had small residual compressive strains, the authors extrapolated their measurements to fully relaxed layers, suggesting that $Ge_{0.9}Sn_{0.10}$ layers should also be direct when unstrained.

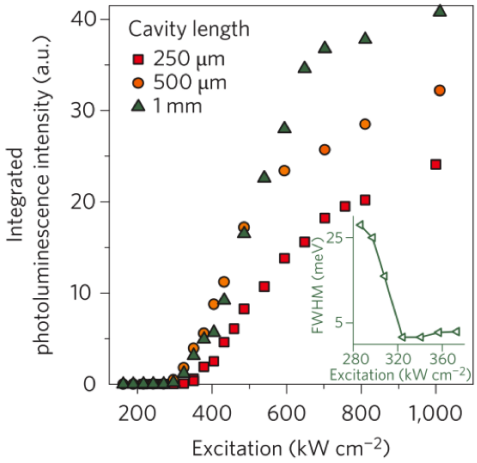

Figure 3.6: The integrated photoluminescence intensity of GeSn Fabry Perot resonators, as a function of excitation power. A clear threshold is evident, indicating lasing. Image from [11].

Most significantly, lasing was achieved in straight FP-waveguide lasers, at temperatures between 20 and 90 K, demonstrating peak modal gains of $\sim$ 110 cm^{-1} at 20 K.

Thresholds, however, were still extremely high, Fig. 3.6, with the onset of gain occurring at $\sim$ 325 kW/cm^2. However, these results were achieved from an un-optimised device with no passivation, and no n-type doping.

A second GeSn laser was since demonstrated in the form of an undercut microdisk cavity [12]. Dry etching techniques were developed to be selective from GeSn to Ge [125], and were used to remove the Ge virtual substrate, Fig. 3.7. This allows for partial relaxation of residual compressive strains in the alloy, providing a lower band-gap around the disk circumference. The lasing characteristic was improved compared to the previous demonstration, with thresholds of 130 kW/cm^2 at 20 K, and lasing up to 130 K in 12.5 % Sn layers. These improvements were attributed to the improved modal confinement in undercut structures, and the addition of passivation by Al_2O_3, which has been shown to passivate GeSn layers [126]. Additionally, lasing was demonstrated in relaxed 8 % Sn layers emitting at around $\sim$ 2 μm, which have almost degenerate Γ and L energies, thereby showing that there is significant scope to tune the laser wavelength over the 2 - 2.5 μm range by changing the Sn content.

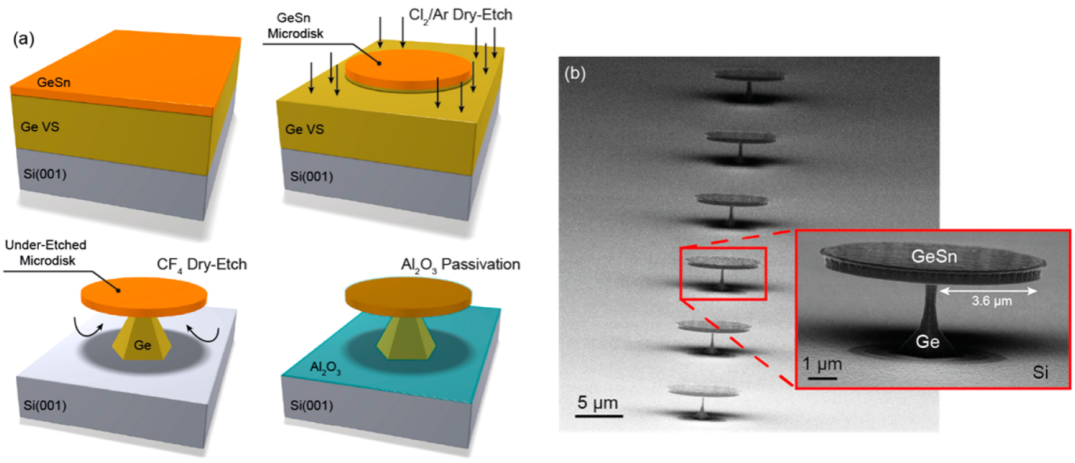

Figure 3.7: a) Illustration of the fabrication of GeSn microdisks. b) scanning electron microscope image of GeSn microdisks. Image from [12].

A reason for the quenching observed in both lasers demonstrated, is the high DOS in the L-valley. Despite being direct-bandgap, the DOS mass discrepancy is sufficiently large ($\sim$ 0.0236 m$_o$ compared to $\sim$ 0.5424 m$_o$ based on k.p modeling of the direct band

effective mass), that achieving high population in the Γ becomes challenging as the quasi-Fermi level reaches the L valley. This is backed up by the fact that in the microdisk laser structures, thermal quenching occurred at lower temperatures for lower Sn concentrations, suggesting that the Γ to L energy differences are a key parameter in the ultimate goal of achieving a room temperature device [127].

The combination of tensile strain and Sn alloying is therefore an interesting prospect, and has been the subject of theoretical work [5, 128, 129]. It opens the door to a further degree of freedom in GeSn alloys, allowing the potential to achieve direct-bandgap with lower Sn concentrations, thereby improving the thermal stability of grown layers. Γ to L energies can be further enhanced in inherently direct alloys, and there is also scope to obtain a group IV material with a band-edge emitting/absorbing in the MIR. Currently, the longest wavelength emission reported in literature is ~ 2.6 μm [130]. In this work, emission past 3 μm wavelength is demonstrated, in Chapter 7. If the level of strain that has been applied to Ge devices can be applied to high Sn content GeSn layers, the entire 3 - 5 μm sensing window may be within reach. This has been theoretically investigated for devices such as photodiodes [131]. Realistically therefore, this allows for the potential to measure the absorptions of gaseous molecules such as methane (CH_4), and even carbon dioxide (CO_2), which have vibrations at ~ 3.3 μm and ~ 4.2 μm respectively [132]; methane detection in particular is discussed in Chapter 7. Currently III-V material systems are required for detection at these wavelengths [133], and therefore huge cost benefits could be gained be the use of strained GeSn layers, which can be grown on 200 mm Si substrates, and processed in Si compatible foundries.

Interestingly, it is the silicon nitride stressor technologies that may pertain most highly to strained GeSn, opposed to the top down approaches that have been used for Ge, which rely on a residual tensile strain in the epilayer. While this is present in Ge due to the difference in thermal expansion coefficients between Ge and Si, the much larger lattice constant of GeSn leads to compressive strain when grown on Ge or Si. The ultimate ability to make use of SiGeSn ternary alloys to impart strain on GeSn layers may well become the method of choice [128, 134], however currently the optical properties or such layers are poor, and silicon nitride stressors can currently allow for an understanding of the optical properties of highly tensile GeSn alloys.

In terms of the potential for lasing, Wirth et al modelled the gain of tensile strained GeSn layers, taking into account the free carrier losses, as well as intra-valence band

absorption [128]. It was demonstrated that theoretically, a $Ge_{0.95}Sn_{0.05}$ layer with 1 % strain, should have higher gain than a fully relaxed $Ge_{0.9}Sn_{0.1}$ layer, for all levels of doping and injection. Interestingly, it was found that with increased levels of tensile strain, gain is diminished due to intra-valence band absorption, which occurs as a result of the VB splitting from tensile strain. There is therefore significant scope to investigate strained GeSn layers. Currently a number of theoretical publications have shown the potential advantages to such layers, however there is limited experimental investigation into the characteristics of tensile GeSn to date [135–137].

4

Fabrication, Characterisation and Growth Techniques

4.1 Fabrication

4.1.1 Facilities

The fabrication work carried out during this PhD was done in the James Watt Nanofabrication Centre (JWNC). The centre is a 1350 m^2 facility with state of the art nano fabrication tools, covering lithography, dry and wet etching, metrology and imaging. For the fabrication of meso-scale features, a clean environment is required with minimal particle contamination. The class of a cleanroom indicates how many particles larger than 500 nm are present in a cubic foot volume of air. The JWNC contains multiple rooms, with classes of 1000, 100, and 10 depending upon the cleanliness requirements of the room.

4.1.2 Cleaving

In this work, the materials provided by collaborators are based on 100 mm Si wafers. In order to be able to effectively process the material, this is required to be cut into small enough samples that can be easily manipulated by tweezers, and are manageable for characterisation. Typically samples of 1×1 cm were used, allowing for a sufficient number of samples from the wafer, but a reasonable sample size to handle. Wafers are diced using either a diamond saw, or cleaved with the aid of a diamond tipped scribe pen.

The wafers are first coated by a polymer which protects the top surface of the samples from any dust or particles produced during cleaving. The wafers used in this work are all based on (100) Si substrates. This gives cleave planes at right angles and therefore allows the samples to be diced into squares.

4.1.3 Cleaning

Samples are cleaned before they are processed. This removes residue which could impede or effect subsequent processing steps. Acetone and isopropyl-alcohol (IPA) are used as standard solvent cleans. Acetone removes organic residue and degreases the sample surface, however when dries it leaves a residue. Samples are therefore moved directly from acetone to IPA, which gives a less effective clean than acetone, but removes the acetone residue.

For certain materials, e.g. silicon, more aggressive acid cleans are available; typically RCA cleans 1 and 2. RCA-1 uses water, ammonium hydroxide (NH_4OH) and hydrogen peroxide (H_2O_2), and removes organic residue from the sample surface. In the process it forms a thin (0.1 nm) SiO_2 layer which self limits the reaction. Typically a dip in hydrofluoric acid is then carried out to remove the oxide layer, and RCA-2 is used to remove metal contaminants deposited during the RCA-1 clean.

While such aggressive cleans are appropriate for cleaning Si surfaces, equivalent cleans would etch Ge at an uncontrollable rate. This is due to the water solubility of the Ge oxide, which means that the chemically oxidised surface is etched by the solution, and continually oxidised and etched. Hydroflouric acid cleans can however be used for Ge, which strips the native oxide. Cyclic cleaning with HF and RO water can leave a hydrogen terminated surface.

4.1.4 Lithography

Lithography is required in order to transfer patterns into semiconductor materials. Samples are coated with a polymer that is either sensitive to a high energy electron beam, or to ultraviolet light. In positive resists, exposure modifies the chemical composition of the polymer causing it to become soluble in a developer. Therefore, selective exposure can allow for a pattern to be transferred into the resist layer. The remaining resist then forms a mask for the next processing step; allowing for selective removal of the semiconductor

material via etch processes, or deposition of metals in the open resist windows, as shown in Fig. 4.1. The two types of lithography used in this work are photolithography, and electron beam lithography. This will be described before further processing techniques such as metal deposition, dry-etching, wet etching, and chemical vapour deposition.

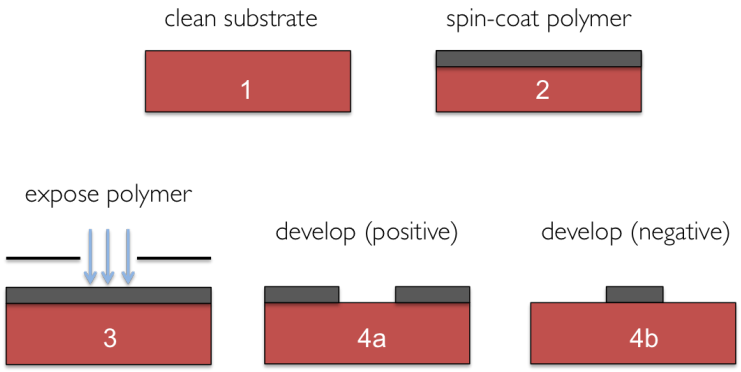

Figure 4.1: Simplified illustration detailing the main steps in a lithography process. The steps are numbered to indicate the correct order of the process.

4.1.5 Electron beam lithography

Electron beam (e-beam) lithography has several advantages over optical lithography. The primary advantage is that of improved resolution. In standard optical lithography processes, i.e. without immersion systems or double exposure techniques, the feature size is theoretically limited by the diffraction limit of the UV light. In electron beam lithography, high energy electrons are use to expose a electron sensitive polymer, and have demonstrated feature sizes down to 5 nm [138]. Given that e-beam lithography is a mask-less technology, it allows the user to customise designs on a given lithography stage, without the requirement for the production of a mask. The main disadvantage of e-beam lithography is throughput, as the electron beam has to scanned over every area to be written, unlike photolithography which is inherently parallel. The electron beam lithography system used in the JWNC is a Vistec VB6 lithography tool. A high energy beam is produced from an electron gun, where high energy electrons are removed from a tungsten tip by the application of an applied electric field. The position of the beam is controlled by magnetic lenses, allowing deflection of the beam by up to 1.3 mm; this region defines a field. In order to write areas larger than this area, a piezo-electric stage is used to move

the sample position relative to the electron gun. This allows for wafers up to 200 mm to be patterned. In principal, the feature size in electron beam lithography is limited by the wavelength of the electron, which at 100 kV is ~ 0.87 pm. In practise this is not the case, however, due to electron scattering mechanisms that serve to broaden the beam.

These mechanisms can be broken broadly into forward scattering and backscattering. High energy beams have long penetration depths and therefore are not highly absorbed in the resist. Secondary electrons are produced from inelastic electron-electron interactions; the angle at which these electrons propagate is a function of their energy, and therefore low energy secondaries are mainly responsible for the resist exposure and give rise to the local broadening of the exposed area. This mechanism describes forward scattering.

Backscattered electrons are generated due to electron-nucleus reactions, which causes broadening on a much larger scale (on the order of 10s of microns). This is particularly problematic in densely patterned arrays where the backscattered beam will serve to re-expose regions surrounding the beam, reducing contrast and altering feature sizes (dependent on resist tone). This is known as the proximity effect, and has significant ramifications for particular shapes and patterns. For instance, the centre of a square written with an electron beam will receive a backscattered dose when writing the the square perimeter. As a result, when writing the square centre itself, a lower dose is required as this region will receive a large enough total dose from the proximity effect from the square sides. This compensated dose can be achieved in dedicated software packages for fracturing patterns for electron beam lithography, such as Layout Beamer, through the use of proximity error correction. Point spread functions are used to determine the backscattered dose as a function of radius away from the point of exposure. This is used to calculate the necessary dose compensations to individual shapes and structures, as well as across arrays of patterns.

4.1.5.1 Electron sensitive resists

Election sensitive polymers are required for e-beam lithography, and as in photolithography, are available in positive and negative tones. In positive photoresists, exposure results in the increased solubility of the film to the developer solution. In negative photoresists the opposite effect happens, i.e. the resist becomes less soluble in developer, and exposed regions are left remaining on the sample surface following development. The two

ebeam resists used predominantly in this thesis are Hydrogen silsesquioxane (HSQ), and polymethyl methacrylate (PMMA), which are negative and positive resists respectively.

HSQ initially has a monomer cage structure, with Si atoms on each corner Fig 4.2. Each Si atom is connected via an oxygen bond, meaning that each Si atom is bonded to 3 others via an oxygen bridge. The remaining bond of each Si atom linked to a hydrogen atom on each corner of the cage. Under exposure to heat, or a high energy electron beam, this hydrogen bond is broken, and in the presence of water vapour, OH are produced. This then reacts to form further Si - O - Si bridges, which connects each cage corner to a neighbouring cage. In this state, HSQ is glass-like. High resolutions can be achieved with HSQ, which in conjunction with its etch resistance, make it appropriate for etching structures in Si and Ge. HSQ can be diluted with Methyl isobutyl ketone (MIBK) to control the thickness. This can be critical as improved resolutions are possible with thinner resists.

HSQ is developed in 25 wt% Tetramethylammonium hydroxide (TMAH). Frequently CD26 developer is used which contains smaller concentrations of TMAH, which can acheive higher resolutions but also results in reduced contrast. In this work, 25 wt% TMAH is used exclusively.

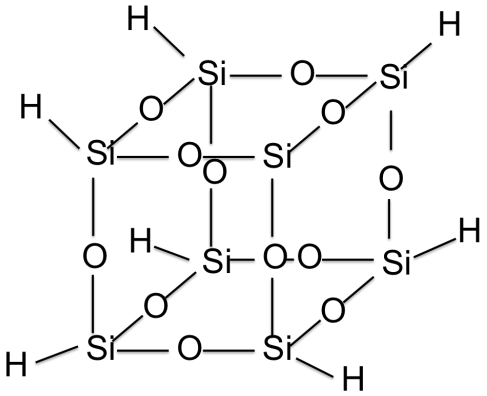

Figure 4.2: Illustration showing the structure of an HSQ monomer cage structure.

PMMA is a high resolution positive tone e-beam resist, formed from long polymer chains of carbon atoms. Adhesion with PMMA is normally excellent, however etch resistance is generally poor. It does have the advantage, however, that solutions can be purchased with different molecular weights. Using a high molecular weight polymer on

top of a lower weight polymer leads to an undercut profile after development. This is illustrated in Fig. 4.3, and can allow for undercut resist profiles which are useful for processes such as lift-off, which is described later. PMMA is developed in MIBK, which can be diluted with IPA in order to increase developer times and provide more controllability.

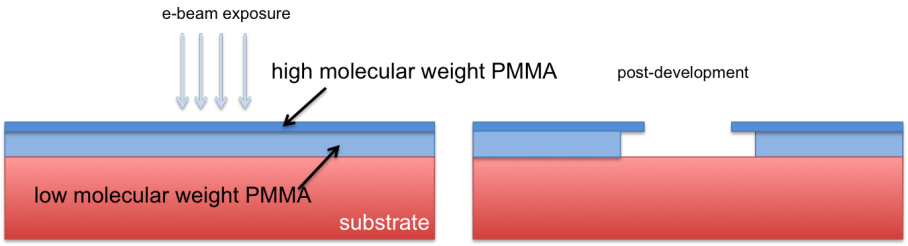

Figure 4.3: Illustration of a polymethyl methacrylate (PMMA) bi-layer, which forms an undercut profile when a high molecular weight variant is spun on a lower molecular weight version.

4.1.5.2 Dehydration bake

Before coating the samples with resist, they are baked at 120 °C in an oven to remove moisture on the sample surface, which helps promote resist adhesion. Without this step resist polymers can bond to unstable water molecules on the sample surface.

4.1.5.3 Spinning

To coat samples with resist a process known as spin coating is used. A sample is held on a chuck by a vacuum, and resist is dropped onto the sample by a calibrated pipette. The sample is then spun, typically between 1000 and 6000 rpm to uniformly coat the sample with resist. The resist thickness is predominantly a function of its viscosity, however, a degree of control is possible by varying the spin speed.

4.1.5.4 Soft baking

After the samples have been spun they are soft baked to remove the solvents in the resist, in preparation for exposure. This is done on a temperature controlled hot plate. Particularly in negative resists such as HSQ, soft-bakes can cause partial cross linking of the polymer and therefore can act as a base exposure dose. Therefore for high contrast

processes typically low soft-bake temperatures are used. In this work, HSQ was generally baked at 90 °C for 2 minutes before exposure.

4.1.5.5 Exposure

Samples are exposed by a Vistec VB6 high resolution lithography tool by a 100 kV electron beam. Features are patterned using vector beam patterning, meaning that individual fields are patterned individually rather than a raster scan over a full chip.

The 10^{20} bit pattern generator splits the 1310.7 μm field size into 1.25 nm steps, which defines the resolution. This beam step size (BSS) can be further increased by changing the variable resolution unit (VRU), giving a BSS which is a multiple of 1.25 nm. The beam spot size can be controlled by a combination of varying the beam current, and by changing a variable aperture in the beam column.

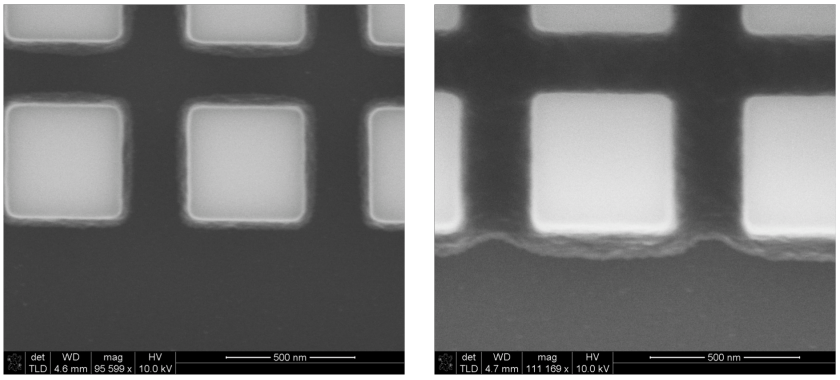

Figure 4.4: Scanning electron microscope (SEM) images showing the effect of dose on 500 nm Hydrogen silsesquioxane (HSQ) squares with 200 nm gap spacings. The left dose is 1400 μC/cm^2, while the right image is 1650 μC/cm^2.

In conjunction with the BSS, the beam current, and spot size define the total dose, which is the areal charge density at the sample surface. Typically doses of $\sim 1000\ \mu C/cm^2$ are used for HSQ features. This is dependant, however, on a number of factors including the pattern geometry and the age of the HSQ, so typically dose tests are run to find the optimum dose for a given pattern. Figure 4.4 shows HSQ squares with a slight overdose (left) and a significant overdose (right). The overdosed pattern is an example of how the backscattered dose causes proximity effects.

4.1.6 Dry Etching

Dry etching makes use of plasmas to both chemically and physically remove and etch materials. Accurate control of a number of parameters, i.e. plasma power, dc bias, temperature, gas flow rates, allow for greater precision than wet etches, with more ability to control the etch speed, and sidewall slope. High aspect ratios can be realised due to the greater anisotropy of dry etches.

4.1.6.1 Reactive Ion Etching

Reactive ion etching makes use of parallel electrode plates to generate an AC electric field. This excitation causes a plasma to be formed in the gas. Within the plasma, the lighter electrons are accelerated at a greater rate than the heavy ions. As a result, a negative charge builds up on the sample plate, which therefore develops a potential difference with respect to the plasma. This in turn causes ions in the plasma to bombard the sample. Etching is therefore part chemical, i.e. due to the chemical reaction of the ion and the sample, and part physical, as the material is sputtered by the accelerated ions. In order to reduce the isotropy of the chemical component of the etch, a passivating gas is also flowed in the chamber, which coats the sample surface to prevent further chemical etching. The physical bombardment of the ions in the vertical direction however, removes the passivation on the horizontal sample surface, meaning that sidewalls are still left passivated, and etches can be highly anisotropic.

Etch rates can be controlled by varying gas flow rates, as well as plasma densities and dc biases. In RIE systems, there is no independent control of plasma density and bias to the sample plate, as both are controlled by the power of the RF signal applied to the electrodes.

4.1.6.2 Inductively coupled plasma

Inductively coupled plasma (ICP) systems make use of an inductive coil to generate dense remote plasmas. However, unlike with RIE systems, these plasmas do not cause acceleration of electrons towards the sample plate, and therefore separate control of the dc bias is required to control the ion bombardment of the sample. This allows extremely dense plasmas to be obtained, which allow for highly chemical etches, but with low damage from low dc biases, which minimises ion bombardment.

4.1.6.3 Etch recipes

In this work, Ge, GeSn and Si are etched using SF_6 and C_4F_8. Etched structures are shown in Fig. 4.5. Fluorine chemistries are used to etch the material while C_4F_8 is used to passivate the sidewalls. The downside of such a chemistry is that C_4F_8 etches HSQ, which therefore limits the selectivity which is achievable. For the etch process used in this work, the selectivity of HSQ to Ge is approximately 3:1.

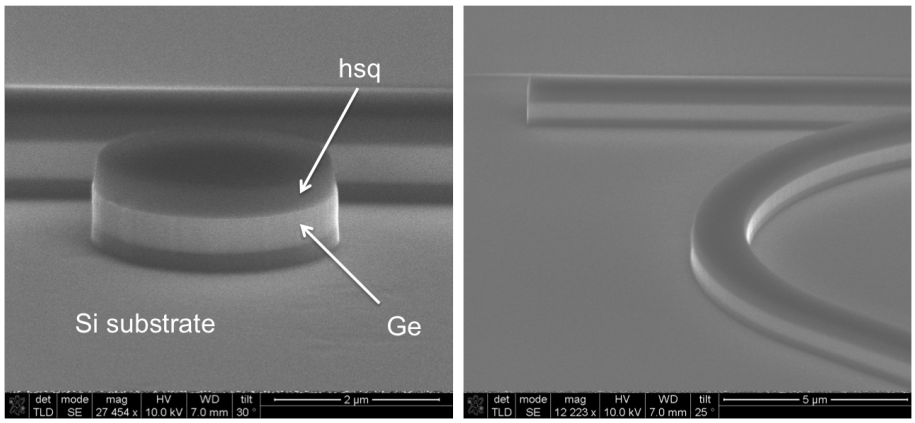

Figure 4.5: Scanning electron microscope image (SEM) of a dry etched Ge on Si feature, using a mixed recipe with SF_6 and C_4F_8.

The recipe used in this work is: C_4F_8/SF_6 = 90/30 sccm, 600 W, 9.8 mTorr, 20 °C. Alternatively, switched recipes alternate between the etchant and passivation gases, known as the Bosch process [139]. Modern etch tools, can provide ms switching time which reduces the so called scalloping effect associated with switched recipes. In this work, only mixed recipes are used, as smooth sidewalls were advantageous to optical devices, as they reduce optical scattering at the sidewalls.

4.1.6.4 Interferometry

In order to provide accurate feedback on the etch depth, an in-situ interferometry technique can be used. A 632.8 nm laser is focused onto the sample surface, in a region that is etched. As the surface is removed by the etch, the interference of the reflected signal causes an oscillation in the measured reflected power as a function of the etch depth. The period of oscillation is a function of the laser wavelength and the material index.

In Ge this results in an oscillation approximately every 60 nm. Furthermore, with epi-layer structures, a sudden change in reflectivity can be observed clearly, providing further information as to the position of the etch.

4.1.7 Dielectric deposition

4.1.7.1 PECVD

Similarly to etch tools, dielectrics can be deposited using plasma-enhanced-chemical vapour deposition (PECVD) tools, which use parallel electrodes like RIE systems or by ICP-PECVD systems, which make use of a coil to generate a remote plasma. PECVD systems generally operate around 300 °C, with the sample sitting directly on a heated lower electrode. Gas is injected via a "shower head" gas inlet at the upper electrode.

In the JWNC, the PECVD silicon nitride tool uses Ammonia (NH_3) and silane (SiH_4) precursors. This results typically in a high hydrogen content in silicon nitride films.

4.1.7.2 ICP

In this work, a Systems 100 ICP deposition tool is used to deposit high stress silicon nitride layers. The layout of the system is shown schematically in Fig 4.6.

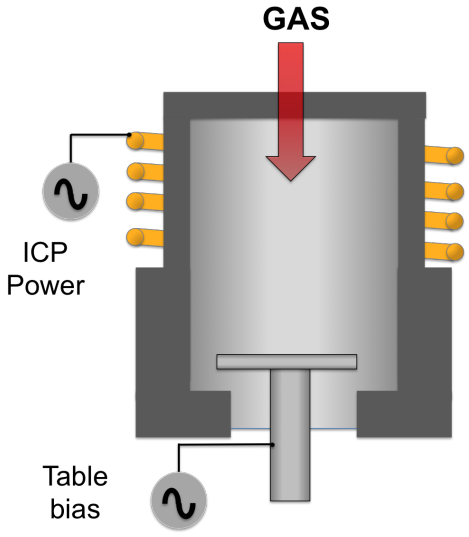

Figure 4.6: Simplified diagram of an inductively coupled plasma (ICP) chamber.

This system has an ICP source connected to the lid to generate a remote plasma, and a process chamber in the lower section. The ICP source consists of a 13.56 MHz RF generator connected to a 180 mm diameter alumina tube surrounded by a copper coil. A separate 13.56 MHz generator is connected to the substrate plate to allow separate control of the bias voltage, therefore decoupling the processes which occur in RIE tools. Nitrogen (N_2) rather than ammonia gas, is flowed through an inlet above the coil, while SiH_4 is inlet through a gas ring close to the sample surface; the flow rates of both gases are controlled by mass flow controllers. The dc bias allows control of the acceleration of nitrogen radicals to the sample surface where Si_xN_y is formed. The properties of the film can be tailored predominantly by altering the gas flow rates, the coil power, the chamber pressure, the dc bias and the temperature. In this work high stress depositions are carried out using this system. The recipe uses SiH_4 and N_2 with flow rates of 7.3 and 6 sccms respectively. A coil power of 300 W is used, at a chamber pressure of 5 mTorr, with platen powers ranging from 2 to 8 W. For low stress recipes the coil power is reduced to 150 W, with zero platen power, and gas flow rates of 7.4 and 6 sccms for SiH_4 and N_2, at pressures of 4.4 mT.

4.1.8 Wet etching

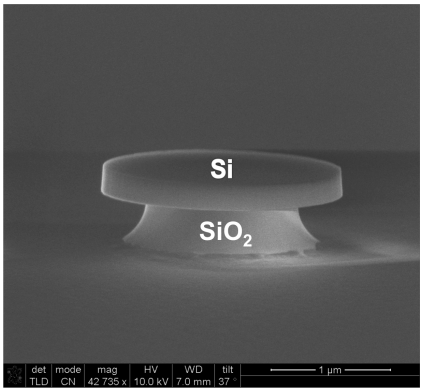

Figure 4.7: A scanning electron microscope image of a dry etched Si disk on a silicon on insulator (SOI) wafer. The exposed oxide has been wet-etched in 5:1 buffered hydrofluoric acid.

A number of wet etches are used in this work, which are purely chemical etches and can be either isotropic or anisotropic. This includes buffered hydrofluoric (HF) acid, which

etches SiO_2 layers, and is frequently used to strip native oxides on Si and Ge. An HF undercut etch is shown in Fig 4.7, where a Si on insulator (SOI) wafer has been dry etched to form a disk, and subsequently wet etched in HF to undercut the SiO_2 layer.

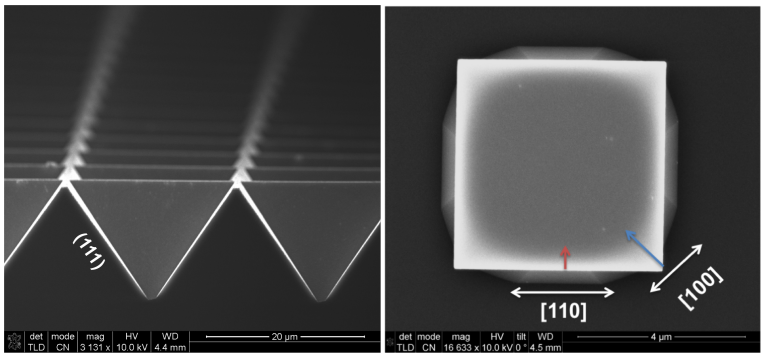

Figure 4.8: Left - A cross sectional scanning electron microscope image of a (100) Si surface etched in Tetramethylammonium hydroxide (TMAH).Right - a dry etched Ge square undercut by TMAH etching.

Tetramethylammonium hydroxide (TMAH) can be used to anisotropically etch Si. It is often for micro machining of bulk Si wafers, and for realising films in MEMs processing [140]. The anisotropy leads to a visible faceting of the etched material. {100} and {110} planes are etched faster than {111} planes, which are the etch stop planes.

The anisotropy and etch rates can be controlled by the temperature of the solution. The careful selection of a mask can therefore allow you to define the resultant geometry in the silicon layer. For example, with circular openings in a silicon nitride hard mask, the Si {110} and {100} planes are etched until the {111} planes are reached, at which point the etch slows significantly. This results in an inverted pyramid structure, shown in Fig 4.8 (left). With a square mask, with its edge aligned to the [110] direction, the corners shall be undercut at a great rate than the sides, shown also in Fig 4.8 (right).

In this work, wet etches were carried out in a custom built etch kit (Prof Jon Weaver). The kit comprises a heated element on which a 2 litre curved base beaker sits. A thermometer provides temperature feedback to a PID controller which modulates the heater to maintain a stable temperature. A condenser tube is used to remove vapour from the etch kit.

4.2 Characterisation techniques

4.2.1 Metrology

A range of tools are used within the facility to measure the metrology of processed or unprocessed samples. These include AFM, optical profilometry, ellipsometry, white light interferometry and use of optical and electron microscopes.

AFM systems use a sharp tip to scan over a sample surface. The tip is attached to a cantilever, which is illuminated by a laser spot, the reflection of which is aligned onto a split photodiode. While the tip is scanned over the sample surface the reflected beam moves on the photodiode, changing the received signal. By these means, nm height variations can be measured, with extremely high lateral resolutions, dependant on the tip size.

Optical profilers use an interferometry technique to measure the height of structures. A broadband white light is used to illuminate the sample through a custom objective, which is scanned in the z direction (away or towards the sample). As the objective is scanned an interference pattern can be built with the reflected light, and a depth image can be built. This has the advantage that large areas can be scanned simultaneously, however the lateral spatial resolution is limited to the diffraction of white light and is therefore several hundred nanometers.

4.2.2 Film stress measurement

Aside from AFM tools, other stylus profilers can be used to measure step heights in a straight line. Such tools can also be used to measure the residual stress in thin films. This can be measured by depositing a film on a 100 mm Si wafer. As the stress in the thin film relaxes, it causes the Si wafer to bend. The radius of curvature before and after the film deposition can be used to extract the film stress. This is calculated via Stoney's equation, Eq. 4.1, which requires only a few well known, or easy to measure parameters:

$$\sigma = \frac{E_S \; t_S^2}{6(1-\nu_s)t_f}\left(\frac{1}{R_{post}} - \frac{1}{R_{pre}}\right) \tag{4.1}$$

where E_s is the Young's modulus of the substrate, t_s is the substrate thickness, t_f is the film thickness, ν is Poisson's ratio for the substrate, and R_{pre} and R_{post} are the pre

deposition and post deposition radii of curvature respectively. This version of Stoney's equation includes Poisson's ratio to account for the fact that unlike cantilevers, the Si wafer bends over 2 axes.

The measurement is based upon a number of assumptions:

- The film is assumed to be significantly thinner than the substrate, i.e. $t_f << t_s$.
- Both the film and substrate thicknesses are assumed to be uniform.
- Both the film and the substrate are assumed to be isotropic, and linearly elastic.
- The stress in the film, and the curvature is assumed to be eqi-biaxial.

Stress measurements are taken using a Bruker Dektak surface profiler. The curvature of a bare 100 mm Si wafer is taken before a high stress silicon nitride is subsequently deposited and the curvature is remeasured. A rig is used to align the the stylus to a particular region of the wafer, to ensure that the same area of wafer is scanned. The film thickness is measured by ellipsometery, or by partially stripping the film by wet-etching, and measuring the step height with a surface profiler. The wafer thickness is measured by a micrometer. The pre and post deposition curvatures are fitted with a 5^{th} order polynomial by the method of least squares, and the stress is then computed using Stoney's equation. It has been shown that stress resolutions of 10 MPa is practical using such a technique. Taking into account the variation of the film thickness, and the wafer thickness, an error of $\pm$ 50 MPa is typical in this work.

4.2.3 Raman

Raman spectroscopy is a powerful technique which can provide feedback on a number of material properties, including strain [89], thermal conductivity [141], and doping density [142].

The classical derivation of Raman scattering begins by considering the polarisation of a molecule, P. An electric field induces a dipole moment when interacting with a material, the magnitude of which is dependant on the materials polarisability, α, as shown in Eq. 4.2.

$$P = \alpha E \tag{4.2}$$

For particular bonds, displacing the atoms with respect to their rest position can alter the polarisability. For a small displacement, dQ, the polarisability can be described as changing linearly with displacement, which in general is due to resonant vibrations of the molecule, and can be described by a co-sinusoidal oscillation. Therefore, by substituting Eqs. 4.3 and 4.4 into Eq. 4.2 the polarisability is given a time dependence.

$$\alpha = \alpha_o + \frac{\delta\alpha}{\delta Q} dQ, \tag{4.3}$$

$$dQ = Q_o cos(2\pi\omega_{vib} t) \tag{4.4}$$

When considering that the electric field inducing the dipole moment is due to an electromagnetic radiation, the field E can be written to include a cosine term, with the frequency of the light:

$$E = E_o cos(2\pi\omega_o t) \tag{4.5}$$

Substituting Eq. 4.5 for E in Eq. 4.2, along with the previous substitutions, allows the polarisability to be expressed as:

$$P = \alpha_o E_o cos(2\pi w_o t) + \left(\frac{\delta\alpha}{\delta Q}\frac{Q_o E_o}{2}\right)\{cos[2\pi(\omega_o - \omega_{vib})t] + cos[2\pi(\omega_o + \omega_{vib})t]\} \tag{4.6}$$

Now there are three terms contributing to the dipole moment - a part at the original frequency of the electromagnetic wave, plus two terms at the sum and difference of the vibrational and electromagnetic frequencies. This oscillating polarisability produces an electromagnetic field, which gives rise to the scattered light. The first term in Eq 4.6. describes Rayleigh scattering, while the second and third both describe types of Raman scattering; stokes and anti-stokes respectively.

Quantum mechanically this can be described as the absorption as a photon to a virtual or vibrational state, which then re-emits at a lower or higher energy than the original photon, as shown in Fig. 4.9. In crystalline materials, the vibrations that cause the oscillation of the polarisability term stem from crystalline vibrations, i.e. phonons. By straining the lattice the phonon modes are changed and this results in a shift to the Raman scattered line. The Raman shift coefficient is shown in Chapter 5.

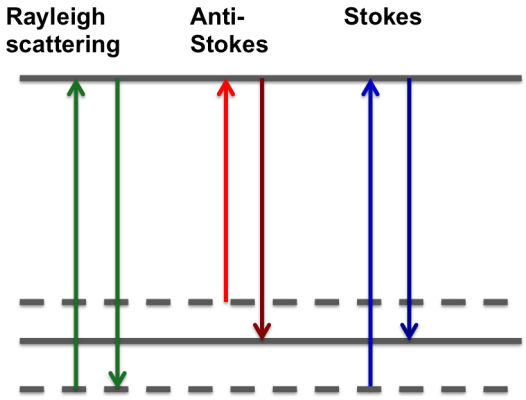

Figure 4.9: Illustration of the quantum mechanical description of Raman scattering. The vertical distance represents energy. A scattered photon can either energy with increased or decreased energy, describing anti-stokes and stokes scattering respectively.

In this thesis, Raman measurements were carried out predominantly on a Witec 300 RAS confocal microscope. A 532 nm ND:YAG is coupled into a microscope column and focused onto a sample through either a 20, 50 or 100 times objective with numerical apertures (NA) of 0.45, 0.5 and 0.9 respectively. The Raman scattered line is collected through the same objective and a notch filter rejects the pump. The filtered light is focused onto the end of an optical fibre which forms the pin-hole in the confocal geometry. A range of fibre diameters can be used which effects the amount of collected light, and the spatial resolution of the measurement.

The fiber couples the scattered light into a grating spectrometer with a CCD camera and a choice of gratings with 1200,1800 and 2400 g/mm. The spectrometers are calibrated using a broadband mercury source which emits a number of discrete spectral lines. With use of the 100 times objective the 532 nm source is focused to a diffraction limited spot. In conjunction with 10 μm core optical fiber, this leads to a spatial resolution of $\sim$ 300 nm. The sample sits on a piezo electric stage which allows Raman maps to be made over an area of 200 $\times$ 200 μm.

4.2.4 FTIR

Fourier transform infra-red spectroscopy (FTIR) is a sensitive spectroscopy technique, which allows for high resolution measurements with accurate frequency measurement

due to the fact that it is in effect self calibrating. An FTIR makes use of a Michelson interferometer in order to obtain the spectral information from a broadband source.

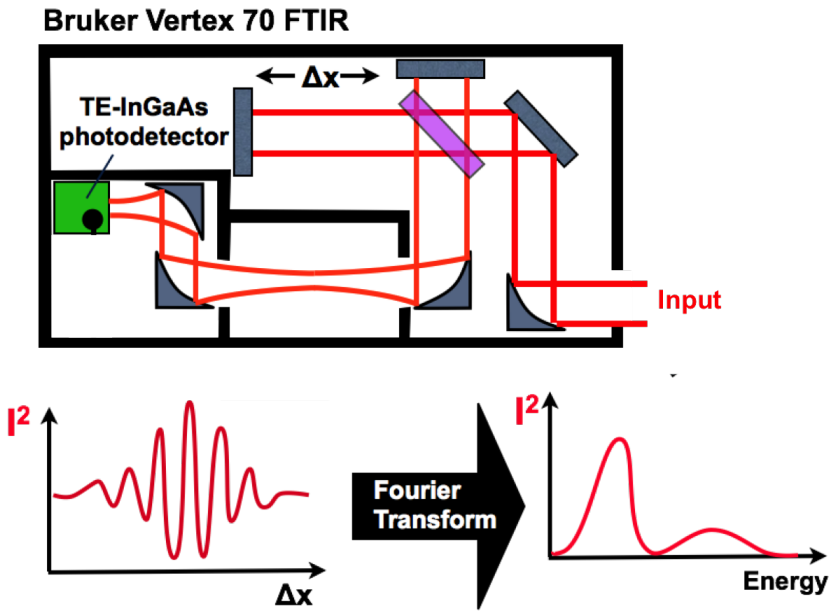

Figure 4.10: Simplified schematic of a Fourier transform infra-red spectrometer. This shows an input beam entering through an optical window, and being coupled into the Michelson interferometer. Emission is subsequently passed through a sample chamber before being focused onto an infra-red photodetector.

The Michelson inteferometer works by splitting the input light with a beam splitter into two arms, with a mirror at the end of each. One of the mirrors is moved by a stepper motor, which leads to destructive and constructive interference with the fixed reference arm. The output intensity is therefore a function of the interference between both arms, and is measured by a photodetector.

In order to generate a spectra, the photocurrent of the diode is measured as a function of position of the movable mirror, producing an interferogram. This has been illustrated in Fig. 4.10. Taking a Fourier transform of the interferogram produces a spectra. The operating principal can be understood most clearly when considering a single wavelength propagating through the Michelson interferometer. As the mirror sweeps, the interference periodically moves from constructive to destructive as the mirror moves over a wavelength, resulting in an interferogram which is a pure sinusoid. The Fourier transform of this

returns the single frequency peak.

In this work, Bruker 66V and Vertex 70 systems are used. The systems at the University of Glasgow are optimised for different wavelengths. The 66V has the advantage that it can be operated under vacuum, to remove absorption peaks from atmosphere. Near-infrared (NIR) measurements are taken on the Vertex 70, which has calcium fluoride (CaF_2) windows and beamsplitters, while mid-infrared (MIR) measurements are taken on the 66V, which has potassium bromide (KBb) windows and beamsplitters, and a range of detectors that cover 2 - 20 μm.

Each system can be operated in a number of modes, which are described below.

4.2.4.1 Fast-scan

In fastscan mode the mirror moves continuously between the positional limits of the mirror. The signal is continuously averaged and can be monitored in real-time. Signal to noise (SNR) is improved as averaging is increased following a square root dependency, i.e SNR $\propto \sqrt{(N)}$, where N is the number of scans. Long measurements can be run to achieve high SNRs. Furthermore, Bruker OPUS software can automatically reject scans if the interferogram is significantly different to the previous measurement, meaning that vibrations or disruptions can be easily removed. A downside of this type of measurement is that any radiation entering the system will be included in the spectra, for instance ambient blackbody radiation from the room.

4.2.4.2 Step-scan

With step scan measurements the signal is modulated at a fixed frequency. This can be achieved by pulsing an electrical device, or by mechanically chopping the source for photoluminescence measurements. Optical choppers are used in this work.

The output of the photodiode pre-amplifier is connected to a lock-in amplifier (LIA), which also takes a reference signal from the mechanical chopper controller. The LIA makes use of the orthogonality of co(sine) functions to extract the components of the signal which have a carrier frequency and phase matching that of the reference signal. The DC signal is then returned to the FTIR system. Not only does this remove ambient radiation from the measurement, but allows for vastly improved SNR.

Unlike in fastscan measurements where the mirror is moved continuously, in step-scan the mirror is moved by a single step at a time, allowing for the lock-in to integrate over a fixed time period before returning the DC signal to the FTIR. Any averaging is done with a stable mirror position and is achieved by increasing the number of co-additions.

One of the draw backs of this method is that any noise due to vibrations of the mirror or inaccuracies of the mirror position will be added across the full spectra and cannot be further averaged out. Of course, multiple step can measurements can be taken and averaged manually.

Another disadvantage is the limited dynamic range of the measurement, which is a by product of the lock-in amplifier used. This means that optical filtering of high intensity peaks is required (i.e. with bandpass or notch filters) in order to avoid saturating the lock-in when investigating low intensity emission at a different spectral position. This can often be problematic, for instance when using an InSb detector with 5 μm cut-off to observe weak emission in the 2 - 3 μm range. With a 1 kHz optical chopper, there is still a heating response from the sample that can be extracted by the lock-in, meaning that blackbody radiation can be observed towards the detector cut-off. If the blackbody radiation is bright compared to the sample emission, then it will saturate the lock-in and cause spurious frequency components to appear in the spectra.

4.2.4.3 Photoluminescence/Absorption/Transmisison

For each type of scan (fast-scan or step-scan) the systems can be either setup to take an input beam from an external window, or to use an internal source. For photoluminescence measurements, a laser is used to excite emission from a sample, which is done outside the system. Parabolic mirrors are subsequently used to collect the emission and couple it through an optical window into the Michelson interferometer.

Alternative measurements can use internal NIR and MIR sources. Emission is coupled into the interferometer, and subsequently through a central chamber. A sample can be placed in the beam path so that a transmission spectra can be generated, which can be adapted to show the sample absorption. In order to obtain the transmission/absorption of the sample the spectral response of the detector and the spectral shape of the source have to be taken into account, which is achieved by dividing the transmission spectra by a reference spectra with an empty sample chamber. A similar practise can be carried out

when examining the transmission of a single layer of a multilayered sample. For instance, when measuring the transmission spectra of silicon nitride on a Si substrate, the total spectra is divided by a reference measurement of just the Si substrate.

4.2.5 Capacitance - voltage

4.2.5.1 Theory

The metal oxide semiconductor (MOS) capacitor is a fundamental building block of semiconductor devices, and is at the heart of planar transistors. As the name suggests, it comprises a metal contact layer, an insulating layer (which is traditionally a oxide but can be any other dielectric), and the semiconductor itself. Capacitance voltage (CV) measurements are a powerful technique, which can reveal many properties of both the semiconductor, and the interface between the dielectric and the semiconductor, such as trap interface density (D_{it}), oxide capacitance C_{ox}, semiconductor doping density, and the trapped charge in the dielectric layer [143].

The operating principal is based on the fact that the total capacitance varies as a function of the dc voltage. The measurement is carried out by slowly varying the bias while applying a small ac signal to probe the capacitance. The measurements in this work are carried out using a Agilent B1500A Semiconductor Device Analyzer and a probe station.

In the ideal MOS capacitor it is assumed that the oxide layer is infinitely resistive. Furthermore, it is assumed that there is no charge present in the oxide or at the semiconductor interface. The band structure for an ideal p-doped MOSCAP is shown in Fig. 4.11. Here χ_s is the electron affinity,ϕ_s and ϕ_m are the semiconductor and metal work functions respectively, ϕ_f is the difference between the Ferm-potential and the intrinsic Fermi-level. Under equilibrium conditions the Fermi-level is constant throughout the semiconductor. It can be seen that when $\phi_m = \phi_s$, the bands are flat, which is the so called 'flatband condition', which in an ideal MOS capacitor can be equivalently stated as:

$$\phi_{MS} = \phi_M - \phi_S = \phi_M - (\chi_s + \frac{E_C - E_i}{q} + \phi_F) = 0 \tag{4.7}$$

Deviation from the flatband condition leads to an accumulation or depletion of carriers from the interface. This results in the conduction and valence bands bending, which is

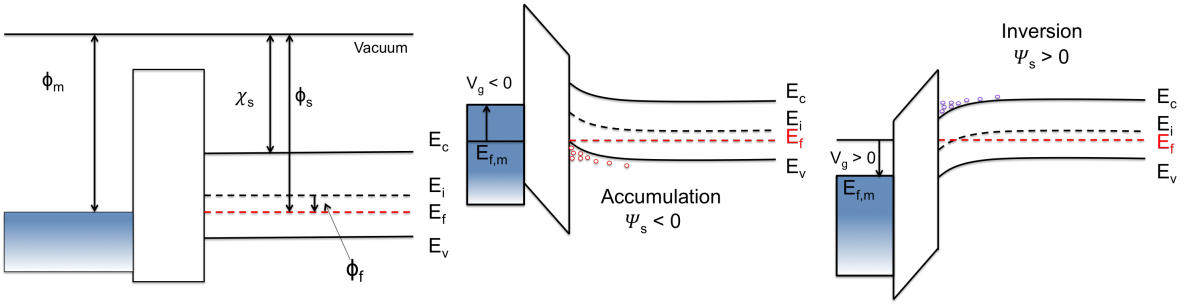

Figure 4.11: Left -Illustration of the flatband condition in an ideal MOS capacitor. Accumulation and inversion regimes are shown; middle and right respectively.

required due to the fact that the difference between the Fermi-level and the band edge is related to the carrier concentration, and that the Fermi-level must be flat in equilibrium. The position of the Fermi-level at the surface with respect to the bulk defines the surface potential, i.e. the potential that would have to be applied to flatten the bands.

$$\psi_s = \frac{E_{i,Surface} - E_{i,Bulk}}{q} \tag{4.8}$$

4.2.5.2 Non-ideal MOS capacitors

In real structures, there are various trapped charges which effect the CV curves. These include fixed charges in the oxide, which cause an additional shift to the flatband voltage. This can occur due to dielectric growth/deposition conditions, during which ions become incorporated in the film. Mobile charges in the dielectric further cause a shift to the flatband voltage, however there is a dependency on the direction of the dc bias sweep which leads to a hysteresis in the CV curves. This hysteresis gives a measure of the mobile charge density. Surface states at the interface between the semiconductor and the dielectric are hugely detrimental to device performance, as explained in Chapter 2 when looking at the non-radiative recombination mechanisms. It is therefore useful to have a measure of the density of interface traps (D_{it}). These surface states can be measured by a number of methods. In general mid-gap states cause a broadening out of the CV curve, which is due to the fact that the rate of change of depletion or accumulation with respect to the dc bias is reduced due to the additional trap centres which have to be depleted or filled. Furthermore, frequently a bump in the CV curve can be observed, which is indicative of mid gap states. This is demonstrated in Fig. 4.12.

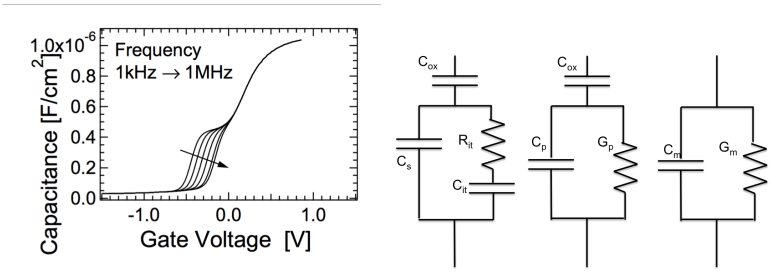

Figure 4.12: Left - CV curves showing the effect of mid-gap interface trap states as a function of ac frequency, image from. Right - Equivalent circuit model of a MOS capacitor including interface traps.

In the conductance method, the parallel conductance of the MOSCAP gives information regarding the trap density due to the fact that filling and emptying traps in response to the ac field is a lossy process. This allows the equivalent circuit to be expressed as shown in Fig. 4.12. It can be seen here that the traps also have a capacitance.

This allows the trap capacitance and conductance to be expressed as:

$$C_{it} = \frac{qD_{it}}{1 + \omega\tau_{it}^2} \tag{4.9}$$

$$\frac{G_{it}}{\omega} = \frac{qD_{it}\omega\tau_{it}}{1 + \omega\tau_{it}^2} \tag{4.10}$$

In these expressions, $\tau_{it} = R_{it}C_{it}$, and $C_{it} = q^2 D_{it}$. When plotting G/ω vs ω, there is a maxima when $\tau_{it} = 2\pi/\omega$, at which point the D_{it} can be approximated as:

$$D_{it} \approx \frac{2.5}{q}\left(\frac{G_p}{\omega}\right)_{max} \tag{4.11}$$

τ_{it} has a dependency on Vg, because generally only the traps near the Fermi-level are involved in the process. The trap capture lifetime is proportional to the difference in energy of the trap and the majority carrier band edge, i.e. $\tau \propto [exp(-q\Delta E/K_b T)]^{-1}$.

A downside of the conductance method is that it is based on the assumption of a single trap energy, when approximating D_{it}. Other methods such as the high-low method [143] can provide the trap concentration as a function of the bandgap. This method compares a CV measurement with no contribution from traps, i.e. a high frequency measurement at low temperature, to a low frequency measurement where the traps can respond. D_{it} can subsequently be calculated using:

$$D_{it} = \frac{C_{ox}}{q}\Big(\frac{C_{lf}/C_{ox}}{1 - C_{lf}/C_{ox}} - \frac{C_{hf}/C_{ox}}{1 - C_{hf}/C_{ox}}\Big) \tag{4.12}$$

4.3 Material growth

4.3.1 Heteroepitaxy

The material used in this work has been grown by collaborators at the L-Ness laboratory in Como, Politecnico di Milano, and at the University of Warwick. In this section, an overview of various growth techniques are given, and the challenges of growing Ge and GeSn epilayers are discussed.

The processing of growing a thin film of a different material to the host substrate is known as heteroepitaxy. Frequently the lattice constant of both materials is different, and this has certain ramifications for the growth of the material. The film can become strained, as it takes the substrate lattice constant, plastic relaxation can occur, meaning that dislocations are formed and strain is relaxed, and alternatively cracks can occur, or the surface can relax by forming undulations.

If the epitaxial layer is sufficiently thin, the difference in the lattice constants of two cubic materials will lead to a biaxial strain $\epsilon = \epsilon_{xx} = \epsilon_{yy}$. As described in Chapter 2, this will lead to a strain in the z-direction coupled through the elastic coefficients. The resulting lattice will therefore be tetragonal, and the materials band structure will be altered according to deformation potential theory. The elastic strain energy in the layer can be given as Eq. 4.13, where μ is the shear modulus, v is Poisson's number, ϵ is the in-plane strain, and t is the thickness.

$$E_{hom} = 2\mu\frac{1+v}{1-v}\epsilon^2 t \tag{4.13}$$

If the elastic energy stored in the film becomes too large, then it becomes energetically favourable for defects (dislocations) to form in the epitaxial layer, rather than continuing to grow as a strained layer. A dislocation is a disruption in the lattice or a missing lattice point, characterised by a Burger's vector, which relaxes the local strain, and therefore decreases the elastic energy in the film. The thickness above which it is energetically favourable to form dislocations is known as the critical thickness, and is dependant on the lattice mismatch between the two layers as well as the elastic properties of each layer, and

the Burger's vector. A misfit dislocation is shown graphically in Fig 4.13, which is where an atomic plane in the substrate ceases to continue into the film, and ends abruptly at the interface.

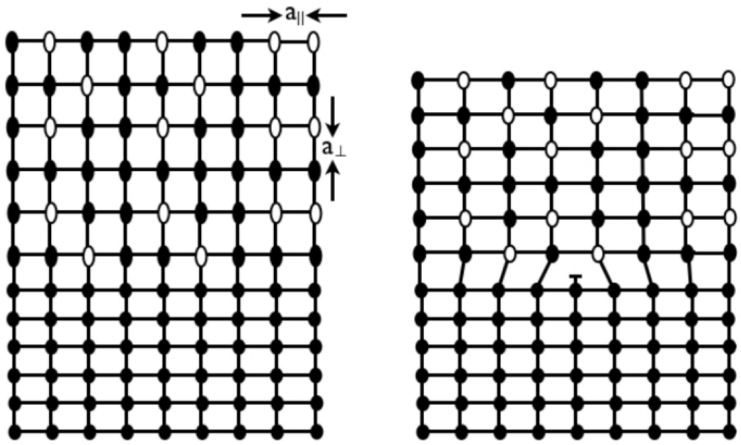

Figure 4.13: Illustration showing the inclusion of a misfit dislocation to relax strain in the epitaxial layer.

There are two possibilities for how this misfit will terminate. There is the possibility that the misfit will extend to the end of the sample edge, or either that a threading dislocation will propagate from the end of a misfit and extend into the epitaxial layer along a crystallographic plane. In Ge, threads lie in the {111} planes. If energy is applied in the form of high temperature anneals, for example, the thread can glide and propagate along the line of the misfit. The removal of threads by this technique is difficult due to the interaction of the threads with each other. As they lie in the {111} plane, the dislocations frequently interact and nucleate on each other, therefore impeding further movement of the thread. The formation of misfits and other material properties can be significantly different depending on the growth mechanism. In the following section a number of growth mechanisms are introduced.

4.3.2 Growth techniques

In this work, all materials were grown using chemical vapour deposition systems; this will therefore be the focus of this section.

Chemical vapour deposition use gaseous sources for the growth process. Precursors are first fed into the reactor, before the gas species are dissociated when heated (or by a plasma). The species are subsequently adsorbed onto the sample surface before chemically reacting to form a solid film. An exhaust system then removes the by-products of the reaction from the chamber. There are a number of variations of CVD; for example reduced pressure CVD, which uses reduced pressures in the sample chamber, in order to allow for lower growth temperatures. In order for growths of germanium and silicon/germanium layers, silane (SiH_4) and germane (GeH_4) gases are used. Doping can be achieved by introducing PH_3 and B_2H_6 for phosphorous (n-type) and and Boron (p-type) doping respectively. For growth of Ge on Si substrates there are significant challenges. The main issue to circumvent is the 4.2 % lattice mismatch between Ge and Si, which leads to a critical thickness of $\sim$ 1 nm. Further complex challenges exist for growth of GeSn layers, which will be discussed later in this chapter.

Generally, for Ge on Si, a two step growth process is carried out to provide high quality Ge epilayers with threading dislocation densities (TDDs) of $\sim 10^7\ cm^{-3}$. Using this method, a thin, highly dislocated, and nearly fully relaxed Ge layer is grown at low temperatures of around 400 °C. This leads to low growth rates of 0.3 nm/s. Such growth temperatures are known to generate monolayer islands, but is sufficiently high to remain crystalline and to proceed in a Frank-van der Merwe type growth mode [59]. Low temperature layers have high threading dislocations of $\sim 10^9$ to $10^{10}\ cm^{-3}$. The next high temperature step is carried out at 670 °C, giving a growth rate of 1.5 nm/s, and a layer of a high crystalline quality during which the layer is smoothed due to the Ge-Ge adatom transport mechanisms which minimise the surface energy.

Finally, high temperature anneals $\sim$ 830 °C are carried out to give energy to allow threads to glide, reducing TDD to $\sim 10^7\ cm^{-3}$ at the top plane. A result of the high temperature anneals, however, is the accumulation of a tensile strain in the Ge layer, which is it odds with the compressive strain which would be expected given the difference in lattice constants. This is due to the difference in thermal expansion coefficients of Si and Ge, which leads to moderate biaxial tensile strain between 0.15 and 0.25 %.

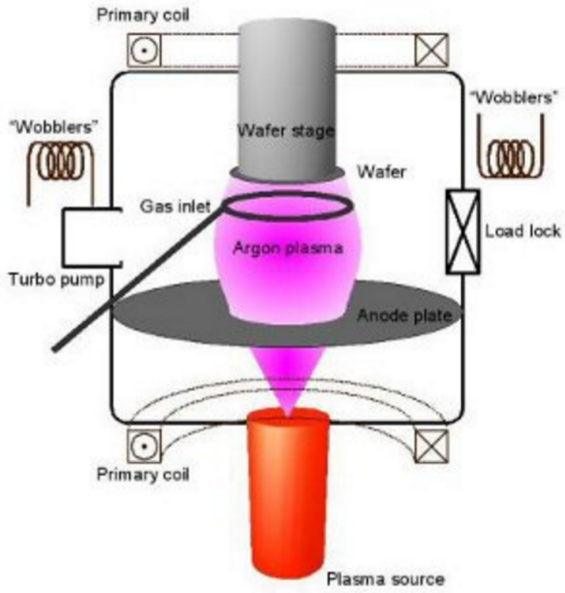

Figure 4.14: Schematic of a low energy plasma-enhanced chemical vapour deposition system, from [13].

4.3.3 Low energy plasma enhanced chemical vapour deposition

The majority of the material used in this work is grown by Low energy plasma enhanced chemical vapour deposition (LEPECVD). This is carried out by collaborators in the L-NESS facility in Como, Politecnico di Milano. The grower for each specific material will be acknowledged within the relevant results section. This technique allows independent control of the growth rate and the wafer surface temperature. The growth rate is dictated by the plasma density, allowing for relatively high growth rates compared to other techniques, while further allowing for low growth temperatures to optimise doping profiles. The LEPECVD reactor is shown in Fig 4.14, from reference [13]. An argon plasma is created between the anode plate and the sample stage; the plasma is low energy to minimise damage to the wafer surface. The appropriate gas for either Si or Ge growth is introduced (SiH_4 or GeH_4 respectively) and the energy in the plasma breaks the gaseous molecules. The plasma is directed towards the sample stage where the precursors readily react with the wafer surface. Regulation of the plasma density and gas flow rates can allow for control of the growth rate between ~ 0.01 nm/s to 10 nm/s. This allows for thick multi-layered structures to be grown quickly compared to conventional CVD techniques.

One downside, however, of LEPECVD is the non-uniformity across 100 mm wafers. The non-uniformity of the plasma coil can cause a variation across the wafer which can range from 0.7 to 1.4 times that of the nominal growth design.

4.3.3.1 Virtual substrates

An alternative method to reduce the threading dislocation density is the use of graded buffers to create virtual substrates. A SiGe alloy can be use to grade from silicon rich, to germanium rich alloys. It has been found that grading rates of approx 12 % per micron achieve low dislocation densities in the buffers. This technique is well suited to LEPECVD growth as the fast growth rates make the 12 μm graded buffers practical. Highly doped n-Ge can therefore be grown on buffers graded up to 100 % Ge. Virtual substrates are also of use for multilayered structures. For example, there is often need for the use of the structures with alternating layers of Ge and SiGe alloys. As explained previously, layers with mismatched lattice constants can be heavily dislocated when grown above the critical thickness. In multilayered structures, as long as each layer is below the critical thickness, the structure can be viewed as having an average Ge content which can be lattice matched to a virtual substrate with the same Ge concentration at the top of the buffer. This is known as strain balancing and allows for thick multi-layered structures to be grown with minimal defects and minimised stress.

4.3.3.2 Ge on insulator

A final alternative is the use of Ge on insulator (GeOI) layers. Ge layers with extremely low defects can be grown on GaAs, which is close to being lattice matched to Ge. The top layer of the Ge epilayer is then bonded to a Si wafer, and the GaAs substrate is removed. In this work, GeOI wafers were provided by IQE, with a thin nominally p-type Ge layer of 50 nm. Re-growth of thick n-type Ge was carried out on these wafers by LEPECVD (L-Ness laboratory, Politecnico di Milano). The ultimate objective of Ge photonics is on chip CMOS integration, therefore such wafers are more interesting for studying the effect of reduced TDDs.

4.3.4 RP-CVD

In this work, the GeSn material was supplied by collaborators Warwick University. This group uses an ASM Epsilon 2000, which is a commercial reduced-pressure CVD, with excellent wafer uniformity and repeatability on 100 mm Si wafers.

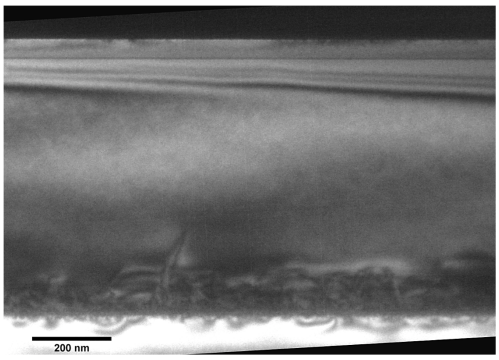

Figure 4.15: Transmission electron microscope (TEM) image of a GeSn epilayer on a Ge virtual substrate, on a Si substrate.

The two step Ge growth process described above was developed by Colace et al [59], and in this work, it was implemented to grow high quality Ge virtual substrates for GeSn epilayers, circumventing the need for expensive Ge substrates. Incorporation of Sn into Ge layers has been investigated for a number of years, in particular following the predictions that GeSn alloys could provide a group IV direct bandgap material. α-Sn and Ge have vastly different lattice constants, differing by approximately 14 %. This results in $Ge_{1-x}Sn_x$ alloys having a large mismatch with a Ge virtual substrate. This leads to high compressive strain for GeSn layers below the critical thickness. Above the critical thickness, it has been observed that GeSn on Ge layers exhibit Lomar dislocations, which propagate in the plane of the interface, and result in a low TDD ($< 10^6$ cm^{-3}) in the alloy.

In order to grow high quality GeSn alloys, growth temperatures have to be kept below 350 °C, due to the tendency of Sn to segregate, the precipitation of α-Sn to β-Sn that occurs at high temperatures. In this work, Digermane (Ge_2H_6) and tin tetracholride ($SnCl_4$) precursors are used. The challenges associated with GeSn growth is detailed in depth the Literature Review chapter. A transmission electron microscope (TEM) image

is shown in Fig. 4.15 (David Pratchett - University of Warwick), of a GeSn epilayer on a Ge virtual substrate, on a Si substrate. The defective interface between the Ge can be observed, which is predominantly confined to the first 100 nm. The GeSn layer is fully pseudomorphic on Ge, and has minimal dislocations.

5

Tensile strained Ge nanopillars

Work from this chapter was published in Optics Express [144], and presented at Group IV photonics 2014 [145], and at the International Conference on Silicon Epitaxy and heterostructures (ICSI) 2015; the proceedings of which were published in a special edition of Thin Solid Films [146].

5.1 Introduction

In order to investigate strain in Ge with silicon nitride stressors, nanostructures were fabricated, as these were expected to give higher levels of strain than previous demonstrations of waveguides with widths > 1 μm [94, 147]. This would allow a means of characterising the strained photoluminescence (PL), and thereby establishing if the Ge band-edge can be moved to the point to which it is close to a direct band-gap material. Aside from improving the light emitting efficiencies, strain can be used to tune the operating wavelength of other devices, such as strained LEDs, photodiodes, modulators and lasers, and therefore the strain distribution in structures has to be understood, with particular emphasis on the effect on the band-structure. In this chapter, the high stress silicon nitride stressor technology is discussed, and the films are characterised. The process development to enable high stressed nano features is shown, and highly strained photoluminescence from nano pillar structures is demonstrated. The structures are further characterised by Raman spectroscopy, and the strain distributions are modelled with finite element modelling.

5.2 Growth

Material growth was carried out by collaborators at the L-Ness laboratory, Como, Politecnico di Milano. A low-energy plasma-enhanced chemical vapour deposition (LEPECVD) tool was used to grow 500 nm of Ge on a 100 mm p-Si (100) wafer, as described in [148], Fig. 5.1. The Ge was in-situ phosphorus doped with $N_d \sim 2.5$ x 10^{19} cm^{-3} as confirmed by Hall-bar measurements at 300 K (Jacopo Frigerio). In order to avoid out-diffusion of the phosphorus dopants [52], the wafer did not receive any cyclic annealing, which is usually carried out in order to reduce the density of threading dislocations [149]. Due to the lack of high temperature anneals, and the low growth temperature of 500 °C, there is negligible strain in the Ge epilayer, which normally accumulates at high temperatures due to the difference in thermal expansion coefficients between Si and Ge.

It was confirmed that the strain in the Ge epilayer was negligible by X-ray diffraction (XRD) measurements. Photoluminescence measurements on blank samples demonstrated a direct band emission at 1.6 μm. This shift from $\sim$1.55 μm (where the direct band is expected) is due to bandgap narrowing (BGN) from degenerate phosphorus doping. This red shift equates to approximately 32 meV of BGN, and is consistent with the experimental work of [150], when taking into account that their model includes a small amount of strain from growth. As result of the low temperature growth the material contained a large number of threading dislocations, on the order of 10^9 cm^{-2} [52]. It should be noted that TDD of 10^7 cm^{-2} can be achieved with the two step Ge growth technique, which was not possible with such high doping densities, as explained previously. The presence of a high TDD will somewhat counteract the PL intensity increase from high n-type doping as the non-radiative lifetime is decreased, however, the high doping level will ensure that the direct transition is bright relative to the indirect, which was thought to be advantageous for these experiments so that the peaks to could be initially distinguished. A further potential ramification, however, of the high TDD is that it can lead to strain non-uniformities in the plane, due to the plastic deformation that can occur in the vicinity of clusters of threads. In this case, brighter emission is still likely to stem from the strained regions, as the electron concentrations should be increased where the bandgap is reduced.

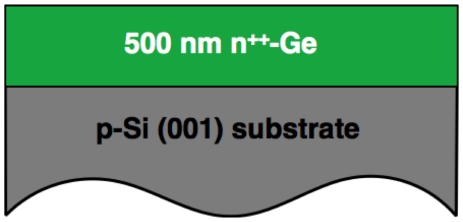

Figure 5.1: Illustration showing the 500 nm Ge n++ layer grown on a (100) p-type Si wafer.

5.3 Characterisation of high stress silicon nitride layers

5.3.1 Deposition parameters

The presence of the stress in silicon nitride films is something which is frequently undesired in processing steps and as a result, something which process engineers try to negate in order to produce thick films without cracking or delamination [151]. However, in this work a high stress film is required in order to transfer the maximum strain into Ge features. In particular, a highly compressive film is desired. When coating a patterned feature, the film is able to relax, and in doing so transfers tensile strain into the underlying feature.

The stress state in CVD deposited SiN films is dependant on the nitrogen content [141], and in particular for compressive stress, the incorporation of N-H bonds [152]. The exact nature of the intrinsic stress is not fully understood, but is thought to be due to the difference in bond lengths between Si-N, and N-H, which leads to compression in the film during CVD deposition. In this work, the silicon nitride is deposited at room temperature, meaning that any differences in the thermal expansion has a negligible effect on the extrinsic stresses, therefore it is the intrinsic stresses such as the N-H content that fully defines the stress state.

An Oxford Instruments System 100 inductively coupled plasma (ICP) plasma enhanced chemical vapour deposition (PECVD) tool was used to deposit silicon nitride layers. The process gasses are nitrogen (N_2), and Silane (SiH_4), which are inlet at two different positions in the chamber (discussed in Chapter 4). N_2 is flowed through an inductive coil, which is driven by a 13.56 MHz source. This forms N radicals that are accelerated towards the sample plate by a DC bias. There is control in the deposition

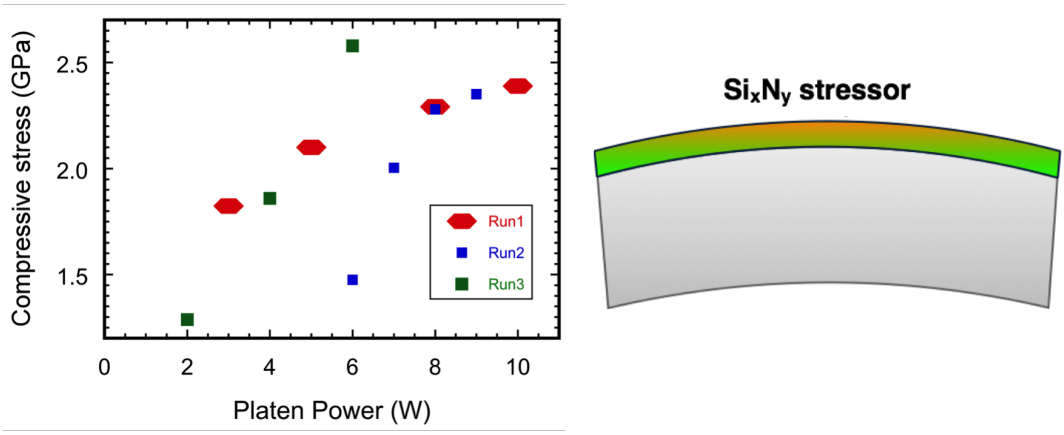

Figure 5.2: Left - Measured compressive stress as a function of the platen power of the inductively coupled plasma deposition tool. Right - Illustration showing the compressive stress in a silicon nitride layer bending a Si substrate.

parameters, in the form of gas flow rates, chamber pressure, temperature, RF powers, and in the case of ICP depositions, DC platen powers. It was found that increasing the platen power had a pronounced effect on the compressive stress, suggesting that the increased ion bombardment facilitates the formation of N-H bonds in the film. This can be further tuned by changing the precursor flow rates, and by altering the coil power. The high stress recipe used in this work is given in Chapter 4. The increasing stress with platen power can be observed in Fig. 5.2, with stresses measured by the curvature method described in Chapter 4.

Initially, the platen powers from 2 - 10 W were examined over the course of 3 separate runs, and it was found that while there was always an a trend of increasing stress with increasing platen power, the absolute stress values varied for a given deposition. As a result, for all experimental work, a 4 inch Si wafer is run, and the stress measured by the curvature technique, before samples containing Ge nano-features are subsequently processed. It was verified that without changing the recipe, and therefore keeping the chamber conditions steady, the stress remained consistent for repeated depositions, i.e. around the expected error from the curvature measurement ($\sim \pm$ 50 MPa). This highlights that the stress can be considered constant for thick depositions.

5.3.2 Absorption

The correlation between the stress with N-H bonds was confirmed using ellipsometry, and transmission measurements on a Bruker 66 V FTIR system. Following the deposition of the wafers, the film was partially stripped by wet-etching. The transmission of a broadband mid-infrared (MIR) source through the wafer was measured by a deuterated triglycine sulfate (DTGS) detector. Two measurements were taken, one through the bare region of the Si wafer, and another through the film and the wafer. The second spectra was divided by the first to remove the contribution of the Si, which in any case should be minimal due to high transparency in the MIR.

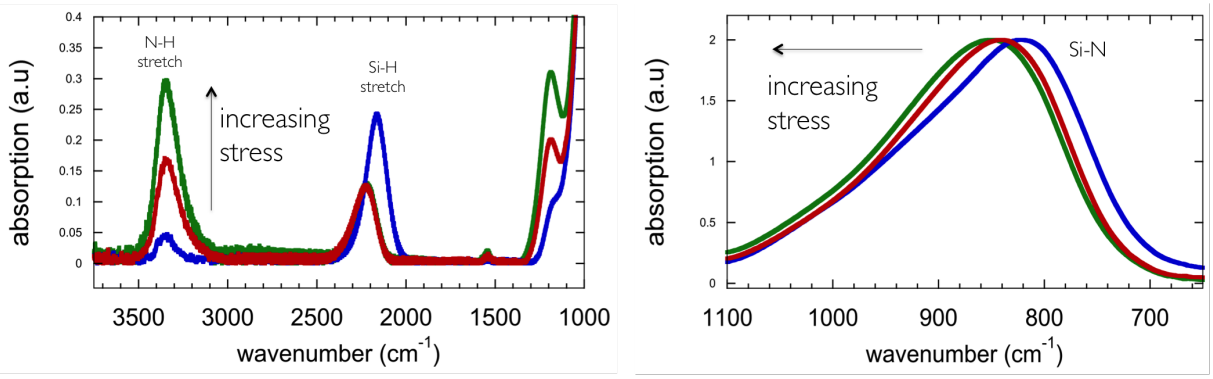

Figure 5.3: Mid infrared transmission of high stress silicon nitride layers with varying stress. Left - shows the N-H and Si-H stretching modes. Right - shows the Si-N vibration.

Clear peaks can be observed relating to the vibrational bonds of the silicon nitride film. As shown in Fig. 5.3, there are N-H and Si-H stretching modes and a Si-N stretching vibration (Fig. 5.3 right). With increasing stress there is a clear increase in absorption from N-H bonds, showing a correlation between stress and N-H content. The ratios of N-H to Si-H bonds can be estimated by integrating the absorption spectra of each bond, taking into account a weighting factor for their absorption cross sections, which has been found to be ~ 1.4 [153]. This suggests therefore, that for the films in Fig. 5.3, there are N-H/Si-H ratios of 0.29, 1.84, and 3.16 for the unstrained (< 50 MPa), 1.9 and 2.3 GPa films respectively. Another noticeable effect is that the Si-H stretching mode vibration shifts slightly to higher energies for the higher stressed films. This has been explained by Blech et al., who proposes that the increased N bonding to Si in Si-H groups causes this shift. The increased electronegativity of the N atoms causes a decrease in the Si-H bond

length, which impacts the frequency of the vibration [154]. Finally, the Si-N bond also shifts to higher frequencies, which is indicative of nitrogen rich films [155].

These absorption peaks can have a detrimental effect on optical devices depending on the wavelength of operation. At telecoms wavelengths (1550 nm), silicon nitride waveguides have shown high losses due to an overtone of the N-H bond at $\sim$ 3 μm wavelength [156]. However, such losses could not be observed by FTIR transmission or by ellipsometery in the NIR with films produced in this work. While the band-edge in strained Ge devices will be moved away from the N-H overtone, this absorption could be problematic in devices such as strained Ge photodiodes, where strain has been applied to give increased absorption at 1550 nm. Highly strained emission of Ge or GeSn emitting near 3 μm wavelength would also experience losses, and therefore careful tuning of the relevant device has to be taken into account to accommodate the intrinsic losses in the film. This is further discussed in Chapter 7.

5.3.3 Ellipsometry

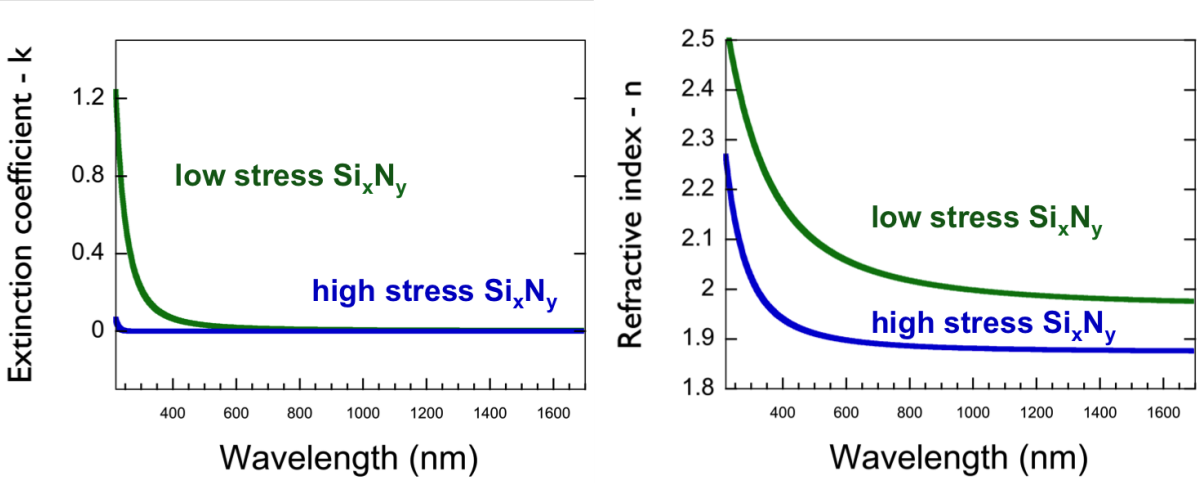

Figure 5.4: Ellipsometry measurements of low and high stress silicon nitride layers. The high stress layers have compressive stresses of $>$ 2 GPa. Left - the extinction coefficient, k. Right - the refractive index, n.

The increased nitrogen trend can also be seen by measuring the optical constants of the film by ellipsometry, Fig. 5.4. Measurements were taken on a J.A. Woollam M-2000

ellipsometer from 193 to 1690 nm, and fitted using a Cauchy model. The index shifts to lower values with increased nitrogen content, and the extinction coefficient at UV wavelengths decreases significantly, which is due to the widening bandgap of the film with increasing nitrogen [155].

5.3.4 Capacitance voltage measurements

Metal oxide semiconductor (MOS) capacitors were fabricated in order to evaluate the electrical properties of the high stress silicon nitride. Pirhanna and RCA cleans were carried out on moderately doped n-type Si wafers with a doping of 1×10^{17} cm^{-3}. The wafers were subsequently deposited with 35 nm of high stress silicon nitride using an Oxford instruments Plasma Pro System 100. Palladium top contacts were deposited by electron beam evaporation, using a shadow mask to define the contacts. A back Palladium contact was deposited on the sample.

The capacitors were measured using a Agilent B1500 parameter analyser. AC frequencies from 1 kHz to 1 MHz examined in order to observe frequency dispersion, which can be a hallmark of midgap states. The capacitance voltage (CV) measurements showed a huge flatband shift of > 5 V. This is indicative of a large amount of fixed positive charge in the film.

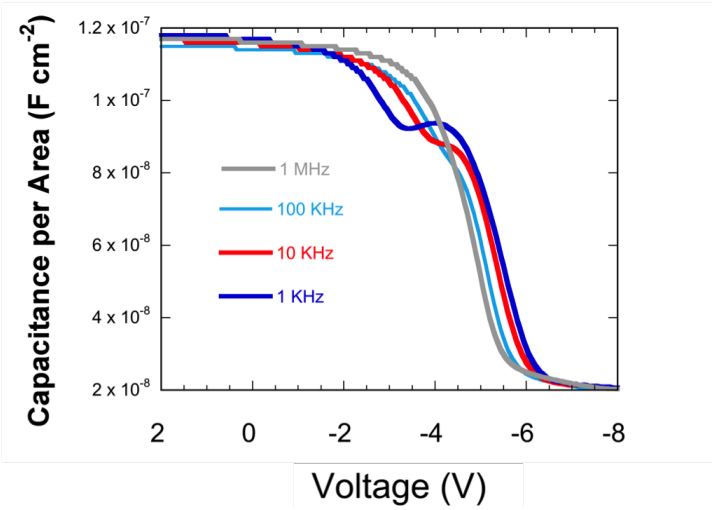

Figure 5.5: Capacitance-voltage measurements of metal oxide semiconductor capacitors, with high stress silicon nitride dielectric layers.

As shown in Fig. 5.5 there is a significant shoulder at low frequencies moving from accumulation to depletion. This is indicative of the presence of mid-gap states in the material, which smear out the CV as the Fermi-level has to move through the trap-states. Such mid-gap states which would in turn increase Shockley Read Hall recombinations. This is an extremely undesirable property as the increase in non-radiative recombination reduces the quantum efficiency of the optical transitions. The conductance method was used, as described in Chapter 4, to give an estimation of the density of interface traps at the silicon nitride/silicon interface. This was found to be extremely high, with a calculated mid-gap Dit of $\sim 10^{15}$ eV^{-1} cm^{-3}.

5.4 Ge material characterisation

In this work, photoluminescence (PL) is used to measure the interband transitions of Ge. To do so, a sample is illuminated by a laser with $\hbar\omega > \mathrm{E}_g$. The pump is absorbed, promoting electrons from the valence band into the conduction band, and thereby generating electron hole pairs. As discussed in Chapter 2, optical transitions have to conserve crystalline momentum, and therefore are vertical in k-space unless indirect, in which case a phonon is required to conserve $\hbar k$. The corresponding absorption of indirect transitions is typically much weaker, with larger penetration depths. The injected carriers reach a thermal equilibrium within their respective bands, and are quickly scattered to the band-edge by optical phonons. Under steady state conditions the carrier distributions can be described by quasi-Fermi levels, which were introduced in Chapter 2. Following injection, carriers can either recombine radiatively, or non-radiatively, with the ratio of the radiative lifetime to the total lifetime defining the internal quantum efficiency:

$$\eta_i = \frac{\tau_{nr}}{\tau_{nr} + \tau_r} \tag{5.1}$$

The radiative transitions allow the band-structure to be probed, as the measured wavelength is related to the energy of the bandgap, with emission intensities following theory of spontaneous emission given in Chapter 2.

Photoluminescence measurements of the n-type Ge epilayers in this chapter are taken on a Bruker Vertex 70 Fourier transform infrared (FTIR) spectroscopy system with an extended InGaAs detector with a cut-off at ~ 2.5 μm. For step scan measurements, the

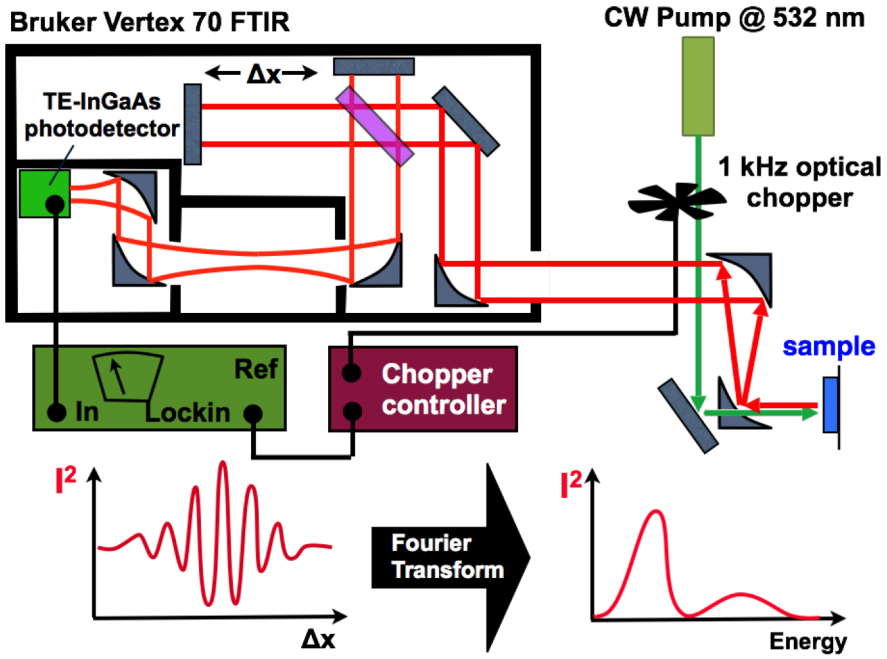

Figure 5.6: Illustration showing the setup for optical characterisation. The pump illuminates the sample through an aperture in a parabolic mirror.

pre-amplifier of the detector is output to a lock-in amplifier, which also takes a reference signal from a 1 kHz optical chopper, which modulates the pump. As explained in Chapter 4, the lock-in extracts the frequency components of the detector signal, which match that of the optical chopper. This has the effect of discriminating against other potential noise signals, such as ambient black-body radiation from the room. Here, a diode-pumped, continuous wave solid-state laser emitting at 532 nm is used as the excitation source. In terms of energy, this corresponds to an excitation high above the Ge band-edge (2.33 eV), so even at low excitation power densities, as the carriers phonon-scatter to the band-edge there is slight sample heating and a small tail towards longer wavelengths is sometimes visible in the photoluminescence. This is the additional blackbody radiation after the removal of the ambient blackbody by the step-scan measurement. The optical setup is shown in Fig. 5.6, which also shows the chopped pump illuminating the sample through an aperture in a parabolic mirror, which collects the sample emission, and couples the signal to the internal interferometer of the FTIR system through a CaF_2 optical window.

5.4.1 Low Temperature Photoluminescence

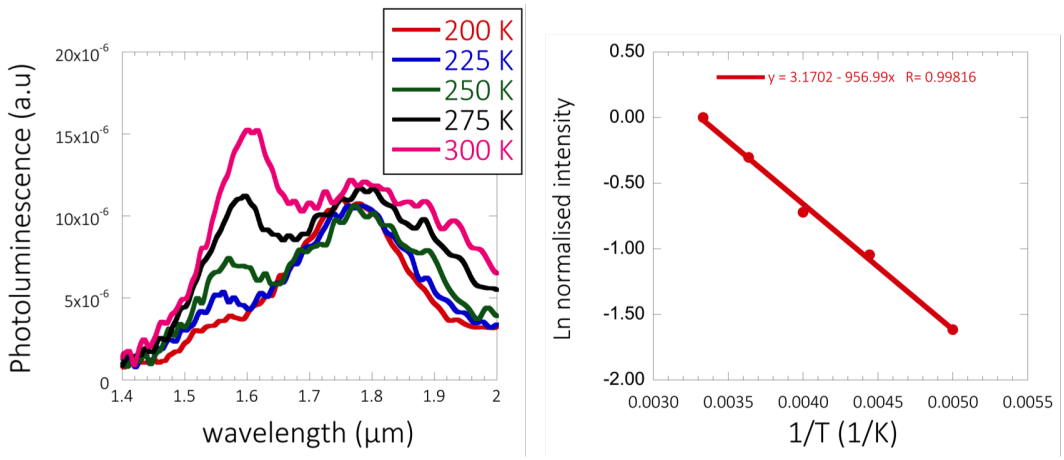

Figure 5.7: Left - Low temperature photoluminescence of n-Ge material with doping of 2.5×10^{19} cm^{-3} (arbitrary units). Right - Arrhenius plot of direct bandgap emission; the intensity has been normalised to the 300 K photoluminescence.

To observe the temperature characteristics of the PL, measurements were taken using an Oxford optical cryostat. The sample is in held under helium (He) in a top loaded chamber, which is in thermal contact with a cold head that is cooled by a closed cycle He compressor. It has been shown that using a pump with energy > 2 eV results in strong absorption (vertical in k-space) from a deep valence band state into the L valley [127]. This is contrary to what could be expected with optical excitation, as it would be usual for to have strongest absorption at the Γ point. The optical excitation of carriers into the indirect band leads to a strong temperature dependance on the carrier concentration at the Γ band, as thermal energy allows electrons in the L to overcome this energy difference. Therefore, a unique feature of a semi-conductor with a quasi-direct bandgap is that increasing the temperature leads to increased direct band recombination, and a brighter PL signal from this transition. Conversely, lowering in temperature reduces the intensity of the direct band. This is opposite in behaviour to direct bandgap materials where increasing the temperature serves to increase non-radiative recombination mechanisms such as Shockley Read Hall (SRH) and Auger recombination.

An un-patterned n-Ge sample was used to demonstrate the dependance of direct band-emission on PL brightness from the direct band, Fig. 5.7. This follows an Arrhenius law,

i.e. an exponential dependance, with the activation energy approximately corresponding to the difference to the Fermi- level (which resides in the L valley in this degenerately doped material) and the Γ valley. Photoluminescence measurements were taken from 300 to 200 K, at which point the direct transition could no longer be observed. The normalised intensity of the direct band was then plotted as a function of inverse temperature, and a linear fit was applied, Fig. 5.7 (right). The slope of this fit gives the activation energy, which in this case was found to be $\sim$ 82.4 meV. This would imply that the Fermi-level lies $\sim$ 58 meV into the L valley, as the 82 meV accounts for the rest of the 140 meV difference between the Γ and L valleys. Using Fermi-Dirac statistics, the calculated Fermi level for n-type doping of 2.5×10^{19} is 43 meV into the L, which is therefore in reasonable agreement, as shown in Fig. 5.8. The discrepancy can be attributed to the fact that this is a 1st order approximation which does not account for other non-radiative processes.

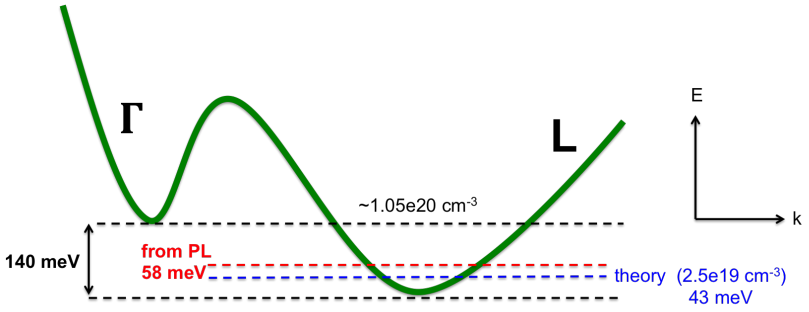

Figure 5.8: Illustration showing the theoretical Fermi level position based on the measured doping concentration, compared to the Fermi level position approximated from photoluminescence measurements.

5.5 Fabrication

The simplified fabrication steps for Ge nanopillars is shown in Fig. 5.9. For optical characterisation, arrays of the features were patterned in HSQ resist using a Vistec VB6 electron beam lithography tool. Separate mm sized arrays were patterned, each containing repetitions of the same feature. This was to allow for PL measurements using a pump with a beam diameter (FWHM) of $\sim$ 300 μm.

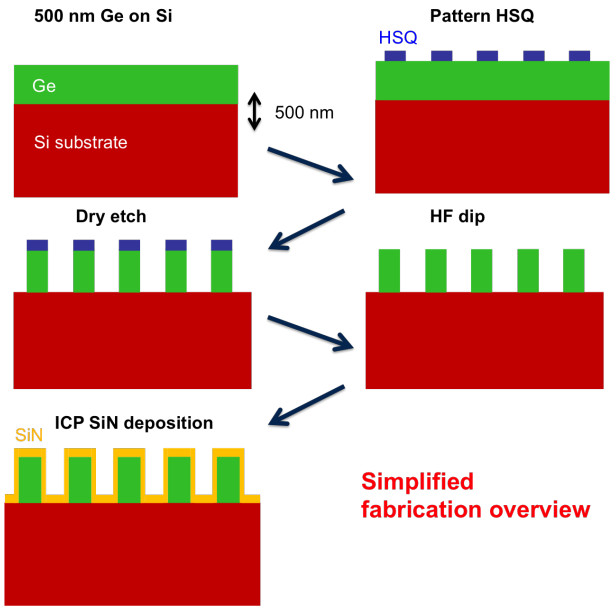

Figure 5.9: Illustration showing the fabrication steps for fabricating Ge pillars or waveguides.

Samples were developed in 25 wt % tetramethylammonium hydroxide (TMAH), at 23 °C, following a high contrast process [157]. Dilute TMAH developers, shown to give higher resolution, were found not to sufficiently clear out the resist between features. The samples were subsequently etched in a mixed SF_6 and C_4F_8 recipe [158] through the Ge epilayer and into the Si, leaving 560 nm tall pillar structures, as measured by SEM. An O_2 plasma ash was carried out to remove residual C_4F_8, and the remaining HSQ mask was subsequently stripped in a buffered HF solution to leave etched Ge features.

5.5.1 Heating

Particularly with such pillar structures, heating has to be considered when measuring the Ge band-edge. Not only is there increased black-body emission, but at sufficiently high temperatures, the band-gap reduces, following Varishni's equation, Eq. 5.2 [159], where $Eg\Gamma_{Ge}(T)$ is the bandgap as a function of temperature, T, $Eg\Gamma_{Ge}(0)$ is the bandgap at zero Kelvin, and α and β are fitting parameters.

$$Eg\Gamma_{Ge}(T) = Eg\Gamma_{Ge}(0) - \frac{\alpha T^2}{T + \beta} \tag{5.2}$$

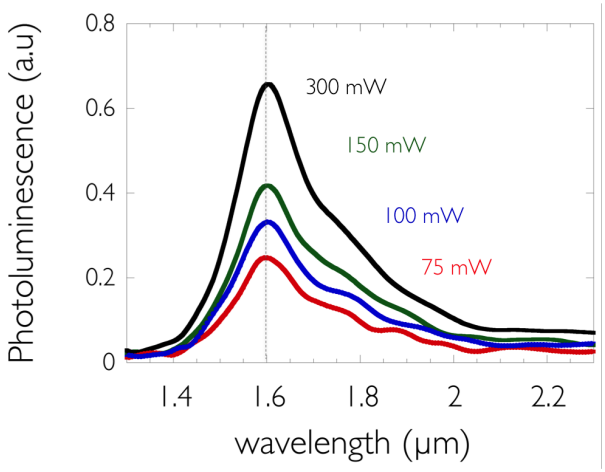

Figure 5.10: Photoluminescence of bare 300 x 300 nm square top Ge nanopillars as a function of pump power.

This has the effect of red-shifting the emission, and could therefore be misconstrued as the presence of tensile strain. In order to eliminate this concern, the pump power was varied to ensure that the peak wavelength position did not vary with the pump power. Neutral density filters were used to vary the pump power from 300 mW to 75 mW. As shown in Fig. 5.10, the Ge pillars showed a stationary peak at around 1.6 μm, thus confirming an absence of significant heating. Despite high pump powers of 300 mW, the large spot size means a pillar at the centre of the spot would only absorb $\sim$ 1 μW of power, as calculated from Eq. 5.3.

$$P(r) = P(\infty)\left[1 - exp\left(\frac{-2r^2}{w_o^2}\right)\right] \tag{5.3}$$

where $P(r)$ is the power in a radius r, $P(\infty)$ is the total power inclosed in the spot, and w_o is the $1/e$ diameter of the Gaussian spot.

5.5.2 Strained Pillars

Initially, three samples were prepared as described in the fabrication section. Each sample contained square top pillars with 300 nm side lengths, etched down to the Si substrate, each with a different thickness of silicon nitride deposited. The first sample received 85 nm, while the second and third had 170 and 255 nm deposited respectively, as measured by ellipsometry. The stress in the film was measured to be $\sim$ 2.40 $\pm$ 0.05 GPa . After

PL characterisation the samples were deposited with a further deposition of 255 nm to provide a range of six silicon nitride thicknesses. Photoluminescence measurements

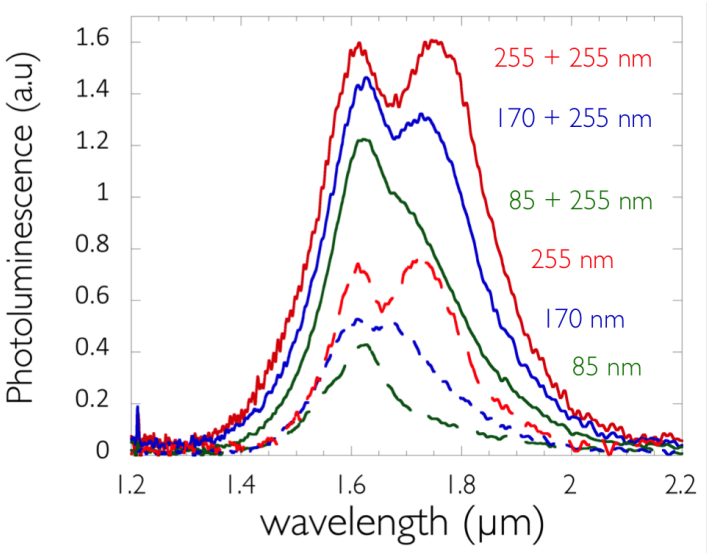

Figure 5.11: Photoluminescence of 300 x 300 nm square top Ge nanopillars strained with high stress silicon nitride layers of varying thickness.

showed an emerging peak from the transition at 1.6 μm. Initially this was thought to be have been due to the additional strain, with the stationary peak from an unstrained region of the pillar. In all cases the emerging peak red-shifted with increasing thickness, Fig. 5.11. The peak position at 1.75 μm would suggest strain levels of up to 0.5 % biaxial tensile strain, if assumed to be Γ to LH transition.

Further samples were fabricated to observe the strain progression in various other geometries. Arrays of 300 nm pillars were included in such samples in order to correlate the results, however the red-shifts could not be replicated. SEM images showed that the silicon nitride was present on the pillars, but PL measurements showed either no shift or negligible red-shifts to the emission. Cross sectional SEM images were investigated but the interface could not clearly be observed, with nitride layers often detaching following the sample cleave.

5.5.3 TEM analysis

The samples were sent to an external department (Dr Ian MacLaren - Physics, University of Glasgow) in order for transmission electron microscope measurements to be taken.

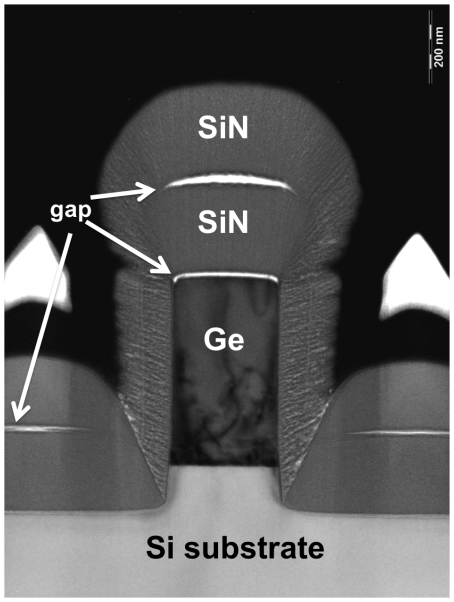

Figure 5.12: Cross sectional dark-field transmission electron microscope image. The image shows poor adhesion at the pillar top surface and between the silicon nitride stressor layers, from the separate depositions.

The pillars were prepared for high resolution imaging using Scanning Transmission Electron Microscope (STEM). A sample of controlled thickness was prepared by using a focused ion beam (FIB) lift-out procedure. The FIB system used was a FEI Nova 200 dual beam instrument. After locating a pillar, it was coated with a thin platinum (Pt) layer using e-beam evaporation, followed by a layer of FIB-deposited platinum to prevent milling, or multiple image scans, from damaging the surface of the TEM cross-section. Subsequently a 15 μm wide and 1 μm thick region of interest was then undercut as a TEM lamella. This was lifted out and attached to an Omniprobe support grid, prior to final FIB milling and polishing. The TEM lamella is ion polished on both sides to a nominal thickness of approximately 300 nm using a reduced beam current. At these thicknesses, the sample is electron transparent.

The STEM investigations were performed on a probe-corrected JEOL ARM 200F equipped with a cold field emission gun (CFEG) and operated at 200 kV. High angle

dark field imaging was performed using a fine probe of 0.1 nm. Upon examination of the resultant images, Fig. 5.12, it was apparent that there was adhesion problems at the pillar top, and between SiN layers. In the dark-field image, the white regions indicate an absence of material, i.e. a gap. This could lead to a complex stress state in the pillar, with marked differences between the stress on the sidewalls and the top plane.

This adhesion was consistent with the adhesion problems observed with high stress silicon nitride on blank n-Ge chips. Following the deposition, cracking of the film occurred within minutes of the deposition. It was initially assumed that the inability of the film to transfer strain on un-patterned regions meant it was energetically favourable for the films to crack, which may not have been the case over nano-sized patterns, where the film appeared to be in-tact.

5.5.4 Adhesion promotion

Various surface preparations were attempted to improve adhesion. One sample used identical processing to the previous samples (showing poor adhesion) as a reference. A further two samples had thin dielectric layers grown prior to the high stress deposition.

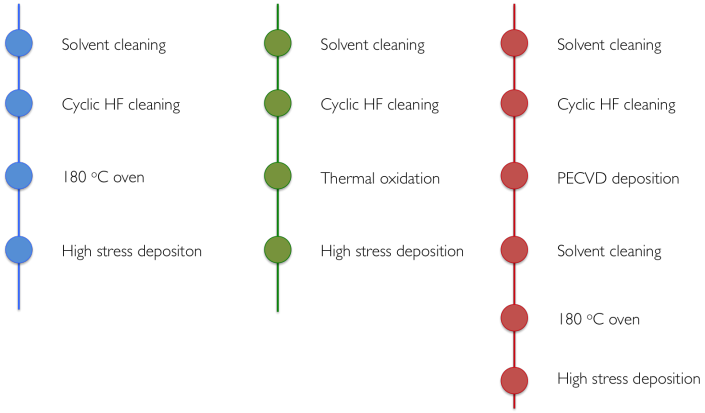

Figure 5.13: Process flows for investigating adhesion of high stress silicon nitride layers.

Thermal oxides were deemed interesting as there is significant work going towards the efficient passivation of Ge. It would therefore be beneficial if such a layer could further promote adhesion to a high stress layer, particularly as recent results have shown that the PL intensity can significantly increase with GeO_2 passivation [160], with similar results

obtained using processes developed within the research group (Kevin Gallacher, Ross Millar) [15].

The second sample therefore had $\sim$ 20 nm of GeO_2 thermally grown in a furnace tube at 550 °C. GeO_2 is water soluble, and therefore the samples were immediately placed in a desiccator for transfer to the ICP tool. The third sample had 20 nm of low stress PECVD silicon nitride deposited at 300 °C. The process for each of the three samples is shown in Fig. 5.13.

For each preparation type, a 1 cm x 1 cm blank sample and a patterned sample were processed, so as to observe the difference in film cracking on un-patterned substrates. Initially it was clear that there was poor adhesion to the GeO_2 coated sample, with immediate cracking observed of the high stress layer. The PECVD coated sample appeared in-tact, and the reference sample showed small amounts of cracking, under optical microscope.

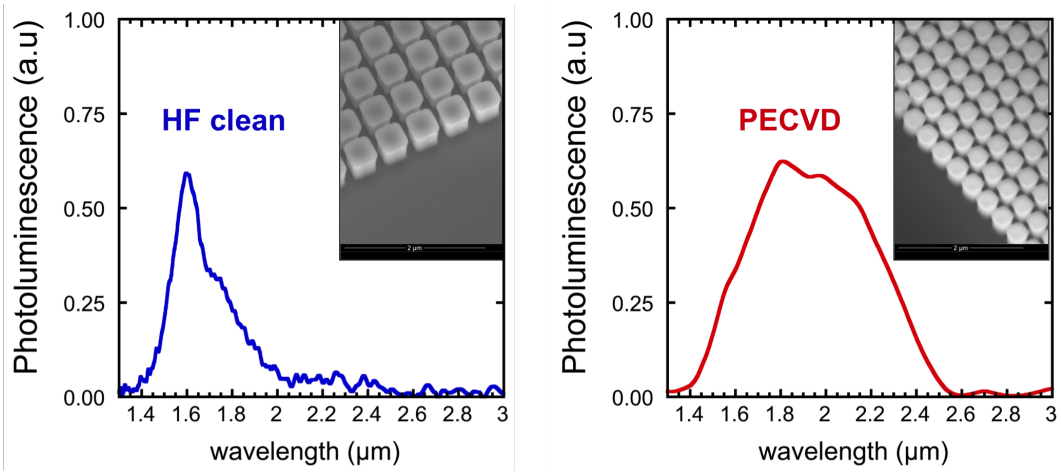

Figure 5.14: Photoluminescence (PL) of 300 x 300 nm square top Ge nanopillars, strained by high stress silicon nitride layers Left - the PL from pillars with an HF clean prior to high stress deposition. Right - PL from pillars with a PECVD silicon nitride adhesion promoting layer prior to the high stress deposition.

Photoluminescence measurements were taken as described previously on the patterned chips. Consistent with the silicon nitride cracking observed on the blank sample pieces (indicating poor adhesion), the GeO_2 samples showed no red-shift. Comparing the HF cleaned pillar samples to those with PECVD silicon nitride adhesion layers, a marked difference in the emission spectra was found, despite near identical SEMs, which highlights

the extent of the difficulty in under covering this issue. The PL for each sample is shown in Fig. 5.14.

5.6 Optical characterisation of tensile strained Ge nanopillars

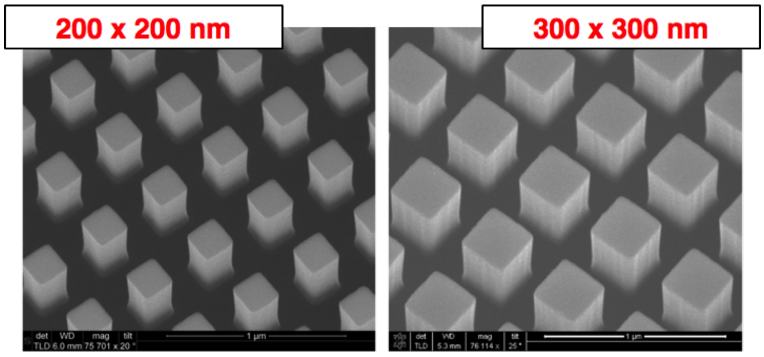

Figure 5.15: Scanning electron microscope of square top Ge nanopillars, dry etched down to the Si substrate.

Further measurement and analysis was continued using pillar samples with a PECVD silicon nitride adhesion layer. Three separate samples were processed, each containing 300 and 200 nm square top pillars. The dry etched samples are shown in Fig. 5.15. The first two chips had silicon nitride stressor layers deposited with $\sim$ 1.9 GPa and $\sim$2.7 GPa compressive stress respectively. The third chip was processed with a low stress ICP deposited silicon nitride layer (<100 MPa) of equivalent thickness to the high stress layers ($\sim$ 150 nm). This reference sample, with the negligibly stressed silicon nitride layer, was used to confirm the absence of any optical effects such as diffraction that might alter the spectral shape of the emission. The sample stage was tilted through $\sim$ 50 $^\circ$ to confirm the spectra remained unchanged, therefore ruling out the presence of cavity effects or diffraction from the pillar array.

The 300 nm pillars showed clear red-shifts to longer wavelengths, Fig. 5.16. For the 1.9 GPa sample, it appeared that both indirect and direct transitions are emitting at approximately the same wavelength, i.e. close to 1.8 μm. This would be consistent with L to HH and Γ to LH transitions. The increase in stress to 2.7 GPa shows the emergence of

a shoulder towards 2.0 μm, which has been attributed to the Γ to LH transition. Based on deformation potential theory, the wavelength of this transition indicates $\sim$ 0.9 % biaxial equivalent strain in the 300 nm pillar. In this case, the biaxial equivalence is based solely on $\Delta E_{\Gamma,LH}$ energy.

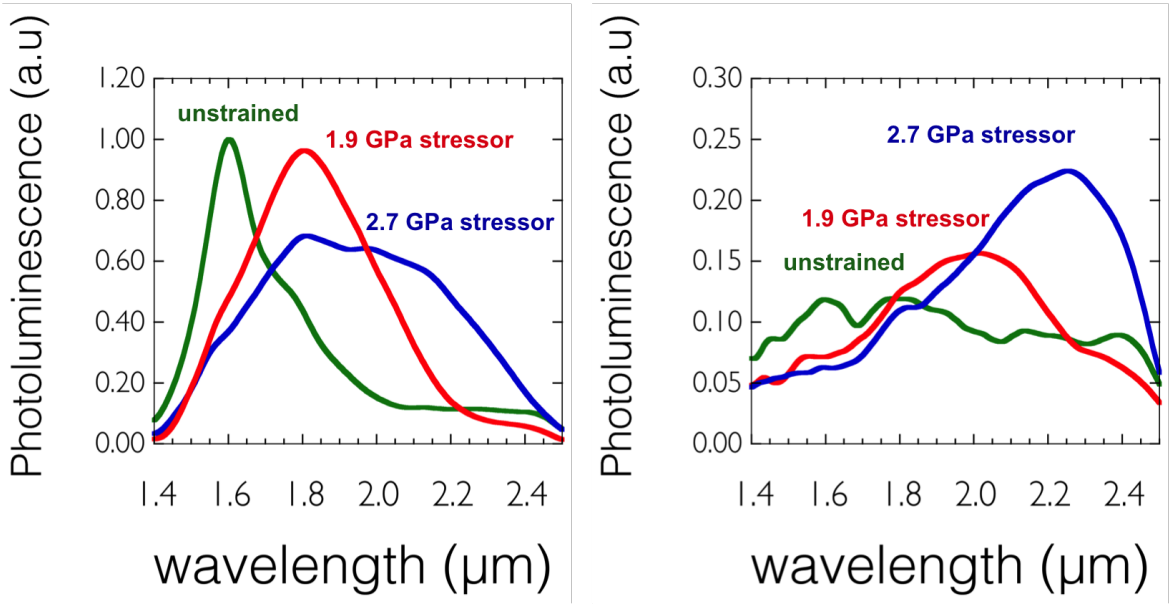

Figure 5.16: Photoluminescence of 300 x 300 nm (Left) and 200 x 200 nm (Right) square top Ge nanopillars with 150 nm high stress silicon nitride. Data normalised to peak intensity of brightest spectra.

The 200 nm pillars demonstrated a reduction in intensity compared to the 300 nm pillars, which is due to the reduction in fill factor compared to 300 nm pillar arrays. Furthermore, the volume to surface area ratios have changed resulting in a difference in the weighting of the respective loss mechanisms. Nevertheless, a clear red-shift was still observed, with a peak close to 2.25 μm for the 2.7 GPa stressor layer, constituting a 650 nm red shift from the unstrained, degenerately doped band-edge. Fig. 5.16 (right), shows the PL of 200 nm pillars. This is a larger redshift reported than in other works using silicon nitride stressors at the time of publication [144]. When approximated using deformation potential theory, this transition equates to a biaxial equivalent tensile strain of $\sim$ 1.35 %.

Complex carrier diffusions are likely to be present in the pillar structures. Geiger et al showed that recombination velocities act predominantly towards the dense network of

threading and misfit dislocations at the Ge/Si interface [52]. This, to some extent will be countered by the strain induced band-gap narrowing at the top plane, which leads to a drift current [9]. Furthermore, surface recombination on the sidewall further complicates the carrier diffusion, particularly with poor density of interface traps (D_{it}). Carrier diffusion throughout the pillar structure would however be consistent with the observed PL. The 300 nm pillars show a shoulder at 1.6 μm even at high strain, indicating photoluminescence from lower strained regions of the pillar. The 200 nm pillar emission appears to be less broad than the 300 nm, suggesting a higher strain uniformity in the structure. This is difficult to quantify properly, with the spectra comprising multiple interband transitions and blackbody heating, however, for the 200 nm structures there is clearly relatively less emission visible at shorter wavelengths.

Especially for the 300 nm pillars, the expected increase in intensity of the Γ to LH transition was not observed. This has in part been attributed to the selection rules under strain. The p like orbital characteristic of the valence bands means that under biaxial tensile strain, the upper most valence band has LH character predominantly in the z-direction (perpendicular to the plane of applied strain) [91]. This means that the transition from the s-like conduction band is strongly coupled to the LH when it is TM, or z-polarised, and therefore emission propagates in the sample plane. Measuring this directly would have required significant modification to the optical setup, and itself would have been complicated by self-absorption of the TM emitted light by adjacent pillars. Therefore, this sample geometry is not suited for edge emission measurements.

The strain dependence of the optical matrix elements is shown in Fig. 5.17, along with an illustration to clarify the polarisations. This highlights the TM dominance of the Γ to LH transition, which the setup is weakly sensitive to. For example, at $\sim$ 1.35 % biaxial strain, there is $\sim$ 12 times the TM to TE emission. Nam et al. confirmed this trend, when collecting the PL perpendicular and parallel to the strain axis. The emission parallel to the strain axis, (i.e. with E field parallel to the strain axis), showed little intensity increase with uniaxial strains up to 1.6 % [90]. Despite the considerations of the polarisation dependance, there is still a discrepancy in emission intensity. For instance, considering biaxial strain of the 200 nm pillars, the Γ to L difference is calculated to be approximately 40 meV, compared to $\sim$ 140 meV in unstrained material. Modelling using an effective mass model, and using Fermi-Dirac statistics shows that this should lead to an $\sim$ 60 times increase in carrier concentration at the Γ, which is directly proportional

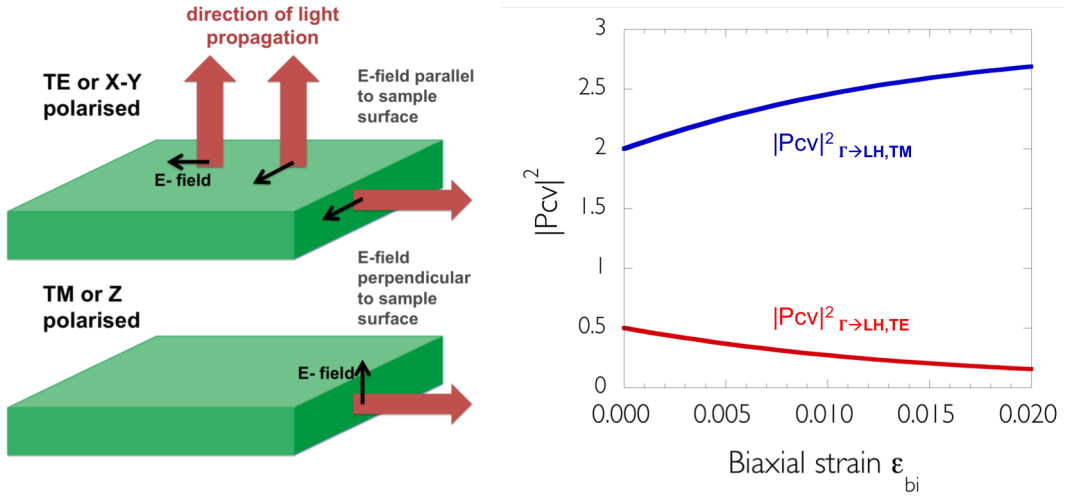

Figure 5.17: Left - Illustration showing the definition of TE and TM polarisations, and the permitted direction of light propagation. Right - The multiplying factor of the average optical matrix element for the Γ to LH transitions in TE and TM polarisations, as a function of biaxial strain.

to the expected intensity increase. This may be slightly overestimated, however, as this assumes that the conduction band carrier distribution under steady state injection can be described by a quasi-equilibrium Fermi-distribution, i.e. described by a single quasi-Fermi level, which may not be the case due to a low L to Γ scattering rate, and injection into the L-valley with a high energy pump [127].

The difference has been attributed to non-radiative loss mechanisms, such as the surface recombination passivation layers which have unfortunately shown poor electrical properties. Further to the surface recombination, a high loss mechanism is expected due to the threading dislocations. From Shockley Read Hall recombination models, it is shown that the maximum recombination occurs when the trap is in the middle of the bandgap. In unstrained Ge, threading dislocations are shown to have energies at around 0.56 eV [161], however, it is currently unknown how this energy changes when the material is highly strained. The polarisation arguments and non-radiative recombination mechanisms should therefore explain the lack of observed intensity increase (i.e. apparent direct bandgap behaviour) compared to theory.

5.7 Raman Spectroscopy of strained Ge nanopillars

Raman spectroscopy can be used to evaluate the strain in crystalline materials. The basic principals of Raman spectroscopy are detailed in Chapter 4 and now the results for strain induced changes to the measured Raman line are summarised here. In crystalline materials, the vibrations that cause the oscillation of the polarisability term stem from vibrations, i.e. phonons. Classically, this can be described by finding the resonant frequency of two masses coupled by a spring. Strain from any principal direction can alter the spring constant in any given direction. Coupling from strain in one direction, to the change in spring constant in another, is described through the strain tensor components, as shown in Eq. 5.4. Here, u_i is the relative displacement of the unit cell atoms, m is the reduced mass of the two atoms, $\mathrm{K}^{(0)}$ is the unstrained effective spring constant, and the $\mathrm{K}^{(1)}$ tensor describes the change to the spring constant with strain.

$$\bar{m}\ddot{u}_i = -K_{ii}^{(0)}u_i - \sum_{jkl} K_{ijkl}^{(1)}\varepsilon_{kl}u_j \tag{5.4}$$

$$K_{ii}^{(0)} = m\omega_0^2, K_{ijkl}^{(1)} = \frac{\delta K_{ij}}{\delta \varepsilon_{kl}}, ijkl = X, Y, Z \tag{5.5}$$

This sum can be fully expanded, and subsequently symmetry considerations allow a number of these terms to be equated. Completing the sum in Eq. 5.4 and substituting these equivalent terms gives a set of simultaneous equations which can be solved by taking the determinant equal to zero, and solving for the eigenvalues, λ. Conveniently, it reduces to a single constant when certain assumptions are made about the strain distribution, i.e. biaxial strain. Some empirical constants, p, q and r are used to denote the three independent K tensor components, e.g., $\mathrm{K}_{xxxx} = \mathrm{K}_{yyyy}$=$\mathrm{K}_{zzzz}$= mp.

$$\begin{vmatrix} p\varepsilon_{xx} + q(\varepsilon_{yy} + \varepsilon_{zz}) - \lambda & 2r\varepsilon_{xy} & 2r\varepsilon_{xz} \\ 2r\varepsilon_{yx} & p\varepsilon_{yy} + q(\varepsilon_{zz} + \varepsilon_{xx}) - \lambda & 2r\varepsilon_{yz} \\ 2r\varepsilon_{zx} & 2r\varepsilon_{zy} & p\varepsilon_{zz} + q(\varepsilon_{xx} + \varepsilon_{yy}) - \lambda \end{vmatrix} = 0$$

The equation yields three solutions for the eigenvalues, λ, which can be expressed as:

$$\lambda = \omega^2 - \omega_0^2 = (\omega + \omega_o)(\omega - \omega_0) = 2\omega_0 \triangle \omega \tag{5.6}$$

Due to polarisation considerations, in the backscatter geometry,with in-plane strain, the Raman line is coupled to the LO phonon in Si and Ge, meaning that only the solution

in Eq. 5.7 is used. It should be noted that this assumes that the off diagonal strain tensor components are zero.

$$\lambda = p\varepsilon_{zz} + q(\varepsilon_{xx} + \varepsilon_{yy}) \tag{5.7}$$

This can be restated in terms of $\Delta\omega$:

$$\Delta\omega = \frac{1}{2\omega_0}(p\varepsilon_{zz} + q(\varepsilon_{xx} + \varepsilon_{yy})) \tag{5.8}$$

This can then be related to the in-plane strains, by assuming that the z-component ε_{zz} is coupled to the in-plane strains through the elastic coefficients C_{11} and C_{12}.

$$\Delta\omega = \frac{(\varepsilon_{xx} + \varepsilon_{yy})}{2}\frac{1}{\omega_0}[-p\frac{C_{12}}{C_{11}} + q] \tag{5.9}$$

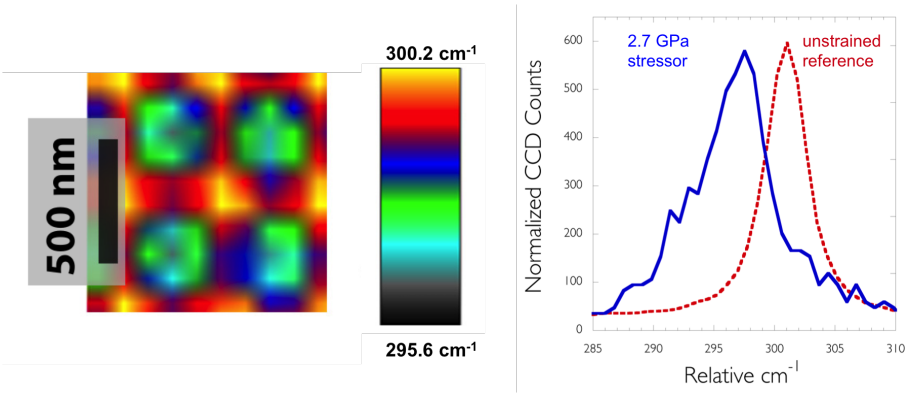

Figure 5.18: Left - Raman map formed by fitting Raman spectra at each pixel with a single Lorentzian, the spectral position is then shown as a colour following the scale shown. Right - Raman spectra from the top centre of a 300 x 300 nm square top Ge pillar strained by a 2.7 GPa stressor layer.

In order to confirm the levels of strain in the pillars, Raman spectroscopy measurements were carried out on the highest strained samples, using a WITec Alpha 300 RAS spectrometer, using a 100 times objective with a numerical aperture of 0.9 (Dr Thomas Dieing, WITec). Only a limited number of samples could be measured at the time. The 532 nm excitation source is absorbed in $\sim$ 20 nm in Ge, and therefore probes the strain in the top plane. The pump power was reduced until heating was eliminated from the measurements. The spatial resolution of the system was such that clear Lorentzian like

peaks could be observed on the 300 nm pillars, but this was not found to be the case for the 200 nm pillars, which could be identified in terms of a shift of the Raman line, however the spatial resolution ($\sim$ 300 nm) was too low to discern differences in strain across the top plane. This resulted in broad spectra that could not be fitted with a Lorentzian function, and therefore the results have been omitted.

A number of 300 nm pillars were measured using an x-y scan, with the resulting spectra fitted by a Lorentzian function, in order to form a map of the spectral position, shown in Fig. 5.18 (left). The highest strained regions in the sample scan area were found to have a Raman line at $\sim$ 296.3 cm^{-1}, Fig. 5.18. If assuming purely biaxial strain, this can be used to calculate the strain using Eq. 6.8, which reduces to $\Delta\omega = \mathrm{b}_{bi}\varepsilon_{bi}$, using the constants in [162]. Here, b_{bi}, the strain shift coefficient is 424 cm^{-1}. This therefore demonstrates a biaxial tensile strain of 0.91 %, which is in good agreement with the PL. Deviation from biaxial strain, however, can introduce error in these approximations, as the Raman line depends on all three components of the strain trace, i.e. ε_{xx}, ε_{yy}, and ε_{zz}, in the absence of shear stresses.

5.8 Finite element modelling

As shown in Eq. 5.9, some knowledge of the strain distribution is required in order to interpret the measured Raman shift. In general, the out of plane stress component has to be zero, as this is unconstricted and would therefore increase or decrease the strain in response to this stress. This leads to the biaxial approximation. However, with the addition of the sidewall stressors such a solution is non trivial, and therefore modelling of the strain distribution is required.

$$\begin{pmatrix} \sigma_{xx} \\ \sigma_{yy} \\ \sigma_{zz} \\ \sigma_{yz} \\ \sigma_{xz} \\ \sigma_{xy} \end{pmatrix} = \begin{pmatrix} C_{11} & C_{12} & C_{12} & 0 & 0 & 0 \\ C_{12} & C_{11} & C_{12} & 0 & 0 & 0 \\ C_{12} & C_{12} & C_{11} & 0 & 0 & 0 \\ 0 & 0 & 0 & C_{44} & 0 & 0 \\ 0 & 0 & 0 & 0 & C_{44} & 0 \\ 0 & 0 & 0 & 0 & 0 & C_{44} \end{pmatrix} \begin{pmatrix} \varepsilon_{xx} \\ \varepsilon_{yy} \\ \varepsilon_{zz} \\ 2\varepsilon_{yz} \\ 2\varepsilon_{xz} \\ 2\varepsilon_{xy} \end{pmatrix} \tag{5.10}$$

Finite element modelling in Comsol Multiphysics was therefore used to model the strain distribution in the pillars structures. The ratio of the top to sidewall nitride was taken to be 3:1 ($\sim$150 nm : 50 nm), following the TEM image in Fig. 5.12. As detailed

in Chapter 2, Eq. 5.10 is the elasticity tensor of Ge, which relates the stress and strain tensors. Due to certain symmetry considerations this can be significantly simplified to only three tensor components. This anisotropy was included in the model and aligned so that the principal axes are aligned to the X, Y and Z directions in the finite element model (FEM). The model was setup with a Si block underneath the Ge pillar, the base of which was set with a fixed constraint, meaning there is zero stress/strain at this boundary. The thickness of the Si slab was varied to that this boundary was sufficiently far from the strained region to give convergence of the solution in the pillar.

$$\varepsilon_{xx} = \frac{1}{E}[\sigma_{xx} - \nu(\sigma_{yy} + \sigma_{zz})] \tag{5.11}$$

$$\varepsilon_{yy} = \frac{1}{E}[\sigma_{yy} - \nu(\sigma_{xx} + \sigma_{zz})] \tag{5.12}$$

$$\varepsilon_{zz} = \frac{1}{E}[\sigma_{zz} - \nu(\sigma_{xx} + \sigma_{yy})] \tag{5.13}$$

The silicon nitride layer was modelled as being isotropically stressed, with the value of stress measured by the curvature technique. The stress strain relationships for isotropic materials do not require a tensor and are instead described by Eqs. 5.11-5.13, where ν is Poisson's ration and E is the Young's modulus. Given that some modelling parameters were not known, such as the Young's modulus of the high stress silicon nitride, the primary goal of the model was to understand the strain distribution, particularly with regard to the silicon nitride on the pillar sidewalls. This is a particularly interesting comparison as other work has more commonly used just a top stressor [9,95]. The Young's modulus was therefore estimated using a literature value for high stress silicon nitride (100 GPa) [94].

5.8.1 Strain distribution

Modelling revealed that there is a complex strain distribution in the pillar structures. At each edge, there is a lateral expansion in the plane of the sidewall, due to the sidewall stressors. This leads to a more uniaxial strain component along this edge. In the pillar top centres, the x and y components of the strain are equal leading to a biaxially strained centre, which is shown in Fig. 5.19. Furthermore, the inclusion of the sidewall stressors was found to increase the depth of which the in-plane strain field penetrates down the

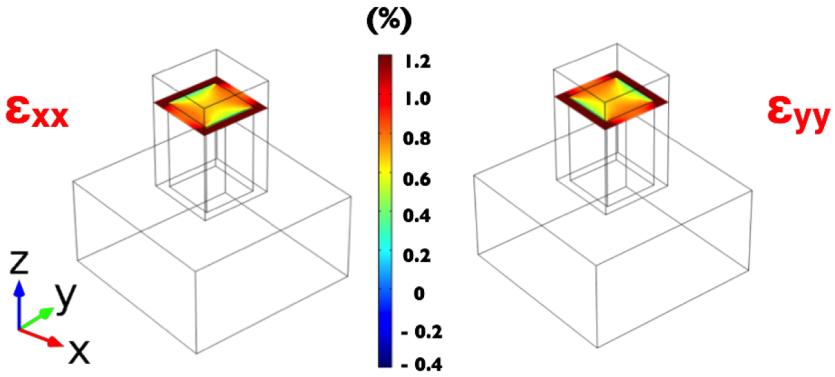

Figure 5.19: Finite element models of Ge nanopillars showing the ε_{xx} and ε_{yy} strain components, in a 2D slice at the top plane of the pillar.

pillar, which is due to the lateral expansion on the sidewalls. The model also showed a reduced compression in the z-direction at the top plane, which is normally expected due to the coupling of the tensile in-plane strain from the top stressor through Poisson's ratio. Furthermore, uniaxial tensile strain was found to be present in the z-direction away from the top plane.

The modelled strain tensor components were used to calculate the Raman line, down the centre of the 300 nm pillar structure, Fig. 5.20. In the experiment, the volume contributing to the Raman line is that over the absorption depth of the source, with weighted contributions accounting for reabsorption of the Raman scattered signal. Therefore, corrections were applied to the calculated Raman line following De Wolf et al. [163] using Eq. 5.14, where α is the absorption coefficient, z is the distance from the top plane, and $\omega(x, z')$ is the calculated Raman shift as a function of position and depth. This resulted in a calculated value of 296.56 cm^{-1}, which is in good agreement with the measured value of 296.3 cm^{-1}. In Fig. 5.20, pillars with top only stressors have been modelled for comparison.

$$\Delta\omega(x) = \frac{\sum_{z'} \Delta\omega(x, z') exp(2\alpha z')}{\sum_{z'} exp(2\alpha z')} \tag{5.14}$$

Furthermore, the Γ to LH emission wavelength was calculated from the strain tensor, which gave a Γ to LH energy of 0.633 eV at the top plane, corresponding to an emission of 1.96 μm at the top. This again appears to be consistent with the experimental results.

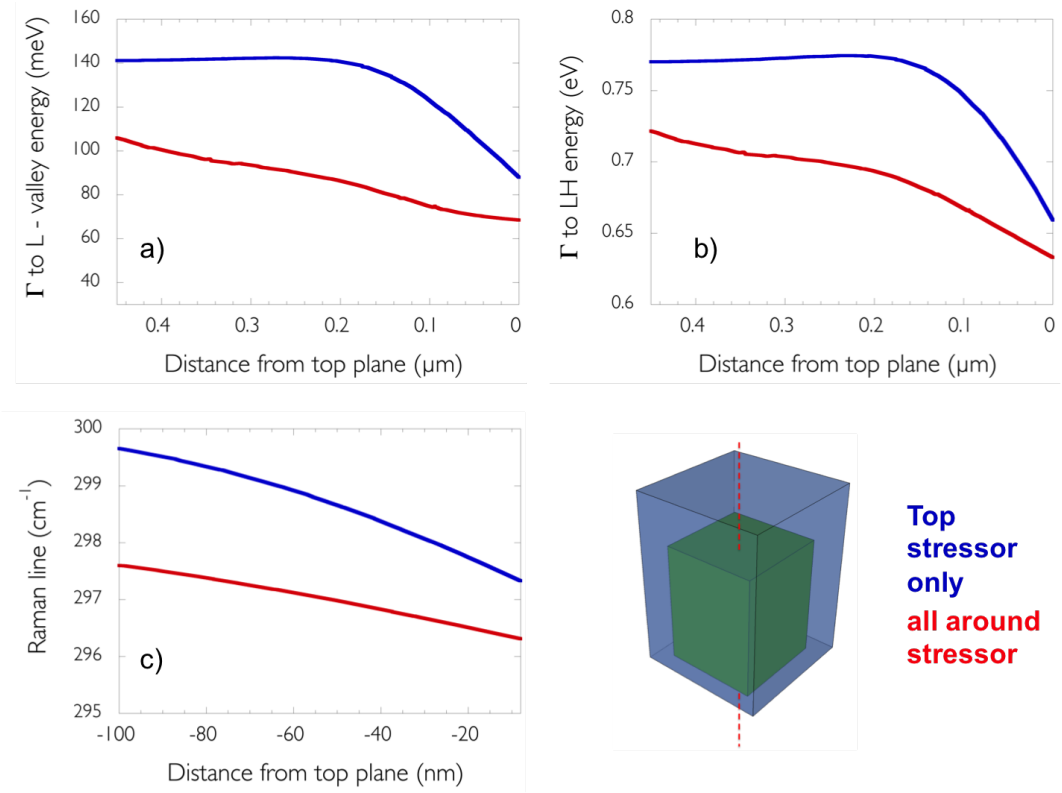

Figure 5.20: Calculations of the material properties of a 300 nm Ge nanopillar based on the finite element modelling of pillars with a top only stressor, and an all-around silicon nitride stressor. a) Γ to L valley energy difference b) Γ to LH. energy c) Calculated Raman line. All figures plotted as a function of distance from the top plane of the pillar. The bottom right figure shows an illustration indicating the line segment down which the calculation was made in the model.

It was found that modelling the 300 nm pillars with a 1.9 GPa stressor predicted a PL peak at $\sim$ 1.85 μm, again, in good agreement with experiment. The 200 nm pillars were not so well reproduced, with emission at 2.02 μm predicted, however, an increased strain uniformity was observed which appeared to be evident from PL. The potential reason for this discrepancy is discussed later in the chapter .

5.8.2 Γ to L energy

As shown in Eq. 5.15, the Γ to L difference is directly related to the strain trace, through deformation potential constants.

$$\Delta E_{\Gamma,L} = \Delta E^{0}_{\Gamma,L} + (\varepsilon_{xx} + \varepsilon_{yy} + \varepsilon_{zz})\left(a_c - (\Xi_d + \frac{1}{3}\Xi_u)\right) \tag{5.15}$$

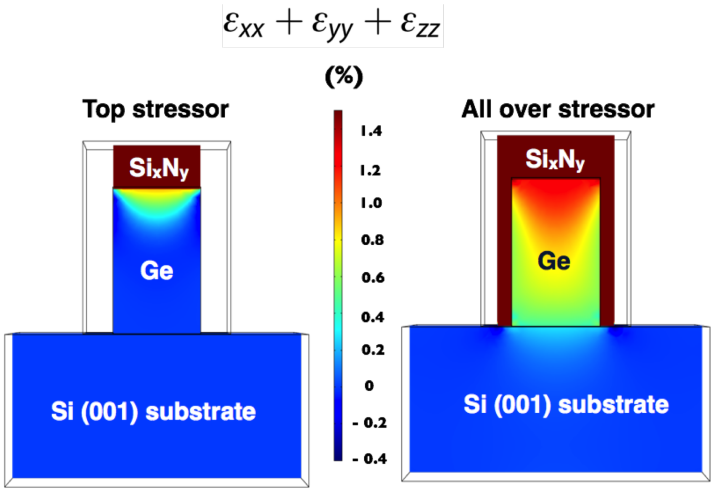

Figure 5.21: Vertical 2D slice of finite element models of 300 nm Ge nanopillars with silicon nitride stressor layers The colour map indicates the sum of the strain trace components.

This increased hydrostatic component from the all-around stressor can be seen in Fig. 5.21. Despite calculated strains of $\varepsilon_{xx} = \varepsilon_{yy} = 0.68$ % at the top plane for the 300 nm pillar, the increased ε_{zz} leads to a band-edge comparable to 0.9 % biaxial strain in terms of Γ to LH emission. Furthermore, the increased hydrostatic strain demonstrated in the model would suggest a Γ to L energy difference comparable to 0.97 % biaxial strain (69 meV), which highlights the potential advantage of this type of strain distribution. Such a strain field should therefore have the effect of decreasing the Γ to L energy difference at a greater rate than purely biaxial strain Fig. 5.20. Clearly, there is also an advantage in the uniformity of the strain field compared to a top only stressor. Even without becoming direct bandgap, this would still be advantageous for a potential laser structure, if this type of strain distribution could be incorporated into a cavity. The required doping to fill the L valley to the level of the Γ would be reduced, which in turn would reduce the free carrier absorption from electrons.

The effects of an increased hydrostatic strain component on the free carrier losses was modelled. An 8 x 8 k.p solver, Nextnano3, was used to calculate the band-structure including the effects of strain. The effective masses for the Γ, HH and LH bands can

then be extracted from the band curvature. This allows the calculation of the effective density of states masses using $m_{dos} = (m_t^2 m_l)^{\frac{1}{3}} d^{\frac{2}{3}}$, where m_t and m_l are the transverse and longitudinal effective masses respectively, and d is the band degeneracy.

The 8 x 8 k.p model does not account for the L valley and therefore the masses are assumed to be unchanged with strain, ($m_t = 0.082$ and $m_l = 1.64$), which has been shown to be a good approximation by 30 x 30 band k.p modelling [3]. While the L-valley mass is not modelled, the band minima is calculated by deformation potential theory.

The total concentration of electrons is the n-type doping concentration plus the injected carrier concentration, $n_{tot} = N_d + \Delta n$. The total carrier concentration in the conduction band is shown as a function of the 3d density of states, g_{3d}, the density of states masses, m_{dos}, and the Fermi-function $F(E, T, E_{f,e})$:

$$n_{tot,n} = \int_{E_L, E_\Gamma min}^{\infty} \Big(g_{3d}(E, E_L, m_{dos_L}) + g_{3d}(E, E_\Gamma, m_{dos_\Gamma}) \Big) F(E, T, E_{f,e}) \tag{5.16}$$

where E_L and E_Γ are the indirect and direct band-edges. The same approach can be taken to express the valence band hole concentration for the LH and HH bands. The electron quasi-Fermi level $E_{f,e}$ can be selected so as to be at the same energy as the Γ band, i.e. at the onset of population inversion. The corresponding carrier injection required can then be computed by carrying out the Fermi integral, which requires a numerical technique, and the free carrier absorption at the wavelength corresponding to the bandgap energy can then be calculated Eq. 5.17, where n_c and n_v are the electron and hole densities, expressed in cm^{-3}, and λ is the wavelength in nm. It should be noted, that a range of p and n-doped Ge wafers were used for the empirical fit to experimental data, and not the free carrier absorption under injection.

$$\alpha_{fc} = -3.4 \times 10^{-25} n_c \lambda^{2.25} - 3.2 \times 10^{-25} n_v \lambda^{2.43} \tag{5.17}$$

Figure 5.22 shows the effect of changing the z-component of the strain while holding the in-plane strain constant at $\varepsilon_{xx} = \varepsilon_{yy} = 1\%$. The fraction of carriers in the Γ band is computed at the level of injection required for the quasi-Fermi level to reach the Γ band minimum, where an n-type doping of 2.5×10^{19} cm^{-3} has been used. The associated free carrier losses from injection are shown in Fig. 5.22. Biaxial coupling is indicated at $\varepsilon_{zz} \sim$ -0.74. For the free carrier absorption, the observed saturation is due to the fact that for

those levels of strain, the 2.5×10^{19} cm^{-3} doping is significant enough for the quasi-Fermi level to reach the Γ. The increase in carriers at the Γ band can be observed in Fig. 5.22 (right). This highlights the potential benefits of an increased hydrostatic component of strain in strained Ge structure, as with an increasing ε_{zz}, the carrier concentration at the Γ increases the achievable gain, while also reducing the total free carrier losses.

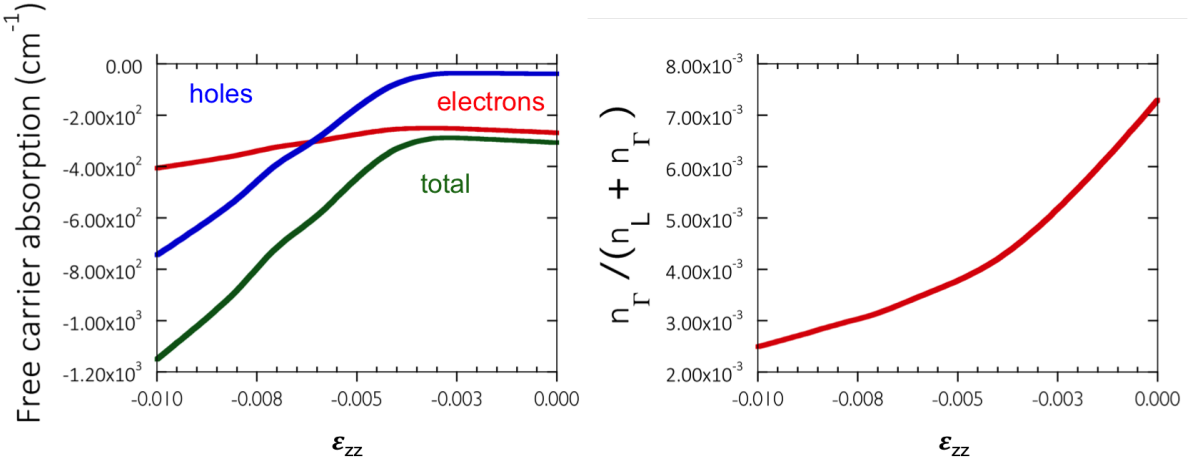

Figure 5.22: Left - Free carrier absorption associated with the carrier injection required to move the electron quasi Fermi level to the Γ minimum, as a function of ε_{zz} for a fixed biaxial in-plane strain of 1%. Right - the fraction of electrons in the Γ band for the same conditions of the quasi-Fermi level.

5.9 Electron energy loss spectroscopy

During a subsequent investigation of 700 x 700 nm square top Ge pillars, samples were sent for TEM imaging. The pillar was analysed by electron energy loss spectroscopy (EELs) (Aneeqa Bashir - School of Physics and Astronomy, University of Glasgow). Fig. 5.23 shows a colour map indicating the elemental composition across the TEM.

It was found that there was a different silicon nitride composition evident on the pillar sidewalls, which contained a higher oxygen content. This therefore adds a further complication in terms of interpreting the modelling, as a stress state of the sidewall silicon nitride could differ from the measured stress on the planar surface. While Raman and PL measurements are both suggestive of biaxial equivalent strains (in terms of the Γ

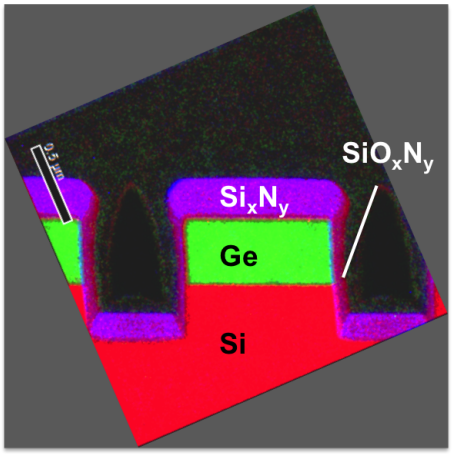

Figure 5.23: Electron energy loss spectroscopy colour map, taken on a lamella of a 700 x 700 nm Ge nanopillar with a high silicon nitride layer.

LH to transition) of at least 0.9 %, there is some doubt about the exact nature of the strain distribution, which would require further experimental verification. Given the lack of frequent access to TEM and EELs analysis, this could not be monitored on a regular basis, and therefore it is unknown if this is an issue that developed at a later date than the initial results, or if this has been persistent throughout the depositions. Furthermore, it us also unknown how the geometry and the ratio of the sidewall area to pillar top area effects the O_2 content, and could therefore be a contributing factor to the slight discrepancy between the model and the 200 nm pillar results.

5.10 Conclusion

High stress silicon nitride processes were developed and characterised, with stresses up to 2.7 GPa. It was found that despite the apparent adhesion of these layers to Ge nano features (by SEM), there was poor or partial adhesion to pillar tops visible when measured by TEM images. Adhesion promoting fabrication processes were developed, and used to show highly red-shifted emission, up to $\sim$ 2.25 μm from 1.35 % tensile strained 200 x 200 nm Ge nanopillars, which at the time of publication was higher red-shifts than other reports using silicon nitride stressors.

Raman measurements confirm a $\sim$0.9 % biaxial equivalent strains in 300 nm pillars. Finite element models were used to give an insight into the effect the strain distribution

caused by the silicon nitride stressors. In these geometries, it was found that there is an enhanced hydrostatic component due to tension in the z-direction from the side-wall stressors, which theoretically is known to reduce the Γ to L-valley energy difference at greater rates than purely biaxial strain. The potential benefits of such a strain distribution were shown by modelling of the carrier statistics, using the effective masses of strained Ge layers calculated by k.p modelling, which showed increased carrier concentration at the Γ and lower free carrier losses with sufficient injection for the onset of population inversion. Further experimental work is required to investigate the strain away from the top plane to confirm the the role of the side-wall stressors.

6

Tensile strained Ge micro-cavities

Work from this chapter was published in Optics Express [164], and presented at Group IV Photonics 2015 [165] and at the Electrochemical Society 2016 [14].

6.1 Introduction

Having demonstrated high levels of biaxial equivalent tensile strain in Ge nanopillars, it was of interest to investigate the strain distribution in structures which could be used as optical cavities. As discussed previously, lasing has been demonstrated in straight Ge on Si waveguides, which exhibit Fabry-Perot (FP) oscillations from the mirror facets [37, 38]. This relies on a the Fresnel reflections at the Ge-Air interface, which gives a maximum reflection of $\sim$ 37 %. Increasing the mirror reflectivity is an efficient means of lowering device thresholds, which was shown theoretically in Chapter 2, by expressing the lasing threshold as a function of the reflectivity of the facets, as well as the loss from material absorption. Therefore, structures with high mirror reflectivities are of interest, which can be achieved in circular cavities in the form of whispering gallery modes. In microdisk and ring structures, such modes satisfy periodic boundary conditions around the cavity circumference. In larger diameter ring resonators, this can perhaps be more simply viewed as waveguide segments with a periodic boundary condition, that requires an integer number of wavelengths round the circumference in order for constructive interference to occur. The Q-factor of a resonator is a measure of its ability to store energy, Eq. 6.1, and therefore is related to cavity losses.

$$Q(\omega) = \omega \times \frac{Maximum\ \ energy\ \ stored}{Power\ loss} \tag{6.1}$$

This can equivalently be stated as:

$$Q(\lambda) = \frac{\lambda_o}{\Delta\lambda} \tag{6.2}$$

The Q factor is directly related to the absorption coefficient, α:

$$Q = \frac{2\pi n_{eff}}{\lambda\alpha} \tag{6.3}$$

where n_{eff} is the effective index of the propagating mode, and λ is the wavelength. In Fabry-Perot cavities, the absorption coefficient, α_m, from mirror reflectivity's of R_1 and R_2, can be expressed as a distributed loss coefficient:

$$\alpha_m = \frac{1}{2d} ln \frac{1}{R_1 R_2} \tag{6.4}$$

This highlights that the effective absorption coefficient from mirror losses can be reduced by increasing the length of the cavity, with length d, however this leads to a device with a large footprint. Whispering gallery modes however, can lead to Qs upwards of 100,000 in structures on the micron scale, which has been readily demonstrated in SOI microrings and highlights the applicability of such cavities for lasers. Micro-disk and ring laser cavities have been demonstrated with a number of III-V materials [166].

Mode profiles in microdisk structures, calculated by a Finite difference time domain method are shown in Fig. 6.1. The modes are labeled as TE $_{nm}$ and TM $_{nm}$ modes, where n is the azimuthal number and m is the radial number, indicating the number of field maxima around the circumference, and in the radial direction respectively. Fig. 6.1 therefore shows $TE_{32,1}$ and $TE_{24,2}$ from left to right.

Compact microdisk and ring resonators are of particular interest for use in strained Ge technologies as the reduced dimensions increase the levels of strain that can be applied externally by silicon nitride stressors. Other groups have shown interest in Ge disks, with early demonstrations of silicon nitride stressed Ge on GaAs microdisks showing $\sim$1 % biaxial tensile strain. Subsequently, disks fully enclosed by silicon nitride were demonstrated to give more uniform strain in the vertical direction to improve the modal overlap with the highly strained region, with biaxial tensile strain up to 1.75 % [167]. Germanium

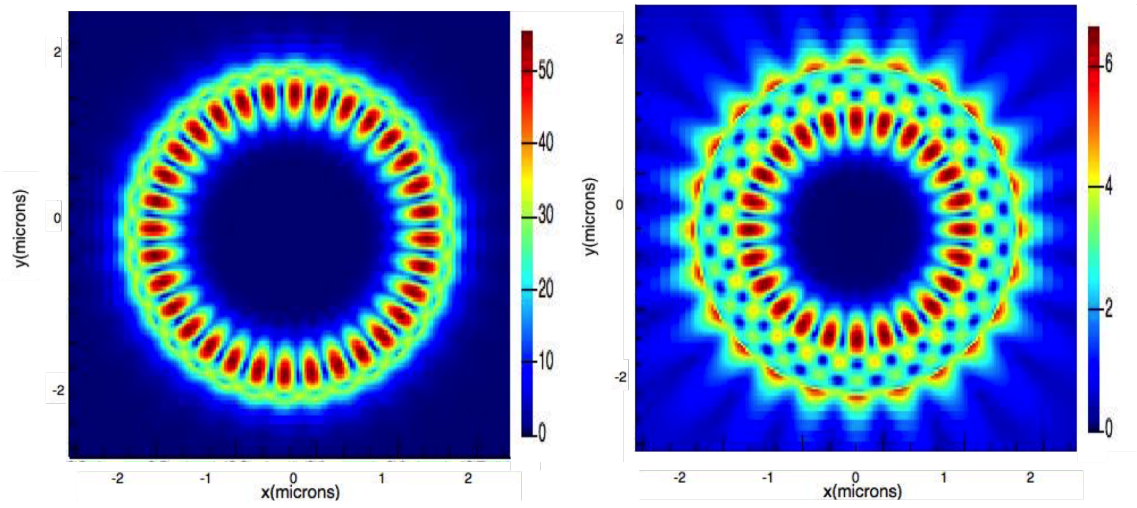

Figure 6.1: Finite difference time domain modelled whispering gallery modes in a GaN microdisks, showing the $TE_{32,1}$ and $TE_{24,2}$ from left to right.

on insulator (GeOI) material systems have also been used for strained microdisks, which was discussed in Chapter 3. This involves a technique where the Ge disk is released, and bonded to the SiO_2 oxide layer by stiction, leading to a tensile strain of around ~ 0.7 % in the Ge disk.

This work focuses on the use of single layer silicon nitride stressors, as future devices will require good thermal conductivity, and the potential for electrically contacting. While the works cited above address a number of the key issues, the inherent need of dielectric lower claddings will not permit these desirable characteristics. The three cavities investigated in this chapter are undercut Ge on Si microdisks, microrings, and racetrack resonators, which are all standard optical cavities capable of exhibiting high Qs. The fabrication techniques used to create these structures are shown, and discussed with the emphasis on the anisotropy of tetramethylammonium hydroxide (TMAH) wet etches, and the resulting impact on the undercut geometry. In ring and racetrack structures, the anisotropy can lead to full undercutting of waveguide segments leaving novel, partially free standing structures. The processes used here are entirely CMOS compatible. Results are first shown for Ge on Si microdisks, which were used to investigate the process, and the silicon nitride stress transfer. Subsequently, further results are then shown for the other investigated micro-cavities, with the emphasis of the analysis on the nature of the applied strain, the in-plane strain uniformity, and effect on the strain distribution on the

band-structure. In particular, the effects of ε_{xy} shear strain components are discussed with regard to the degradation of carrier concentration at the Γ valley. The highest strained cavities show in-plane tensile strains of > 2 % at the top surface, as measured by Raman spectroscopy, and photoluminescence (PL) up to the detector cut-off of 2.5 μm wavelength, which is higher strain levels reported than in other works using silicon nitride stressor layers.

6.2 Growth and material properties

A 380 nm thick Ge epilayer was grown in a Low–energy–plasma–enhanced–chemical–vapour–deposition (LEPECVD) tool at low temperatures of 500 °C, in order to avoid out-diffusion of degenerate phosphorus doping of 2.5×10^{19} cm^{-3} [52]. Activated dopant densities were measured using hall bar measurements at 300 K, and by infrared reflectance techniques [168]. This results in a Ge epilayer with negligible strain from growth, which was confirmed by XRD. The material is from the same wafer used to fabricate Ge nanopillar structures, and the reduced thickness is merely due to the non-uniformity of the plasma in the growth system, as explained in Chapter 4.

As before, high doping levels were seen as advantageous in order to give a bright PL signal, and increased carrier concentration at the Γ-valley, however in an optimised device doping levels can be reduced to minimise free carrier absorption. This would also allow for high temperature anneals in order to reduce the threading dislocation density and induce a small, beneficial, tensile strain in the Ge layer from the mismatch in thermal expansion coefficients compared to the Si substrate. As reported in the previous chapter, a detrimental aspect of the low temperature growth is the high number of threading dislocations which lead to significant Shockley-Read-Hall (SRH) recombination.

6.3 Fabrication development

6.3.1 Isotropic dry etching

Initially, dry etch techniques were investigated to give an isotropic etch underneath the Ge layer, which tends to give improved control over wet etches in terms of etch depth accuracy. Whereas a mixed recipe can simultaneously etch and passivate, the reduction,

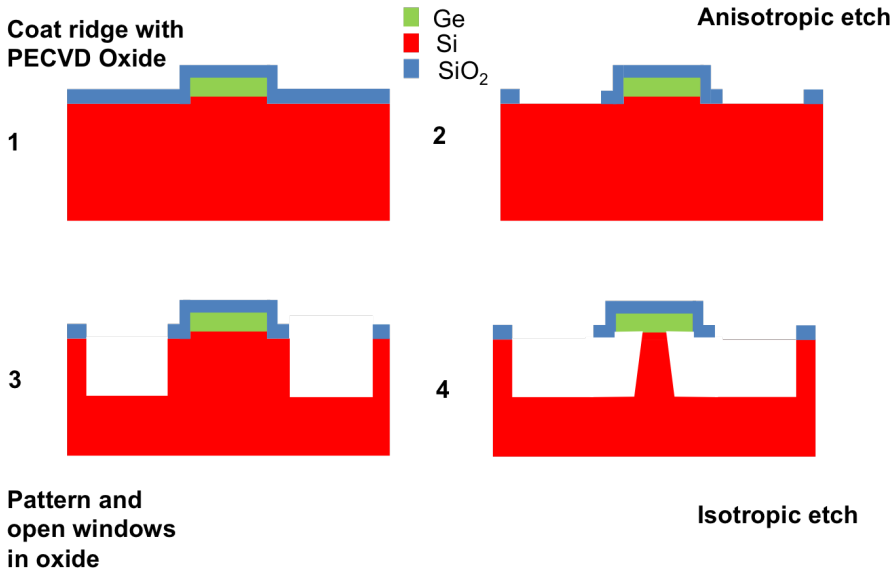

Figure 6.2: Illustration of the dry etch process used to investigate undercutting a Ge micro-feature.

or complete removal of the passivation gas can allow for isotropic etching. This was investigated with Ge ridges.

The process is shown in Fig. 6.2. Ridges were patterned by e-beam lithography in HSQ resist, and dry etched into the Si layer, using a mixed SF_6 and C_4F_8 recipe. The residual HSQ was left on the ridges. Subsequently, a 1 μm thick SiO_2 layer was deposited in a PECVD tool to ensure there was a sufficiently thick hard mask to protect the Ge layer, given that the selectivities were unknown. Windows were then patterned in PMMA by e-beam lithography, and the SiO_2 layer was then etched in CHF_3 and O_2 down to the Si layer. Finally, the undercutting dry etch step in SF_6 was run in 1 minute long iterations, with inspection of the sample by SEM between each etch. SEM images of the process can be seen in Fig. 6.3. While it appeared that the etch was undercutting the Ge structure successfully, after stripping the SiO_2 in a buffered HF solution it was found that there was significant damage to the Ge layer. It is likely that deeper anisotropic dry etches would be required in order to prevent the isotropic etch reaching the Ge layer from the underside. This would therefore begin to push the tolerances of the hard masks, and also result in a tapered Si post, with a waist significantly lower than directly under the Ge feature. Whilst dry etching would provide greater control of the etch rates, it was

seen that wet–etching would be a viable alternative and such processes were subsequently investigated.

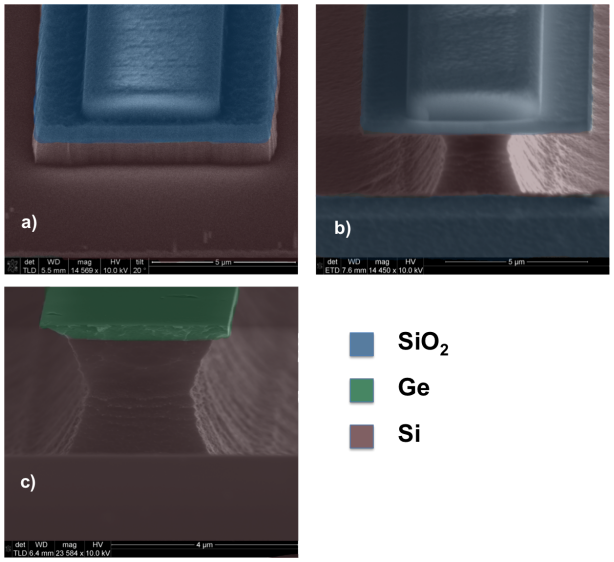

Figure 6.3: Scanning electron microscope (SEM) images of a Ge ridge undercut by SF_6 dry etching. a) Dry etched Ge ridge, edged through to the Si, with a SiO_2 mask. b) Following 3 minutes dry etching in SF_6, c) post SiO_2 removal in buffered HF.

6.3.2 Wet Etching

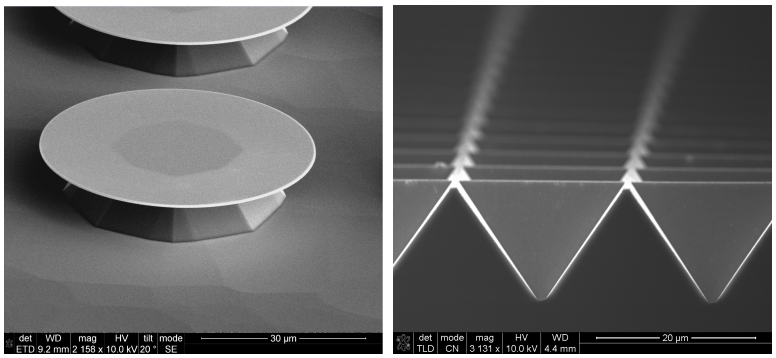

Figure 6.4: Left - Scanning electron microscope (SEM) image of a 50 μm diameter Ge disk, wet etched in tetramethylammonium hydroxide (TMAH). Right - Cross sectional SEM of a wet etched (100) Si surface.

Standard Si wet etches include potassium hydroxide (KOH) and tetramethylammo-

nium hydroxide (TMAH), which both negligibly etch Ge and are therefore appropriate candidates. Wet etches were initially investigated using 25 wt % TMAH. Due to the different bonding energies of the Si crystal planes, etching is anisotropic. This has been exploited in the fabrication of solar cells in (100) Si, which leaves square based pyramids with {111} sidewalls, Fig. 6.4, and enhances transmission in the visible spectrum. When etching these surfaces the etch is self limited as the {111} planes act as etch stops.

Etching temperatures between 50 °C and 90 °C are typical for TMAH [169]. Higher temperatures increase the etch rate, and increases the anisotropy between the {111} and {110} planes. The addition of Isopropyl-alcohol (IPA) decreases the etch rate linearly with increasing percentage volume of IPA, and has been demonstrated to reduce the roughness of the Si surface [140]. The reaction for etching is shown in Eq. 6.5.

The etch rate to Ge is negligible, which significantly simplifies processing by alleviating the need for masking of the dry etched cavity. It was confirmed by AFM that there was no significant roughening of the Ge surface during the time-scale of the undercut etch. It was found that the anisotropy between the {111} and {110} planes can lead to the novel, partially free-standing structures when undercutting particular geometries. Wet etches were carried out in a dure which sits in a base with a heating element. Feedback from a thermometer in the solution allows for temperature control via a PID controller. Initial trials for undercutting circular structures showed a lateral etch rate of $\sim$ 500 nm/minute at 80 °C, measured by SEM. While this is harder to accurately control compared to dry etching the minimal damage to Ge layers was seen as significantly advantageous. Lower temperature etches were subsequently investigated to improve the controllability of the etch.

$$Si + 4OH^- \longrightarrow Si(OH)_4 + 4e^- \tag{6.5}$$

6.3.3 Undercutting profiles of Ge cavities

In waveguide geometries the orientation of the waveguide influences the extent of the undercut, due to the anisotropy of the etch. For instance, in waveguides aligned to the [110] direction, the undercutting plane is the {111}. This results in a significantly slower etch compared to waveguides orientated in the [100] direction, which are undercut by the {110} planes. This can be seen clearly in Fig. 6.5 with a range of Ge features, which were

dry etched into the Si before wet etching. The ratio of the etch rates from the (111)/(110) is approximately 1:65 [170], however small misalignments of the ridges with respect to the crystallographic planes can cause a significant reduction in this ratio.

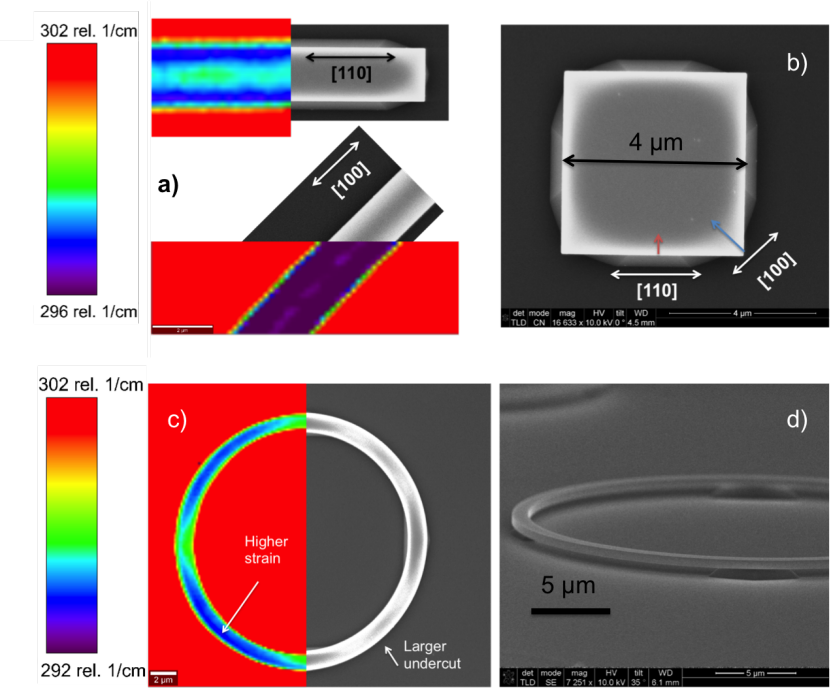

Figure 6.5: a) Raman maps of undercut Ge ridges lying in the [110] and [100] directions, overlaying scanning electron microscope (SEM) images of the features. b) SEM of a Ge square undercut by TMAH etching showing increased undercutting parallel to the [100] direction. c) SEM of an undercut Ge microring cavity, overlaid with a Raman spectroscopy map. d) SEM image of a partially free-standing microring structure.

The increased undercut reduces the deformation resistance and allows for an increased strain transfer into the Ge ridge. This difference can be seen when examining the Raman shift of both structures, which were strained by identical high stress silicon nitride layers, with the larger shift showing higher tensile strain as discussed in Chapter 5. In 20 μm diameter ring structures with 1.5 μm wide waveguide widths, this effect could be observed as the waveguide segment moves periodically from lying in the [110] direction to the [100]. Increased undercutting could be observed in waveguide segments parallel to the $\langle 100 \rangle$ direction, which could then be observed as increased strain, as shown in Fig. 6.5 c.

Further process development revealed that increased etch times lead to completely

undercut waveguide segments in the ⟨100⟩, leaving 4 support posts around the structure, where the tangent to the curve lies in the ⟨110⟩, as shown in Fig. 6.5 d. Once the waveguide segments in the regions tangential to the ⟨100⟩ are fully released, the post segments become truncated as further etching acts parallel to the waveguide segment. Interestingly, in circular geometries such as microdisks the etch was found to leave a faceted post, however the undercutting distance from the disk circumference to the facet edge was found to be constant regardless of the crystallographic plane, which, conveniently is ideal for a symmetric strain transfer.

6.4 Strained Ge mirodisks

The limits of strain transfer were investigated with a range of microdisks with varying diameters, with an undercut etch of $\sim$ 1300 nm. 4, 5, 6, 10, 20 and 50 μm diameter disks were patterned by electron beam lithography in HSQ resist, and dry etched in a mixed SF_6 and C_4F_8 recipe. The structures were cleaned in a buffered HF solution to remove the native oxide, which is critical to avoid hillock formation, before immediately being wet-etched in TMAH and IPA at 80 °C for 3 minutes,. Fig. 6.6 shows three stages of the process, including the dry etch (a) , the wet etch (b), and the silicon nitride coated feature, (c).

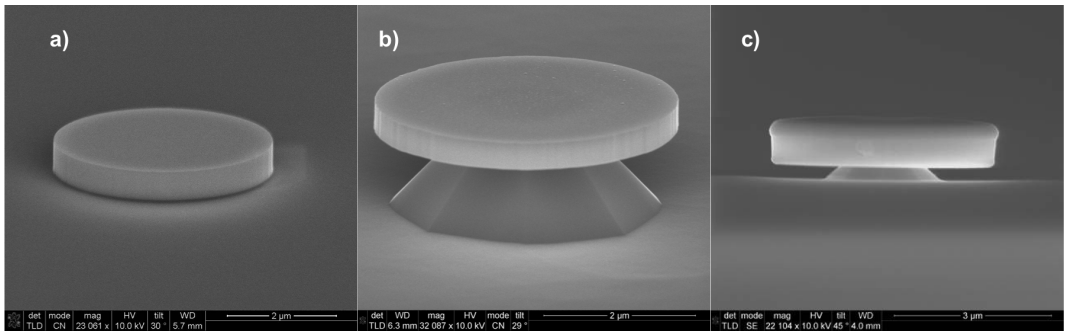

Figure 6.6: a) Ge microdisk dry etched down to the Si substrate. b) Ge microdisk with wet etch to undercut the Si. c) Silicon nitride coated undercut Ge microdisk.

At the point of development the only readily accessible means of quantification of the strain was photoluminescence (PL). The disk structures were coated incrementally by 150 nm of high stress silicon nitride, and PL measurements were taken on the 4 μm disk

structure. The samples had standard solvent cleans between depositions. There appeared to be negligible observable difference between the 2nd and 3rd depositions (300 nm and 450 nm respectively). The final structures were therefore left with a 450 nm thick film with an average compressive stress of $\sim$ 2.45 GPa.

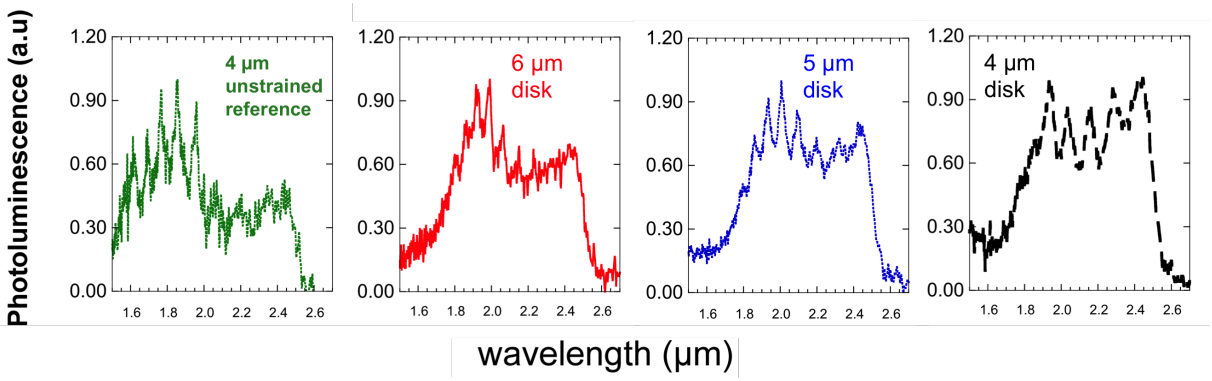

Figure 6.7: Photoluminescence (PL) from Ge microdisks. From left to right - unstrained undercut 4 μm disk, 6 μm , 5 μm and 4 μm strained Ge disks. All strained disks are undercut by $\sim$ 1300 nm and stressed by a 2.45 GPa 450 nm thick silicon nitride stressor layer.

Photoluminescence measurements were taken using the setup described in Chapter 5. A Bruker Vertex 70 was used to collect emission from the sample, which was pumped by a 532 nm solid state source. Collection is from the surface normal, or x-y plane, which, as in Chapter 5 has certain ramifications for the observation of TM coupled interband transitions. The measurements were run in fast-scan mode, meaning ambient blackbody radiation could be observed towards the detector cut-off of 2.5 μm. Background measurements of the ambient blackbody were taken and subtracted from the sample scans in order to observe photoluminescence. However, due to a slight increase in the local temperature due to the laser heating, there is a differential heating tail observable in the measurements after subtraction of the ambient blackbody. This is observable in photoluminescence in Fig. 6.7, particularly in the unstrained reference samples. Although heating in such structures can be prevalent, it is likely to be negligible in these measurements. Despite using a high power pump with CW power of 300 mW, the large beam diameter leads to injection in the range of 10s of μWs per disk. The use of large disk arrays therefore not only allows a simplification for the measurement in terms of alignment and collection, but it means that a bright average signal can be seen under low injection.

Resonances were observed on all disks in the PL spectra. Previous reports have concluded that resonances with comparable free spectral ranges (FSRs) were whispering gallery modes. In order to clarify this, Ge squares were patterned and PL measurements were taken. They showed comparable FSRs to the disk structures, suggesting that in the disks, the mode propagates at least partially along the disk diameter, rather than round the circumference of the structure as with true whispering gallery modes. The presence of quasi radial modes has been discussed in [99]. As stated, with this optical setup, PL measurements have only been taken on the disk arrays, rather than individual disks. As a result no attempt will be made to quantitatively analyse the Q factors of the observed resonances, as any finite difference in the cavities in the array would cause the resonances to broaden, leading to an inaccurate analysis of cavity losses. However, some general trends can be observed. As seen in Fig. 6.7 the strained sample appears to have lower Qs than the unstrained reference sample. This could be in part due to the increased free carrier absorption associated with the longer wavelength emission, which follows a $\lambda^{2.25}$ dependency for electrons. The change in Q from strained to unstrained samples at comparable wavelengths is likely due to the increase in the mirror losses due to the presence of the silicon nitride on the disk sidewalls.

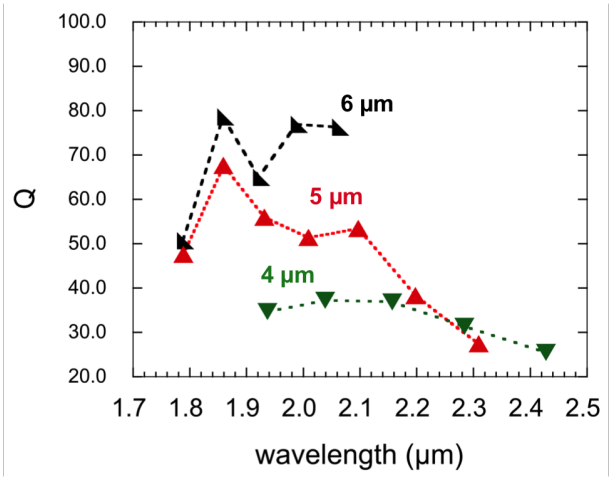

Figure 6.8: (Top Left) Measured Q of the 4, 5 and 6 μm Ge microdisk Fabry-Perot resonances.

Increasing cavity diameters also appears to increase cavity Qs, as shown in Fig. 6.8, which is attributed to the reduction of round trip losses from the 'mirrors'. This trend

is not necessarily the same for whispering gallery modes, which are expected to have much higher Qs and therefore be favoured in lasing applications. No whispering gallery modes could clearly be observed with the surface normal collection of the disks. The Qs demonstrated here are extremely low, but in keeping with Fabry-Perot like modes for micron sized cavities. For instance, using Eq. 6.3 and 6.4, the maximum Q from a Fabry Perot mode directly across the disk diameter of a 6 μm disk is ~ 80.

Further trends from the PL give an insight into the strain in the disks. An increased red-shift with decreasing cavity diameter is observed moving from the 6 μm to 4 μm disks, Fig. 6.7. It can be seen that the resonances at shorter wavelengths become more heavily attenuated in the smaller features, and there is an increased intensity associated with the resonances towards the detector cut-off at 2.5 μm.

The modulation of the spectra by such resonances somewhat obscures the various interband transitions that allow a quantification of strain levels. However, an argument can be made to give an approximation to position of the band-edge, by assuming that absorption is extremely high below the wavelength of (above the energy) of the direct band transition. Both Γ to HH, and Γ to LH transitions are involved in the emission process, but each would represent significantly different transition energies. At high levels of strain, however, and as discussed in Chapter 2, Γ to HH and Γ to LH transitions become highly polarisation dependent; TE modes couple to Γ to HH transitions, while Γ to LH transitions couple to TM modes. Given that modes of both polarisations are present in the disk, it can only be feasible for the first observable resonance to relate to the Γ to HH transition. Otherwise, if it coupled to the Γ to LH transition, there could be TE modes support at shorter wavelengths that were not attenuated heavily by this transition. For the highest strained sample, the resonance at ~ 1.94 μm would suggest strain of ~ 2 %, based on deformation potential theory.

6.4.1 Raman spectroscopy

As detailed in Chapter 5, Raman spectroscopy can be used to calculate the local strain, in the volume set by approximately half the absorption depth of the excitation source, and the spatial resolution of the measurement.

$$\varepsilon_{bi} = \frac{\omega_{strained} - \omega_o}{-424} \tag{6.6}$$

This requires the assumption that the z-component of the strain is coupled to the in-plane strain by the relationship $\varepsilon_{zz} = -(C_{12}/C_{11})(\varepsilon_{xx} + \varepsilon_{yy})$ which results in a strain calculated by Eq. 6.6, where ω_o is the unstrained Raman line ($\sim$ 300.9 cm^{-1}). This can provide useful insight into the strain distribution across the surface, which can be correlated to finite element models to infer the strain state at other regions of the disk. Initial Raman spectroscopy measurements were carried out using a Horiba Jobin Yvon Raman spectrometer, on disks of all diameters. A 50 times objective was used to focus the 532 nm pump to a spot of 3 μm.

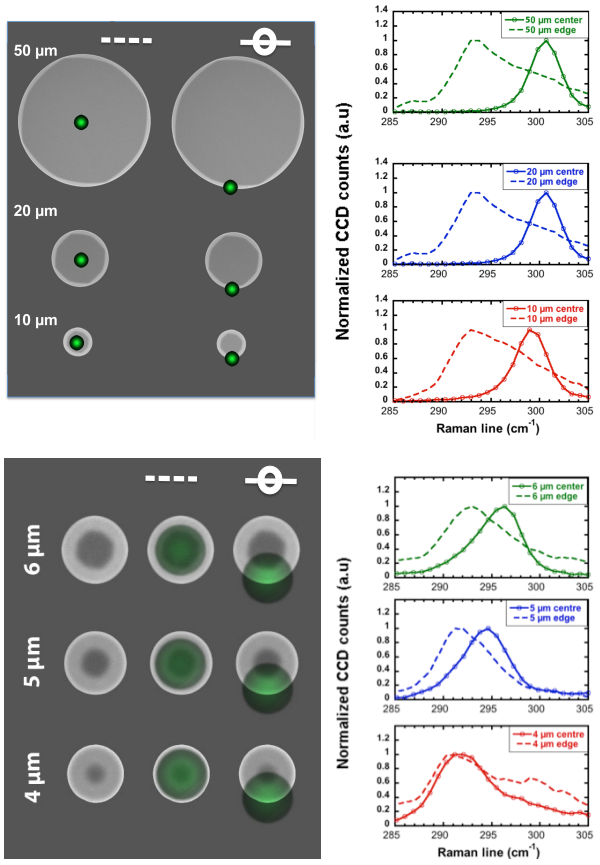

Figure 6.9: Raman spectroscopy measurements taken near the disk edge and in the disk centres, for diameters ranging from 50 to 4 μm. The approximate position of the laser spot is shown graphically, on top of top down SEM images.

As seen in Fig. 6.9, a clear trend is visible across all disks, with increased strain for the smaller disks, as expected. This figure also shows the Raman spectra at the disk edge and

near the disk centre. The approximate position of the spot has been shown graphically in Fig. 6.9, overlying SEM images of all the structures. With the assumption of biaxial strain, this Raman would suggest >2 % tensile strain in the 4 μm disk, which is at the level of strain where a transition to direct bandgap is expected. Interestingly, while the largest disks (20 μm, 50μm) appear unstrained at the disk centre, they showed high levels of strain at the disk edge, up to 1.6 %, where whispering gallery modes would be expected to propagate.

It is evident that particularly for the larger diameter disks, the Raman spectra from the disk edge cannot be fitted with a single Lorentzian. This broadening is due to the fact that the total measured Raman line has contributions from the full area of the pump. The contribution from the Raman line at each position within the spot is weighted by the Gaussian shape of the beam, which in this instance has a full width half maximum of $\sim$ 3 μm. As shown in Eq. 6.7, with the spot centre at position x_o, there are contributions from surrounding locations x', with the appropriate Gaussian weighting. This highlights the need for improved spatial resolutions to allow for strain mapping of the structures.

$$\Delta\omega(x_o') = \frac{\int_{x'} \Delta\omega(x') exp\Big(-2\frac{(x'-x_o)^2}{b^2}\Big)}{\int_{x'} exp\Big(-2\frac{(x'-x_o)^2}{b^2}\Big)} \tag{6.7}$$

6.5 Strained Ge micro-cavities

6.5.1 Sample design

Further different optical cavities were subsequently investigated. Micro-ring and racetrack structures were seen as worthy of investigation as there are various advantages to their use as optical cavities, Fig. 6.10. Waveguide widths can be designed to give single mode operation, and coupler segments to bus waveguides are simplified. Furthermore, larger circumference structures could be used which serve to reduce bending losses, while keeping the reduced lateral dimensions which are important for strain transfer.

Arrays of 4, 5 and 6 μm diameter disks and rings were fabricated in order to allow for low injection PL measurements, and to observe the strain progression as a function of undercut. Furthermore, larger diameter rings and racetrack structures were included on the samples for investigation with a high spatial resolution Raman system. These

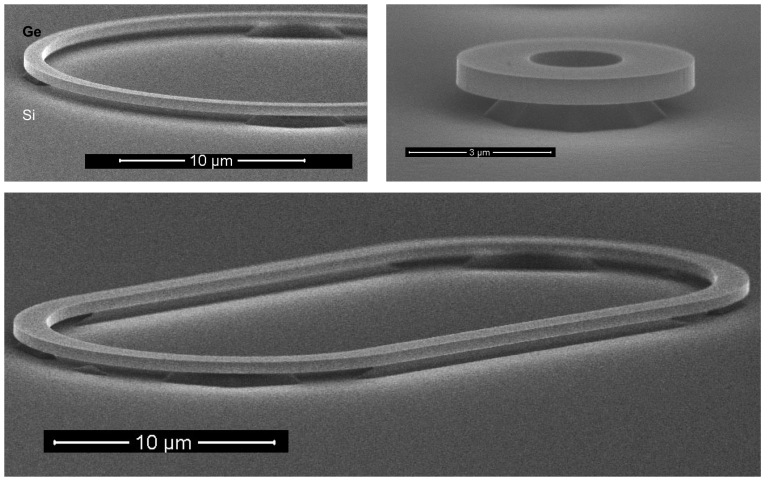

Figure 6.10: Ge micro-cavities undercut by wet-etches. Top Left - Ge on Si microring structure with fully undercut waveguide segments. Top right - 5 μm diameter Ge microring with 1.5 μm waveguide segment. Bottom - Ge racetrack cavity showing partially free standing waveguide segments.

structures had a range of diameters and waveguide widths. The elongated straight sections of the racetrack resonators were orientated along the [100] direction to ensure the increased undercutting described earlier in the chapter.

Three samples were fabricated using the processes described previously. The first sample had a dry etch in a mixed SF_6 and C_4F_8 recipe through the Ge epilayer to the Si, but no wet etch undercut. The second and third samples had identical dry-etches and subsequent wet etches in TMAH to undercut the structures by $\sim$ 625 nm and $\sim$1250 nm respectively. All samples had 20 nm PECVD silicon nitride deposited at 300 °C to promote adhesion for the high stress layer. Subsequently, a 300 nm thick high stress silicon nitride layer was deposited on all samples, in keeping with the saturation of strain transfer measured on previous devices. The stress in the film was measured using the curvature technique described in Chapter 4, and was found to be $\sim$ 2.37 GPa.

6.6 Optical Characterisation

A clear increase in red-shift in the PL is observed with increasing undercut for all cavity structures, Fig. 6.11. The absence of resonances in the ring structures further confirm that the resonances observed in the disks were Fabry-perot like, i.e. predominantly across the

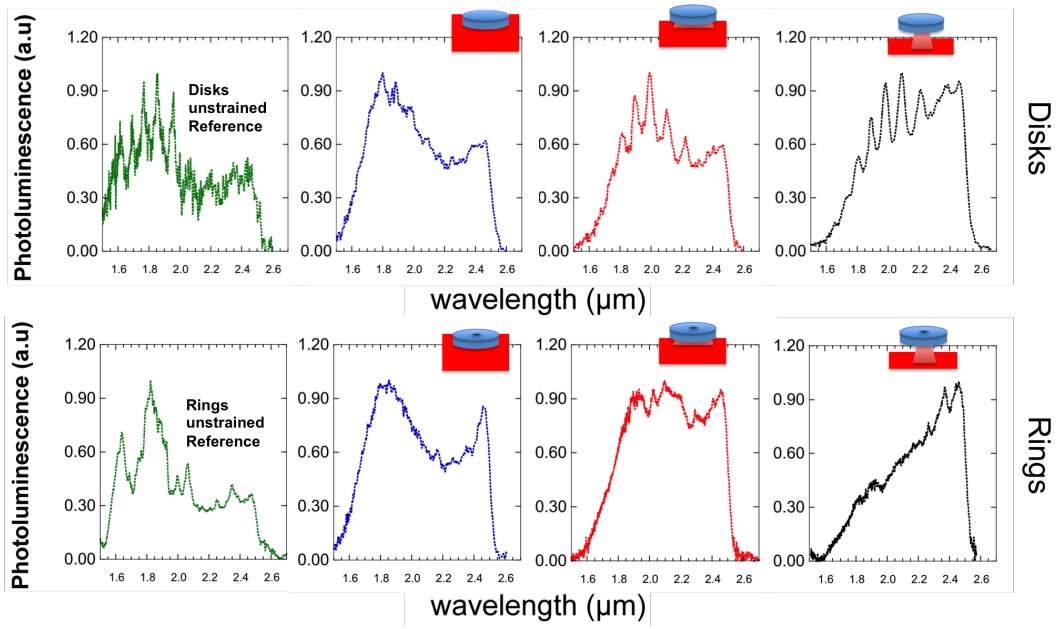

Figure 6.11: Top row - The photoluminescence (PL) from 4 μm Ge microdisks as a function of undercut. The green spectra (left) is without any applied stress. The blue, red and black spectra related to undercuts of 0, $\sim$ 625 and $\sim$ 1250 nm respectively, all with 2.37 GPa, 300 nm thick silicon nitride stressor layers. Bottom Row - same progression as top row, for 4 μm diameter Ge microrings with 1.5 μm thick waveguide segments. The detector cut-off is $\sim$ 2.5 μm. The inset illustrations indicate approximate undercut level.

diameter of the disks. Spectral peaks relating to interband transitions were significantly clearer in ring geometries, and allow another clear means of quantifying the strain in the cavity. In all cases there appears to be a broad stationary peak close to 1.8 μm, which is consistent with L to HH transition, which is insensitive to strain. Partially undercut devices show peaks close to 2.2 μm, indicating strains of $\sim$ 1.5 %. The 4 μm ring with 1250 nm undercut demonstrates a shift of the assumed Γ to LH transition towards 2.5 μm. Using deformation potentials, this would suggest a biaxial equivalent strain of $\sim$ 1.8 %. It should be noted that emission at longer wavelength is no longer observable due to the detector cut-off at $\sim$ 2.5 μm. A greater insight into the strain distributions is discussed in the following sections.

6.7 Raman spectroscopy

6.7.1 Heating

A further investigation was carried out using a Witec 300 Raman system, which can achieve high spatial resolutions of $\sim$ 300 nm. Previous measurements of Ge nanopillars were taken by Witec (Thomas Dieing), however subsequently the system was available for use at the University of Glasgow. This was used to quantify the in-plane strain at the top surface of the micro-cavities. The Horiba system previously used, used neutral density filters to control the laser power, whilst on the Witec system, the laser power is continuously tunable. This allowed for a greater investigation into the heating caused by the laser spot, which causes a red shift in the relative Raman line [142], and therefore could be misinterpreted for strain.

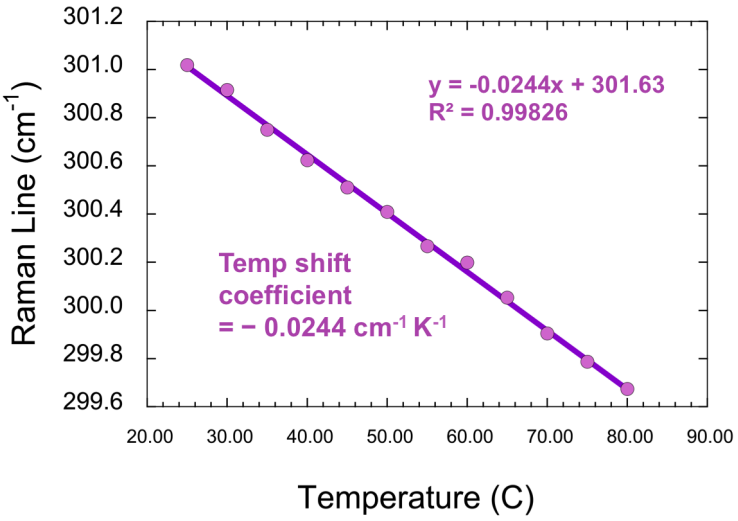

Figure 6.12: Raman spectral position as a function of temperature for bulk Ge.

The sensitivity of the Ge Raman line to temperature is documented in the literature, but was experimentally verified. A peltier cooler was used in conjunction with a calibrated thermocouple, and a Labview program acting as a PID controller, to heat the sample to a stable temperature ($\pm$ 0.1 deg C). The Raman line was then measured with a low intensity pump, which had been confirmed not to shift the bulk Raman line at room temperature. The data points were fitted using a least mean squares method, giving temperature shift coefficients of -0.0244 cm^{-1} K^{-1}. The linear fit is shown in Fig. 6.12.

Undercut, unstrained Ge disks were subsequently measured with various pump powers. At levels of power where the disks could be feasibly mapped (i.e using an 100 times objective, with integration times per pixel of < 10 seconds), regions at the disk edge showed Raman spectra of ~ 300.5 cm^{-1}, implying a local temperature increase of ~ 20 °C, which leads to a potential overestimation of the biaxial strain by 0.001 (i.e. 0.1 % strain), which is well within the uncertainty given by the range of Raman phonon deformation potentials in the literature, and is therefore seen to be an acceptable error on the strained samples. It should be noted that the Raman shift coefficient used here -424 cm^{-1} is the most conservative quoted in literature (-415 cm^{-1} and 390 cm^{-1} are also quoted [9, 10]).

6.7.2 Strain progression

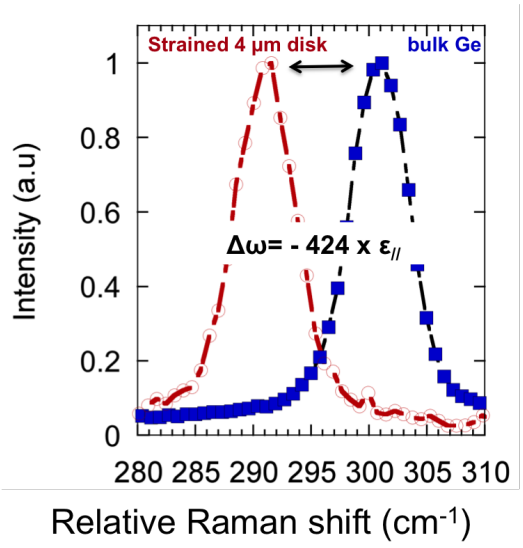

Figure 6.13: Raman spectra from a 4 μm disk with a 2.45 GPa stressor showing a large shift of ~ 9.9 cm^{-1}. This corresponds to a biaxial tensile strain of ~ 2.3 %.

All of the strained samples were subsequently analysed, using a 100 times objective with a 0.9 NA to focus the 532 nm Nd:YAG to a diffraction limited spot. The 4 μm disk with 2.45 GPa stressor, for which the PL was shown in Fig. 6.7, demonstrated large Raman shifts of ~ 9.9 relative cm^{-1} Fig. 6.13. Compared to the previous measurement of the sample on the Horiba system, the spatial resolution of the system allows for clear

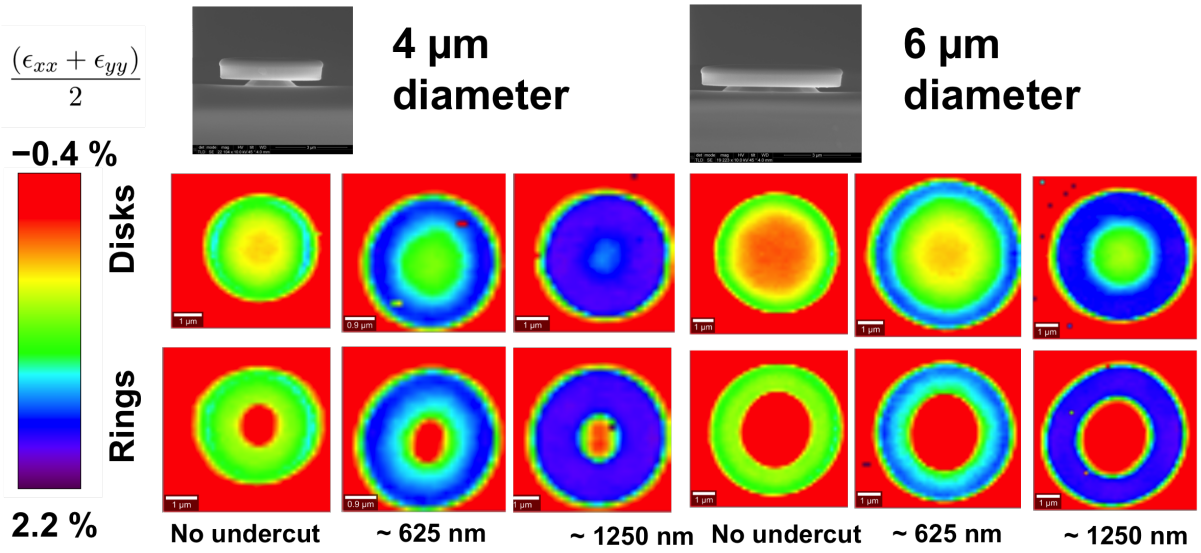

Figure 6.14: Raman maps showing the in-plane strain of 4 and 6 μm diameter Ge disks and rings stressed by 2.37 GPa silicon nitride stressors. The undercut and cavity type is indicated on the plot.

Lorentzian peaks, with comparable full width half maxima compared to the measured Raman line of epitaxial layers. Assuming the biaxial approximation outlined previously, this would suggest in-plane strains of 2.3 %, when using $\varepsilon_{bi} = \Delta\omega/-424$. Approximation of the band-edge from PL measurements suggested strains of $\sim$ 2 %, which is therefore in good agreement with the Raman measurements. Small discrepancies are expected when comparing Raman measurements to PL on structures with strain gradients in the vertical direction. Carrier diffusion in PL will result in recombination throughout the structure, therefore probing a larger volume compared to the Raman measurement, where the scattered pump will undergo significant self-absorption, and therefore only constitute a measurement of the top surface ($\sim$ 10 nm).

The trend of increasing in-plane strain at the top surface with increasing wet etch undercut is shown by the Raman measurements in Fig. 6.14, for the 4 and 6 μm diameter disks and rings. Even with no undercut, there are in-plane strains of greater than 1 % observed at the top plane, which is perhaps of interest for electrically contacted devices where an undercut could pose issues for electrical injection.

From Raman spectroscopy measurements there are trends observable with regard to the in-plane uniformity. For the 4 μm diameter cavities this is clearest when viewing a

histogram of the spectral position of the Raman line, Fig. 6.15. The increasing undercut clearly leads to a more homogeneous strain distribution at the top plane, as well as an increase in the peak level of strain. In both these geometries, the Raman shift for the fully undercut structures is comparable, indicating a biaxial tensile strain of ~ 2 %. This agrees well with the PL measurements which inferred strains of ~ 1.8 %.

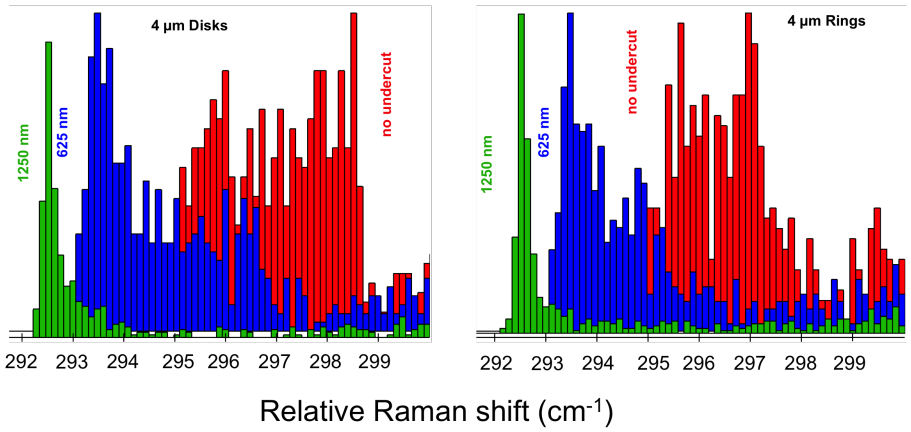

Figure 6.15: Histograms of the spectral position of the Raman lines across 4 μm diameter disks and rings, for varying undercut. All features with 2.37 GPa silicon nitride stressor layers.

For a larger diameter structure, such as the 6 μm diameter cavities shown in Fig. 6.14, there is an observable difference between the disks and the rings. This is particularly evident for the highest undercut structures, the histogram of which is shown in Fig. 6.16. Over the area formed by the ring structures, there is increased strain compared to a comparable area on the disks. This is due to the reduced deformation resistance of the waveguide segment compared to the microdisks, and could be advantageous for modal gain in strained Ge lasers. However the slightly more subtle effects of the strain distribution on the band structure have to be taken into account, which is discussed later in the Chapter.

The trend of in-plane strain with increased ring diameter was further examined using non-undercut structures so as to eliminate any influence from the wet-etch step. Rings with constant waveguide widths but varying diameter were measured. Given the constant width, it might be intuitive to expect comparable strain levels with little dependency on the diameter. This was found not to be the case, and as shown in Fig. 6.16, there was a trend of decreasing strain with increased diameter. This has been attributed to the

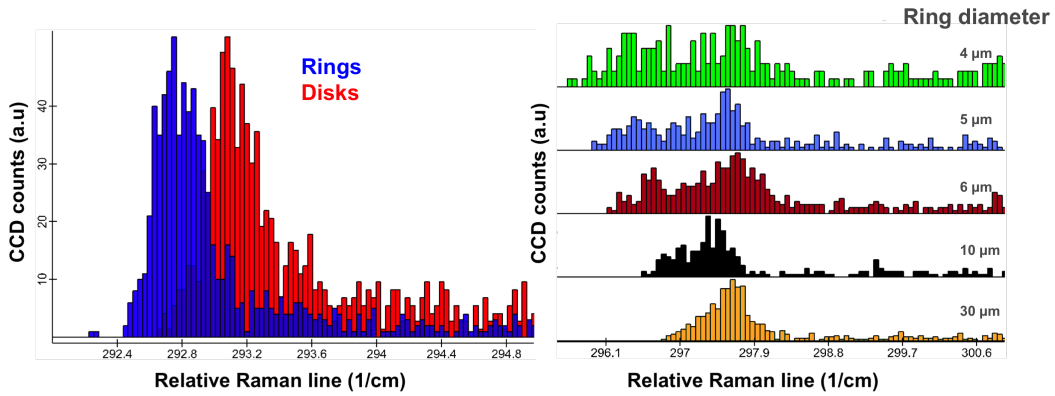

Figure 6.16: Left - Histogram of the measured Raman line across strained 6 μm diameter disk and ring cavities. The ring has a 1.5 μm waveguide width. Both structures had the same wet etch step and high stress silicon nitride layers. Right - Histograms for rings of varying diameter with no undercut and constant waveguide width of 1.5 μm. This shows the trend of decreasing in-plane strain with increasing diameter.

change in stress transfer in the structures. For smaller diameters, the silicon nitride can transfer strain both transverse to the waveguide segment, and along the waveguide length, which, due to the small radius is effectively small, and therefore leads to a near biaxial strain. For larger diameters the stress transfer is dominated by the uniaxial component transverse to the waveguide segment, as the longitudinal strain becomes impeded by the length of waveguide segment, which is effectively increasing with larger diameters. This results in a strain profile similar to that in straight waveguides. This trend is discussed further in the Finite Element Modelling section.

6.7.3 Racetrack structures

The straight waveguide segments of Racetrack structures were measured by Raman spectroscopy. Peak strains of $\sim$ 1.3 % were measured for 1 μm wide waveguide segments in fully released sections. The strain from Raman has been calculated assuming a biaxial approximation, despite some groups using uniaxial approximations for waveguides. While the in-plane strain is predominantly transverse to the waveguide length, there is not the associated compression parallel to the waveguide length, meaning that uniaxial models are not appropriate.

$$\Delta\omega = \frac{(\varepsilon_{xx} + \varepsilon_{yy})}{2} \frac{1}{\omega_0} [-p\frac{C_{12}}{C_{11}} + q] \tag{6.8}$$

As shown in Eq. 6.8 (a less simplified expression for the biaxial Raman shift), the measured Raman line is for the average of the in-plane strains, which is in effect the biaxial equivalent strain [147]. This approximation holds as long as the strain in the z-direction is coupled to the in-plane components by Poisson's ratio. These assumptions used for interpreting the strain in straight waveguides in other works [147].

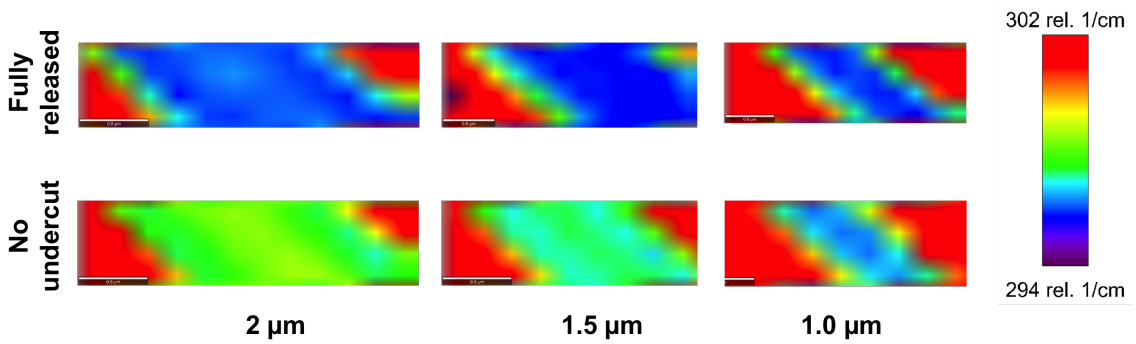

Figure 6.17: Raman spectroscopy maps of straight waveguide segments on strained racetrack resonators. The waveguide width, and the level of undercut is shown on the figure.

Figure 6.17 shows that the strain of fully undercut structures showed little dependence on the waveguide width, suggesting that strain levels have begun to reach a saturation point. This was not the case for waveguides segments with no undercut, also shown in Fig. 6.17. These structures are likely more appropriate for partially relaxed GeSn layers, where reduced strain is required. This would allow for devices with a narrow Si post directly underneath the gain medium, which improves heat-sinking, and could in principal be used for electrical injection. Furthermore, racetrack cavities could be coupled easily to bus waveguide. Interestingly, strained Ge emission could potentially be guided in unstrained Ge bus waveguides, if emission is past 2 μm wavelength [73].

6.8 Finite Element Modelling

As discussed in Chapter 5, the strained Raman line reflects the in-plane strain, as shown in Eq. 5.8. However, this is under the assumption of zero shear strain, and a strain in

the z-direction coupled to the in-plane components by Poisson's ratio. As for the pillar structures therefore, finite element modelling (FEM) is required to give a further insight into the strain distribution, which is inaccessible by experiment using the techniques in this work.

A cross sectional TEM image of a 4 μm disk with a 2.45 GPa silicon nitride stressor had been taken using the method described in Chapter 5 (Aneeqa Bashir), Fig. 6.18. The curvature observed (150 nm vertical displacement at the disk edge) was used to calibrate finite element model. The model has the X and Y directions are orientated along $\langle 100 \rangle$ crystallographic directions, and includes the anisotropy of the Ge elasticity tensor, also shown in Chapter 5. When the vertical displacement matched that of the TEM, the in-plane strain at the top surface was found to be ~ 2.1 %, which is in excellent agreement with the Raman and PL measurements, confirming the self consistency of the model. Furthermore, the modelled in-plane strains for varying undercuts were also in good agreement with experimental results.

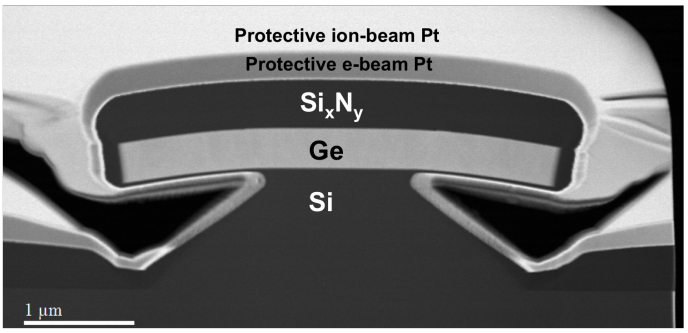

Figure 6.18: Transmission electron microscope image of a 4 μm Ge microdisk with 2.45 GPa stressor layer.

6.8.1 Strain distribution of Ge disks

The nature of the top plane strain from a silicon nitride stressor to a 4 μm Ge disk is shown in Fig. 6.19. The ratio of ε_{xx} to ε_{yy} is plotted to indicate where regions of the disk are biaxially strained, and where there is a move to more uniaxial-like strains. It can be seen that large portions of the disk are close to biaxial with $\varepsilon_{xx} = \varepsilon_{yy}$, however this moves to a more uniaxial strain in the radial direction towards the disk edge, and around the post segment. This radial strain component moves periodically from the [100] (X or Y)

to the [110] round the disk circumference. When this strain component is aligned to the [100] direction, it is aligned to the axes of the cubic crystal, and therefore the material is uniaxially expanded but the tetragonal symmetries remain. In the [110] directions, however, the ε_{xx} and ε_{yy} strains are approximately equal, but cubic or tetragonal symmetry is broken as the unit cell is sheared. The stress and strain tensors for this configuration were given in Chapter 2. The ε_{xy} shear component is shown in Fig. 6.19.

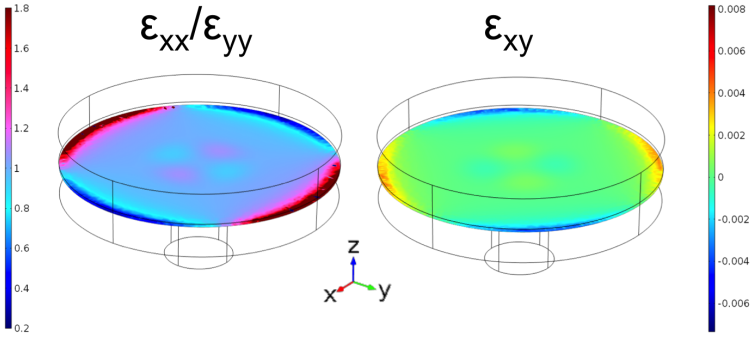

Figure 6.19: COMSOL Multiphysics models of 4 μm Ge microdisks with high stress silicon nitride layers. A 2D slice of the 3D model is shown. The left image shows a colour map of the ratio of ε_{xx} to ε_{yy}. The right image shows the shear strain, ε_{xy}, present at the edge of the disk. The model includes the anisotropy of the Ge elasticity tensor. X and Y directions are orientated along $\langle 100 \rangle$ crystal planes. Image published in [14].

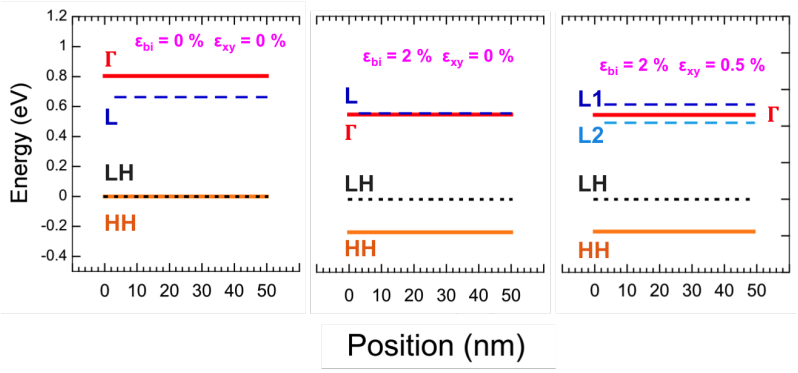

Figure 6.20: Illustration of the band edges for various strain conditions. The inclusion of ε_{xy} shear strains is shown to split the L valley.

This has ramifications for the band structure, which is illustrated in Fig. 6.20. Applying purely biaxial strain moves the bands in accordance with the deformation potentials

shown in Chapter 2, however the inclusion of off diagonal shear strains lifts the degeneracy of certain bands. In the case of Ge, The L-valley lies in the ⟨111⟩ directions, which has glide reflection symmetry. For Ge therefore, ε_{xy} shear strain lifts the degeneracy of the L-valleys, with half of the band reducing in energy and the other half raising to higher energies.

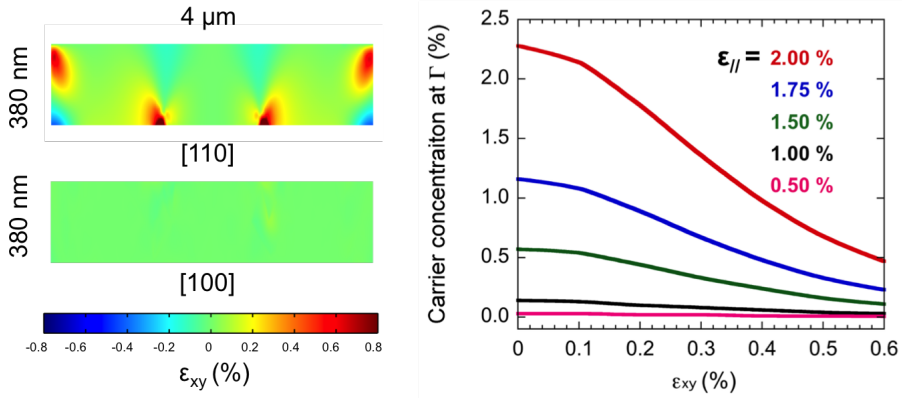

Figure 6.21: Left - vertical 2D slices of a finite element model of a strained 4 μm diameter Ge microdisk. Two orientations are shown to highlight the presence of shear strains due to uniaxial strain components in the [110] directions. Right - The carrier concentration at the Γ is shown, expressed as the percentage of the total conduction band concentration. This is shown for a range of biaxial strains, as a function of the ε_{xy} tensor component. Image published in [14].

This can lead to severe degradation of the concentration of electrons at the Γ point, which as discussed in Chapter 2 is crucial to obtaining population inversion. It should be noted that the carrier occupation calculated by Fermi-Dirac statistics is multiplied by the band degeneracy, therefore the shear strained, split L-valley at low energy is not as detrimental to carrier concentration the Γ as a fully four-fold degenerate band at that energy.

In order to investigate the presence of shear away from the top plane, cross sectional slices were examined in the 4 μm disks, parallel to the ⟨100⟩ and ⟨110⟩ directions, Fig. 6.21. As expected, where the uniaxial strain component is aligned to the [100] direction, there is negligible ε_{xy} shear strain. In the ⟨110⟩ directions there are significant shear strains which extend inwards from the disk edge. The effect of these shear strained regions will of course depend on the modal overlap with the strain field, but should be considered when

calculating the optical gain achievable in such cavities. While this effect had been noted for straight waveguide segments, it has so far been neglected when considering circular cavities. The shear strained regions at the disk edge have ε_{xy} values predominantly between 0.3 and 0.5 %.

The effect of the shear strain on the Γ carrier concentration was calculated using nextnano3. Fig. 6.21 shows the ratio of the electrons in the Γ to the L, as a function of ε_{xy}, for a range of biaxial strains. As an example, it can be seen that for $\sim$ 0.4 % ε_{xy} there would be a carrier concentration reduction of $\sim$ 60 %. This effectively moves the material from being direct to indirect.

It should be noted that the Raman secular equation shown in Chapter 5 was solved to determine if the levels of shear strain present at the top plane were significant enough to change the measured Raman spectra. This was found not be the case, as the in-plane components dominate to the point where the additional shearing negligibly changes the Raman shift.

6.8.2 Ring Resonators

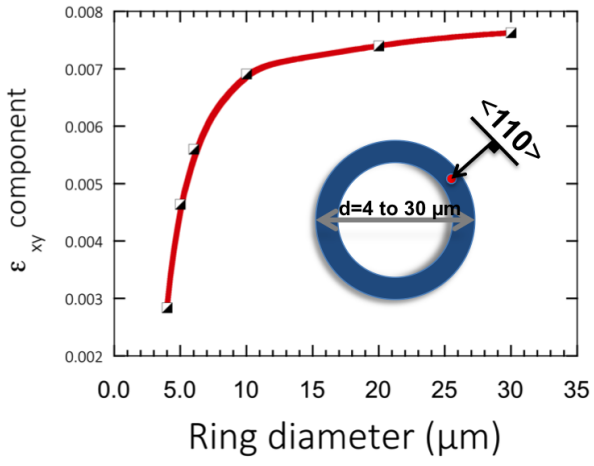

Figure 6.22: Calculated ε_{xy} shear strain component from finite element models of strained Ge ring resonators. The extracted tensor component is from the midpoint of the waveguide segment with a tangent in the ⟨110⟩ direction. The point probed is 100 nm from the top surface

A range of ring structures with no undercut were modelled in order to observe the effect

of increasing the diameter on the strain distribution. Finite element models show that as the diameter is increased, the strain transverse to the waveguide segment dominates the tangential strain, Fig. 6.22. This confirms the trends observed with Raman measurements shown in Fig. 6.16. This increased transverse strain exacerbates the ε_{xy} shear component, which was found by finite element modelling to scale with increasing ring diameter, when calculated at a point with a tangent in the [110] direction, Fig. 6.22. This highlights that despite apparent advantages such as reduced bending losses, small disks structures are most appropriate where high levels of strain are required.

6.8.3 Vertical strain gradient

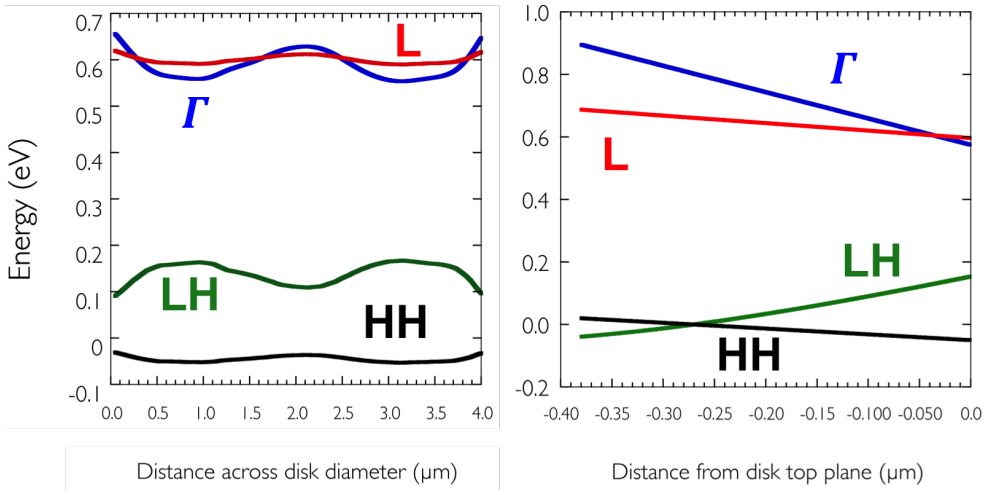

Figure 6.23: Left - Band structure calculated from the strain trace measured by Raman spectroscopy, across the diameter of a 4 μm disk a compressively stressed silicon nitride layer with a stress of 2.45 GPa. Right - Band energies as a function of depth in a strained 4 μm diameter Ge microdisk, based on a finite element model from COMSOL multiphysics.

For the highest strained cavities demonstrated here, strains have been measured at the top plane which indicate a transition to direct-bandgap is likely. This is backed up by the recent results of El Kurdi et al., who showed by low temperature PL that disks with an average strain of 1.67 % have approximately degenerate Γ and L valleys [99]. For the highest strained 4 μm disk, the band-structure was calculated based on the strain trace from Raman measurements, and is shown in Fig. 6.23. Even when using more conservative

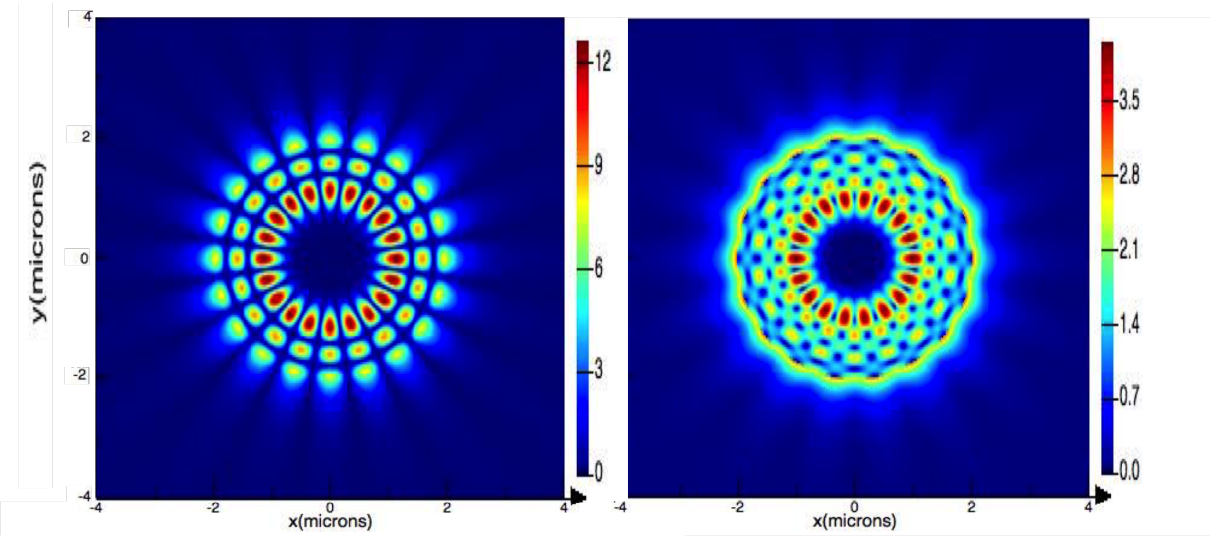

Figure 6.24: Whispering gallery modes for TM and TE polarisations, in a 4 μm Ge microdisk, at a wavelength of 2.4 μm. Modes were calculated in Lumerical FDTD solutions.

deformation potentials, reported in Chapter 2, there are clearly regions that should be direct bandgap.

An issue with single layer stressors however, that cannot easily be mitigated, is the high vertical gradient caused by the stressor. The band-edges were computed as a function of depth in a 4 μm diameter strained Ge disk, Fig. 6.23. The strain components were extracted from finite element models using Comsol multiphysics, from a vertical line segment at a point 0.75 μm inwards from the disk edge, where the ε_{xy} shear component is negligible, and where the in-plane strain was at its highest. Clearly a gradient is present, with the lower region of the disk actually under compressive strain. This is unavoidable without the use of a bottom stressor, which unfortunately, inherently cannot be used for future electroluminescence (EL) compatible devices. The disks presented here, however, demonstrate significantly higher strains compared to other disks with top only stressors [171] [10]. In reference [10], it was shown that modal gain is theoretically possible with top only stressors, with a strain of only $\sim$ 1.3 % at the top plane. In the structures here, the top $\sim$ 170 nm is above 1 % biaxial tensile strain. A finite difference time domain method was used to calculate the whispering gallery modes of a 4 μm diameter, 380 nm thick Ge disk. The Fourier transform of the time dependant E-field is used to calculate the spectral position of the resonances. The model uses the dispersion curves for unstrained

Ge and therefore does not include changes to the refractive index due to strain. TM and TE modes at 2.4 μm wavelength are shown in Fig. 6.24, highlighting that higher order modes, with a wavelength close to that of the band-edge should propagate near the highest strained regions of the disk, and where ε_{xy} shear strains are negligible.Such structures should therefore be capable of exhibiting modal gain, in theory, however a more rigorous analysis of the total modal gain is required, which is detailed in the Conclusions and Future work chapter. To investigate this experimentally, material with significantly lower threading dislocation densities (TDD) will be required, as defective Ge on Si layers have been shown to have excess carrier lifetimes of $\sim$ 1 ns, making population inversion extremely challenging, as the carrier concentration is expressed as $\Delta n = G\tau$ where G is the generation rate and τ is the excess carrier lifetime.

There is potential to design cavities which increase the modal overlap in the vertical direction with the higher strained regions of the disk. SiGe layers with Ge contents above 75 % remain highly selective to TMAH etching [172], and would potentially allow for the lower half of the disk to be transparent to the optical mode, with a reduced index that serves to push the mode higher into the strained Ge region. Furthermore, something that has not been considered in literature is the increased index of highly tensile regions of Ge. Through Kramers-Kronig's relationship, the increased absorption can be seen to translate to an increased index. This has been exploited in Ge Mach-Zehnder modulators, where one arm has been strained by a piezoelectric stressor [100]. This could potentially lead to preferential guiding of light in the higher strained regions of the disk. There also scope to reduce the losses from the compressively strained lower region of the disk by n-type doping only the upper portion of the disk. This would reduce additional free carrier losses from a region of the disk where it can be accepted that no gain will occur. Such devices should be the focus of future work.

6.9 Discussion

As shown previously in Fig. 6.21, when computing the carrier concentration at the Γ as a function of biaxial strain, there is no dramatic change when moving from indirect to direct bandgap at room temperature, as the large density of states of the L valley holds $>$ 97 % of the conduction band carriers. However, similarly to Chapter 5, the large intensity increases associated with increased strain were not observed. Similar arguments with

regard to the TM polarisation of the emission can be applied, but with such large tensile strain it was expected that a substantial increase would be visible.

Fabrication was repeated on GeOI material (Andrea Ballabio - L-Ness, Politecnico di Milano), which has negligible threading dislocations due to the growth of Ge on lattice matched GaAs. Undercut etches were carried out using buffered HF and 300 nm thick silicon nitride stressors were deposited. Similarly to the 4 μm Ge on Si disks with 2.45 GPa stressors, emission was observed towards the detector cut-off, and Raman measurement showed strain of $\sim$ 2 % at the top plane. The change in emission intensity was also found to be minimal, which effectively rules out the possibility that the high TDDs of the Ge on Si material were having a significant detrimental effect on the strained emission. The lack of increased intensity is therefore attributed to electronic properties of the stressor and adhesion promoting silicon nitride layers, which were discussed in Chapter 5. This is further discussed, and addressed in Chapter 7.

The structures demonstrated in this work have peak strains at the top plane higher than reported elsewhere, by using silicon nitride stressor technologies. With regard to other reports of disks with single layer silicon nitride stressors, the highest shown to my knowledge has been 1.3 % strain at the top plane [10]. This has been exceeded in doubled bonded structures, using a process described in Chapter 3, which showed strain of $\sim$ 2 % by Raman spectroscopy, in 200 nm thick Ge layers [99]. These devices however, used Au in the flip-chip bonding process, highlighting that such process flows could not be used for CMOS integration. The top 200 nm region of the disks demonstrated here, have comparable strain distributions to the double bonded structures, suggesting that if increased modal overlaps with the upper disk segment could be achieved, there should theoretically be comparable gains achievable. This is discussed in the Future work section. Other demonstrations of highly strained microdisks have 0.7 % biaxial strain, albeit with improved uniformity from bonding to a SiO_2 layer [8] and more recent results have shown 1.1 % by releasing SiO_2 membranes on the underside of Ge disks transferring moderate tensile strain [173].

For the highly strained micro-cavities, it was found that the PL showed better agreement with Raman measurement when neglecting the effects of bandgap narrowing (BGN) from doping. In the literature, it is not consistently considered when determining strain from PL. Simplistically, the phenomena stems from the impurity band formed from dopant ions, which reduces the band-gap by electron impurity interactions [174]. Phosphorous

doping results in a shallow impurity state, 12 meV below the L-valley in unstrained Ge however, there appears to be no reports of how this changes with strain, and therefore how the BGN is altered. It is possible that the effect has been somewhat absorbed into the determination of deformation potentials from experiment. As an example, a Γ to LH transition at 2.5 μm would suggest biaxial tensile strain of $\sim$ 1.8 %, and if subtracting 32 meV BGN from doping this would reduce to $\sim$ 1.6 %. A further investigation, comparing otherwise identical disks with different doping levels would be required to further clarify this.

6.10 Conclusion

CMOS compatible, undercut Ge micro-cavities, including disks, rings, and racetrack structures were fabricated using a combination of dry etching, and wet etching in TMAH. The wet etch step allows the Ge layer to act as the mask, and therefore simplifies processing. Furthermore, the anisotropy of the wet-etch allows the fabrication of partially free-standing structures. Undercut cavities were subsequently coated with a high stress silicon nitride layer in order to move the band-structure closer to direct bandgap. In-plane strains of up to $\sim$ 2.3 % were measured in the highest strained cavities, which showed photoluminescence towards the detector cut-off, of 2.5 μm. The in-plane strain was then experimentally shown to increase with increasing undercut, by both Raman, and PL measurements, on both disk and ring cavities. Analysis of the in-plane strains by Raman spectroscopy gave an insight into the apparent benefits of micro-ring structures, in terms of increased uniformity, and increased strain transfer at the top plane. Raman measurements also revealed the trend of biaxial to uniaxial stress transfer from small circumference (4 μm) to larger circumference (30 μm) rings with constant waveguide size. Analysis of a disk structure by finite element modelling showed a uniaxial stress transfer in the radial direction at the disk edge, which moves periodically from the [100] to [110] directions. It was found that in the [110] directions shear strains are induced with respect to the Ge unit cell, which serve to reduce the carrier concentration at the Γ, and would therefore reduce available gain. The presence of such effects in circular strained micro-cavities has not been reported elsewhere. These effects are also present in ring cavities, and increase for increasing ring diameter. It is shown that racetrack structures can be fabricated using identical processing techniques, with waveguide segments aligned to the

[100] directions to avoid these shear strain components. While these structures have reduced levels of strain, there are further advantages such as improved heat-synching and ease of electrically contacting strained cavities, which may be applicable to both Ge and GeSn material systems.

While the enhanced emission properties expected with strain were not observed, the technique has demonstrated that strains upward of 2 % are achievable with single layer silicon nitride stressors. There is potential to integrate thermally grown oxides or alternative passivation layers to improve the surface recombination, and from comparison to other works in the literature, the structures should theoretically be capable of exhibiting gain, with improved passivation and reduced TDDs.

7

Tensile Strained GeSn alloys

7.1 Introduction

As introduced in Chapter 2, alloying Ge with Sn was predicted to be an approach to obtaining a direct-bandgap material. The predicted Sn content for this transition, however, varied substantially, from as little as 6.3 % [103] to 21 % Sn [101]. A number of challenges existed in obtaining concentrations even at the level of the lower bound. There is a large lattice mismatch ($\sim$ 14 %) between the two materials, which along with a solid solubility limit of $\sim$ 1 % α-Sn in Ge, made obtaining the required Sn concentration impossible with equilibrium growth conditions.

As discussed in Chapter 3, a number of techniques had to be employed in MBE and CVD systems to solve such issues, but their development has lead to a resurgence in the scientific interest of GeSn alloys. In 2015, the incorporation of Sn up to 12.6 % [11] in device grade layers was achieved, showing bright photoluminescence, and lasing at emission wavelengths of 2.34 μm at 20 K. Wirth et al. used a low temperature photoluminescence technique to confirm that these layers possess a fundamental direct bandgap, which was the first experimental verification of a direct bandgap in a Group IV material. A range of lower Sn concentrations were also investigated in this work, all of which had residual compressive strains, which serves to counteract the effect of the Sn alloying, moving the Γ to higher energies and making the material more indirect. While only the 12.6 % Sn sample was found to have a direct bandgap as grown, they calculated that GeSn layers with greater than 9 % Sn will also be direct when extrapolating their results to fully relaxed alloys.

Lasing was demonstrated in straight waveguides using the thickest 12.6 % GeSn layers at temperatures ranging from 20 - 90 K, however thermal quenching was observed which was in part attributed to the small Γ to L valley separation, as well as the Shockley-Read-Hall (SRH) recombination [127]. Furthermore, the waveguides were unpassivated, meaning there is significant scope to improve these promising results, with the ultimate goal being the demonstration of a room temperature laser.

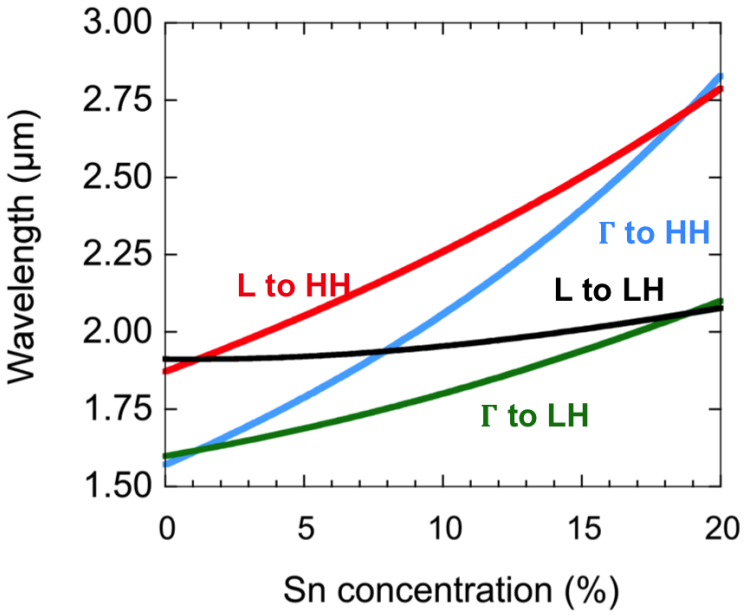

Figure 7.1: Calculated emission wavelengths of GeSn alloys of varying concentrations. The layers modelled are pseudomorphically grown on Ge virtual substrates (VS) and are therefore compressively strained.

When growing GeSn on Ge virtual substrates, there is an inherent need for strain relaxation in order to reach a direct bandgap. This can be seen from Fig. 7.1, which shows a transition to direct bandgap at $\sim$ 19.5 % for fully compressive pseudomorphic GeSn layers. These Sn contents are well above what has been achieved for device grade layers, with current growth techniques. For this calculation, the bandgap and lattice bowing parameters used by Wirth et al. [11] have been used for the GeSn bandgaps and the effect of the compressive strain from pseudomorphic growth has been taken into account using a linear extrapolation of the Ge and Sn deformation potential constants, and the elastic coefficients. A small, 0.18 % tensile strain in the Ge virtual substrate has

been assumed.

These calculations highlight that for such layers, strain engineering is critical in creating a direct bandgap material. It is highly desirable, however, that compressive strain relaxation occurs by other means other than misfit formation. More complex growth schemes can be used in order to produce a virtual substrate with a lattice constant more closely matched to the GeSn alloy. For instance, SiGeSn ternary alloys could be used as a virtual substrate, which can combine the desired properties of having a larger bandgap than the active layer, and a similar lattice constant. However, in order to lattice match the two layers a larger Sn concentration would be required in the VS than in the active [175]. Furthermore, the optical properties of SiGeSn ternary alloys demonstrated so far have been poor.

The application of external stress can be used to relax compressive strains and even induce tensile strain in fully strained or partially relaxed GeSn alloys. The band structure of GeSn changes with strain in a similar manner to Ge, except with the advantage that the Γ-valley is already considerably closer to the L when relaxed. This could allow for lower Sn concentrations with better thermal stability and lower misfit densities, but while still moving the material to direct bandgap. Furthermore, there is also the possibility of starting with higher Sn concentrations, and straining the material to create a source operating in the mid-infrared. While the long term goal may be the realisation of strain balanced GeSn/SiGeSn multiple quantum well (MQW) structures with tensile GeSn wells, silicon nitride stressor technologies allow significant scope for investigating and demonstrating the potential for tensile strained GeSn alloys.

In this chapter, the potential of this approach is demonstrated, as two highly compressively strained GeSn on Ge layers are strained to become tensile. This is a significant result, as alloys that are inherently indirect as grown, are made direct bandgap by strain engineering, without the formation of dislocations which are known to degrade non-radiative lifetimes. Such technologies are extremely applicable to rom temperature GeSn lasers. Initially, the as grown epilayers are characterised by low temperature photoluminescence, Raman, and XRD. For each alloy, a range of undercut resonant cavity structures were fabricated, as in Chapter 6. The structures are undercut and silicon nitride stressors are deposited to apply tensile strain. The strained cavities are characterised by photoluminescence and Raman spectroscopy, and tensile strained GeSn layers emitting > 3 μm are demonstrated. To my knowledge, there has so far been no other demonstration of

GeSn emission in the mid infra-red (MIR) past 2.6 μm [130]. It is shown that the emission of such structures has a good overlap with the methane absorption spectra, further highlighting the potential for such materials as sources for MIR gas sensing.

7.2 Growth

A commercial ASM Epsilon 2000 reduced pressure chemical vapour deposition (RP-CVD) tool was used to grow nominally undoped, 40 nm thick GeSn epilayers on Ge virtual substrates (Maksym Myronov - Warwick University). Firstly, a 650 nm Ge virtual substrate (VS) layer is grown on a (100) Si substrate, using the two temperature growth technique described in ref [149]. The VS is thermally annealed at 830 °C in order to minimise threading dislocations. In doing so, the anneals cause a small tensile strain to accumulate in the Ge layer due to the difference in the thermal expansion coefficients of Ge and Si. The TDD of VSs from the same growth system have been measured by using decorative etching, with atomic force microscope (AFM) scans to count the pits, resulting in TDDs of $\sim 2.85 \times 10^7$ cm^{-2}.

Following this, GeSn layers were grown on the Ge VSs using digermane (GeH_6) and tin-tetrachloride ($SnCl_4$) in a hydrogen atmosphere, at pressures below 100 Torr.

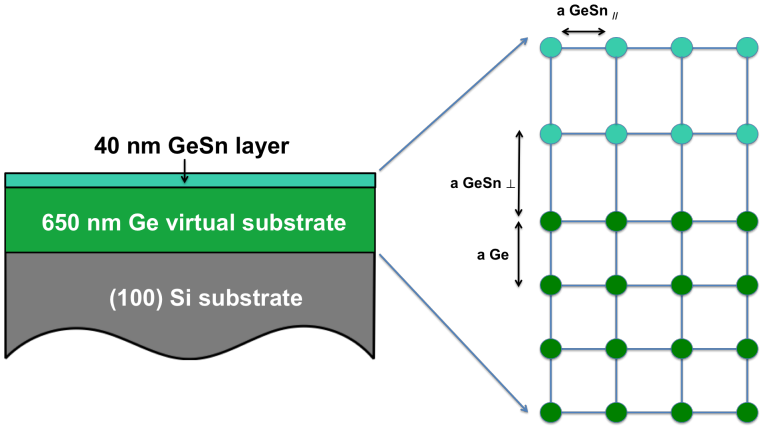

Figure 7.2: Illustration showing the wafer structure for the GeSn alloys used in this work. The resulting compressive strain from the growth on Ge virtual substrates is shown.

The growth of the GeSn alloys is done at low temperatures < 350 °C, in order to prevent Sn diffusion and precipitation to β-Sn. In order to ensure high quality GeSn layers

with minimal dislocations, the samples were grown below the critical thickness [176]. The larger lattice constant of GeSn alloys compared to the Ge virtual substrate leads to a compressive strain in the layer, as shown in the illustration in Fig. 7.2.

7.3 Material Characterisation

7.3.1 X-Ray diffraction

Two different Sn concentrations were grown, and the material was characterised by X-Ray Diffraction reciprocal space mapping XRD-RSM about the (224) reflection (Maksym Myronov, David Pratchet - University of Warwick). Measurements showed that the GeSn layer is fully strained, and pseudomorphic on the Ge VS. Omega-2-Theta (004) reflections (Fig. 7.3) were subsequently taken at a later date (Ross Millar, Derek Dumas, Matt Steer) which provide accurate measurements of the out of plane lattice constant, and confirmed that no relaxation had taken place for the layers since growth. The material's elastic coefficients can subsequently be used to calculate the in plane strain of the Ge, which was found to have an in-plane tensile strain of 0.182 %, which is typical for the thermal anneal cycles used (830 °C).

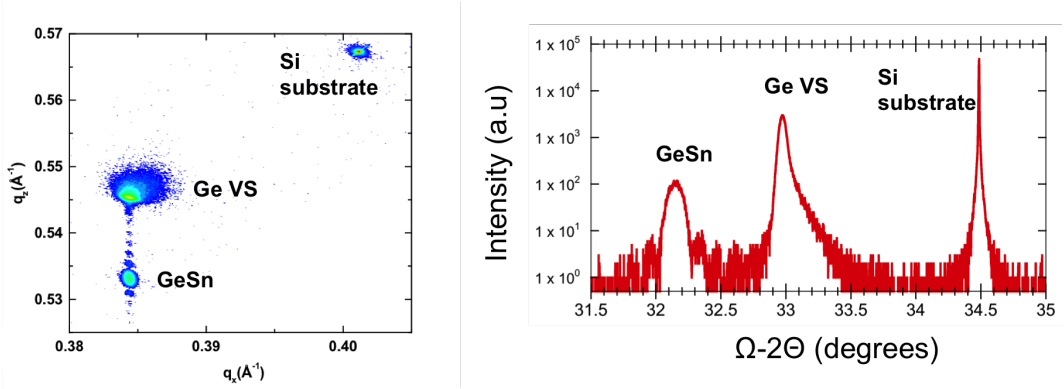

Figure 7.3: Left - X-ray diffraction reciprocal space maps about the (224) reflection showing pseudomorphic growth of GeSn on the Ge virtual substrate (VS). Right - omega-2-theta (004) scan of GeSn on a Ge VS on a Si substrate.

$$a_{bulk} = \frac{a_{\perp} - \mu a_{\parallel}}{1 - \mu} \tag{7.1}$$

Using the omega-2-theta scans, the in-plane and out of plane lattice constants of the GeSn layers were measured, and the bulk lattice constant is then calculated based on the elastic constants, using Eq. 7.1, where $\mu = -2C_{12}/C_{11}$. This can then be used to determine the Sn concentration in the alloy, by comparing it to the theoretical bulk lattice constant, $a\_Ge_{1-x}Sn_x$, which is given in Eq 7.2, where a_Ge and a_Sn are the Ge and Sn lattice constants respectively, and b_{GeSn} is the lattice bowing parameter. A lattice bowing of -0.0041 nm has been used [176].

$$a\_Ge_{1-x}Sn_x = (1-x)a\_Ge + (x)a\_Sn - x(1-x)b_{GeSn} \tag{7.2}$$

The two layers were found to have Sn contents of 8.4 and 10.7 % , with compressive strains of 1.1 % and 1.44 % respectively. This compressive strain moves the Γ-valley to significantly higher energies than in the relaxed structure, meaning the alloys should be indirect, based on the material parameters used to calculate the band structures in Fig. 7.1, with bandgap bowing parameters of 1.95 and 0.68 eV for the 300 K direct and indirect bandgaps respectively. It is worth noting that from the temperature dependent measurements of Wirth et al, the 11 % sample was found to be slightly indirect with measured Γ to L difference of -5 meV, with 0.41 % compressive strain. The most comparable sample to the 8.4 % Sn material in this work was an 8% Sn sample and it was found to be indirect, even when the authors extrapolated to zero strain.

7.3.2 Raman

Raman measurements were taken on the epilayers in order to determine strain shift coefficients. A confocal WiTec Alpha 300 RAS system was used for the measurements, with an excitation source emitting at 532 nm. As can be seen from Eqs. 7.3 and 7.4, the Raman shift can be found as a function of Sn content and of strain, both with linear terms which, in the case of strain, assume a biaxial configuration. In these Eqs, ω_{GeSn}, and ω_{Ge} are the unstrained Raman frequencies of GeSn and Ge respectively, $\omega_{\mathrm{GeSn\_Strained}}$ is the strained GeSn Raman frequency, and a and b are the Sn shift and strain shift coefficients respectively. The strain shift coefficient for Ge was derived in Chapter 5, and is based on the assumption that the out of plane strain component is coupled to the in-plane via $-2C_{12}/C_{11}$. The elastic coefficients in this work are taken as a linear extrapolation between that of Ge and Sn.

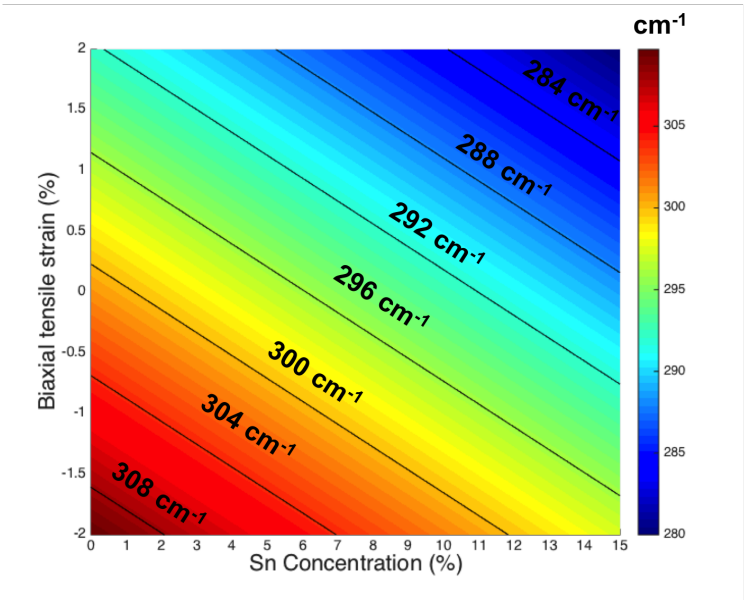

Figure 7.4: Calculated Raman line for GeSn layers with varying Sn concentration and biaxial tensile strain. Sn and strain shift coefficients of 83.1 cm^{-1} and 435 cm^{-1} respectively are used.

$$\omega_{\mathrm{GeSn}} = \omega_{\mathrm{Ge}} + \mathrm{a}x \tag{7.3}$$

$$\omega_{\mathrm{GeSn\_Strained}} = \omega_{\mathrm{GeSn}} + \mathrm{b}\epsilon_{\parallel} \tag{7.4}$$

As shown in Fig. 7.4, a particular Raman shift cannot uniquely identify Sn concentration and strain. However, if it is know that the GeSn layer is fully strained then this can be used to estimate the Sn concentration and a pseudomorphic shift coefficient can be derived, however this is dependant on the strain state of the virtual substrate. Using a Sn shift coefficient of 83.1 cm^{-1} [137], the XRD data infers a Raman shift coefficient of $\sim$ 420 $\pm$ 4.6 cm^{-1}, which relates to the Ge-Ge longitudinal optical phonon vibration. This is, unsurprisingly, extremely close to that of Ge (424 cm^{-1}) , and close to values reported in the literature [125] [137].

In binary alloys there are typically three observable Raman lines. In this instance there are Ge-Ge, Ge-Sn, and Sn-Sn vibrations. The GeSn vibration is expected to be around 260 cm^{-1} and could not be observed under low injection. The Sn-Sn vibration

should be $\sim 190\ \mathrm{cm}^{-1}$, however it is expected to be significantly weaker due to the reduced concentration of Sn-Sn bonds. The extraction of strain shift coefficient is important for an estimation of the strain following the application of external stress via a silicon nitride layer. It would be advantageous to have numerous Sn concentrations in order to more reliably extract the strain shift coefficients, which may change slightly with increasing Sn concentration, however the values calculated are well within the range reported in the literature.

7.3.3 Photoluminescence

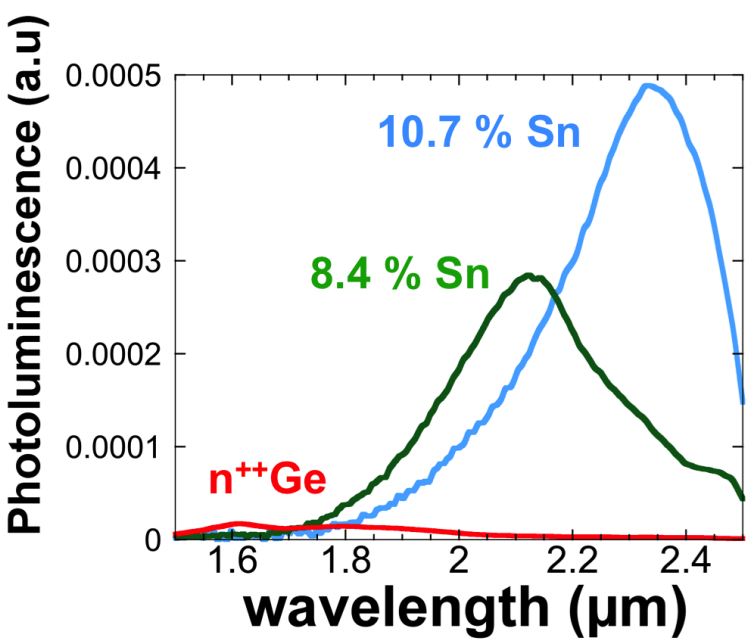

Figure 7.5: Room temperature photoluminescence of n-Ge, and GeSn layers with varying Sn concentration.

Photoluminescence measurements were taken at room temperature to investigate the bandgaps of the two alloys. A 532 nm diode pumped solid state laser was used to optically pump the sample and the PL was measured by a TE-InGaAs detector on a Bruker Vertex 70 FTIR system. The PL peaks at wavelengths of $\sim 2.15\ \mu$m and $\sim 2.35\mu$m, Fig. 7.5, correspond to energies of ~ 0.577 eV and ~ 0.528 eV. Both peaks were considerably brighter than Ge epilayers with degenerate n-type doping, used in Chapter 5 and 6. This

could be attributed to low concentration of defects in the GeSn layer, which is fully strained and therefore should have minimal dislocations, while the Ge epilayer contained high levels of dislocations (10^9 cm^{-2} [52]). Alternatively, it was thought to be feasible that the enhanced intensity could be due to the lower Γ to L energy, leading to higher electron concentration at the Γ valley. This would assume that the observed transitions were from the direct band.

Due to the large discrepancy in the bandgap bowing parameters of GeSn alloys still found in the literature, identifying the various interband transitions from photoluminescence measurements can be challenging. Fig. 7.6 highlights this issue, by showing that depending on the bowing parameters used, there are PL energies which could potentially correspond to either of two interband transitions, especially at higher Sn concentrations.

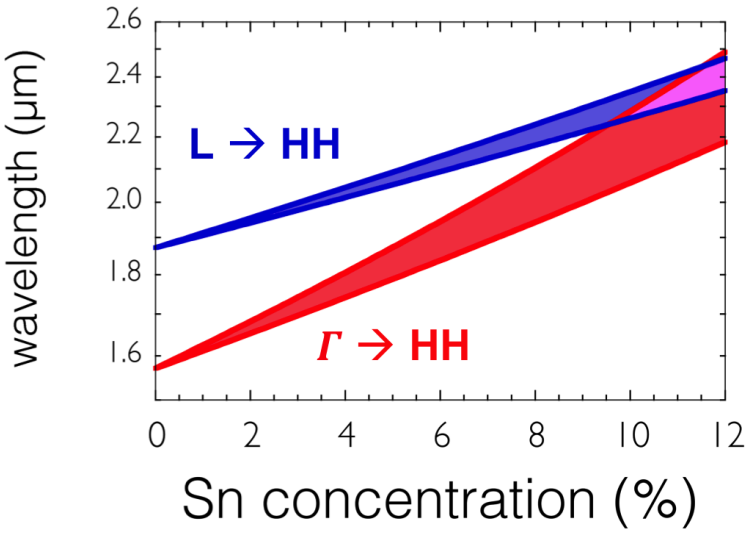

Figure 7.6: Calculated L to heavy-hole (HH) and Γ to HH transitions for GeSn layers pseudomorphicly grown on Ge virtual substrates with tensile strains 0.182 %, using two different pairs of band-gap bowing parameters reported in literature (cited in text).

Upper bounds for the direct and indirect bowing are 2.6 and 0.91 eV respectively [5], and the lower bounds for the direct and indirect are 1.95 and 0.68 eV respectively [11]. The bandgaps are computed as described for Fig. 7.1, where the growth of the GeSn alloy is assumed to be latticed matched to a Ge VS with biaxial tensile strain of 0.18 %. Given the high compressive strain of the alloys, the HH valence band should be the ground state, and therefore it should be the dominant valence band in the transition. It can be seen

that the observed PL could be assumed to be either the Γ to HH or L to HH transition, depending on the constants used.

7.3.4 Low temperature Photoluminescence

In order to investigate the nature of the interband transitions, temperature dependant measurements were taken. The temperature dependence of the intensity can provide information about the material bandstructure. At room temperature, the thermal spread of electrons in energy can mean that two valleys in close energy proximity (i.e. Γ and L) can both be populated under injection, or with n-type doping. Even when indirect, the emission from the Γ band can in some cases dominate the emission spectra, due to the increased radiative recombination rates over the indirect transition. At low temperatures, however, the thermal spread of carriers is reduced, and they cluster around band minima, as the Fermi-function becomes more like a step-function. Therefore if indirect, the direct band emission will reduce with temperature (as seen in Chapter 5 for n-type Ge), and if direct bandgap, an intensity increase will be seen. The technique can therefore be used to discriminate whether an observed interband transition is indirect or direct, particularly when the valleys are in close proximity, and was used by Wirth et al, in conjunction with a joint density of states model to prove the direct bandgap of $Ge_{0.874}Sn_{0.126}$. It should be noted however, that increased luminescence intensity for indirect bandgap transitions has been reported for high quality Ge layers, and for indirect transitions in GeSn [99, 161, 177] due to the temperature dependence of non-radiative mechanisms such as SRH and Auger recombination, and therefore the technique appears to be primarily applicable to samples where direct bandgap emission is observable at room temperature due to the enhanced radiative recombination rates, where the material could feasibly be either direct or indirect. In this circumstance the temperature dependence serves to differentiate the material's band-structures.

Low temperature PL measurements were taken down to 20 K, shown in Fig. 7.7. Both samples were found to have only a single peak present throughout the measured temperature range. If the 10.7 % Sn layer was direct, or close to direct, there should be a marked difference in the intensity increases observed due to the difference in non-radiative lifetimes of direct and indirect transitions, as carriers condensate near the band-edge. The integrated intensity as a function of temperature was found to be near identical, with

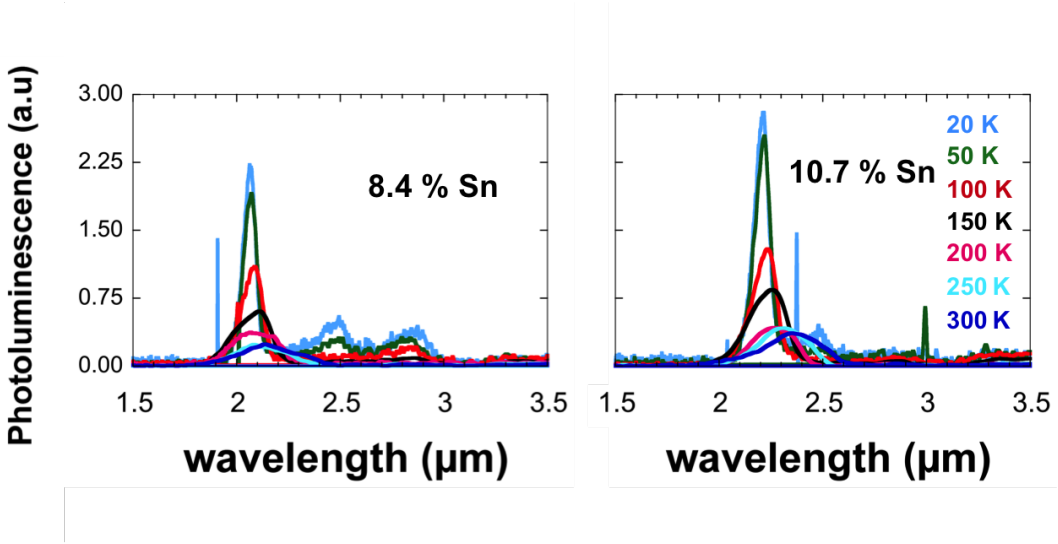

Figure 7.7: Low temperature photoluminescence from GeSn layers taken from 300 - 20 K.

both materials showing close to a 2.5 times increase. Furthermore, the full width half maxima of the PL peak for both transitions are very comparable, Fig. 7.8. The extreme similarity between the PL from both alloys suggests that the transitions are from the L to HH transition, and therefore in better agreement with the bandgap bowing parameters in [11].

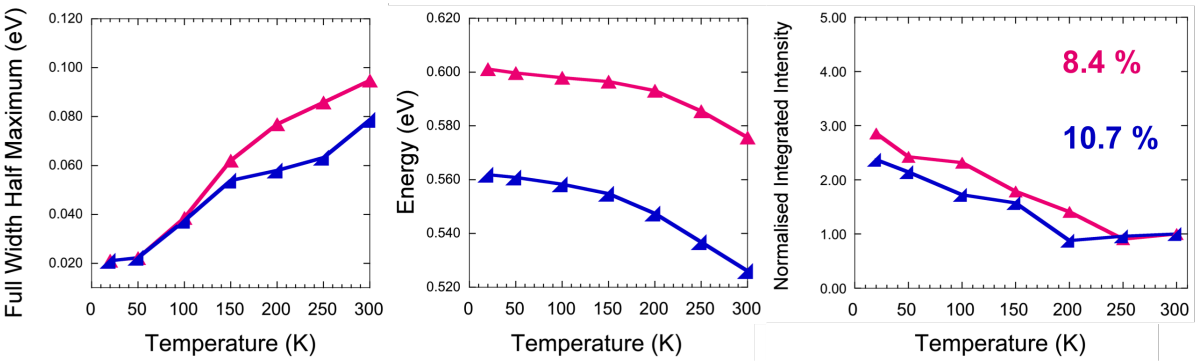

Figure 7.8: The full width half maximum (left), photoluminescence (PL) peak position (mid) and the integrated PL intensity (right) of GeSn alloys as a function of temperature from 300 - 20 K.

Considering the fact that these are phonon assisted transitions, the increased brightness compared to n-doped Ge layers is perhaps more surprising. However, aside from

the huge difference in dislocation densities in the alloy itself, there is also a discontinuity from the GeSn to the Ge and therefore it is likely that there is reduced recombination velocities to the Ge VS where threads and misfits will be present. This is in keeping with the work of Pezzoli et al, who showed that growing a SiGe barrier in a Ge micro-crystal, significantly reduced surface recombination velocities to the defective Ge/Si interface [15].

7.4 Fabrication of strained GeSn/Ge microdisks

7.4.1 Fabrication process

In order to investigate the effect of tensile strain on the epilayers, microdisk structures were fabricated using the demonstrated processes in Chapter 6. For the undercut etch, selective dry etches between GeSn and Ge were considered, such as CF_4 [125], however considering the thickness of the GeSn layer ($\sim$ 40 nm), it was decided that such disks would be prone to significant heating when illuminated by a pump. Instead it was decided to wet etch the Si using tetramethylammonium hydroxide (TMAH) (Chapter 6), thereby undercutting the virtual substrate, Fig. 7.9.

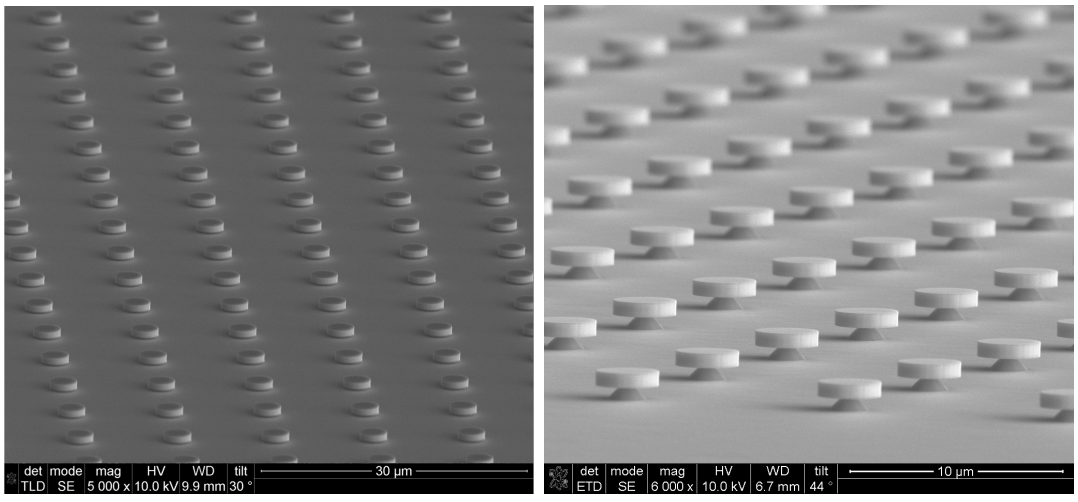

Figure 7.9: Array of 3 μm diameter GeSn/Ge microdisks. The dry etched disks are shown on the left, and the disks undercut by tetramethylammonium hydroxide wet etching are shown on the right.

Given the thickness of the GeSn, the effect of vertical strain gradient is minimal,

allowing for the assumption of near homogeneous vertical strain in the epilayer. This would not have been the case for fully released GeSn epilayers, as the use of single stressors results in compressive strains at the bottom of the structure.

Arrays of 3 and 4 μm diameter disks were fabricated in both material systems. With fully compressive strained GeSn layers, high strain transfer is required from the stressor, so racetrack structures were neglected. Such structures could be advantageous for thicker, partially relaxed films, as discussed in Chapter 6.

The samples were patterned by a Vistec VB6 lithography tool, using HSQ resist, and dry etched using a mixed recipe of SF_6 and C_4F_8, which effectively etches the GeSn as well as Ge. The samples were undercut by $\sim$ 1 μm in 25 wt % TMAH and IPA. A 1.5 x 1.5 mm square was patterned, where minimal strain transfer is expected, thereby giving a reference region with high stress silicon nitride but with the same strain as the unprocessed epilayer.

Despite the difference in thicknesses of 40 nm GeSn to 650 nm Ge, there is more elastic energy in the compressively strained alloy compared to the small amount of tensile strain in the Ge VS. This can be seen from Eq. 7.5

$$E_{strain} = 2\mu\frac{1+\nu}{1-\nu}\varepsilon^2 t \tag{7.5}$$

where ν is Poisson's number, E is the elastic modulus, ε is the biaxial strain, t is the thickness and μ the shear modulus is

$$\mu = \frac{E}{2(1+\nu)} \tag{7.6}$$

Using the strain measured by XRD, the 10.7 % sample has $\sim$ 4 times the elastic energy of the Ge VS, while the 8.4 % sample has $\sim$ 2.5 times the energy of the VS. In both cases, this leads to a moderate relaxation of compressive strain when the disks are undercut. The disks were subsequently processed with a PECVD adhesion layer, and coated with a 300 nm thick silicon nitride stressor with compressive stress of $\sim$ 2.4 GPa.

7.4.2 Raman spectroscopy of strained disks

Raman spectroscopy was used to quantify the transferred strain in the disk structures, using the setup described previously in this chapter. Measurements were taken near the

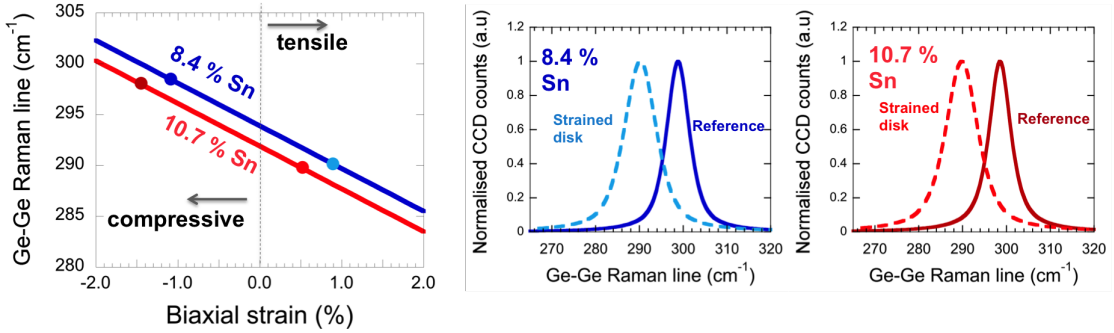

Figure 7.10: Left - the Raman line for the two GeSn alloys is shown as a function of strain using the extracted strain shift coefficient. Points have been marked on the lines showing the position of the measured Raman spectra, on unpatterned reference samples and on strained disks. The Lorentzian fits to the spectra are shown for both alloys (middle and right).

disk edge of 3 μm disks with $\sim$ 2.4 GPa stressor layers. Large shifts of $\sim$ 10 cm^{-1} were observed, which is consistent with the $\Delta\omega$ observed in Ge disks in Chapter 5, with comparable strain shift coefficients. Figure 7.10 shows the Raman line as a function of strain for the two alloy concentrations used in this work. Points are marked to indicate the position of the Raman peak from reference measurements, and from measurements of the strained disks. Lorentzian fits to both these spectra are shown for the 8.4 and 10.7 % samples. Clearly, the strained disks have been moved from highly compressive to tensile strained, with the 8.4 and 10.7 % having tensile strains of $\sim$ 0.9 % and 0.5 % respectively. This is significant, as it is believed that this is the first demonstrations of a tensile strain in GeSn induced by silicon nitride stressors.

7.4.3 Photoluminescence of strained GeSn disks

Photoluminescence measurements were taken using the method described in Chapters 4 and 5. As in Chapter 6, resonances are observable in the PL, which in this case are due to the propagation of emitted light from the GeSn layer into the Ge VS. As a result, higher Q resonances were observable due to the transparency of the Ge at the emission wavelength of the GeSn alloys [178]. The PL from an wet-etched 3 μm 10.7 % Sn microdisk is shown in Fig. 7.11.

The photoluminscence of the strained structures were subsequently investigated. The expected wavelength of the emission was such that a nitrogen cooled InSb detector was

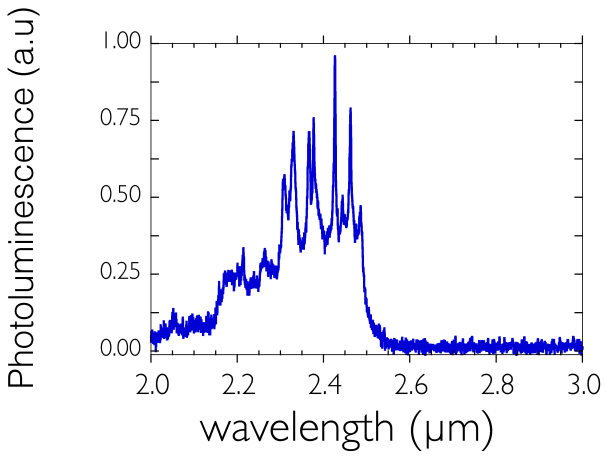

Figure 7.11: Room temperature photoluminescence of a 3 μm diameter, undercut GeSn/Ge microdisk with a Sn content of 10.7 %. A TE-InGaAs detector with a $\sim$ 2.5 μm cut-off was used.

used, in conjunction with a Si based 1650 nm longpass filter to reject the pump at 532 nm, and to give a minimum of $\sim$ 80 % transmission up to 5 μm wavelength. It was found that on the mm sized reference square (coated by high stress silicon nitride but confirmed to have negligible strain by Raman spectroscopy) there was a significant reduction in intensity (measured with a TE-InGaAs detector). Emission from strained GeSn disks was significantly red-shifted, with PL observable above 3 μm, Fig. 7.12, which was in keeping with the levels of strain measured by Raman spectroscopy. However similarly to the reference sample, emission intensities from the disks were low to the extent that what appears to be interband transitions were of a similar intensity to the blackbody emission from local heating from the pump, which gives rise to the emission towards the 5 μm detector cut-off. The spectra is further complicated due to dips in the transmission at $\sim$ 3.1 and 4.26 μm. To highlight this, the transmission from a broadband MIR source is included in Fig. 7.12, where such dips can be observed. The nature of these absorption lines are explained later in the chapter.

7.5 Strained GeSn/Ge disks with Al_2O_3 passivation

In previous chapters, the expected intensity increase with applied strain was not observed. It was argued that this was in part due to polarisation considerations regarding the Γ to

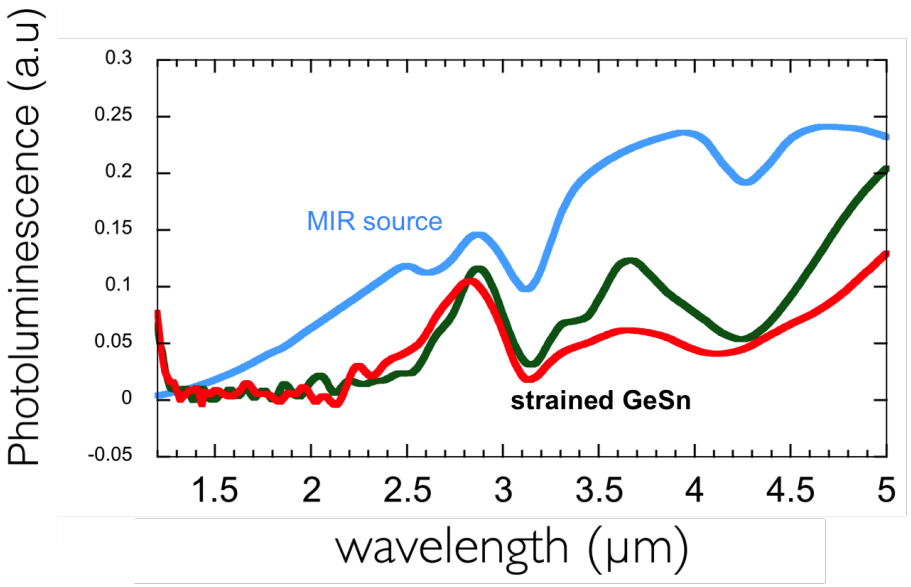

Figure 7.12: Photoluminescence of strained GeSn alloys with 10.7 % Sn content. Green - 3 μm diameter microdisk. Red - 4 μm diameter microdisk. Blue - broadband mid-infrared (MIR) globar. The spectra have been scaled for clarity compared to the MIR source. Low emission intinsities mean that the disk PL is comparable to the blackbody emission seen towards the detector cut-off at $\sim$ 5 μm.

LH transitions, and also due to the electrical properties of the silicon nitride layers. Such large reductions in intensities, however, had not been observed to the extent as with these GeSn samples. This reduction was detrimental enough that it impaired the ability to distinguish between blackbody modulated by absorption bands, and interband emission.

Alternative passivation layers were incorporated into the dielectric layer stack in order to investigate to what extent the apparent reduction in quantum efficiency was due to the electrical, and even physical damage from the high bombardment high stress process. Four identical pieces of 10.7 % GeSn were processed with 3 μm undercut disks, following the process described previously. One sample was left uncoated, as a reference, while another was coated with 20 nm PECVD silicon nitride (the standard layer for adhesion promotion in this work) and the final two received an Al_2O_3 layer deposited by atomic layer deposition (ALD). One of the Al_2O_3 coated samples was subsequently coated with a further 20 nm of PECVD silicon nitride. Results on GeSn MOS capacitors with Al_2O_3 dielectric layers showed that forming gas anneals (FGAs) can improve the density of interface traps (Dit)

at the interface, to approximately 2e12 cm^{-2} eV^{-1} at the midgap [126]. Before deposition the samples were given solvent cleans in acetone and IPA. Cyclic cleaning with DI water and 5:1 buffered HF was carried out before the samples were blow dried with N_2, and then immediately transferred to the ALD tool to minimise the formation of a native oxide. The Al_2O_3 layers were deposited at 290 °C with alternate pulses of Trimethyl Aluminum (TMA) and DI-H_2O.

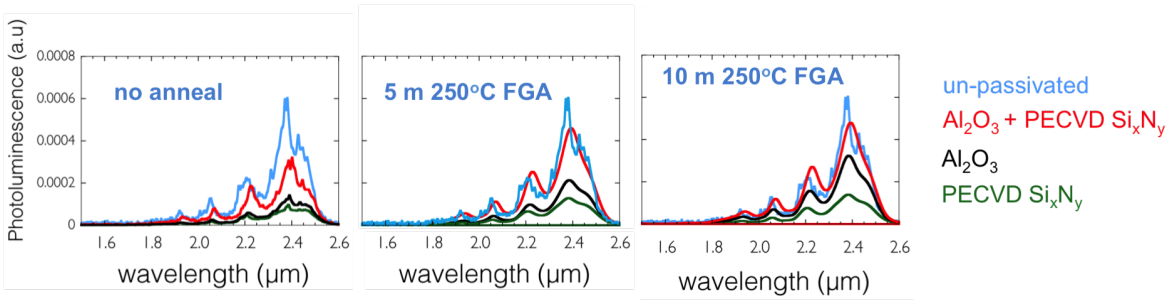

Figure 7.13: Photoluminescence (PL) of GeSn microdisks with Sn contents of 10.7 %. A number of passivation layers are shown, and the PL is shown for samples with no anneal, and for 5 and 10 minutes in forming gas.

Photoluminescence measurements were taken on all of the samples, the results of which can be seen in Fig. 7.13. As deposited, there is a significant reduction in intensity between the PECVD coated and bare samples. Perhaps unexpectedly, there were observable differences between both of the Al_2O_3 samples, with the only difference being the subsequent PECVD deposition. This has been attributed to the 300 °C deposition temperature on the PECVD tool, acting as a short anneal.

The samples were subsequently given FGAs, which were limited to temperatures of 250 °C, despite the fact that higher temperature depositions of Al_2O_3, and PECVD silicon nitride had shown no signs of inducing Sn precipitation or strain relaxation. This decision was made in order to keep thermal processes to an absolute minimum, before a detailed analysis of the thermal budget of the alloys can be carried out for future work. This will require a further means of analysing Sn precipitation, such as TEM imaging, which can be used to investigate the thermal budget of different alloy concentrations [179].

As shown in Fig. 7.13, 5 minute FGAs improved the emission intensity of all samples. After a subsequent 5 mins FGA no further change was observed on sample with ALD and PECVD layers. Critically, the samples showed no blueshift which has been observed

following the bulk precipitation of β-Sn at high temperature anneals, above 400 °C [180]. While the passivation was far from optimised, the emission intensity was sufficiently comparable to unpassivated structures that high stress layers could be investigated. The optimisation of GeSn passivation will be the subject of future work.

7.5.1 Enhanced Photoluminescence from Al_2O_3 passivation

High stress layers were deposited on all samples but the uncoated reference. The layers had measured stresses of $\sim$ 2.3 GPa and were 300 nm thick. Significant cracking of the high stress layer was immediately observable on the sample with only Al_2O_3. Photoluminescence measurements indicated that there was no strain transfer from silicon nitride in this sample. Further PL measurements were used to compare the emission intensities of the remaining strained pieces, both with PECVD adhesion promoting layers, with and without Al_2O_3 passivation. The incorporation of the Al_2O_3 layer clearly gives rise to an higher PL intensity compared to using just a PECVD adhesion layer, suggesting that the PECVD layer alone was severely effecting the non-radiative lifetime. On this sample interband transitions could be clearly differentiated from blackbody radiation, which is evident due to the emission returning close to zero intensity before a blackbody tail begins to appear at $\sim$ 4.25 μm (Fig. 7.14). The inset of Fig. 7.14 shows that there is approximately a 17.5 times increase in the peak emission intensity of the strained sample with the additional Al_2O_3 layer.

Raman spectroscopy showed that the processed samples had strains of $\sim$ 0.43 % at the top plane, comparable to the previous samples. According to deformation potential theory, and using a linear extrapolation of the deformation potential constants between Ge and Sn it appears that emission at these wavelengths has to be from direct transitions. Experimentally, 11.1 % GeSn layers were shown to be direct bandgap when extrapolating to zero strain, and therefore the tensile strained emission at longer wavelengths, from a sample with comparable Sn contents suggests that the strained microdisks are direct bandgap.

The nature, however, of the two peaks visible in the PL is unclear, Fig. 7.14. It was not evident if this was the observation of two transitions, or from a single peak modulated by an absorption band. As shown previously in Fig. 7.12 a dip in the MIR transmission signal was found at $\sim$ 3.1 μm. This was subsequently found to be due to the build up of water

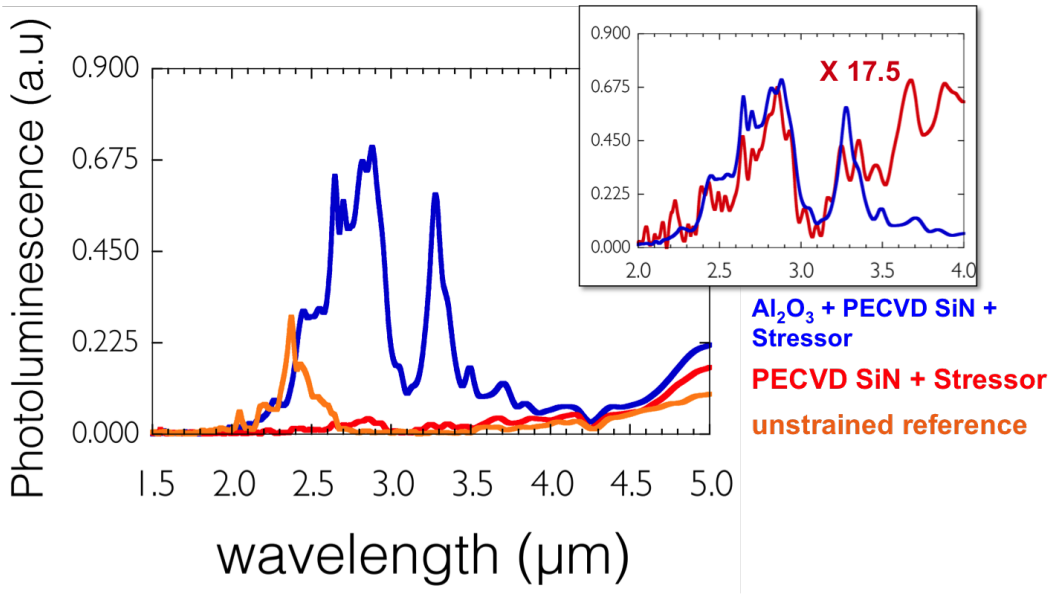

Figure 7.14: Comparison of the photoluminescence (PL) of 3 μm diameter 10.7 % Sn GeSn microdisks, with no passivation, a PECVD silicon nitride adhesion layer and silicon nitride stressor layer, and a Al_2O_3 passivation layer with a PECVD silicon nitride adhesion layer and stressor. The sub figure shows the comparison of the two stressed samples.

condensation in the InSb dewar, which when cooled with liquid N_2 leads to an absorption band from ice. The dewar was evacuated with a turbo pump and the absorption band was found to be completely removed from the spectra, shown in Fig. 7.15. No significant change to the PL was found, however, and the two peaks remained visible in the PL.

It was thought that there could be potential for there to be absorption from the high stress silicon nitride layer, which as shown in Chapter 5, has an absorption band from the N-H stretching mode at $\sim$ 3 μm, however as shown in Fig. 7.15 this appears to be slightly misaligned with the dip in the spectra, closer to 3.1 μm. The final possibility considered was that the short and long wavelength peaks were from the Γ to HH and Γ to LH transitions respectively, as the LH valence band will be the ground state under tensile strain. The energy separation of the two peaks would be relatively consistent with the calculated valence band splitting of $\sim$ 35 meV.

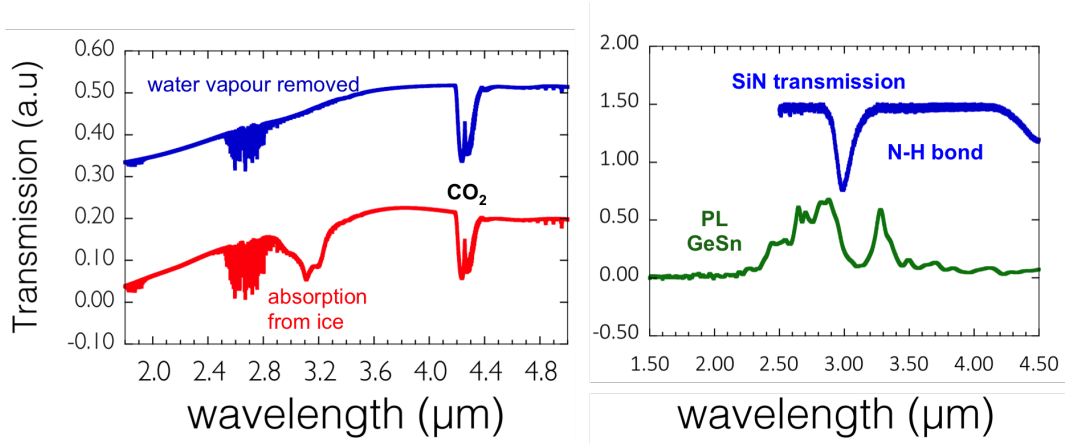

Figure 7.15: Left - Mid-infrared transmission from an internal globar on a Vertex 70 FTIR system. The lower curve shows the absorption band due to the formation of moisture in the dewar, which freezes when the detector is liquid nitrogen cooled. The upper curve shows the detector response after pumping out the detector dewar. Spectra offset for clarity. Right - the GeSn photoluminescence is shown with the transmission from a high stress silicon nitride layer, in the vicinity of the N-H stretching mode.

7.5.2 Strained GeSn microdisks with Al_2O_3 passivation layers

A further set of 8.4 % and 10.7 % samples were processed using the techniques detailed previously, in order to examine the properties of both strained alloys. They included the Al_2O_3 layers and FGAs, shown to significantly improve the emission of highly strained GeSn layers. The post FGA PL did not return to the full intensity of the un-coated structures, and therefore it was expected that the relative intensity increases with strain may not be so significant. Each sample contained disks of 10, 6, 5, 4 and 3 μm diameters, with $\sim$ 1.2 μm undercuts and 300 nm of high stress silicon nitride with compressive stress of $\sim$ 2.3 GPa.

Raman measurements were taken across all samples. The spectra were fitted with Gauss-Lorentz functions, and histograms were formed using a binning width of 0.2 cm^{-1}. The histograms for 8.4 and 10.7 % disks are shown in Fig. 7.16. For correlating the strain to PL measurements, Gaussian functions were fitted to the Raman histograms, and the upper bounds of the strain were estimated by taking the strain value at the 1/e point of the low frequency side of the fit. It should be noted that this may appear as a fairly arbitrary approximation. However, the higher strained regions of the disks should be much

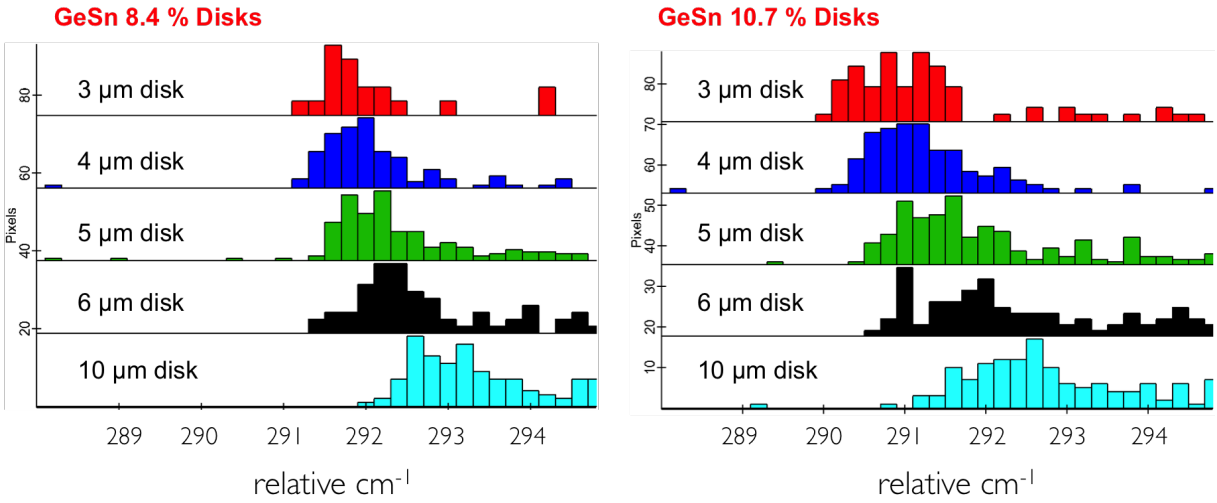

Figure 7.16: Histograms showing the frequency of the measured Raman line per spectral position for strained GeSn microdisks. The plots are offset for clarity.

more relevant for interpreting the PL, as these regions should have increased radiative recombination. A more accurate means of fitting the PL dependency from the Raman would require a complex function, as there is a non-linear dependency on the PL intensity from the strain, which varies with a number of material properties, such as the carrier lifetime, and the density of states

The room temperature PL of disk arrays was examined, and a clear progression could be seen, particularly with the 10.7 % alloy, Fig. 7.17. The upper bound of the strain fit from Raman is marked on the figure. For the 10.7 % Sn alloy, the emergence of the long wavelength peak previously observed in the original samples can be seen with increasing strain. It is apparent from Fig. 7.17, that the peak does not red-shift through ~ 3.1 μm, and the progression appears consistent with the increased red-shift from strain moving the emission over an absorption band, rather from a separate interband transition. This is most likely due to either absorption from the N-H bond in the silicon nitride layer, or from scattering processes due to the change of index associated with the N-H vibration. This could suggest that a part of the spectra is obscured from the measurement. Even for 10 μm diameter disks it appears as if a sharp absorption edge modulates the low energy (long wavelength) side of the spectra. The 8.4 % alloys there is also a red shift observable, with emission towards 3 μm wavelength in the 3 μm diameter disk. Here it also appears

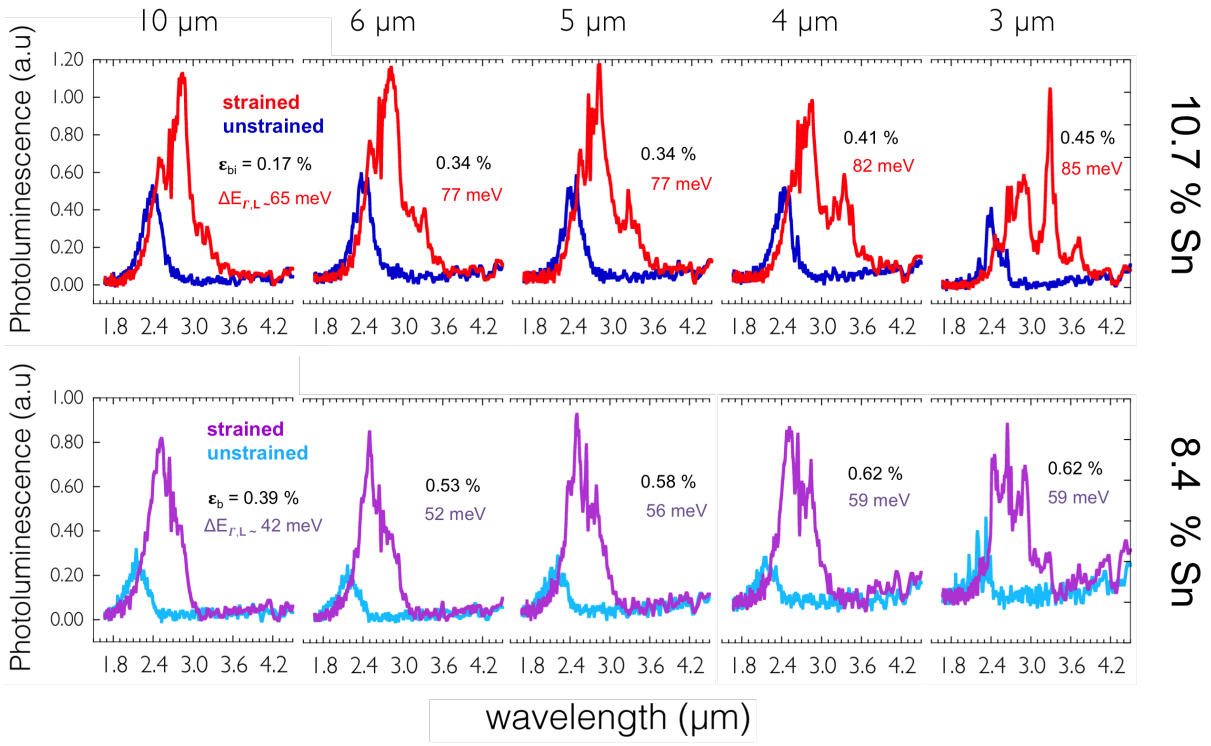

Figure 7.17: Photoluminescence from strained GeSn microdisks. The strain from the Raman line is added next to the relevant spectra, and the corresponding calculated L to Γ energy difference listed. The disk diameters are marked at the top of the plot.

that the longer wavelength emission is approaching a sharp absorption edge or scattering centre.

In all cases the samples showed an increased PL intensity with applied strain. The disk arrays had varying fill factors, as it was seen as advantageous to maximise the PL signal in a given array, and therefore only the relative intensity increase with respect to the unstrained sample should be considered, and not the absolute intensities. It should be noted that (to my knowledge) photoluminescence from GeSn has not previously been observed at wavelengths past 2.6 μm [130].

7.5.3 Low temperature photoluminescence

Low temperature measurements were taken on the strained micordisks for both alloys, from temperatures of 300 K to 20 K, which as described previously, can give an insight to

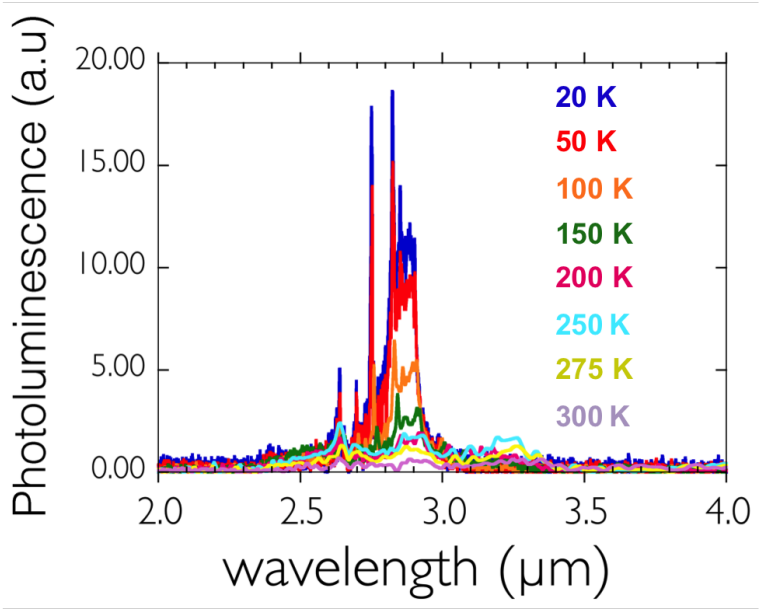

Figure 7.18: Low temperature photoluminescence (PL) from the a strained 3 μm diameter 10.7 % Sn GeSn microdisk with Al_2O_3 passivation The room temperature PL was shown in Fig. 7.14 .

the band structure. The 3 μm 10.7% Sn disks used to investigate the passivation layers were also measured; the low temperature PL for this sample is shown in Fig. 7.18. The longer wavelength peak initially increases in intensity but subsequently disappears from the spectra at temperatures below 250 K. If this had been due to emission from a Γ to LH transition, it would be expected that this peak would dominate the spectra at low temperature, as the Fermi-function approaches a step function and carriers condensate around the band minima. The contrary behaviour is therefore more in keeping with the tail of a peak blue shifting with decreasing temperature, into an absorption band.

A similar trend was found for the 3 μm disks in the second 10.7 % Sn sample. The integrated PL intensity is plotted as a function of temperature for both alloys in Fig. 7.19. In the top left panel, strained 10.7 % Sn 3 μm disks are compared with unstrained and unpassivated disks of the same size and material, and 10.7 % epilayers. It is interesting to note that for the reference disk sample, the PL intensity showed a different temperature dependence compared to the unprocessed epilayer, showing minimal sensitivity to temperature. This has been attributed to the likely increased surface recombination added by the etching processes, which decreases the non-radiative lifetime and therefore changes

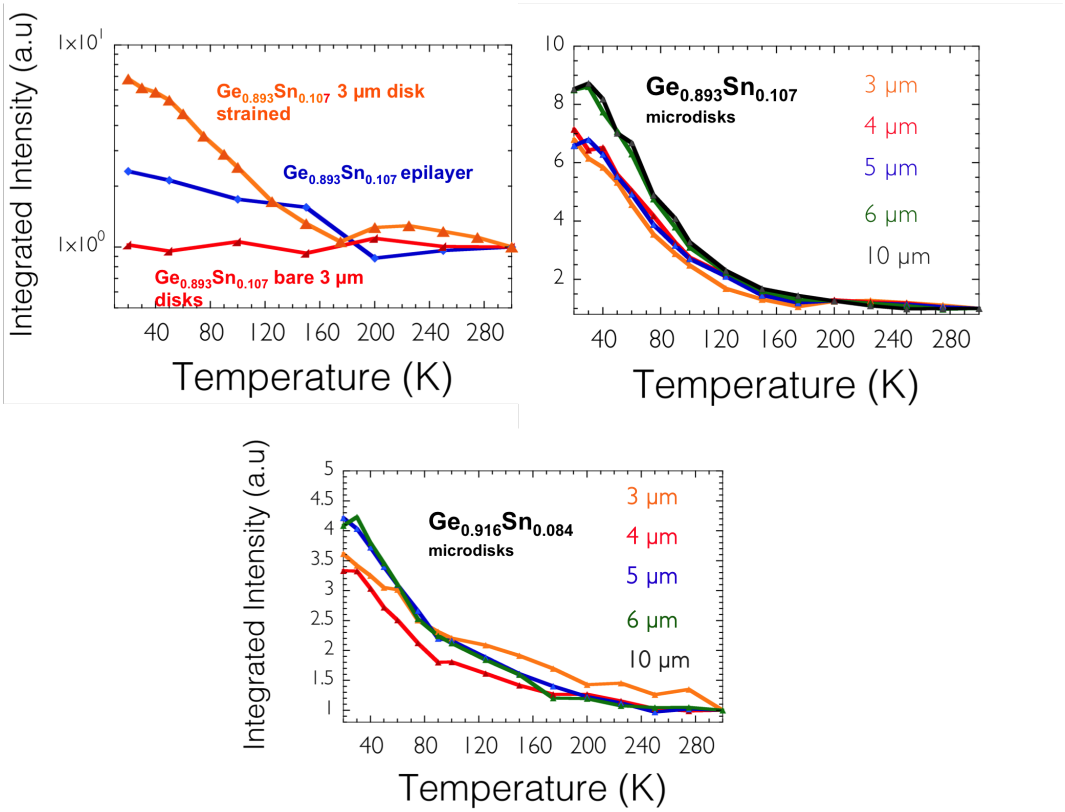

Figure 7.19: Integrated emission intensity for a strained GeSn microdisks. The alloy concentration and disk diameters are marked on the figure.

the temperature dependance of the PL. This is fairly analogous to the difference in the temperature dependence of the indirect transition in Ge, between highly defective layers, and those with minimal dislocations.

The strained samples show an increased integrated intensity at low temperature compared to both the unpassivated disks and the epilayer, which has been shown to be a hall-mark of direct bandgap materials [11, 181]. All data has been normalised to the 300 K integrated PL intensity, therefore the absolute increased luminescence from the bare to the strained disks at 20 K is not evident in this plot. The integrated PL intensities for the full range of disk diameters are also shown for both alloys. For each alloy the samples show minimal dependence on the disk strain, however curiously the 10 and 6 μm disks showed larger relative increases compared to the higher strained 3 and 4 μm disks.

The general similarity between the disks is perhaps not unexpected given that from

the 3 μm disk to the 10 μm disk are both significantly direct, by approximately 85 and 65 meV respectively, according to modelling of the bandgaps, and therefore another non-radiative process could be dominating the observed thermal quenching. For comparison, the 8.4 % Sn samples temperature dependence is shown in Fig. 7.19, showing a similar temperature dependance to the 10.7 % samples but with a reduced total relative increase, suggesting that the dependence does somewhat scale with the Γ to L energy difference, i.e, the level of directness.

7.5.4 Arrhenius law

The thermal quenching of the PL with increasing temperature can, to the first order, be described by an Arrhenius law, Eqs. 7.7-7.8, where I_o is the integrated intensity approximated at 0 K, E_a is the activation energy, A is a constant, and K_b is Boltzman's constant.

$$I(t) = \frac{I_o}{1 + Aexp(-E_a/K_bT)} \tag{7.7}$$

This can be rearranged in the following form:

$$ln\left(\frac{I_o}{I(t)} - 1\right) = ln(A) - \frac{E_a}{K_bT} \tag{7.8}$$

When plotting the left hand side of Eq.7.8 versus $1/T$, the resulting slope gives the activation energy scaled by Boltzman's constant, i.e. E_a/K_b. At high temperature this is expected to be dominated by the Γ to L energy difference, as at high temperatures, electrons can thermalise into the L-valley. Strange et al [177] showed that the activation energy showed some dependence on $\Delta E_{\Gamma,L}$, but also that thicker layers with higher dislocation densities reduces activation energies for otherwise comparable layers.

As in Ref. [177], the Arrhenius plot showed two separate regimes at high and low temperatures, as shown in Fig. 7.20 for the 3 μm 10.7 % Sn sample. The inset shows how after initially increasing in intensity there is a point at which the emission suddenly decreases, before subsequently increasing again, which could be related to the obscured emission at 3.1 μm. The measured activation energy E_a was found to be - 14.7 meV using the fit in Fig. 7.20, but -21.4 meV if fitting to only data points before the 'dip'. The 8.4 % 3 μm disk showed a similar activation energy of -19.6 meV. For each alloy, the 4, 5 and 6 μm disks were comparable, with the 8.4 % Sn samples giving E_a of $\sim$ -15 meV,

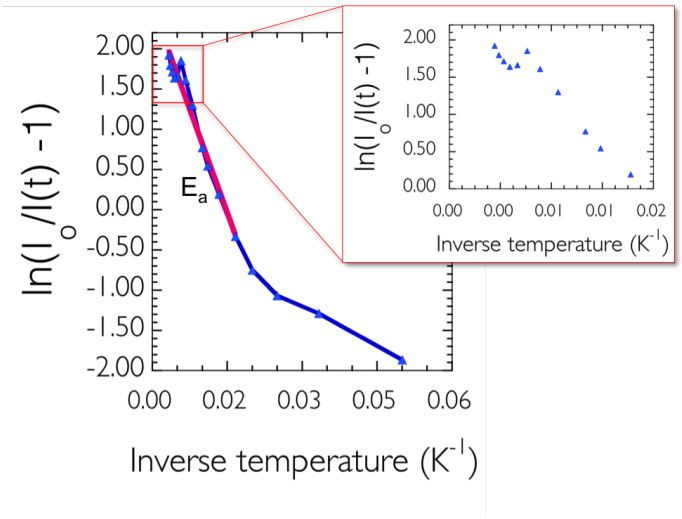

Figure 7.20: Arrhenius plot for a 3 μm 10.7 % GeSn microdisk. This behaviour shows two regimes at high and low temperature. The sub plot shows a zoom of the high temperature behaviour.

and the 10.7 % Sn giving $E_a \sim$ -17.5 meV. Again, this shows only a weak dependence on the expected Γ to L energies, suggesting that another mechanism dominates the thermal quenching. At low temperatures, there was a general trend to lower activation energies (< - 10 meV), which is more in keeping with a shallow impurity such as a Sn vacancies [177] therefore only dominating for low temperatures where K_bT is of an equivalent order (i.e < 100 K), i.e. where the thermal energy of the carriers would not be sufficient to overcome a low energy trap.

7.5.5 Low Temperature Interband transitions

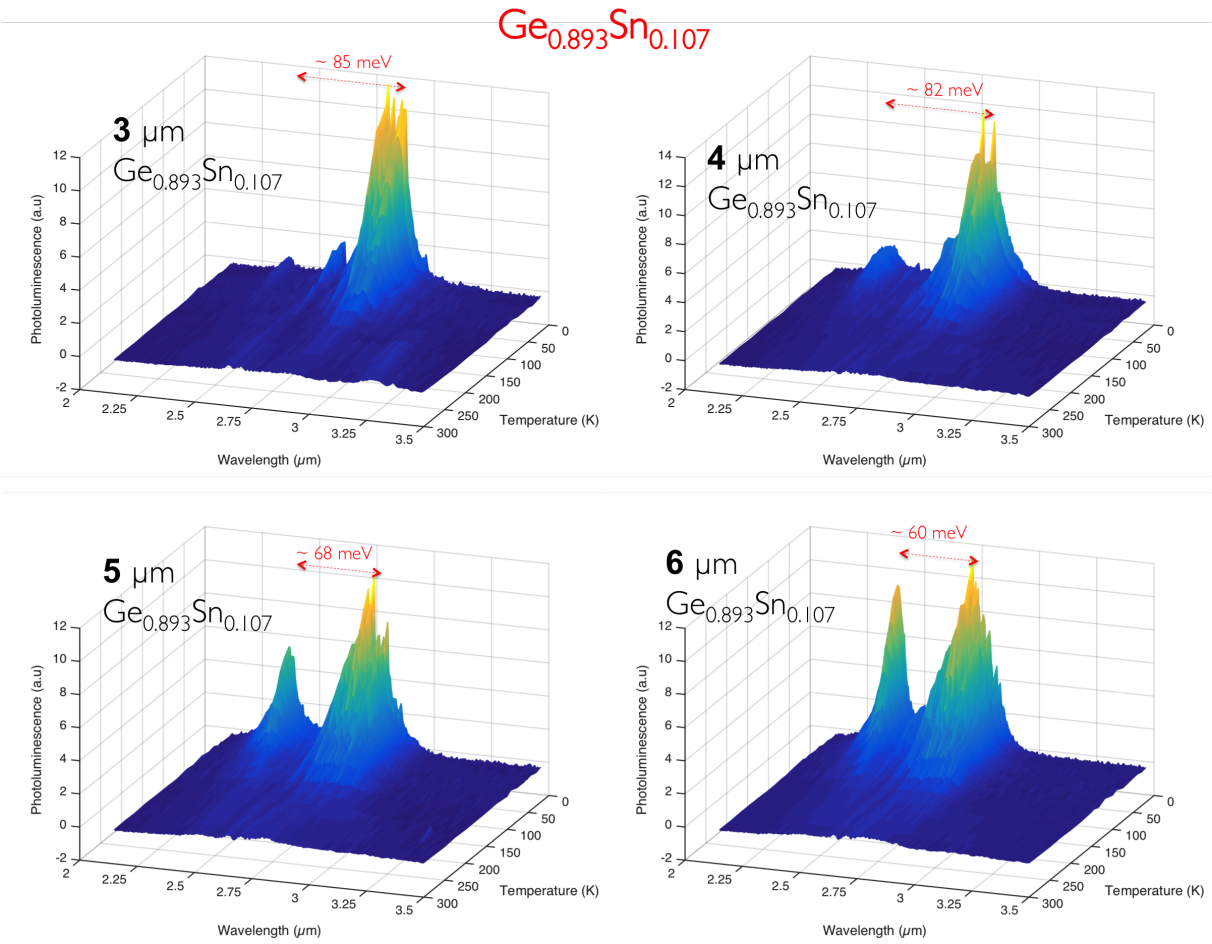

Figure 7.21: 3d mesh plots of the low temperature photoluminescence (PL) of 10.7 % GeSn microdisks. The Figures show PL intensity as a function of wavelength and temperature.

The evolution of the PL at low temperatures for the 10.7 % alloy can be seen in the 3D plots shown in Fig. 7.21, which show the PL intensity as a function of temperature and wavelength. It can be seen that for the larger diameter disks (4 - 6 μm) there is the emergence of a high energy (lower wavelength) peak at low temperatures. This peak position remains relatively constant across all 10.7 % disks at around 2.4 μm at 20 K, and at $\sim$ 2.25 to 2.3 μm for the 8.4 % Sn sample. For clarity, the short and the long wavelength peaks are referred to as peaks A and B respectively.

For both alloys, there is a clear progression. As the strain in the disk reduces, peak B moves to shorter wavelengths, and the intensity of peak A increases the closer they are in proximity. There is potential for peak A to be a direct bandgap transition from Γ to the HH band, which is the lower energy valence band under biaxial tensile strain. The emergence of peak A with decreasing strain could be a by-product of the increased overlap with the tail of the quasi-Fermi level in the valence band. However, for 0.46 % biaxial strain the calculated LH to HH difference is only 37 meV, less than half of the observed energy difference in the peaks.

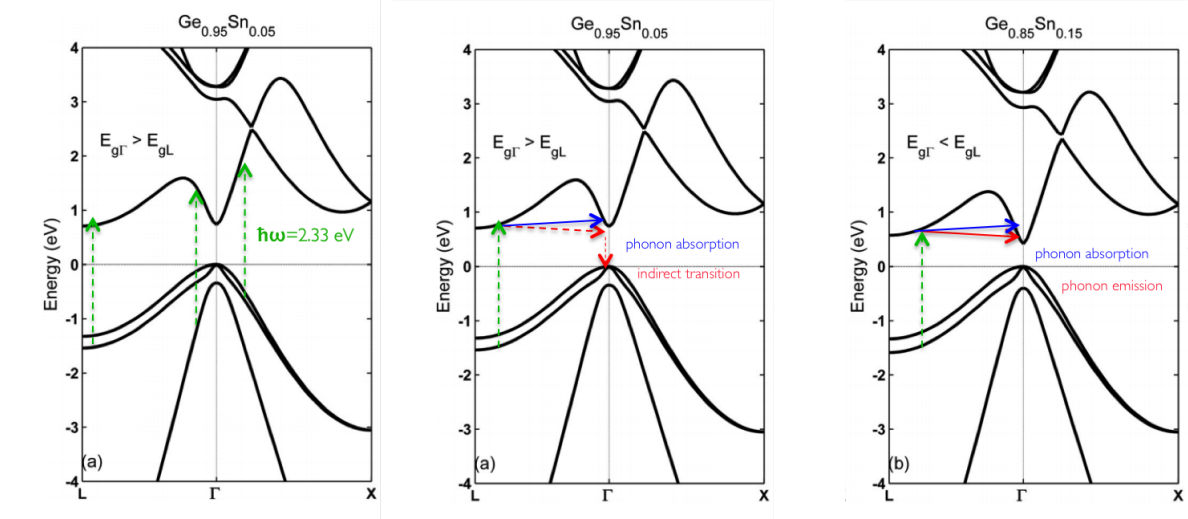

Figure 7.22: Bandstructure calculations of GeSn alloys of varying Sn concentration, from [5]. The left figure have been altered to show the possible transitions for a green photon (532 nm wavelength). The middle and right plots show possible scattering mechanisms from the L-valley.

A second possibility considered was that peak A is from an indirect transition. Considering the GeSn band structure, the energy of the 532 nm pump (2.33 eV) leads to absorption between a number of bands, as shown in Fig. 7.22 (left). Clearly, the transition is energetic enough to move carriers directly into the L valley, as well as transitions from the HH LH, and SO near the Γ. It is likely, however, that significantly more carriers will be injected into the L, due to the vastly increased DOS. The direct bandgap emission will therefore have some dependence on carriers being scattered from the L valley to the Γ-band. As shown in Fig. 7.22 (mid & right), phonon scattering can occur for either

the emission or absorption of a phonon. If the Γ valley is higher in energy than the L then this must occur via phonon absorption. For scattering by phonon emission, the Γ must be lower then the L in energy by at least the energy of the phonon. In Ref. [182], low temperature (4.3 K) PL measurements showed multiple peaks due to various phonon assisted transitions from the L-valley. This leads to measured longitudinal optical (LO), transverse optical (TO) , and transverse acoustic (TA) phonon energies of $\sim$ 30, 36 and 8 meV respectively, for carriers scattered from the L valley close to the Γ. With the addition of Sn and strain, however, these phonon energies will change and therefore these energies should be considered to be an approximation.

The L to Γ scattering could therefore be crucial for understanding the PL spectra. It could give rise to a potential explanation for the presence of two peaks in this work. It is therefore possible that in the highest strained samples, the $\Delta_{\Gamma,L}$ is sufficiently large that carriers in the L valley can phonon scatter and combine at the direct band. With decreasing strain, and therefore reduced $\Delta_{\Gamma,L}$, the scattering is reduced, and phonon assisted process from the L could lead to an indirect transition. A similar argument has been made for the bottleneck in low temperature emission of narrowly direct Ge layers. It would however, be surprising that the indirect peak could have intensities comparable to the direct transition. This could in part be due to the fact that with preferential pumping of carriers into the L valley, the carriers do not reach a thermal equilibrium within the conduction band with low L to Γ scattering. Furthermore, the joint density of states of the L to VB should be higher than that of the direct.

The peak position of the assumed direct transition (peak B) at 20 K was plotted against the upper bound strain measured by Raman spectroscopy. As shown in Fig. 7.23, this appears to be in good agreement with the Γ to LH transition, when using the bandgap bowing, Varshni coefficients, and Sn deformation potentials reported in [11]. The 20 K peaks were chosen due to the fact that the peaks have blue shifted from the apparent absorption at 3.1 μm. It was found, however, that the corresponding low wavelength peak was not in good agreement with any of the interband transitions using these parameters, regardless of the phonon energy considered (assuming Ge values). This could suggest that further work is required to narrow down the range of bandgap bowing parameters. For the purposes of future work, the theory of the indirect transition could be tested by using a lower energy pump that is closer in resonance to the direct band. If the hypothesis is correct, the high energy (low wavelength) peak should be significantly reduced in intensity.

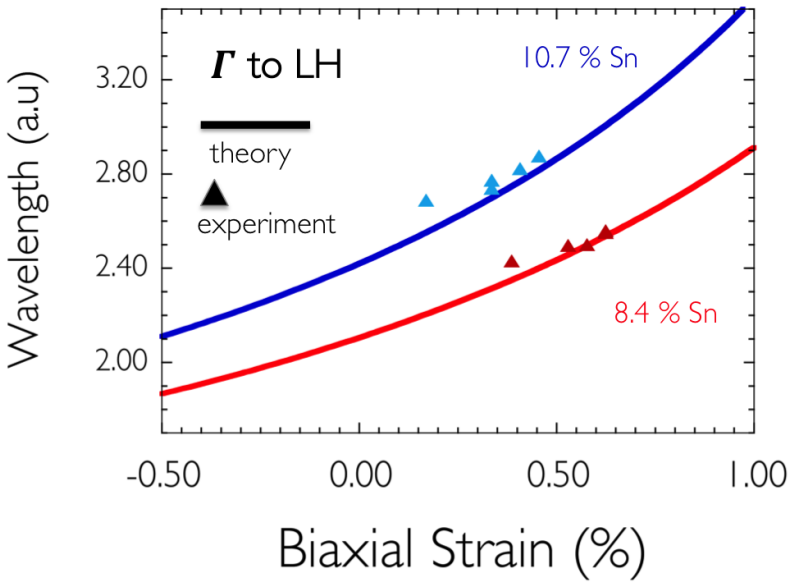

Figure 7.23: The calculated Γ to LH transition at 20 K using the Sn material parameters from [11]. Experimentally measured peak positions are plotted as a function of the strain measured by Raman spectroscopy, showing excellent agreement with the theory.

At this stage in the work, the assertions of an indirect transition are somewhat tentative, and will require more experimental analysis.

7.6 Gas Sensing

As discussed in Chapter 1, the MIR gas sensing market is growing rapidly, with applications ranging from pollution monitoring, to national security. Obtaining a source that can be monolithically integrated on a Si platform would revolutionise the industry, dramatically cutting costs by elevating the need for expensive quantum cascade lasers, or III-V materails. Given the emergence of the strained GeSn PL into the 3 μm window, the spectral overlap with methane (CH_4) was investigated. Calum MacGregor (Gas Sensing Solutions) modelled the expected spectrum resulting from the emission 10.7 % Sn 3 μm diameter disk, through a 20 mm path-length of 5 % methane. As shown in Fig. 7.24, there is significant overlap with the long wavelength tail.

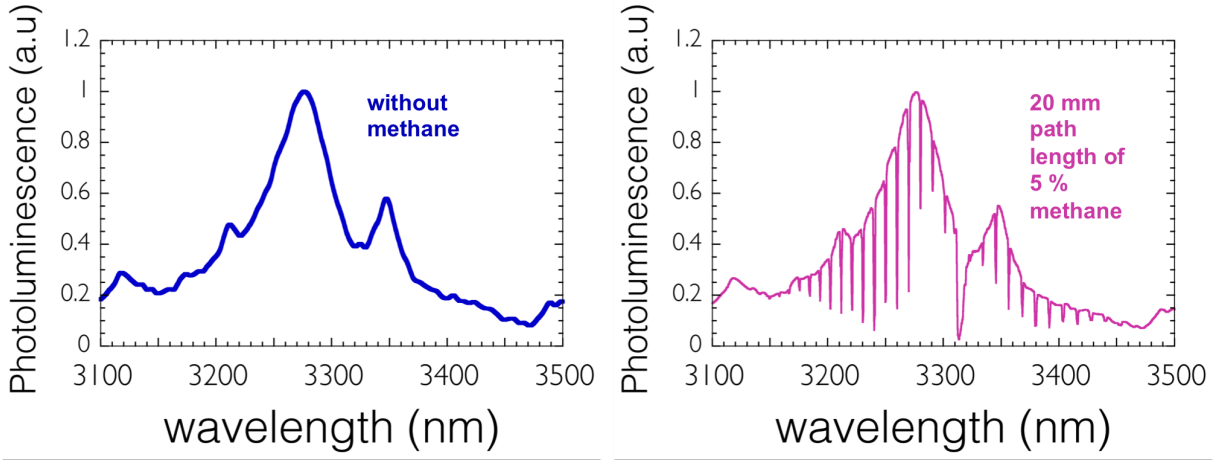

Figure 7.24: The emission of a strained 10.7 % GeSn layer used to model the resulting spectra through a 20 mm path length of 5 % methane.

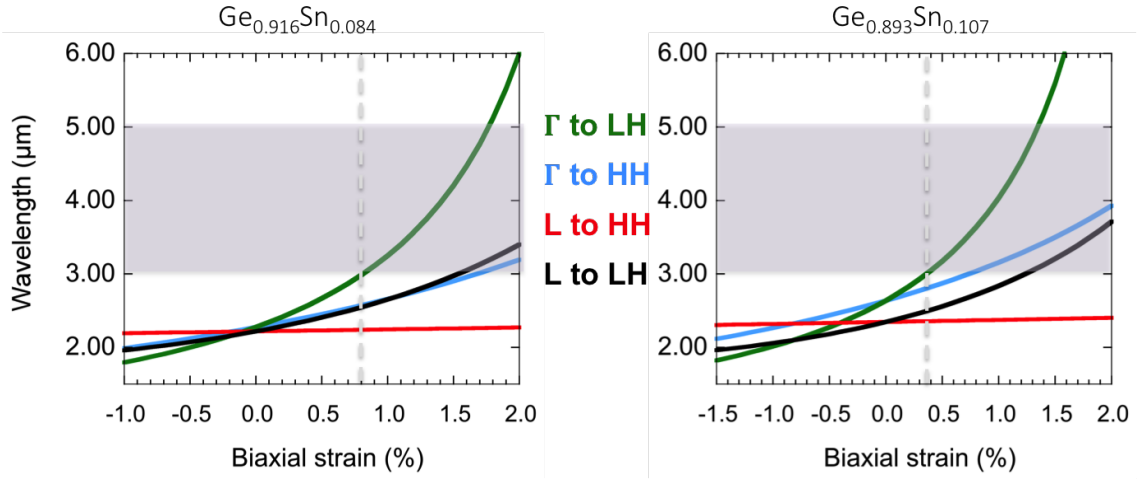

Figure 7.25: GeSn interband transitions as a function of biaxial strain. The 3 - 5 μm sensing window is shaded on the plot. The corresponding strain required for a transition to reach this window is marked with a dashed line.

This highlights the potential for GeSn layers to be used in the MIR for Gas sensing. In practise, longer wavelength devices may be limited to light emitting diodes (LEDs) opposed to lasers, as with high levels of strain splitting in the valence band, intra-valence absorption losses can begin to impede the possibility of lasing as the LH to SO energy difference approaches that of the direct transition [128]. Nevertheless, the fact that fully

pseudomorphic layers can be strained to emit at $\sim$ 3 μm, gives confidence that thicker, more relaxed epilayers (as grown) can be strained to emit further into the MIR. This can be observed looking at the deformation potentials in Fig. 7.25, where the 3 - 5 μm regime has been marked in the shaded region for each alloy. Considering partially relaxed GeSn layers, with residual compressive stresses of $\sim$ 0.57 % (as in [11]), a swing in the strain state of up to 2 % would allow for the entire 3 - 5 μm region to be covered.

7.7 Conclusion

To conclude, 40 nm thick GeSn alloys were grown on 650 nm thick Ge virtual substrates, on a Si (100) substrate. The epilayers were characterised by XRD and found to have Sn contents of 8.4 and 10.7 %, with compressive strains of 1.1 and 1.44 % respectively. While the 10.7 % alloys should be direct bandgap when relaxed, the high compressive strain means that indirect transitions are observed. This was confirmed by comparing the low temperature PL of both emission alloys, with both materials showing extremely comparable behaviour in terms of the relative integrated PL intensity and the width of the peak. The Raman strain shift coefficient was found to be 420 cm^{-1}, by using a Sn shift coefficient of 83.1 [137] and the in-plane strain measured by XRD.

The techniques developed in Chapter 6 were used to fabricate undercut GeSn/Ge microdisks, which causes a small relaxation in the GeSn alloy. Raman spectroscopy showed that a tensile strain could be induced with the application of silicon nitride stressors.

It was found that incorporating Al_2O_3 layers significantly improved the strained PL intensities, when incorporated before stressor deposition. The inclusion of such layers resulted in an emission increase of $\sim$ 17.5 times. Using the developed processes a range of microdisk diameters were fabricated for the 8.4 % and 10.7 % alloys, with diameters from 10 to 3 μm. A progression in the red-shift was observable for both samples, and it appeared that the presence of the two peaks in the 10.7 % GeSn sample is due to the modulation of the spectra by an absorption line. Nevertheless, emission $>$ 3 μm could be observed, which to my knowledge is the longest wavelength demonstrated from GeSn alloys.

Temperature dependent PL measurements showed a significant difference between unstrained and strained 10.7 % Sn disks, with the latter showing a relative intensity increase of $\sim$ 7 times at 20 K compared to 300 K. For the 8.4 % strained disks, a similar

trend was present however with a less marked intensity increase, suggesting that this behaviour does indeed scale with the level of directness. It was observed however, that the unstrained disks showed a different temperature dependence to the epilayer structures, suggesting that the non-radiative lifetime difference that is likely caused by the dry etch process can give rise to a change in low temperature behaviour. This in turn suggests that care has to be taken when interpreting the temperature dependence. The low temperature PL measurements revealed a higher energy (shorter wavelength) peak, that appeared to scale in intensity with the level of proximity to the direct transition in energy. The strain from Raman spectroscopy, and the peak PL position of the long wavelength peak showed excellent agreement with the Γ to LH transition, however the short wavelength peak could not be identified as an interband transition. It is tentatively stated that the transition could be due to an indirect transition, due to the high level of injection into the L valley when using a 2.33 eV optical pump. The scaling in intensity could be attributed to the increased probability of scattering to the Γ band with increased levels of directness. However, as stated, the peak position did not agree well with the L to HH transition, suggesting either more work is required to reduce the discrepancy of bandgap bowing parameters, or that the peak is due to another, currently unknown transition. In future work, this could be tested by using a pump with an energy closer to that of the direct bandgap.

Finally, the emission from a 3 μm diameter 10.7 % Sn microdisk was shown to cover the methane absorption lines, which is suggestive that strained GeSn technologies could be used for group IV compatible gas sensing in the MIR.

8

Conclusions and Future Work

8.1 Conclusion

The bottleneck caused by the losses of metal interconnects in modern ICs has led to an increased drive into the research of Si compatible light sources, in order to provide on chip, or chip to chip optical communication. Ideally such a component could be monolithically integrated on a Si platform. This cannot be easily achieved with direct bandgap III-V materials, which generally have to be flip-chip bonded to Si substrates and are therefore not suitable for large scale integration. Ge was seen as an interesting candidate for a Si compatible light source, as it has been used extensively in CMOS processes for strained SiGe channels. While it is an efficient absorber, Ge has inherently poor optical emission properties, due to an indirect bandgap. The direct bandgap, however, is only 140 meV above the indirect band. This energy difference can be overcome by filling the L-valley states with carriers from degenerate n-type doping, leading to an increased carrier concentration at the Γ. This technique led to the demonstration of the first optically and electrically pumped Ge lasers, however these devices had high lasing thresholds due to the associated free carrier and intra-valence band losses, and since then researchers have focused on investigating means of increasing the Γ valley concentration, and lowering these thresholds. This can be achieved by the application of biaxial tensile strain, or by alloying Ge with Sn, both of which lower the energy of the Γ band at a greater rate than the indirect L-valley, eventually transforming Ge into a direct bandgap material. For biaxial tensile strain, the crossover to direct bandgap was predicted to be between 1.6 and 2 %, with recent experimental evidence suggesting values closer to the lower bound.

It is only recently that CVD techniques have allowed for the growth of device grade GeSn layers with sufficient Sn contents for a transition to direct bandgap ($\sim$ 9 %), and lasing has since been demonstrated in Fabry-Perot cavities and microdisks at low temperatures [11, 12].

For GeSn layers, the application of tensile strain was predicted to further improve the potential gain, and the combination of techniques can allow for a monolithic Si compatible light-source with a tunable operating wavelength. In this work, the process induced straining of Ge and GeSn alloys was studied by using high stress silicon nitride stressor technologies. Such technologies are of significant interest as, like Ge, they have already been incorporated in CMOS process flows for the strain induced mobility enhancement of p-channel transistors. The conclusions of the results chapters are presented below, and the future investigations required to progress the work are subsequently detailed.

8.1.1 Tensile strained Ge nanopillars

In Chapter 5, a high compressive stress silicon nitride process was developed and characterised. Mid-infrared (MIR) transmission measurements showed that with increased stress there is an increase in the concentration of N-H bonds, which have absorption due to a vibrational stretching mode at $\sim$ 3 μm. When such layers are deposited on wafers or nano or micro-patterned structures, the compressive stress in the film relaxes, inducing a tensile strain in the underlying feature. These films were deposited on Ge nanopillar structures, in order to investigate the strained photoluminescence (PL) and measure the energies of the interband transitions. Absorption measurements were neglected to avoid the complexities added by periodic arrays.

Processing techniques were developed to promote adhesion of the high stress layer, which were initially found (by transmission electron microscope (TEM) images) to have only partial adhesion to nano-features. This was not detectable by scanning electron microscope (SEM) images. These processes were applied to Ge nanopillars, with varying film stress and pillar size. The strain from PL measurements suggested peak biaxial equivalent tensile strains of 1.35 % in 200 x 200 nm square top pillars, and $\sim$ 0.9 % in 300 x 300 nm structures. The corresponding emission intensity expected with strain, however, was not observed. This was in part attributed to the polarisation dependence of the emission, as the Γ to LH transition becomes highly polarised with the electric field

perpendicular to the strain axis, meaning that emission propagates in the sample plane. The remaining discrepancy was attributed to the poor electrical properties of the silicon nitride adhesion and stressor layers, which serves to counteract the enhanced electron concentration at the direct band from strain.

The strain in 300 nm pillars was confirmed by Raman spectroscopy, however the spatial resolution of the system did not allow for the observation of clear Raman spectra from the 200 nm pillars. Finite element modelling was used to model the strain distribution in the pillars, including the presence of high stress nitride layers on the pillar sidewalls. The models were in good agreement with experiment in terms of the calculated Raman line and the Γ to LH transition for the 300 x 300 nm pillar structures. Interestingly, it was found that there is an increased hydrostatic strain component in the structures due to the effect of tension in the z-direction, which decreases the Γ to L valley energy gap at a greater rate than pure biaxial strain. The nextnano3 package was used to calculate the effective masses under tensile strain, and used to model the injection required for the electron quasi-Fermi level to reach the Γ valley based on Fermi-Dirac statistics. The corresponding loss from free carrier absorption was calculated, and it was shown that increasing the hydro-static component results in a significant increase in the carrier concentration at the Γ, along with a reduction in free carrier losses. At the time of publication [144], these PL measurements demonstrated a larger red-shift than other works using silicon nitride stressor techniques.

8.1.2 Tensile strained Ge micro-cavities.

In Chapter 6, strained and undercut Ge on Si micro-cavities were investigated, which are capable of guiding an optical mode. Wet etching in TMAH and IPA was used to undercut the cavities, which has extremely high selectivities between Ge and Si, allowing for a mask-less, CMOS compatible process. 4, 5 and 6 μm diameter microdisks, undercut by $\sim$ 1300 nm, with 2.45 GPa stressor layers were initially measured and showed highly red-shifted emission towards the TE-InGaAs detector cut-off of 2.5 μm. Low Q Fabry-Perot (FP)-like resonances were observed from across the disk diameter but no whispering gallery modes could be observed in the photoluminescence. The FP resonance obscured interband transitions but based on the spectral position of the highest energy resonance, the strain from PL was estimated to be approximately 2 % for the 4 μm disks. A huge relative Raman shift of $\sim$ 9.9 cm^{-1} was observed for this structure, confirming a tensile

strain of $\sim$ 2.3 % at the top $\sim$ 10 nm of the disk, which is the depth probed by the 532 nm source. This is higher strain than other demonstrations using these techniques, and theoretically large enough for the transition to a direct-bandgap material, based on deformation potential theory.

A further range of micro cavities were investigated, including ring and racetrack structures. Micro-ring structures were used in order to evaluate if the reduced lateral dimensions compared to microdisks would be more conducive for a higher and more homogeneous in-plane strain transfer. Furthermore, it was considered that there would be potential for undercut microrings to be scaled to allow design of coupling segments to bus waveguides, and diameters tuned to adjust bending losses and the free spectral range. It was found that the anisotropy of the TMAH wet etch allowed for the creation of novel, partially free standing cavities, as the etch undercuts waveguide segments lying in the [100] direction at a greater rate than those in the [110] direction.

The photoluminescence of microdisks and rings with 4, 5 and 6 μm diameter were measured as a function of the size of the undercut etch. The emission wavelength, and the strain at the top plane was found to increase with increasing undercut. Interband transitions could be more easily discerned with the ring samples due the removal of the broad FP modes, and what has been attributed to Γ to LH transitions were observed towards the detector cut-off of 2.5 μm for the smallest structures, with the largest undercuts. Raman spectroscopy showed comparable strains for the disk and rings at small diameters, however towards larger diameters the in-plane strain in the rings appeared more homogeneous. Raman maps of 4 to 20 μm diameter rings with a constant waveguide width showed that the in-plane strain reduces as the larger diameters inhibit a biaxial-like strain distribution, with the strain tending to uniaxial in the direction transverse to the waveguide segment.

Cross sectional TEM images of the highest strained microdisk showed a large vertical deflection at the disk edge of $\sim$ 150 nm. Finite element models of the 4 μm disk, calibrated with the TEM measurement, showed an in-plane biaxial strain of 2.1 % at the top plane, therefore in excellent agreement with the Raman measurement. These models were used to investigate the strain field in the regions of the disk inaccessible to experiment. It was found that in circular geometries, there is a uniaxial strain components acting in the radial direction around the disk circumference. When this lies in the [110] directions it induces off diagonal shear strains, which remove the glide symmetry of the crystal and induce

an energy splitting of the L valley. This splitting has a detrimental effect on the carrier concentration at the Γ point, and therefore also on potential optical gain. These shear strain components have been considered for straight waveguides but their presence has so far been neglected in the literature for such resonator structures. In ring structures, the increased uniaxial component at larger diameters, translates to increased shear strains when the waveguide segment lies in the [110] direction. The shear strain component was found to scale with increasing diameter, suggesting that the apparent advantages of higher strain uniformity compared to disk structures is negated by the increased L-valley splitting. Therefore, microdisk structures are most suitable for high strain applications. It was shown by finite difference time domain modelling in the Lumerical software package, that higher order whispering gallery modes can be supported with field maxima away from the shear strained region of 4 μm diameter microdisks.

It was expected that a high vertical strain gradient would be present, from modelling in [171]. This was confirmed using the finite element models of the 4 μm disk in this work. Here however, the top 170 nm of the disk possesses biaxial tensile strains $> 1\%$, compared to the 1.3 % strain at the top plane in other work. These cavities should be capable of exhibiting modal gain, which, as discussed in the future work section, requires further quantification. Race-track structures provide an alternative cavity structure where reduced strain is required, for instance in partially relaxed GeSn structures. Such cavities give flexibility to design coupling segments and allow for high strain transfer, but with a partial Si post on the waveguide underside, thereby giving the prospect of electrically contacting directly underneath a highly strained waveguide segment.

8.1.3 Tensile Strained GeSn alloys

In Chapter 7, tensile strained GeSn alloys were demonstrated using silicon nitride stressors, producing emission in the mid-infrared, > 3 μm. To my knowledge, tensile strained GeSn alloys have not been demonstrated by such techniques, and emission past 2.6 μm has not been reported. In this work, this was achieved using 40 nm thick GeSn alloys, which were grown pseudomorphically on 650 nm thick Ge virtual substrates, on (100) Si substrates (Maksym Myronov - University of Warwick). The epilayers were characterised by XRD and found to have Sn contents of 8.4 and 10.7 %, with compressive strains of

1.1 and 1.44 % respectively. While the 10.7 % alloys should be direct bandgap when relaxed, the high compressive stress means that the material is indirect as grown. This was confirmed by comparing the low temperature PL of both alloys. Both materials showed extremely comparable behaviour in terms of the relative integrated PL intensity at low temperature, and the corresponding FWHM of the PL emission. The Raman strain shift coefficient was measured, and found to be 420 cm^{-1}, by using a Sn shift coefficient of 83.1 cm^{-1} and using the in-plane strain measured by XRD.

GeSn/Ge microdisk cavities were fabricated and undercut by TMAH wet etching techniques, which induces a small relaxation of the GeSn layer due to the high levels of elastic energy in the alloy. The samples were coated with high stress silicon nitride layers, and Raman measurements demonstrated tensile strain for both alloy concentrations. Initial PL measurements at room temperature showed highly red-shifted emission past 3 μm wavelength for 10.7 % alloys, but the emission intensities were lower than that of the unstrained samples, and interband peaks were difficult to discern from the tail of blackbody radiation. It was found that ALD deposited AL_2O_3 layers significantly improved the PL intensities when integrated into layer stacks before the high stress depositions, and given anneals in forming gas. The emission intensity of 10.7 % Sn strained microdisks with AL_2O_3 passivation showed a $\sim$ 17.5 times intensity increase compared to those without, indicating a reduction in surface recombination velocities. The PL from the passivated sample showed increased intensities compared to the unstrained sample, and emission at 3 μm wavelength.

Using the developed processes a range of undercut microdisk diameters were fabricated for the 8.4 % and 10.7 % alloys, with diameters from 10 to 3 μm. A progression in the red-shift was observable for both samples, and it appeared that for the 10.7 % Sn alloys, the highest strained disks had spectra which were modulated by an absorption line at $\sim$ 3.1 μm, close to that of the N-H vibration in the silicon nitride stressor. Nevertheless, emission $>$ 3 μm could be observed, which is believed to be the longest wavelength emission demonstrated by GeSn alloys. This demonstrates that fully pseudomorphic GeSn alloys on Ge can be made direct bandgap by the application of tensile strain, which is significant as these layers have minimal threading and misfit dislocations compared to partially relaxed GeSn alloys. From deformation potential theory and the band-gap bowing parameters used in ref [11], this suggests that the highest strained disks are direct

by as much as 85 meV. This is hugely significant, as the Γ to L energy has been cited as a roadblock for room temperature lasing [127].

Temperature dependent PL measurements showed a significant difference between unstrained and strained GeSn disks. The 10.7 % disks showed increased integrated PL intensities at low temperature compared to the unstrained disks, which is a hallmark of a transition to a direct bandgap. For the 8.4 % strained disks, a similar trend was present however with a less marked intensity increase, suggesting that this behaviour scales with the level of directness, in keeping with [11]. It was observed however, that the unstrained disks showed a different temperature dependence to the unpatterned epilayers, suggesting that the non-radiative lifetime difference that is likely caused by the dry etch process can give rise to a change in low temperature behaviour. This in turn suggests that care has to be taken when interpreting the temperature dependence.

The temperature dependent PL measurements also revealed a higher energy (shorter wavelength) peak emerging at low temperatures, which appeared to scale in intensity with the level of proximity in energy to the direct transition. The strain from Raman spectroscopy, and the peak PL position of the long wavelength peak showed excellent agreement with the Γ to LH transition, however the short wavelength peak could not be identified as an interband transition. It is tentatively ascribed that the transition could be due to an indirect transition, due to the high level of injection into the L valley when using a 2.33 eV PL pump. The scaling in intensity could be attributed to the increased probability of scattering to the Γ band with increased levels of directness. However, as stated, the peak position did not agree well with the L to HH transition, suggesting either more work is required to reduce the discrepancy of bandgap bowing parameters, or that the peak is due to another, currently unknown transition. In future work, this could be tested by using a pump with an energy closer to that of the direct bandgap.

Finally, the room temperature PL from a 3 μm diameter 10.7 % Sn microdisk with $\sim$ 0.45 % tensile strain was shown to have good overlap with the methane absorption line at $\sim$ 3.26 μm, suggesting that there is excellent potential to use strained GeSn as a Si compatible source for MIR gas detection and sensing. For partially relaxed GeSn layers with high Sn contents, there is potential for emission to cover the full 3 - 5 μm sensing window, based on the levels of strain that have been demonstrated in this work. Gas sensing in the MIR has not been demonstrated using Group IV sources, and could have potential to

drastically decrease the costs of MIR sensing, which have thus far relied on QCLs or expensive III-V materials. Given that the layers used in this work are pseudomorphic on Ge, the results represent the minimum that is achievable using strain engineering techniques. The techniques demonstrated in this work could prove to be essential in developing room temperature GeSn lasers.

As discussed in the introduction, the effect of the longer wavelength emission for tensile strained Ge and GeSn effectively rules out integration with long haul optical fiber networks, which operates at 1550 nm wavelength. On chip, and chip to chip communication, however is still viable, and could utilise a range of available technologies. For the longest wavelength emission demonstrated in this work, passive elements such as waveguides could still use silicon on insulator platforms, which have been shown to be low loss up to ~ 3.4 μm [45]. Particularly for GeSn sources, however, passive Ge optics may be more suitable, as the Ge virtual substrate could potentially also be used for MIR waveguides, which have demonstrated low losses in the MIR [73]. Such technologies could allow for both optical interconnects, and MIR sensing in optical circuits.

8.2 Future work

The future work is now detailed, which would be conducive to further progressing the results obtained in this thesis. This has been broken broadly into categories, which are shown below.

8.2.0.1 Passivation

While highly strained Ge micro cavities have been demonstrated, and highly red-shifted emission was evidenced, the full extent to which the high stress layer degraded the internal quantum efficiency was not apparent until the later work with GeSn layers. Therefore, a primary focus of future work should be to integrate thermally grown GeO_2 passivation layers into high stress layer stacks.

The development of a thermal GeO_2 passivation for Ge has been achieved within the research group (Kevin Gallacher, Muhammad Mirza, Ross Millar) and has demonstrated increased photoluminescence intensities on Ge micro-crystals, Fig. 8.1 [15]. Other groups have shown a similar effect for unstrained Ge microdisks [183]. This indicates there is an

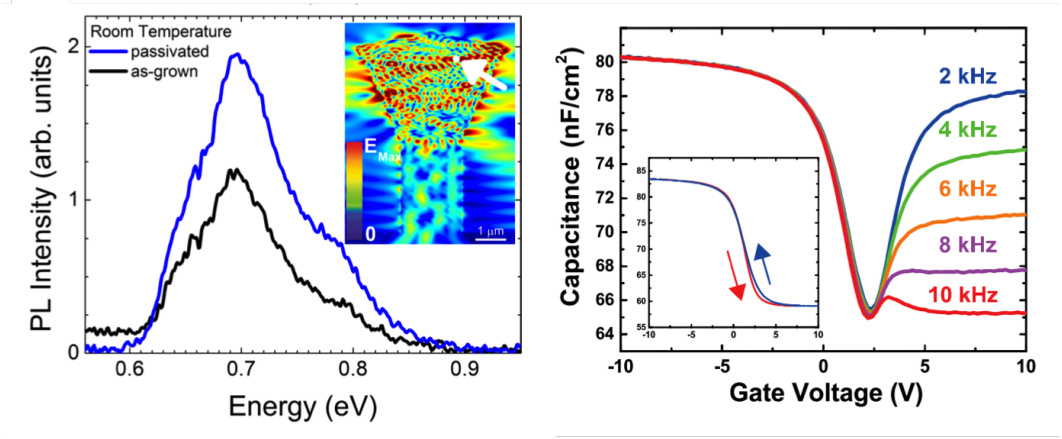

Figure 8.1: Left - Room temperature photoluminescence of Ge micro crystals with and without GeO_2 passivation. Right - room temperature capacitance voltage (CV) measurements for Ge metal oxide semiconductor capacitors with a silicon nitride/GeO_2 dielectric layer stack. The CV shows hysteresis < 300 mV and minimal frequency dispersion. Images from [15].

efficient reduction in the surface states, which leads to a loss mechanism at the interface. D_{it} values of $\sim 4.5 \times 10^{11}$ cm^{-2} eV^{-1} have been achieved by Fukuda et al, with GeO_2 layers [184].

Due to the water solubility of GeO_2, the thermally grown oxides require immediate capping by the subsequent deposition of a dielectric. ALD deposited layers are ideal for such an application, as the conformal growth allows for passivation (or capping) of the underside of undercut disks. Furthermore, it has been shown that a thin ALD deposited layer can subsequently have a thermally grown oxide grown underneath, effectively meaning that the oxide is inherently capped from the point of growth [185]. These techniques should be investigated for Ge on Si microdisk cavities, as to my knowledge, no other group has integrated efficient passivation layers under high stress silicon nitride stressors.

Furthermore, these developments will also allow for the investigation of nitride stressors on other Ge photonics components such as waveguide coupled photodiodes, and QCSE modulators. The strain induced band gap narrowing can potentially allow for compact Ge photodiodes, with increased absorption at 1550 nm wavelength. Moderate strain could also counter the blue shift from quantum confinement in QCSE devices, allowing for high contrast ratios at telecoms wavelengths. In order for such devices to be

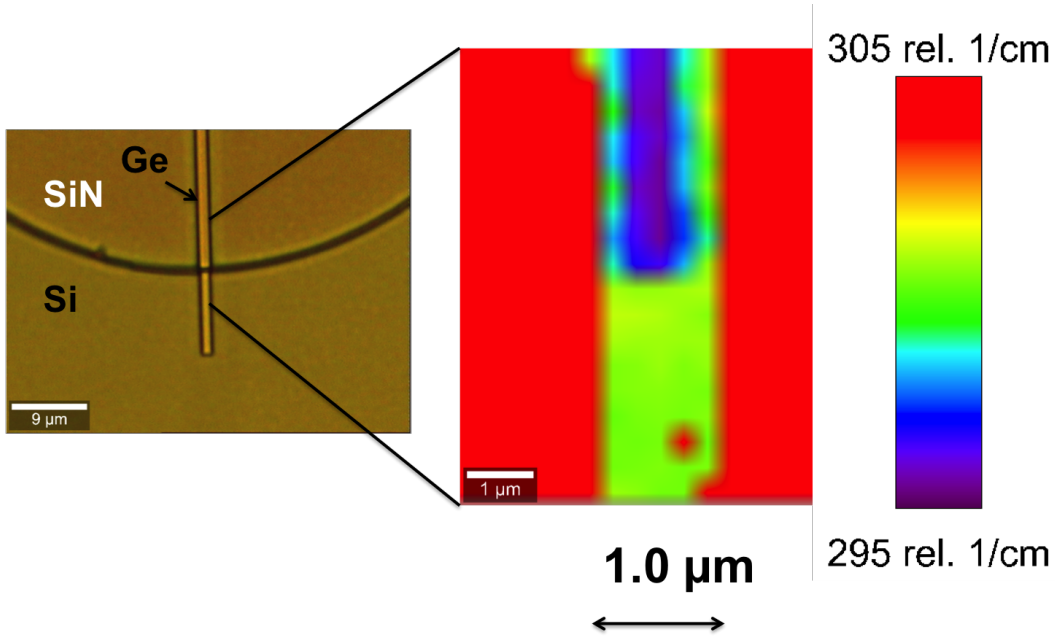

Figure 8.2: Optical image of a 1 μm wide Ge ridge etched down to the Si substrate, partially coated with a 300 nm thick high stress silicon nitride layer which has been deposited by a lift-off process. The image also shows a Raman map, highlighting the spectral position of the Raman line, therefore indicating that there is local tensile strain present under the nitride layer.

fabricated, further work will have to be carried out to incorporate metal contacts with the processing for high stress silicon nitride layers. This was investigated during the PhD, on p-i-n photodiode ridges. Even with the use of PECVD silicon nitride adhesion layers, the high stress layer cracked visibly over metal contacts, before via holes could be etched. It was found that, with the room temperature silicon nitride deposition, a lift-off process could be used to selectively deposit stressor layers, for example over Ge ridges. This is shown in Fig. 8.2, with Raman spectroscopy maps showing the local transfer of a high tensile strain. Such techniques could be used to enable the investigation of a range of photonics devices.

8.2.0.2 Ge microdisks

With regard to the microdisk structures in particular, a theoretical investigation will be required to account for the effect of the high vertical strain gradient of the structure.

Modelling in [10] showed that single layered stressors could provide a small net gain, based on a structure with only 1.3 % biaxial tensile strain at the top plane. This is suggestive that the higher strained cavities in this work should be capable of providing increased modal gain, however a detailed theoretical analysis would be required to quantify this. The calculated band-edges in the vertical direction (shown in Chapter 6) can be used to calculate the carrier concentration as a function of depth in the disk, based on the assumption that the carrier densities can be described by a single quasi-Fermi level in the conduction and valence bands - i.e. the bands are in a quasi-thermal equilibrium. This can be used to compute the free carrier absorption as a function of depth. For a given injection, the gain can then be computed using the model for absorption coefficient, with the addition of a population inversion term.

$$g(\hbar\omega) = \frac{\hbar e^2}{2\pi m_o c \varepsilon_o} \frac{1}{n_r} \frac{|p_{cv}|^2}{m_o} \left(\frac{2m_r}{\hbar^2}\right)^{3/2} (\hbar\omega - E_g)^{1/2}(1 + Fc - Fv) \tag{8.1}$$

This can be achieved by assuming parabolic bands, and using the transverse and longditudinal masses calculated by 8x8 k.p modelling. As described in Chapter 5, this can be expressed as a density of states mass for each band. These masses can then be used to compute the reduced masses (m_r), and therefore the joint density of states for Γ to HH and Γ to LH transitions. The quasi-Fermi levels are computed by inverting the Fermi integral (shown in Chapter 5), and the occupation probabilities for electrons and holes are evaluated at the conduction and valence band energies E_c' and E_v', which correspond to a transition at the photon energy, E_{ph}.

$$Ec' = Eg + (m_r/m_c)(E_{ph} - (E_c - E_v)) \tag{8.2}$$

$$Ev' = Ev - (m_r/m_c)(E_{ph} - (E_c - E_v)) \tag{8.3}$$

These energies are calculated using Eqs. 8.2 and 8.3, where E_c and E_v are the conduction and valence band edges. The fermi functions Fc and Fv are then evaluated at these energies for a given photon energy:

$$Fc(Ef_c, Ec') = \frac{1}{1 + exp((Ec' - Ef_c)/K_bT)} \tag{8.4}$$

$$Fv(Ef_v, Ev') = \frac{1}{1 + exp((Ev' - Ef_v)/K_bT)} \tag{8.5}$$

The modelling of gain in microdisk structures was underway but not sufficiently complete to include in this thesis, and should be completed for future work.

A further consideration has not so far been considered for strained Ge light emitters, is the modification to the index of Ge with applied strain. This has been demonstrated in modulators, using piezo electric materials to induce a strain in Ge [100], causing a phase shift in one arm of a Mach-Zehnder interferometer. Through Kamers-Kronig relationship, it can be shown that an increased absorption coefficient leads to a higher index. This could result in the preferential guiding of light in the highest strained regions of the disk, potentially improving modal overlap with the gain region.

Further experimental work could also be used to supplement these calculations. Time resolved pump probe measurements will be a key means of determining the extent to which such cavities can demonstrate lasing. Initially, thinner layers should be examined with more uniform strain, in order to quantify intra-valence band and free carrier absorptions, and potential gain available for a range of doping levels. The results can then allow for accurate calculations of modal gain, based on the strain distributions calculated by finite element modelling.

$$\omega_p = \left(\frac{n_e q^2}{m^* \epsilon_o}\right)^{\frac{1}{2}} \tag{8.6}$$

An alternative means of examining the carrier statistics at the surface is by measuring the reflectance due to the free carrier plasma frequency, Eq. 8.6 [168]. The plasma frequency is a function of both the carrier density, and the effective mass of the valley populated by the carriers. It was used by Carrol et al [79] to quantify the excess carrier concentration under injection for Ge epilayers, and could be extremely useful for measurements of strained Ge structures. In particular, due to the difference in effective masses, it is feasible that the reflectance could be fitted to evaluate the contributions from carriers populating the Γ and L valleys. By measuring this as a function of optical injection, and observing the point at which the Γ valley is populated, the Γ to L energy difference could be extracted. The opposite trend would be true of direct bandgap Ge or GeSn materials. This could also be measured as a function of the pump energy. As discussed in Chapter 7, the 532 nm wavelength pump has an energy of 2.33 eV, and can inject carries

directly into the L valley. Comparing this to a lower energy pump which is resonant with the direct band, the L to Γ valley phonon scattering could be better understood. These measurements pertain to both Ge and GeSn material systems.

8.2.1 GeSn

With regard to GeSn layers, further work is required to understand the processing limitations set by a given alloy concentration. A quantification of the thermal budgets will be required to facilitate fabrication and efficient passivation of GeSn devices. In particular, the formation of β-Sn precipitates needs to be monitored, as a function of anneal temperature and time. Anneals within the acceptable thermal range can then be used in the development of passivation using ALD deposited dielectrics. The quality of such passivation layers can be measured by means of CV, and X-ray photoelectron spectroscopy, and the corresponding effect on the carrier lifetime can be extracted by fitting to low temperature PL measurements. With regard to the material properties, it is clear that there is still some discrepancy in the bowing the parameters and possibly the deformation potential constants. While the Γ to LH transition appeared in excellent agreement with experiment in this work, there is still be a potential discrepancy in the point at which a crossover to direct bandgap is found, with recent reports showing a direct bandgap crossing at 6.7 % [186]. To quantify these parameters, a range of material growths would be required. In particular, a range of epilayer thicknesses of a constant alloy concentration would provide a range of different strains which could be accurately measured by XRD. The corresponding progression of photoluminescence could help verify deformation potential constants. This could be done for a number of Sn concentrations, alloying for further quantification of the direct and indirect bandgap bowing parameters. Once efficient passivation techniques have been demonstrated and thicker GeSn epilayers are grown, lasing in tensile strained GeSn should be investigated in microdisk cavities. The potential for improved gain compared to compressive or fully relaxed layers has been shown in the literature [5, 128, 129], and the strained samples should demonstrate lasing at higher temperatures than previous devices. The intra-valence band splitting will be important to measure, as reports have shown that above a particular tensile strain (Sn content dependent), the net gain should begin to degrade due to absorption from the SO band.

There should also be further work into the use of GeSn emitters for gas sensing. This could run in parallel with the investigation of Ge MIR waveguides, as GeSn emission could be routed on chip via Ge waveguides formed by the virtual substrate layer. High Q cavities can be implemented to allow for evanescent sensing of a gas with an absorption line at the emission wavelength.

8.2.2 Other work

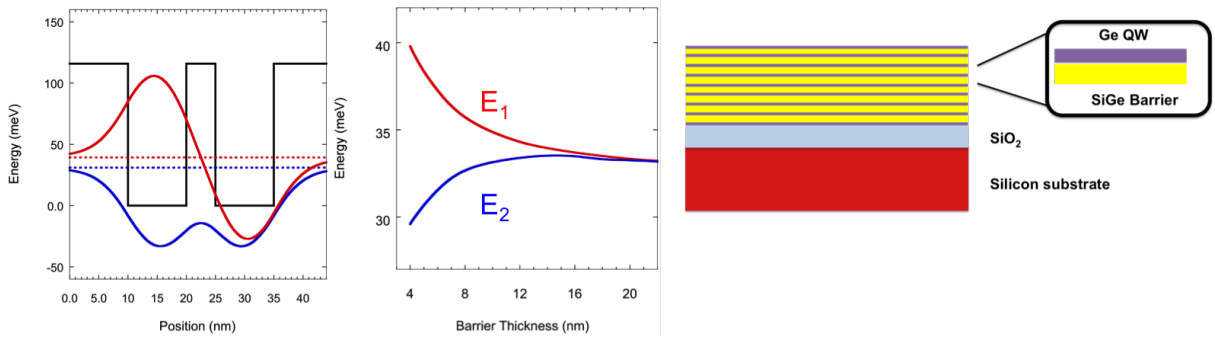

Figure 8.3: Left - calculated wave functions for 2 Ge quantum wells separated by a 4 nm thick SiGe buffer. The dashed lines indicate the eigenenergies of the wave-functions. Middle - The eigenenergies of the wave functions are plotted as a function of the barrier thickness, highlight the point at which the wells become highly coupled, which leads to the formation of mini bands. Right - An illustration of the MQW structure designed.

A number of other incomplete works were commenced during this PhD, which could also be the subject of future work. Strain balanced, n-type Ge/SiGe multiple quantum well wafers were designed, grown on both GeOI and SiGe graded buffer layers. These structures were grown by Andrea Bilbao (L-Ness laboratory, Politecnico di Milano). These have the advantage of reduced threading and misfit dislocations compared to Ge on Si structures. Multiple quantum wells have been a key step in the progression of III-V lasers, due to improved carrier confinement and differential gain compared to bulk devices. They could turn out to be key to Ge light emitter technologies, particularly as the 2 dimensional density of states could lead to a reduced carrier injection required to fill the L valley, before populating the Γ valley. The ground state in the Γ however does increase in energy. In order to investigate this, 3 samples with 10 nm n-Ge wells but with barrier thicknesses varying rom 4 to 20 nm were designed, in order to modify the density of function from

2D to more bulk like in highly coupled wells, Fig 8.3. The epilayers were found to show bright PL compared to GeOI wafers with identical doping. Future work should involve the fabrication of undercut microdisk cavities with silicon nitride stressor layers. The temperature dependence of the PL will be studied as a function of injection level in order to extracted the rate at which the L-valley fills.

Bibliography

[1] Gordon E. Moore. Cramming more components onto integrated circuits. *Proceedings of the IEEE*, 86(1):82–85, 1998. vii, 1, 2

[2] Jifeng Liu, Xiaochen Sun, Dong Pan, Xiaoxin Wang, Lionel C Kimerling, Thomas L Koch, and Jurgen Michel. Tensile-strained, n-type Ge as a gain medium for monolithic laser integration on Si. *Optics express*, 15(18):11272–7, sep 2007. vii, 3, 27, 29, 45, 46

[3] Moustafa El Kurdi, Guy Fishman, Sbastien Sauvage, and Philippe Boucaud. Band structure and optical gain of tensile-strained germanium based on a 30 band k.p formalism. *Journal of Applied Physics*, 107(1):013710, 2010. vii, 4, 45, 47, 118

[4] Samik Mukherjee, Kai Miao, Abhijeet Paul, Neophytos Neophytou, Raseong Kim, Junzhe Geng, Michael Povolotskyi, Tillmann Christoph Kubis, Arvind Ajoy, Bozidar Novakovic, James Fonseca, Hesameddin Ilatikhameneh, Sebastian Steiger, Michael McLennan, Mark Lundstrom, and Gerhard Klimeck. Band structure lab, May 2006. viii, 28

[5] Suyog Gupta, Blanka Magyari-Köpe, Yoshio Nishi, and Krishna C. Saraswat. Achieving direct band gap in germanium through integration of Sn alloying and external strain. *Journal of Applied Physics*, 113(7), 2013. ix, xviii, 40, 41, 59, 162, 181, 199

[6] Birendra Dutt, Devanand S. Sukhdeo, Donguk Nam, Boris M. Vulovic, and Krishna C. Saraswat. Roadmap to an Efficient Germanium-on-Silicon Laser: Strain vs. n-Type Doping. *IEEE Photonics Journal*, 4(5):2002–2009, oct 2012. x, 47

[7] M. J. Suess, R. Geiger, R. A. Minamisawa, G. Schiefler, J. Frigerio, D. Chrastina, G. Isella, R. Spolenak, J. Faist, and H. Sigg. Analysis of enhanced light emission from highly strained germanium microbridges. *Nat. Photon.*, 7(6):466–472, 06 2013. x, 48, 49

[8] David S Sukhdeo, Jan Petykiewicz, Shashank Gupta, Daeik Kim, Sungdae Woo, Youngmin Kim, Jelena Vučković, Krishna C Saraswat, and Donguk Nam. Ge microdisk with lithographically-tunable strain using CMOS-compatible process. *Optics Express*, 23(26):33249, 2015. x, 50, 51, 151

[9] G Capellini, C Reich, S Guha, Y Yamamoto, M Lisker, M Virgilio, A Ghrib, M El Kurdi, P Boucaud, B Tillack, and T Schroeder. Tensile Ge microstructures for lasing fabricated by means of a silicon complementary metal-oxide-semiconductor process. *Optics Express*, 22(1):399, 2014. x, 51, 52, 109, 114, 139

[10] Abdelhamid Ghrib, Moustafa El Kurdi, Mathias Prost, Sébastien Sauvage, Xavier Checoury, Grégoire Beaudoin, Marc Chaigneau, Razvigor Ossikovski, Isabelle Sagnes, and Philippe Boucaud. All-Around SiN Stressor for High and Homogeneous Tensile Strain in Germanium Microdisk Cavities. *Advanced Optical Materials*, 3(3):353–358, March 2015. x, 52, 53, 139, 149, 151, 197

[11] S. Wirths, R. Geiger, N. von den Driesch, G. Mussler, T. Stoica, S. Mantl, Z. Ikonic, M. Luysberg, S. Chiussi, J. M. Hartmann, H. Sigg, J. Faist, D. Buca, and D. Grützmacher. Lasing in direct-bandgap GeSn alloy grown on Si. *Nature Photonics*, 9(2):88–92, jan 2015. x, xix, 5, 41, 42, 57, 154, 155, 162, 164, 177, 182, 183, 185, 188, 192, 193

[12] Daniela Stange, Stephan Wirths, Richard Geiger, Christian Schulte-Braucks, Bahareh Marzban, Nils Von Den Driesch, Gregor Mussler, Thomas Zabel, Toma Stoica, Jean-Michel Hartmann, Siegfried Mantl, Zoran Ikonic, Detlev Grützmacher, Hans Sigg, Jeremy Witzens, and Dan Buca. Optically Pumped GeSn Microdisk Lasers on Si. *ACS Photonics*, 3(7):1279–1285, jul 2016. x, 5, 58, 188

[13] Stefano Carlo Cecchi. *Deposition and Characterization of Silicon-Germanium Heterostructures for Thermoelectric Devices*. PhD thesis, Politecnico di Milano, 2013. xi, 86

[14] Ross Millar, Kevin Gallacher, Jacopo Frigerio, Andrea Ballabio, Aneeqa Bashir, Ian MacLaren, Giovanni Isella, and Douglas J Paul. Engineering Large In-Plane Tensile Strains in Ge microdisks, Microrings and Racetrack Optical Cavities. *ECS Transactions*, 75(8):633–640, 2016. xv, xvi, 122, 145, 146

[15] Fabio Pezzoli, Anna Giorgioni, Kevin Gallacher, Fabio Isa, Paolo Biagioni, Ross W. Millar, Eleonora Gatti, Emanuele Grilli, Emiliano Bonera, Giovanni Isella, Douglas J. Paul, and Leo Miglio. Disentangling nonradiative recombination processes in Ge micro-crystals on Si substrates. *Applied Physics Letters*, 108(26), 2016. xix, 106, 165, 194, 195

[16] CISCO. The Zettabyte Era: Trends and Analysis. *Cisco*, (May 2015):1–29, 2015. 1

[17] J.S. Kilby. The integrated circuit's early history. *Proceedings of the IEEE*, 88(1):109–111, 2000. 1

[18] B Y M Mitchell Waldrop, O F Moore S Law, and More Interesting. More Than Will Soon Abandon Its Pursuit. *Nature*, 530:145, 2016. 1

[19] ICT Energy. ICT Energy Strategic Research Agenda. (611004):1–60, 2016. 1

[20] Hadi Esmaeilzadeh, Emily Blem, Renée St. Amant, Karthikeyan Sankaralingam, and Doug Burger. Dark silicon and the end of multicore scaling. *IEEE Micro*, 32(3):122–134, 2012. 2

[21] Gaurav Chandra, Pawan Kapur, and Krishna C Saraswat. Scaling trends for the on chip power dissipation. In *Proc of IEEE interconnect technology conference (IITC), Burlingame, CA*, pages 170–172, 2002. 2

[22] D.A.B. Miller and H.M. Ozaktas. Limit to the Bit-Rate Capacity of Electrical Interconnects from the Aspect Ratio of the System Architecture. *Journal of Parallel and Distributed Computing*, 41(1):42–52, feb 1997. 2

[23] D. Miller. Device Requirements for Optical Interconnects to Silicon Chips. *Proceedings of the IEEE*, 97(7):1166–1185, jul 2009. 2

[24] D.A.B. Miller. Rationale and challenges for optical interconnects to electronic chips. *Proceedings of the IEEE*, 88(6):728–749, jun 2000. 2

[25] F Y Gardes, D J Thomson, N G Emerson, and G T Reed. 40 Gb/s silicon photonics modulator for TE and TM polarisations. *Optics Express*, 19(12):11804, 2011. 2

[26] Yurii Vlasov and Sharee McNab. Losses in single-mode silicon-on-insulator strip waveguides and bends. *Optics express*, 12(8):1622–1631, 2004. 2

[27] Christopher T DeRose, Douglas C Trotter, William a Zortman, Andrew L Starbuck, Moz Fisher, Michael R Watts, and Paul S Davids. Ultra compact 45 GHz CMOS compatible Germanium waveguide photodiode with low dark current. *Optics express*, 19(25):24897–904, Dec 2011. 2, 44

[28] J. Van Campenhout, P. Rojo Romeo, P Regreny, C Seassal, D. Van Thourhout, S Verstuyft, L. Di Cioccio, J.-M. Fedeli, C Lagahe, and R Baets. Electrically pumped InP-based microdisk lasers integrated with a nanophotonic silicon-on-insulator waveguide circuit. *Optics Express*, 15(11):6744, 2007. 3

[29] Alexander W Fang, Hyundai Park, Oded Cohen, Richard Jones, Mario J Paniccia, and John E Bowers. Electrically pumped hybrid AlGaInAs-silicon evanescent laser. *Optics express*, 14(20):9203–9210, 2006. 3

[30] Roger Chen, Thai-Truong D. Tran, Kar Wei Ng, Wai Son Ko, Linus C. Chuang, Forrest G. Sedgwick, and Connie Chang-Hasnain. Supporting Info Nanolasers grown on silicon. *Nature Photonics*, 5(February):1–18, 2011. 3, 56

[31] Alan Y. Liu, Chong Zhang, Justin Norman, Andrew Snyder, Dmitri Lubyshev, Joel M. Fastenau, Amy W K Liu, Arthur C. Gossard, and John E. Bowers. High performance continuous wave 1.3 μ m quantum dot lasers on silicon. *Applied Physics Letters*, 104(4):3–7, 2014. 3

[32] Haisheng Rong, Ansheng Liu, Richard Jones, Oded Cohen, Dani Hak, Remus Nicolaescu, Alexander Fang, and Mario Paniccia. An All-Silicon Raman Laser. *Nature*, 433(7023):292–294, 2005. 3

[33] Haisheng Rong, Richard Jones, Ansheng Liu, Oded Cohen, Dani Hak, Alexander Fang, and Mario Paniccia. A continuous-wave raman silicon laser. *Nature*, 433(7027):725–728, 02 2005. 3

[34] T. J. Kippenberg, J. Kalkman, A. Polman, and K. J. Vahala. Demonstration of an erbium-doped microdisk laser on a silicon chip. *Physical Review A - Atomic, Molecular, and Optical Physics*, 74(5):72–75, 2006. 3

[35] A. Polman, B. Min, J. Kalkman, T. J. Kippenberg, and K. J. Vahala. Ultralow-threshold erbium-implanted toroidal microlaser on silicon. *Applied Physics Letters*, 84(7):1037–1039, 2004. 3

[36] Marvin L. Cohen and T. K. Bergstresser. Band structures and pseudopotential form factors for fourteen semiconductors of the diamond and zinc-blende structures, 1966. 4

[37] Jifeng Liu, Xiaochen Sun, Rodolfo Camacho-Aguilera, Lionel C. Kimerling, and Jurgen Michel. Ge-on-si laser operating at room temperature. *Opt. Lett.*, 35(5):679–681, Mar 2010. 4, 45, 122

[38] Rodolfo E Camacho-Aguilera, Yan Cai, Neil Patel, Jonathan T Bessette, Marco Romagnoli, Lionel C Kimerling, and Jurgen Michel. An electrically pumped germanium laser. *Optics express*, 20(10):11316–20, may 2012. 4, 122

[39] Roman Koerner, Michael Oehme, Martin Gollhofer, Marc Schmid, Konrad Kostecki, Stefan Bechler, Daniel Widmann, Erich Kasper, and Joerg Schulze. Electrically pumped lasing from Ge Fabry-Perot resonators on Si. *Optics express*, 23(11):14815–22, Jun 2015. 4, 46

[40] Chris G. Van de Walle. Band lineups and deformation potentials in the model-solid theory. *Phys. Rev. B*, 39:1871–1883, Jan 1989. 4, 42, 47

[41] A. R. Goi, K. Syassen, and M. Cardona. Direct-band-gap absorption in germanium under pressure. *Physical Review B*, 39(17):12921–12924, 1989. 4, 47

[42] M. V. Fischetti and S. E. Laux. Band structure, deformation potentials, and carrier mobility in strained Si, Ge, and SiGe alloys. *Journal of Applied Physics*, 80(4):2234, 1996. 4, 42, 47

[43] Kelin J. Kuhn, Anand Murthy, Roza Kotlyar, and Markus Kuhn. (Invited) Past, Present and Future: SiGe and CMOS Transistor Scaling. *IEEE Transactions on Electron Devices*, 54(9):3–17, 2010. 4, 44, 51

[44] Ravi Pillarisetty. Academic and industry research progress in germanium nanodevices. *Nature*, 479(7373):324–328, 2011. 5, 44

[45] Goran Z Mashanovich, Milan M Milošević, Milos Nedeljkovic, Nathan Owens, Boqian Xiong, Ee Jin Teo, and Youfang Hu. Low loss silicon waveguides for the mid-infrared. *Optics express*, 19(8):7112–7119, 2011. 6, 194

[46] Richard Soref. Mid-infrared photonics in silicon and germanium. *Nature Photonics*, 4(8):495–497, aug 2010. 6

[47] Mid IR Sensors Market shares Strategies and Forecasts Worldwide 2013 to 2019. http://www.prnewswire.com/news-releases/mid-ir-sensors-market-shares-strategies-and-forecasts-worldwide-2013-to-2019-264400631.html. Accessed: 2016-09-28. 6

[48] Federico Capasso, Jerome Faist, and Carlo Sirtori. Comments on quantum cascade lasers. *Physica Scripta*, T68:113–116, 1996. 6

[49] C. Davisson and L. H. Germer. Diffraction of electrons by a crystal of nickel. *Phys. Rev.*, 30:705–740, Dec 1927. 11

[50] C.C. Davis. *Lasers and Electro-optics: Fundamentals and Engineering*. Cambridge University Press, 1996. viii, 21

[51] Laura M. Giovane, Hsin-Chiao Luan, Anuradha M. Agarwal, and Lionel C. Kimerling. Correlation between leakage current density and threading dislocation density in SiGe p-i-n diodes grown on relaxed graded buffer layers. *Applied Physics Letters*, 78(4):541, 2001. 26

[52] R. Geiger, J. Frigerio, M. J. Süess, D. Chrastina, G. Isella, R. Spolenak, J. Faist, and H. Sigg. Excess carrier lifetimes in Ge layers on Si. *Applied Physics Letters*, 104(6):062106, feb 2014. 26, 91, 109, 125, 162

[53] Gennadii Levikovich. Bir and Grigorii Ezekielevich Pikus. *Symmetry and strain-induced effects in semiconductors [by] G. L. Bir and G. E. Pikus. With foreword by J. C. Hensel. Translated from Russian by P. Shelnitz. Translation edited by D. Louvish.* Wiley New York, 1974. 36

[54] Stefan Birner, Tobias Zibold, Till Andlauer, Tillmann Kubis, Matthias Sabathil, Alex Trellakis, and Peter Vogl. Nextnano: general purpose 3-d simulations. *IEEE Transactions on Electron Devices*, 54(9):2137–2142, 2007. 38

[55] Gareth Jones and Eoin P O Reilly. Improved Performance of Lone-Wavelength Strained Bulk-like Semiconductor Lasers. 29(5), 1993. 38, 42

[56] J. Menéndez and J Kouvetakis. Type-I Ge/Ge 1-x-ySi xSn y strained-layer heterostructures with a direct Ge bandgap. *Applied Physics Letters*, 85(7):1175–1177, 2004. 42

[57] J J Wortman and R A Evans. Young's modulus, shear modulus, and poisson's ratio in silicon and germanium. *Journal of Applied Physics*, 36(1):153–156, 1965. 42

[58] M. Tanenbaum, L. B. Valdes, E. Buehler, and N. B. Hannay. Silicon n-p-n grown junction transistors. *Journal of Applied Physics*, 26(6):686–692, 1955. 44

[59] Lorenzo Colace, Gianlorenzo Masini, and Gaetano Assanto. Ge-on-Si approaches to the detection of near-infrared light. *IEEE Journal of Quantum Electronics*, 35(12):1843–1852, 1999. 44, 85, 88

[60] Michael Jutzi, M Berroth, Gerd Wöhl, M Oehme, and E Kasper. Ge-on-Si vertical incidence photodiodes with 39-GHz bandwidth. *IEEE Photonics Technology Letters*, 17(7):1510–1512, 2005. 44

[61] Jurgen Michel, Jifeng Liu, and Lionel C. Kimerling. High-performance Ge-on-Si photodetectors. *Nature Photonics*, 4(8):527–534, jul 2010. 44

[62] Solomon Assefa, Fengnian Xia, and Yurii a Vlasov. Reinventing germanium avalanche photodetector for nanophotonic on-chip optical interconnects. *Nature*, 464(7285):80–4, Mar 2010. 44

[63] Nicholas J. D. Martinez, Christopher T. Derose, Reinhard W. Brock, Andrew L. Starbuck, Andrew T. Pomerene, Anthony L. Lentine, Douglas C. Trotter, and Paul S. Davids. High performance waveguide-coupled ge-on-si linear mode avalanche photodiodes. *Opt. Express*, 24(17):19072–19081, Aug 2016. 44

[64] Ryan E Warburton, Giuseppe Intermite, Maksym Myronov, Phil Allred, David R Leadley, Kevin Gallacher, Douglas J Paul, Neil J Pilgrim, Leon J M Lever, Zoran Ikonic, Robert W Kelsall, Edgar Huante-Ceron, Andrew P Knights, and Gerald S Buller. Ge-on-si single-photon avalanche diode detectors: Design, modeling, fabrication, and characterization at wavelengths 1310 and 1550 nm. *IEEE Transactions on Electron Devices*, 60(11):3807–3813, 2013. 44

[65] D. C. S. Dumas, K. Gallacher, S. Rhead, M. Myronov, D. R. Leadley, and D. J. Paul. Ge/sige quantum confined stark effect electro-absorption modulation with low voltage swing at $\lambda = 1550$ nm. *Opt. Express*, 22(16):19284–19292, Aug 2014. 44

[66] Yu-Hsuan Kuo, Yong Kyu Lee, Yangsi Ge, Shen Ren, Jonathan E Roth, Theodore I Kamins, David A B Miller, and James S Harris. Strong quantum-confined Stark effect in germanium quantum-well structures on silicon. *Nature*, 437(7063):1334–6, oct 2005. 44

[67] Papichaya Chaisakul, Delphine Marris-Morini, Mohamed-Said Rouifed, Jacopo Frigerio, Daniel Chrastina, Jean-René Coudevylle, Xavier Le Roux, Samson Edmond, Giovanni Isella, and Laurent Vivien. Recent progress in GeSi electro-absorption modulators. *Science and Technology of Advanced Materials*, 15(1):014601, feb 2014. 44

[68] J L Liu, W G Wu, Alexander Balandin, G L Jin, and K L Wang. Intersubband Absorption in Boron-Doped Multiple Ge Quantum Dots. *Applied Physics Letters*, 74(2):185–187, 1999. 44

[69] R. P G Karunasiri, J. S. Park, Y. J. Mii, and K. L. Wang. Intersubband absorption in Si1-xGex/Si multiple quantum wells. *Applied Physics Letters*, 57(24):2585–2587, 1990. 44

[70] J. S. Park, R. P G Karunasiri, and K. L. Wang. Intervalence-subband transition in SiGe/Si multiple quantum wells-normal incident detection. *Applied Physics Letters*, 61(6):681–683, 1992. 44

[71] K. Gallacher, A. Ballabio, R. W. Millar, J. Frigerio, a. Bashir, I. MacLaren, G. Isella, M. Ortolani, and D. J. Paul. Mid-infrared intersubband absorption from p-Ge quantum wells grown on Si substrates. *Applied Physics Letters*, 108(9):091114, Feb 2016. 44

[72] Usman Younis, Sudheer K. Vanga, Andy Eu-Jin Lim, Patrick Guo-Qiang Lo, Andrew A. Bettiol, and Kah-Wee Ang. Germanium-on-soi waveguides for mid-infrared wavelengths. *Opt. Express*, 24(11):11987–11993, May 2016. 44

[73] Milos Nedeljkovic, Jordi Soler Penadés, Colin J. Mitchell, Ali Z. Khokhar, Stevan Stanković, Thalia Dominguez Bucio, Callum G. Littlejohns, Frederic Y. Gardes, and Goran Z. Mashanovich. Surface-grating-coupled low-loss ge-on-si rib waveguides and multimode interferometers. *IEEE Photonics Technology Letters*, 27(10):1040–1043, 2015. 44, 143, 194

[74] Leonetta Baldassarre, Emilie Sakat, Jacopo Frigerio, Antonio Samarelli, Kevin Gallacher, Eugenio Calandrini, Giovanni Isella, Douglas J. Paul, Michele Ortolani, and Paolo Biagioni. Midinfrared Plasmon-Enhanced Spectroscopy with Germanium Antennas on Silicon Substrates. *Nano Letters*, 15(11):7225–7231, 2015. 44

[75] K. Gallacher, P. Velha, D. J. Paul, S. Cecchi, J. Frigerio, D. Chrastina, and G. Isella. 1.55 μm direct bandgap electroluminescence from strained n-ge quantum wells grown on si substrates. *Applied Physics Letters*, 101(21), 2012. 45

[76] Papichaya Chaisakul, Delphine Marris-Morini, Giovanni Isella, Daniel Chrastina, Nicolas Izard, Xavier Le Roux, Samson Edmond, Jean-Ren Coudevylle, and Laurent Vivien. Room temperature direct gap electroluminescence from Ge/Si0.15Ge0.85 multiple quantum well waveguide. *Applied Physics Letters*, 99(14):141106, 2011. 45

[77] Yijie Huo, Hai Lin, Robert Chen, Maria Makarova, Yiwen Rong, Mingyang Li, Theodore I. Kamins, Jelena Vuckovic, and James S. Harris. Strong enhancement of direct transition photoluminescence with highly tensile-strained Ge grown by molecular beam epitaxy. *Applied Physics Letters*, 98(1):96–99, 2011. 45, 47

[78] Rodolfo E Camacho-Aguilera, Yan Cai, Neil Patel, Jonathan T Bessette, Marco Romagnoli, Lionel C Kimerling, and Jurgen Michel. An electrically pumped germanium laser. *Opt. Express*, 20(10):11316–20, May 2012. 45

[79] Lee Carroll, Peter Friedli, Stefan Neuenschwander, Hans Sigg, Stefano Cecchi, Fabio Isa, Daniel Chrastina, Giovanni Isella, Yuriy Fedoryshyn, and Jérôme Faist. Direct-Gap Gain and Optical Absorption in Germanium Correlated to the Density of Photoexcited Carriers, Doping, and Strain. *Physical Review Letters*, 109(5):057402, aug 2012. 46, 47, 198

[80] Xiaoxin Wang, Lionel C. Kimerling, Jurgen Michel, and Jifeng Liu. Large inherent optical gain from the direct gap transition of Ge thin films. *Applied Physics Letters*, 102(13):131116, 2013. 46

[81] M. Virgilio, C. L. Manganelli, G. Grosso, G. Pizzi, and G. Capellini. Radiative recombination and optical gain spectra in biaxially strained n-type germanium. *Physical Review B*, 87(23):235313, jun 2013. 47

[82] Zhores Alferov. Double heterostructure lasers: Early days and future perspectives. *IEEE Journal on Selected Topics in Quantum Electronics*, 6(6):832–840, 2000. 47

[83] M. Prost, M. El Kurdi, a. Ghrib, S. Sauvage, X. Checoury, N. Zerounian, F. Aniel, G. Beaudoin, I. Sagnes, F. Boeuf, and P. Boucaud. Tensile-strained germanium microdisk electroluminescence. *Optics Express*, 23(5):6722, mar 2015. 47

[84] R. Jakomin, M. De Kersauson, M. El Kurdi, L. Largeau, O. Mauguin, G. Beaudoin, S. Sauvage, R. Ossikovski, G. Ndong, M. Chaigneau, I. Sagnes, and P. Boucaud. High quality tensile-strained n -doped germanium thin films grown on InGaAs buffer layers by metal-organic chemical vapor deposition. *Applied Physics Letters*, 98(9):6–9, 2011. 47

[85] Meera Chandrasekhar and Fred H. Pollak. Effects of uniaxial stress on the electroreflectance spectrum of Ge and GaAs. *Physical Review B*, 15(4):2127–2144, 1977. 48

[86] Jose R Sánchez-Pérez, Cicek Boztug, Feng Chen, Faisal F Sudradjat, Deborah M Paskiewicz, R B Jacobson, Max G Lagally, and Roberto Paiella. Direct-bandgap light-emitting germanium in tensilely strained nanomembranes. *Proceedings of the National Academy of Sciences of the United States of America*, 108(47):18893–8, nov 2011. 48

[87] Cicek Boztug, Jos R. Snchez-Prez, Jian Yin, Max G. Lagally, and Roberto Paiella. Grating-coupled mid-infrared light emission from tensilely strained germanium nanomembranes. *Applied Physics Letters*, 103(20):201114, 2013. 48, 50

[88] A.G Fallis. Etch Rates for Micromachining Processing. *Journal of Chemical Information and Modeling*, 53(9):1689–1699, 2013. 48

[89] C.-Y. Peng, C.-F. Huang, Y.-C. Fu, Y.-H. Yang, C.-Y. Lai, S.-T. Chang, and C. W. Liu. Comprehensive study of the Raman shifts of strained silicon and germanium. *Journal of Applied Physics*, 105(8):083537, 2009. 49

[90] Donguk Nam, David S. Sukhdeo, Shashank Gupta, Ju Hyung Kang, Mark L. Brongersma, and Krishna C. Saraswat. Study of Carrier Statistics in Uniaxially Strained Ge for a Low-Threshold Ge Laser. *IEEE Journal on Selected Topics in Quantum Electronics*, 20(4):16–22, jul 2014. 49, 109

[91] Y. Sun, S. E. Thompson, and T. Nishida. Physics of strain effects in semiconductors and metal-oxide-semiconductor field-effect transistors. *Journal of Applied Physics*, 101(10):1–22, 2007. 50, 109

[92] David S. Sukhdeo, Donguk Nam, Ju-Hyung Kang, Mark L. Brongersma, and Krishna C. Saraswat. Direct bandgap germanium-on-silicon inferred from 57% ?100? uniaxial tensile strain [Invited]. *Photonics Research*, 2(3):A8, apr 2014. 50

[93] Jan Petykiewicz, Donguk Nam, David S. Sukhdeo, Shashank Gupta, Sonia Buckley, Alexander Y. Piggott, Jelena Vučković, and Krishna C. Saraswat. Direct Bandgap Light Emission from Strained Germanium Nanowires Coupled with High-Q Nanophotonic Cavities. *Nano Letters*, page acs.nanolett.5b03976, 2016. 50

[94] A. Ghrib, M. de Kersauson, M. El Kurdi, R. Jakomin, G. Beaudoin, S. Sauvage, G. Fishman, G. Ndong, M. Chaigneau, R. Ossikovski, I. Sagnes, and P. Boucaud. Control of tensile strain in germanium waveguides through silicon nitride layers. *Appl. Phys. Lett.*, 100(20):201104, 2012. 51, 90, 114

[95] M de Kersauson, M El Kurdi, S David, X Checoury, G Fishman, S Sauvage, R Jakomin, G Beaudoin, I Sagnes, and P Boucaud. Optical gain in single tensile-strained germanium photonic wire. *Optics express*, 19(19):17925–34, sep 2011. 51, 114

[96] A. Ghrib, M. El Kurdi, M. de Kersauson, M. Prost, S. Sauvage, X. Checoury, G. Beaudoin, I. Sagnes, and P. Boucaud. Tensile-strained germanium microdisks. *Applied Physics Letters*, 102(22), 2013. 52

[97] Gary Shambat, Szu-Lin Cheng, Jesse Lu, Yoshio Nishi, and Jelena Vuckovic. Direct band Ge photoluminescence near 1.6?μm coupled to Ge-on-Si microdisk resonators. *Applied Physics Letters*, 97(24):241102, 2010. 52

[98] M. Prost, M. El Kurdi, a. Ghrib, S. Sauvage, X. Checoury, N. Zerounian, F. Aniel, G. Beaudoin, I. Sagnes, F. Boeuf, and P. Boucaud. Tensile-strained germanium microdisk electroluminescence. *Optics Express*, 23(5):6722, mar 2015. 52

[99] M. El Kurdi, M. Prost, A. Ghrib, A. Elbaz, S. Sauvage, X. Checoury, G. Beaudoin, I. Sagnes, G. Picardi, R. Ossikovski, F. Boeuf, and P. Boucaud. Tensile-strained germanium microdisks with circular Bragg reflectors. *Applied Physics Letters*, 108(9), 2016. 53, 57, 132, 148, 151, 163

[100] Michele Virgilio, Bernd Witzigmann, Gabriele Bolognini, Subhajit Guha, Thomas Schroeder, and Giovanni Capellini. CMOS-compatible optical switching concept based on strain-induced refractive-index tuning. *Optics express*, 23(5):5930–40, mar 2015. 54, 150, 198

[101] David Jenkins and John Dow. Electronic properties of metastable Ge_{x}Sn_{1-x} alloys. *Physical Review B*, 36(15):7994–8000, 1987. 54, 154

[102] K. Alberi, J. Blacksberg, L. D. Bell, S. Nikzad, K. M. Yu, O. D. Dubon, and W. Walukiewicz. Band anticrossing in highly mismatched Snx Ge1-x semiconducting alloys. *Physical Review B - Condensed Matter and Materials Physics*, 77(7):2–5, 2008. 55

[103] Wan Jian Yin, Xin Gao Gong, and Su Huai Wei. Origin of the unusually large band-gap bowing and the breakdown of the band-edge distribution rule in the Snx Ge1-x alloys. *Physical Review B - Condensed Matter and Materials Physics*, 78(16):1–4, 2008. 55, 154

[104] R. W. Olesinski and G. J. Abbaschian. The Ge-Sn (Germanium-Tin) system . *Bulletin of Alloy Phase Diagrams*, 5:265?271, June 1984. 55

[105] B. Predel. *Ge-Sn (Germanium-Tin): Datasheet from Landolt-Börnstein - Group IV Physical Chemistry · Volume 5F: "Ga-Gd – Hf-Zr" in SpringerMaterials (http://dx.doi.org/10.1007/10501684_1506).* Springer-Verlag Berlin Heidelberg. Copyright 1996 Springer-Verlag Berlin Heidelberg. 55

[106] B. Vincent, F. Gencarelli, H. Bender, C. Merckling, B. Douhard, D. H. Petersen, O. Hansen, H. H. Henrichsen, J. Meersschaut, W. Vandervorst, M. Heyns, R. Loo, and M. Caymax. Undoped and in-situ B doped GeSn epitaxial growth on Ge by atmospheric pressure-chemical vapor deposition. *Applied Physics Letters*, 99(15):7–10, 2011. 55, 56

[107] O. Gurdal, P. Desjardins, J. R. a. Carlsson, N. Taylor, H. H. Radamson, J.-E. Sundgren, and J. E. Greene. Low-temperature growth and critical epitaxial thicknesses of fully strained metastable Ge[sub 1?x]Sn[sub x] (x?0.26) alloys on Ge(001)21. *Journal of Applied Physics*, 83(1):162, 1998. 55

[108] E Kasper, M Kittler, M Oehme, and T Arguirov. Germanium tin: silicon photonics toward the mid-infrared [Invited]. *Photonics Research*, 1(2):69–76, 2013. 55

[109] Regina Ragan and Harry a. Atwater. Measurement of the direct energy gap of coherently strained Sn[sub x]Ge[sub 1?x]/Ge(001) heterostructures. *Applied Physics Letters*, 77(21):3418, 2000. 55

[110] Gang He and Harry A. Atwater. Interband Transitions in Sn_{x}Ge_{1-x} Alloys. *Physical Review Letters*, 79(10):1937–1940, 1997. 55

[111] S. Wirths, D. Buca, and S. Mantl. Si-Ge-Sn alloys: From growth to applications. *Progress in Crystal Growth and Characterization of Materials*, 62(1):1–39, 2016. 55

[112] Jennifer Taraci, John Tolle, J. Kouvetakis, M. R. McCartney, David J. Smith, J. Menendez, and M. A. Santana. Simple chemical routes to diamond-cubic germanium-tin alloys. *Applied Physics Letters*, 78(23):3607–3609, 2001. 55

[113] M. Bauer, J. Taraci, J. Tolle, A. V G Chizmeshya, S. Zollner, David J. Smith, J. Menendez, Changwu Hu, and J. Kouvetakis. Ge-Sn semiconductors for band-gap and lattice engineering. *Applied Physics Letters*, 81(16):2992–2994, 2002. 55

[114] Shotaro Takeuchi, Akira Sakai, Osamu Nakatsuka, Masaki Ogawa, and Shigeaki Zaima. Tensile strained Ge layers on strain-relaxed Ge1 - xSnx/virtual Ge substrates. *Thin Solid Films*, 517(1):159–162, 2008. 56

[115] F. Gencarelli, B. Vincent, L. Souriau, O. Richard, W. Vandervorst, R. Loo, M. Caymax, and M. Heyns. Low-temperature Ge and GeSn chemical vapor deposition using Ge 2H 6. *Thin Solid Films*, 520(8):3211–3215, 2012. 56

[116] R. Roucka, J. Mathews, R. T. Beeler, J. Tolle, J. Kouvetakis, and J. Menédez. Direct gap electroluminescence from Si/Ge1-y Sny p-i-n heterostructure diodes. *Applied Physics Letters*, 98(6), 2011. 56

[117] G. Grzybowski, R. T. Beeler, L. Jiang, D. J. Smith, J. Kouvetakis, and J. Menéndez. Next generation of Ge 1-ySn y (y = 0.01-0.09) alloys grown on Si(100) via Ge3H8 and SnD4: Reaction kinetics and tunable emission. *Applied Physics Letters*, 101(7):6–11, 2012. 56

[118] Joe Margetis, Seyed Amir Ghetmiri, Wei Du, Benjamin R Conley, Aboozar Mosleh, Richard Soref, Greg Sun, Lucas Domulevicz, Hameed A Naseem, Shui-Qing Yu, and John Tolle. Growth and Characterization of Epitaxial Ge1-XSnx Alloys and Heterostructures Using a Commercial CVD System. *Meeting Abstracts*, MA2014-02(6):1830, 2014. 56

[119] Robert Chen, Hai Lin, Yijie Huo, Charles Hitzman, Theodore I. Kamins, and James S. Harris. Increased photoluminescence of strain-reduced, high-Sn composition Ge 1-xSnx alloys grown by molecular beam epitaxy. *Applied Physics Letters*, 99(18):6–9, 2011. 56

[120] M. Oehme, M. Schmid, M. Kaschel, M. Gollhofer, D. Widmann, E. Kasper, and J. Schulze. GeSn p-i-n detectors integrated on Si with up to 4% Sn. *Applied Physics Letters*, 101(14), 2012. 56

[121] John Hart, Thomas Adam, Yihwan Kim, Yi Chiau Huang, Alexander Reznicek, Ramsey Hazbun, Jay Gupta, and James Kolodzey. Temperature varying photoconductivity of GeSn alloys grown by chemical vapor deposition with Sn concentrations from 4% to 11%. *Journal of Applied Physics*, 119(9), 2016. 56

[122] S. Gupta, B. Vincent, B. Yang, D. Lin, F. Gencarelli, J. Y J Lin, R. Chen, O. Richard, H. Bender, B. Magyari-Kope, M. Caymax, J. Dekoster, Y. Nishi, and K. C. Saraswat. Towards high mobility GeSn channel nMOSFETs: Improved surface passivation using novel ozone oxidation method. *Technical Digest - International Electron Devices Meeting, IEDM*, pages 375–378, 2012. 56

[123] Yuan Dong, Wei Wang, Xin Xu, Xiao Gong, Dian Lei, Qian Zhou, Zhe Xu, Wan Khai Loke, Soon-Fatt Yoon, Gengchiau Liang, and Yee-Chia Yeo. Germanium-Tin on Si Avalanche Photodiode: Device Design and Technology Demonstration. *IEEE Transactions on Electron Devices*, 62(1):128–135, Jan 2015. 56

[124] M Oehme, J Werner, M Gollhofer, M Schmid, M Kaschel, E Kasper, and J Schulze. Room Temperature Electroluminescence from GeSn Light Emitting pin Diodes on Si (August 2011). *IEEE Photonics Technology Letters*, 23(23):1751–1753, 2011. 56

[125] Suyog Gupta, Robert Chen, Yi Chiau Huang, Yihwan Kim, Errol Sanchez, James S Harris, and Krishna C Saraswat. Highly selective dry etching of germanium over germanium-tin (Ge 1-xSnx): A novel route for Ge1-xSnx nanostructure fabrication. *Nano Letters*, 13(8):3783–3790, 2013. 58, 160, 165

[126] Suyog Gupta, Robert Chen, James S. Harris, and Krishna C. Saraswat. Atomic layer deposition of Al2O3 on germanium-tin (GeSn) and impact of wet chemical surface pre-treatment. *Applied Physics Letters*, 103(24):10–14, 2013. 58, 170

[127] Richard Geiger. *Direct Band Gap Germanium for Si-compatible Lasing*. PhD thesis, Swiss Federal Institute of Technology Zurich, 2016. 59, 99, 110, 155, 193

[128] S. Wirths, Z. Ikonic, A. T. Tiedemann, B. Holländer, T. Stoica, G. Mussler, U. Breuer, J. M. Hartmann, A. Benedetti, S. Chiussi, D. Grützmacher, S. Mantl, and D. Buca. Tensely strained GeSn alloys as optical gain media. *Applied Physics Letters*, 103(19):0–5, 2013. 59, 60, 184, 199

[129] David S. Sukhdeo, Krishna C. Saraswat, Birendra, Dutt, and Donguk Nam. Theoretical Modeling for the Interaction of Tin alloying with N-Type Doping and Tensile Strain for GeSn Lasers. page 10, 2015. 59, 199

[130] Yiyin Zhou, Wei Dou, Wei Du, Thach Pham, Seyed Amir Ghetmiri, Sattar Al-Kabi, Aboozar Mosleh, Murtadha Alher, Joe Margetis, John Tolle, Greg Sun, Richard Soref, Baohua Li, Mansour Mortazavi, Hameed Naseem, and Shui Qing Yu. Systematic study of GeSn heterostructure-based light-emitting diodes towards mid-infrared applications. *Journal of Applied Physics*, 120(2):0–7, 2016. 59, 157, 175

[131] Qingfang Zhang, Yan Liu, Jing Yan, Chunfu Zhang, Yue Hao, and Genquan Han. Simulation investigation of tensile strained GeSn fin photodetector with Si_3N_4 liner stressor for extension of absorption wavelength. *Optics Express*, 23(2):739, 2015. 59

[132] Jane Hodgkinson and Ralph P Tatam. Optical gas sensing: a review. *Measurement Science and Technology*, 24(1):012004, 2013. 59

[133] Kuijun Wu, Faquan Li, Xuewu Cheng, Yong Yang, Xin Lin, and Yuan Xia. Sensitive detection of CO2 concentration and temperature for hot gases using quantum-cascade laser absorption spectroscopy near 4.2 μm. *Applied Physics B: Lasers and Optics*, 117(2):659–666, 2014. 59

[134] G Sun, R A Soref, and H H Cheng. Design of a Si-based lattice-matched room-temperature GeSn/GeSiSn multi-quantum-well mid-infrared laser diode. *Optics express*, 18(19):19957–65, Sep 2010. 59

[135] R. R. Lieten, J. W. Seo, S. Decoster, A. Vantomme, S. Peters, K. C. Bustillo, E. E. Haller, M. Menghini, and J. P. Locquet. Tensile strained GeSn on Si by solid phase epitaxy. *Applied Physics Letters*, 102(5):3–8, 2013. 60

[136] Wei Wang, Wan Khai Loke, Tingting Yin, Zheng Zhang, Vijay Richard D'Costa, Yuan Dong, Gengchiau Liang, Jisheng Pan, Zexiang Shen, Soon Fatt Yoon, Eng Soon Tok, and Yee-Chia Yeo. Growth and characterization of highly tensile strained Ge1?xSnx formed on relaxed InyGa1?yP buffer layers. *Journal of Applied Physics*, 119(12):125303, 2016. 60

[137] Robert Chen, Hai Lin, Yijie Huo, Charles Hitzman, Theodore I. Kamins, James S. Harris, R. Cheng, W. Wang, X. Gong, L. Sun, P. Guo, H. Hu, Z. Shen, G. Han, and Y.-C. Yeo. Relaxed and Strained Patterned Germanium-Tin Structures: A Raman Scattering Study. *ECS Journal of Solid State Science and Technology*, 2(4):P138–P145, 2013. 60, 160, 185

[138] Joel K W Yang, Bryan Cord, Huigao Duan, Karl K Berggren, Joseph Klingfus, Sung-Wook Nam, Ki-Bum Kim, and Michael J Rooks. Understanding of hydrogen silsesquioxane electron resist for sub-5-nm-half-pitch lithography. *Journal of Vacuum Science & Technology B: Microelectronics and Nanometer Structures*, 27(6):2622–2627, 2009. 63

[139] Schilp Andrea Laermer, Franz. Patent : Method of anisotropic etching of silicon. (6531068), March 2003. 69

[140] Kalpathy B Sundaram, Arun Vijayakumar, and Ganesh Subramanian. Smooth etching of silicon using TMAH and isopropyl alcohol for MEMS applications. *Microelectronic Engineering*, 77(3-4):230–241, 2005. 72, 128

[141] Jiro Yota. Effects of Deposition Method of PECVD Silicon Nitride as MIM Capacitor Dielectric for GaAs HBT Technology. *ECS Transactions*, 35(4):229–240, 2011. 74, 92

[142] Qingwei Li, Changhong Liu, Xueshen Wang, and Shoushan Fan. Measuring the thermal conductivity of individual carbon nanotubes by the Raman shift method. *Nanotechnology*, 20(14):145702, 2009. 74, 138

[143] Dieter K. Schroder. *Semiconductor Material and Device Characterization*. Wiley-Interscience, 2006. 80, 82

[144] R.W. Millar, K. Gallacher, A. Samarelli, J. Frigerio, D. Chrastina, G. Isella, T. Dieing, and D.J. Paul. Extending the emission wavelength of Ge nanopillars to 2.25 μm using silicon nitride stressors. *Opt. Express*, 23(14):18193–18202, Jul 2015. 90, 108, 189

[145] R. W. Millar, K. Gallacher, A. Samarelli, D. C. S. Dumas, J. Frigerio, D. Chrastina, G. Isella, and D. J. Paul. Process induced tensile strain of Ge on Si nanopillars by ICP-PECVD SiN stressor layers. In *11th International Conference on Group IV Photonics (GFP)*, pages 235–236, Aug 2014. 90

[146] R.W. Millar, K. Gallacher, A. Samarelli, J. Frigerio, D. Chrastina, T. Dieing, G. Isella, and D.J. Paul. Expanding the Ge emission wavelength to 2.25 μm with Si_xN_y strain engineering. *Thin Solid Films*, 602:60 – 63, 2016. The 9th International Conference on Silicon Epitaxy and Heterostructures. 90

[147] G. Capellini, C. Reich, S. Guha, Y. Yamamoto, M. Lisker, M. Virgilio, A. Ghrib, M. El Kurdi, P. Boucaud, B. Tillack, and T. Schroeder. Tensile Ge microstructures for lasing fabricated by means of a silicon complementary metal-oxide-semiconductor process. *Opt. Express*, 22(1):399–410, Jan 2014. 90, 143

[148] G. Isella, D. Chrastina, B. Rössner, T. Hackbarth, H.-J. Herzog, U. König, and H. von Känel. Low-energy plasma-enhanced chemical vapor deposition for strained Si and Ge heterostructures and devices. *Solid-State Electron.*, 48(8):1317–1323, August 2004. 91

[149] L Colace, G Masini, F Galluzzi, G Assanto, G Capellini, L. Di Gaspare, E Palange, and F Evangelisti. Metal-semiconductor-metal near-infrared light detector based on epitaxial Ge/Si. *Applied Physics Letters*, 72(24):3175–3177, 1998. 91, 157

[150] Rodolfo Camacho-Aguilera, Zhaohong Han, Yan Cai, Lionel C. Kimerling, and Jurgen Michel. Direct band gap narrowing in highly doped Ge. *Applied Physics Letters*, 102(15):152106, 2013. 91

[151] P.J French, P.M Sarro, R Mallée, E.J.M Fakkeldij, and R.F Wolffenbuttel. Optimization of a low-stress silicon nitride process for surface-micromachining applications. *Sensors and Actuators A: Physical*, 58(2):149–157, 1997. 92

[152] J Ashley Taylor. The mechanical properties and microstructure of plasma enhanced chemical vapor deposited silicon nitride thin films. *Journal of Vacuum Science & Technology A: Vacuum, Surfaces, and Films*, 9(4):2464, 1991. 92

[153] W. A. Lanford and M. J. Rand. The hydrogen content of plasma-deposited silicon nitride. *Journal of Applied Physics*, 49(4):2473, 1978. 94

[154] Michael Blech, Abdelazize Laades, Carsten Ronning, Bernd Schröter, Christian Borschel, Daniel Rzesanke, and Alexander Lawerenz. Detailed Study of PECVD Silicon Nitride and Correlation of Various Characterization Techniques. *24th European Photovoltaic Solar Energy Conference and Exhibition*, pages 507–511, 2009. 95

[155] L Wang, H S Reehal, F L Mart nez, E San Andr s, and A del Prado. Characterization of nitrogen-rich silicon nitride films grown by the electron cyclotron resonance plasma technique. *Semiconductor Science and Technology*, 18(7):633–641, 2003. 95, 96

[156] S C Mao, S H Tao, Y L Xu, X W Sun, M B Yu, G Q Lo, and D L Kwong. Low propagation loss SiN optical waveguide prepared by optimal low-hydrogen module. *Opt. Express*, 16(25):20809–20816, 2008. 95

[157] W Henschel, Y M Georgiev, and H Kurz. Study of a high contrast process for hydrogen silsesquioxane as a negative tone electron beam resist. *Journal of Vacuum Science & Technology B: Microelectronics and Nanometer Structures*, 21(5):2018, 2003. 101

[158] Muhammad M. Mirza, Donald A. MacLaren, Antonio Samarelli, Barry M. Holmes, Haiping Zhou, Stephen Thoms, Douglas MacIntyre, and Douglas J. Paul. Determining the Electronic Performance Limitations in Top-Down-Fabricated Si Nanowires with Mean Widths Down to 4 nm. *Nano Lett.*, 14(11):6056–6060, 2014. 101

[159] Y.P. Varshni. Temperature dependence of the energy gap in semiconductors. *Physica*, 34(1):149–154, 1967. 101

[160] Xuejun Xu, Hideaki Hashimoto, Kentarou Sawano, Hiroshi Nohira, and Takuya Maruizumi. Enhanced light emission from germanium microdisks on silicon by surface passivation through thermal oxidation. *Applied Physics Express*, 9(5):052101, 2016. 105

[161] F. Pezzoli, F. Isa, G. Isella, C.?V. Falub, T. Kreiliger, M. Salvalaglio, R. Bergamaschini, E. Grilli, M. Guzzi, H. von Känel, and L. Miglio. Ge Crystals on Si Show Their Light. *Physical Review Applied*, 1(4):044005, may 2014. 110, 163

[162] D.J Lockwood. *Light Scattering in Semiconductor Structures and Superlattices*, volume 273 of *NATO ASI Series*. Springer US, Boston, MA, 1991. 113

[163] Ingrid De Wolf, H. E. Maes, and Stephen K. Jones. Stress measurements in silicon devices through Raman spectroscopy: Bridging the gap between theory and experiment. *Journal of Applied Physics*, 79(9):7148–7156, may 1996. 115

[164] R. W. Millar, K. Gallacher, J. Frigerio, A. Ballabio, A. Bashir, I. MacLaren, G. Isella, and D. J. Paul. Analysis of Ge micro-cavities with in-plane tensile strains above 2 %. *Opt. Express*, 24(5):4365–4374, Mar 2016. 122

[165] R. W. Millar, K. Gallacher, J. Frigerio, D. Chrastina, G. Isella, and D. J. Paul. Highly strained Ge on Si microdisks with silicon nitride stressors. In *2015 IEEE 12th International Conference on Group IV Photonics (GFP)*, pages 65–66, Aug 2015. 122

[166] S. L. McCall, A. F J Levi, R. E. Slusher, S. J. Pearton, and R. A. Logan. Whispering-gallery mode microdisk lasers. *Applied Physics Letters*, 60(3):289–291, 1992. 123

[167] Moustafa El Kurdi, Mathias Prost, Abdelhamid Ghrib, Sebastien Sauvage, Xavier Checoury, Gregoire Beaudoin, Isabelle Sagnes, Gennaro Picardi, Razvigor Ossikovski, and Philippe Boucaud. Direct Band Gap Germanium Microdisks Obtained with Silicon Nitride Stressor Layers. *ACS Photonics*, 3(3):443–448, 2016. 123

[168] Marco P. Fischer, Christian Schmidt, Emilie Sakat, Johannes Stock, Antonio Samarelli, Jacopo Frigerio, Michele Ortolani, Douglas J. Paul, Giovanni Isella, Alfred Leitenstorfer, Paolo Biagioni, and Daniele Brida. Optical activation of ger-

manium plasmonic antennas in the mid-infrared. *Phys. Rev. Lett.*, 117:047401, Jul 2016. 125, 198

[169] K. Biswas and S. Kal. Etch characteristics of KOH, TMAH and dual doped TMAH for bulk micromachining of silicon. *Microelectronics Journal*, 37(6):519–525, June 2006. 128

[170] K. Tokoro, D. Uchikawa, M. Shikida, and K. Sato. Anisotropic etching properties of silicon in KOH and TMAH solutions. *MHA'98. Proceedings of the 1998 International Symposium on Micromechatronics and Human Science. - Creation of New Industry - (Cat. No.98TH8388)*, pages 65–70, 1998. 129

[171] A. Ghrib, M. El Kurdi, M. de Kersauson, M. Prost, S. Sauvage, X. Checoury, G. Beaudoin, I. Sagnes, and P. Boucaud. Tensile-strained germanium microdisks. *Appl. Phys. Lett.*, 102(22):221112, 2013. 149, 191

[172] E C S Transactions and The Electrochemical Society. Silicon And SiGe Alloys Wet Etching Using TMAH Chemistry V. Loup. 58(6):47–55, 2013. 150

[173] Abdelrahman Z. Al-Attili, Satoshi Kako, Muhammad K Husain, Frederic Y Gardes, Satoshi Iwamoto, Yasuhiko Arakawa, and Shinichi Saito. Tensile strain engineering of germanium micro-disks on free-standing SiO 2 beams. *Japanese Journal of Applied Physics*, 55(4S):04EH02, 2016. 151

[174] V. Palankovski, G. Kaiblinger-Grujin, and S. Selberherr. Study of dopant-dependent band gap narrowing in compound semiconductor devices. *Materials Science and Engineering B: Solid-State Materials for Advanced Technology*, 66(1):46–49, 1999. 151

[175] P. Moontragoon, R. A. Soref, and Z. Ikonic. The direct and indirect bandgaps of unstrained Si xGe 1-x-ySn y and their photonic device applications. *Journal of Applied Physics*, 112(7), 2012. 156

[176] F. Gencarelli, B. Vincent, J. Demeulemeester, A. Vantomme, A. Moussa, A. Franquet, A. Kumar, H. Bender, J. Meersschaut, W. Vandervorst, R. Loo, M. Caymax,

K. Temst, and M. Heyns. Crystalline Properties and Strain Relaxation Mechanism of CVD Grown GeSn. *ECS Journal of Solid State Science and Technology*, 2(4):P134–P137, 2013. 158, 159

[177] D. Stange, S. Wirths, N. von den Driesch, G. Mussler, T. Stoica, Z. Ikonic, J. M. Hartmann, S. Mantl, D. Grützmacher, and D. Buca. Optical Transitions in Direct-Bandgap Ge 1? x Sn x Alloys. *ACS Photonics*, 2(11):1539–1545, nov 2015. 163, 178, 179

[178] Li Shen, Noel Healy, Colin J. Mitchell, Jordi Soler Penades, Milos Nedeljkovic, Goran Z. Mashanovich, and Anna C. Peacock. Mid-infrared all-optical modulation in low-loss germanium-on-silicon waveguides. *Optics Letters*, 40(2):268, 2015. 167

[179] Robert Chen, Yi Chiau Huang, Suyog Gupta, Angie C. Lin, Errol Sanchez, Yihwan Kim, Krishna C. Saraswat, Theodore I. Kamins, and James S. Harris. Material characterization of high Sn-content, compressively-strained GeSn epitaxial films after rapid thermal processing. *Journal of Crystal Growth*, 365:29–34, 2013. 170

[180] Robert Chen, Yi Chiau Huang, Suyog Gupta, Angie C. Lin, Errol Sanchez, Yihwan Kim, Krishna C. Saraswat, Theodore I. Kamins, and James S. Harris. Material characterization of high Sn-content, compressively-strained GeSn epitaxial films after rapid thermal processing. *Journal of Crystal Growth*, 365:29–34, 2013. 171

[181] Xiaochen Sun, Jifeng Liu, Lionel C. Kimerling, and Jurgen Michel. Direct gap photoluminescence of n -type tensile-strained Ge-on-Si. *Applied Physics Letters*, 95(1), 2009. 177

[182] R. R. Lieten, K. Bustillo, T. Smets, E. Simoen, J. W. Ager, E. E. Haller, and J. P. Locquet. Photoluminescence of bulk germanium. *Physical Review B - Condensed Matter and Materials Physics*, 86(3):035204, jul 2012. 182

[183] Xuejun Xu, Hideaki Hashimoto, Kentarou Sawano, Hiroshi Nohira, and Takuya Maruizumi. Enhanced light emission from germanium microdisks on silicon by surface passivation through thermal oxidation. *Applied Physics Express*, 9(5):052101, 2016. 194

[184] Yukio Fukuda, Yuya Yazaki, Yohei Otani, Tetsuya Sato, Hiroshi Toyota, and Toshiro Ono. Low-temperature formation of high-quality GeO2 interlayer for high-κ gate dielectrics/Ge by electron-cyclotron-resonance plasma techniques. *IEEE Transactions on Electron Devices*, 57(1):282–287, 2010. 195

[185] Mitsuru Takenaka, Rui Zhang, and Shinichi Takagi. MOS interface engineering for high-mobility Ge CMOS. *IEEE International Reliability Physics Symposium Proceedings*, (V):1–8, 2013. 195

[186] Thomas R Harris, Mee-Yi Ryu, Yung Kee Yeo, Buguo Wang, C L Senaratne, and John Kouvetakis. Direct bandgap cross-over point of Ge1-ySny grown on Si estimated through temperature-dependent photoluminescence studies. *Journal of Applied Physics*, 120(8):85706, 2016. 199